FE DIC potential for the mechanical characterization of textile reinforcements

Taiwei Xu

To cite this version:

Taiwei Xu. FE DIC potential for the mechanical characterization of textile reinforcements. Material chemistry. Université Paul Sabatier - Toulouse III, 2023. English. NNT : 2023TOU30158 . tel-04382803

HAL Id: tel-04382803
https://theses.hal.science/tel-04382803

Submitted on 9 Jan 2024

THÈSE

En vue de l'obtention du

DOCTORAT DE L'UNIVERSITÉ DE TOULOUSE

Délivré par:
Université Toulouse 3 Paul Sabatier (UT3 Paul Sabatier)

Présentée et soutenue par :
Taiwei XU

le 19 Septembre 2023

Titre :
FE DIC potential for the mechanical characterization of textile reinforcements

---

École doctorale et discipline ou spécialité :
ED MEGEP : Génie mécanique, mécanique des matériaux

Unité de recherche :
Institut Clément Ader, CNRS UMR 5312

Directeur/trice(s) de Thèse :

Jean-Noël PÉRIÉ	MCF HDR, IUT de Toulouse	Directeur
Rébecca BONNAIRE	Maître assistant, IMT Mines Albi	Co-Directrice

Jury :

Michel CORET	PRU, École Centrale de Nantes	Rapporteur
Nahiene HAMILA	PRU, École Nationale d'Ingénieurs de Brest Bretagne	Rapporteur
Emmanuel DE LUYCKER	MCF, École Nationale d'Ingénieurs de Tarbes	Examinateur
Damien SOULAT	PRU, Ecole Nationale Supérieure des Arts et Industries Textiles	Examinateur

Acknowledgments

The doctoral studies have been a significant opportunity for me to gain a deeper understanding of my field of study and to develop a new perception of myself. This academic journey has played an important role in my life. As I near the completion of this journey, I reflect on the various challenges and experiences along the way, and I am reminded of how much help and support I have received from others. Without their encouragement, I would not have had the courage to embark on this unforgettable voyage, let alone overcome the numerous difficulties that I have faced. This brings to mind a famous quote: *"Ce qui est le plus pitoyable pour l'homme, c'est de ne pas avoir la connaissance et de ne pas pouvoir se contraindre. —— Montaigne "*

As I review my three years of doctoral studies, my heart is filled with gratitude and emotion, as it has been the most unforgettable experience along my life's journey. I am deeply appreciative of the immense support I have received from my supervisors, colleagues, family, and friends throughout this process. Before my thesis is completed, I would like to take this opportunity to express my sincere gratitude. No amount of words can truly capture the magnitude of my appreciation.

First and foremost, I would like to express my sincere gratitude to my supervisors, Mr. Jean-Noël Périé and Ms. Rébecca Bonnaire, for their invaluable guidance and meticulous supervision throughout the process of writing my thesis. Through their rigorous academic attitude and unwavering support, I not only learned the essence of academic research but also experienced their patience and genuine concern for their students' learning. Three years ago, when I was uncertain about my future direction after completing my master's degree, my supervisors provided me with the opportunity to continue my studies and have been guiding me along the right path ever since. Despite the challenges posed by the pandemic, my supervisors always went above and beyond to assist me in any way possible, saving me time and connecting me with their colleagues to address my academic queries. I deeply appreciate and admire their profound knowledge, rigorous attitude, and unwavering patience, and I am committed to continuing to learn from them throughout my life.

Furthermore, I am grateful for my supervisors' tolerance and patience in explaining complex concepts and alleviating my difficulties and challenges encountered during the progress of my dissertation. I sincerely apologize for any inconvenience I may have caused them during these three years, and I would like to express my deepest gratitude and utmost respect to both of them.

I would also like to extend my gratitude to my colleagues, Dr. Ali Rouwane and Dr. Raphaël Fouque. The initial phase of my PhD journey was particularly challenging, and in addition to the support from my supervisors, Ali and Raphaël also provided me

with invaluable assistance in addressing various academic inquiries. They were like elder brothers, patiently answering my questions and providing me with advice whenever needed. I sincerely thank them for their generosity in helping me and apologize for any disruptions I may have caused them. I am committed to learning from their expertise and incorporating greater rigor into my academic work.

I would like to express my sincere gratitude to Mr. Jean-Charles Passieux for his invaluable support in developing the program for my thesis. The Pyxel program, which was developed by Mr. Jean-Charles Passieux, proved to be the optimal choice in meeting the requirements of my thesis, which is based on the DIC-FE algorithm and necessitated program modifications. Whenever I encountered questions about the application of the program, Mr. Passieux generously provided assistance and answered my inquiries without hesitation. Additionally, he offered valuable advice tailored to the specific needs of my thesis.

I would like to extend my heartfelt appreciation to Mr. Michel Cavarero, Mr. Laurent Crouzeix, Mr. Tristan Mangeard, Mr. Olivier Cherrier, Ms. Nathalie Rocher Gleizes, Mr. Didier Adé, Mr. Jérôme Eydoux, and Mr. Jean-Michel Mouys for their invaluable assistance in conducting my experiments. Experimentation can be laborious yet immensely fascinating, and I am truly grateful to them for their technical and hardware support when I faced challenges, as well as their unwavering patience in helping me successfully complete my experiments. Collaborating with them has afforded me the opportunity to acquire knowledge and skills that are beyond the scope of textbooks. My sincere thanks to all of them.

Furthermore, I express my deep gratitude to Mr. Nicolas Laurien and intern Cherfils Laurent for their invaluable assistance in the final phase of my thesis. With the guidance of my two supervisors, they played a pivotal role in designing and fabricating the main support structure of the miniature tensile machine utilizing 3D printing technology. Their contribution has been instrumental in enhancing the quality of my thesis, and I am truly appreciative of their assistance.

Lastly, I extend my heartfelt appreciation to my laboratory, ICA - Clement Ader Institute, for providing me with an excellent working environment and state-of-the-art laboratory equipment, which were crucial in completing my thesis. I am also grateful to my colleagues in the laboratory for fostering a harmonious and enjoyable working atmosphere, and for enriching my experience with diverse cultural perspectives.

I am also deeply grateful to my parents for their unwavering support, especially during the challenging times when I was unable to reunite with them for three years due to the ongoing pandemic. I appreciate their understanding and encouragement throughout my academic journey. I am particularly thankful for their support in enabling me to come to France for my studies, which has been a precious and fulfilling experience in my life.

Words alone cannot adequately convey the depth of my gratitude to my dear supervisors, colleagues, family, and friends. I simply wish for your continued good health and utmost happiness. Please accept my heartfelt best wishes, and I eagerly anticipate the opportunity to meet you all again in the future.

Résumé

Pour les composites concernés, la mise en forme du renfort textile a un effet direct sur les propriétés mécaniques du composite une fois consolidé. Mesurer la déformation des renforts textiles lors de leur formage, à différentes échelles, à l'aide de la Corrélation d'Images Numériques (CIN) semble une voie prometteuse pour développer et valider la modélisation. Cependant, une mesure traditionnelle de CIN se confronte à des défis majeurs en raison de leurs propriétés physiques, de leur structure, des grandes déformations induites et de la cinématique particulièrement complexe. De plus, les informations fournies par un tel outil sont difficilement comparables aux résultats des simulations numériques. La thèse se focalise sur le test d'extension de biais. Elle propose le développement d'outils non traditionnels dans ce domaine, qui comprennent la CIN éléments finis (CIN-EF) et des tests menés *in-situ* dans un scanner à rayons X, pour améliorer le lien entre modèles et mesures. La thèse est divisée en trois parties. La première propose de mesurer la déformation par FE-DIC à la surface de plusieurs tissus typiques. Pour limiter les incertitudes de mesure, l'étude porte sur l'évolution de l'erreur ultime et des résidus de corrélation lorsque l'on fait varier la taille et l'orientation du maillage. La deuxième partie propose une approche incrémentale qui permet, cette fois, de réduire les erreurs de mesure dues aux très grandes déformations, en profitant de l'évolution des résidus de corrélation fournis par le FE-DIC. La dernière partie propose un premier pas vers l'assimilation des données images, qui exploiterait les essais *in-situ.* Il est démontré que les données tomographiques collectées peuvent être utilisées pour produire des modèles basés sur l'image, et que la machine de test spécialement développée permet de collecter des informations précieuses à la fois à la surface et à l'intérieur du tissu lorsqu'il se déforme.

Mots clés : *Composites, Renfort textile, Tissu, Corrélation d'Images Numériques, CIN-EF, Micro-tomographie RX, Modèles basés image numérique, Eléments Finis, Essais in-situ*

Abstract

For the composites concerned, shaping the textile reinforcement has a direct effect on the mechanical properties of the consolidated composite. Measuring the deformation of textile reinforcements during forming at different scales using DIC seems to be a promising way to develop and validate the modelling. However, a traditional Digital Image Correlation (DIC) measurement faces significant challenges due to their physical properties, structure, large deformations and complex kinematics. In addition, the information provided is difficult to compare with the results of numerical simulations. The thesis focuses on the bias extension test. It proposes the development of non-traditional tools, including finite element DIC (FE-DIC) and *in-situ* testing in an X-ray CT, to better bridge models and measurements. The thesis is divided into three different parts. The first proposes to measure the deformation by FE-DIC on the surface of several typical fabrics. To limit the measurement uncertainties, the study focuses on the evolution of the final error and the correlation residuals when we vary the size and orientation of the mesh. The second part proposes an incremental approach that allows, this time, to reduce the measurement errors due to very large deformations, taking advantage of the evolution of the correlation residuals provided by the FE-DIC. The last part proposes a first step towards the assimilation of image data, which would exploit the *in-situ* tests. It is shown that the tomographic data collected can be used to produce image-based models, and that the specially developed testing machine allows information to be collected both at the surface and inside the tissue as it deforms.

Keywords : *Composites, Textile reinforcement, Fabric, Digital Images Correlation, FE-DIC, X-ray micro-tomography, Digital Image Based modelling, Finite elements, in situ testing*

Contents

List of Figures

Introduction

Composite materials are used extensively in the aerospace and increasingly in the automotive sectors due to their excellent specific properties. Among all the manufacturing processes, the stamping of commingled thermoplastic fabrics is particularly attractive because it allows the rapid production of complex mechanical parts (Svensson et al., 1998). However, the shaping of the textile reinforcements can generate defects that are likely to impact the mechanical properties (Bhat et al., 2009; Soukane and Trochu, 2006). It is therefore crucial to study the deformation mechanisms of reinforced fabrics during this phase of the manufacturing process (Dufour et al., 2014). Many methods have consequently been developed to investigate a correlation between the mechanical properties of consolidated composites and the deformations of the reinforcing textiles. However, modeling or measuring such deformations during forming is particularly challenging due to the physical properties and architecture of fabrics.

The behavior of the fabric indeed depends on its initial architecture, the behavior of the yarns (De Luycker and Hamila, 2023) (thus on the fibers and the friction between fibers), the friction between yarns and between layers (Hivet et al., 2012), the friction with the mould (Gorczyca-Cole et al., 2007) and of course on the loading history. Different types of experiments were therefore proposed to better understand the mechanics of the fabric and to build more meaningful models (Gasser et al., 2000; Buet-Gautier and Boisse, 2001; Hivet and Boisse, 2008; Kashani et al., 2017). For example, a series of tests have been devised to generate plane shear, biaxial tension (Willems et al., 2008), compaction, bending and possibly combined loads (Bhat et al., 2009). Among the most popular methods to explore the mechanical behaviour of the continuous fibres reinforcement, we could mention the picture frame test (Mohammed et al., 2000b; Lebrun et al., 2003; Harrison et al., 2004; Peng et al., 2004; Launay et al., 2008; Willems et al., 2008; Cao et al., 2008; Bel et al., 2012), the bias extension test (Ackermann, 1984; Buckenham, 1997; Zhu et al., 2007b; Willems et al., 2008; Taha et al., 2013; Wang et al., 2014; Boisse et al., 2017), and the punch test (Toloczko et al., 2000; Guduru et al., 2006; Egan et al., 2007; Wakeman et al., 2006; Boisse et al., 2011; Wang et al., 2014; Patou et al., 2019). During such experiments, researchers have observed the same defects as in a textile reinforcement molding process. Some have analyzed and modeled three types of defects (wrinkling, buckles due to yarn curvatures, and large slippages) that may appear during textile composite reinforcement or prepreg forming (Boisse et al., 2016). The comparison between models and simulations is still a hot topic in this field (Gasser et al., 2000; Buet-Gautier and Boisse, 2001; Xue et al., 2005; Badel et al., 2008a, 2007; Lomov et al., 2008; Hivet and Boisse, 2008; Durville, 2010; Daelemans et al., 2016; Kashani et al., 2017; Boisse et al., 2018b).

For this type of study, optical full field measurements, which are deemed to be minimally invasive, are generally preferred to investigate the deformation (Li et al., 2023). Digital image correlation (DIC) has gradually become the reference technique (Lomov et al., 2008). As far as the analysis of the internal architecture is concerned, the RX micro-tomography (μCT) is very attractive. This technique has become popular in laboratories and has already contributed greatly to a better understanding of the material and its behaviour in many fields (London et al., 1990; Salvo et al., 2003; Emerson et al., 2017; Wang et al., 2018b; Garcea et al., 2018; Depuydt et al., 2019; Wang et al., 2018b; Tretiak and Smith, 2019; Yang et al., 2019; Parai and Bandyopadhyay-Ghosh, 2019; Di Lecce et al., 2020). The study of textile preforms has been a particular beneficiary of μCT. (Desplentere et al., 2005; Barburski et al., 2015). The reconstructed images even makes it possible to go as far as image-based modelling at (or below) the yarn scale (Badel et al., 2008b; Huang et al., 2019; Wang et al., 2020). However, we found no studies of *in-situ* bias extension testing in micro-CT.

In this thesis we fosus on the bias extension test. The experiment consists in performing a tensile test on a fabric in which the warp and weft yarns are initially oriented at 45° from the loading axis. The test indeed leads to a piecewise homogeneous deformation field at first order (Boisse et al., 2017). It consequently provides a simple characterization of the in-plane shear behavior in the central gauge region. Moreover, beyond a certain deformation, slippage occurs (Zhu et al., 2007b). Furthermore, on closer inspection, we note the presence of interesting transition layers associated with the bending stiffness of the fibers. This test is therefore rich enough to update part of the models and to challenge them (Boisse et al., 2017).

If the DIC measurement is undeniably useful for challenging models in this context (Jauffrès et al., 2010; Zhu et al., 2011), the complex movement between the threads and the large deformation of the fabric can however lead to significant measurement errors (Zhu et al., 2007b; Aimène et al., 2010). In addition, comparing data from subset based DIC and EF simulation is tricky. In this work, we suggest using a global approach to DIC, and more specifically the FE DIC (Sun et al., 2005; Besnard et al., 2006). It is indeed particularly tempting to use the very same mesh as that used for the simulation (Passieux et al., 2015) to measure the displacement field, so as to compare directly nodal measured and computed displacement fields. To our knowledge, this approach to DIC has not been used in the present context. Our ultimate aim is to carry out measurements at yarn scale, in order to feed a test/calculation dialogue at this scale. The effect of the FE mesh used on the FE-DIC measurement uncertainties is the first point to be considered. A proposal for an incremental approach to reduce the level of error observed for large deformations will be considered in a second step. As far as the simulation of the deformation of the fabric on the yarn scale is concerned, it seems essential that it be carried out from a representative CAD (Badel et al., 2008b).

This manuscript is composed of 4 chapters

- The first chapter is essentially a bibliographical survey. After some general remarks on composites, the main manufacturing processes are recalled. The classical mechanical characterisation techniques developed for fabrics are also presented. The principles of image correlation, particularly FE-DIC, and X-ray tomography are explained.

- The second chapter proposes two advances. The first is an atypical sample preparation for the tensile test. Three different materials are investigated. The novelty, in addition to dealing with the speckle problem, is the addition of a frame to the specimen. The second development relates to using Finite Element Digital Image Correlation (FE-DIC) in this context. More specifically, the influence of the mesh (element size and mesh orientation) on the final error and on the correlation residuals observed during the tests is studied in detail. A draft generation of synthetic data based on simulations of the deformation of a realistic model is also proposed.

- In chapter 3, incremental approaches of the FE-DIC are proposed so as to limit the considerable errors observed in the measurement of the displacement field in large deformation. The idea is to update the reference image from time to time to remedy changes in texture and a fatally poorly described cinematic. The idea of the proposed work is to rely on the correlation residue to automate this procedure in a reasonable way. Two typical reinforcement materials are then studied.
- The last chapter aims at the joint use of tomography and FE-DIC for the study of the behavior of a fabric subjected to an in situ bias extension test. In a first step, tomographic images of representative samples are exploited to create image-based models. Here again, a specific preparation of the sample simplifying its handling is suggested. A suitable machine has been developed. Tests were first carried out ex situ. Instrumented by FE DIC, they make it possible to take control of the machine, to understand the effect of speckling and to check the feasibility of surface optical measurements. Unpublished bias extension tests are then carried out.

CHAPTER 1

General literature review

Sommaire

1.1 General information on composite materials

A composite material is defined as a material composed of two or more components with different properties or different organizations. In most cases, the two major components are the matrix (*e.g.* polymer, metal, ceramic) and the reinforcement (*e.g.* fiber, particle, whisker). It is the assembly of these constituents, as illustrated in Fig.1.1, which gives the new material "enhanced" properties (Ashby and Bréchet, 2003) particularly attractive in the field of transport. The nature and the distribution of the reinforcement in the matrix obviously plays an essential role in the actual performances of the structures.

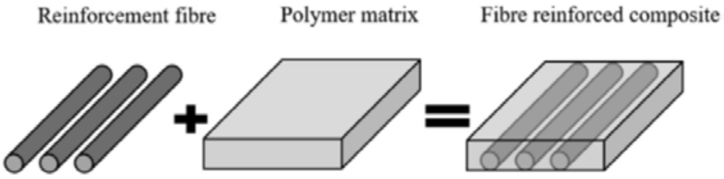

Figure 1.1: Fiber-reinforced composites: The general structural assembly.(Hesseler et al., 2021)

The requirements for the development of civil aircraft are safety, economy, comfort and, increasingly, environmental protection. To meet these requirements, the airframe of a civil aircraft must be designed using materials exhibiting exceptional specific mechanical characteristics (rigidity, strength, etc.). Long-fibre reinforced composite materials with polymer matrices are excellent candidates in this respect (Ashby and Bréchet, 2003). They also offer the particularity of being able to be easily functionalized, for example for structural health monitoring purposes (Ye et al., 2005). The application of composite materials in the aerospace field covers a wide spectrum of applications, from structural parts (e.g., primary structures such as fuselages, wings, central wing boxes, etc. - secondary structures such as ailerons, flaps, etc. - aerodynamic fairings, etc.) to aircraft cabin parts. They account for more than 50 % by weight of the airframes in the latest aircraft designs (Chatterjee and Bhowmik, 2019). Thermoset matrix based composites are currently the most present in primary structures (Soutis, 2005a). These materials still raise many questions, for example on recyclability (Zhang et al., 2020), impact resistance (Vieille et al., 2013), non-destructive testing (Towsyfyan et al., 2020), repair (Katnam et al., 2013), etc. Thermoplastic composites could be formidable options in the future (Barile et al., 2020), especially from a manufacturing/assembly (Offringa, 1996) and potentially ecological point of view (Bernatas et al., 2021).

Depending on the constituents and manufacturing method selected, the placement of the fibers will be more or less easy to control. The latter can indeed generate defects in the architecture which will affect the final behavior of the structure (Hassan et al., 2017). In what follows, we provide an overview of the main constituents and the main related existing manufacturing techniques.

1.1.1 The fabric reinforcement material

There are different ways to classify fiber reinforced composites. The first one is based on the structure and properties of the material. For instance, according to the structure of the material, the fiber reinforced composites can be continuous, woven fabric or short chopped. Subdivided further, reinforcing materials can also be divided into unidirectional, bidirectional, random orientaion, etc. Fig.1.2 shows the classification of composite materials with respect to reinforcement. In the following, only continuous fibre reinforced are considered because this thesis is focused on the underlying kinematics of fabrics.

It is also possible to classify according to the type of material :

1. Glass fiber ;
2. Carbon fiber ;
3. Organic fiber (Aromatic polyamide fiber, aromatic polyester fiber, polyolefin fiber, etc.) ;
4. Metal fiber (Tungsten wire, stainless steel wire, etc.) ;
5. Ceramic fiber (Alumina fiber, silicon carbide fiber, boron fiber, etc.).

The most widely used reinforcing materials are glass fiber and carbon fiber, so in this thesis we focus on these two materials and introduce carbon/PPS for analogous experiments.

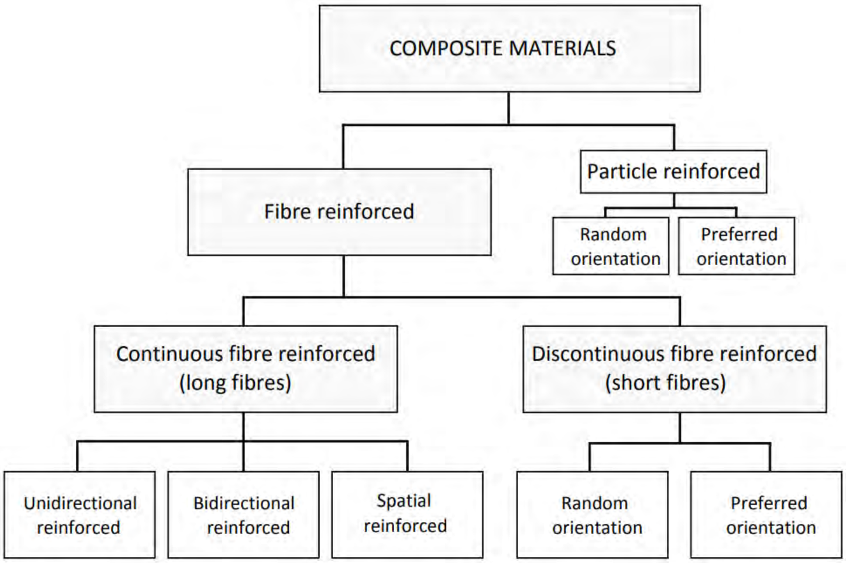

Figure 1.2: Classification of composite materials with respect to reinforcement. (Altenbach et al., 2004)

1.1.1.1 Glass fiber

Glass fiber reinforced composites (Joshi et al., 2004) are a promising and extremely versatile reinforcing material because their properties can be tailored to satisfy a variety of specific requirements as Tab 1.2. In addition to this, the different types of raw glass materials are one of the reasons for the diversity of glass fibers as well as their high plasticity. Glass fiber has the properties of high tensile strength, dimensional stability, high heat resistance, good thermal conductivity, great fire resistance, compatibility with organic, great durability matrices, etc. The main reason for choosing glass fiber as a reinforcing material in many cases, which is the main advantage of glass fiber, is the ability to increase the tensile strength and toughness of the composite. In order for glass fibers to satisfy the requirements of different types of composites, the production process of glass fibers is particularly important, and this is the process that directly determines the physical properties such as strength and toughness of glass fibers.

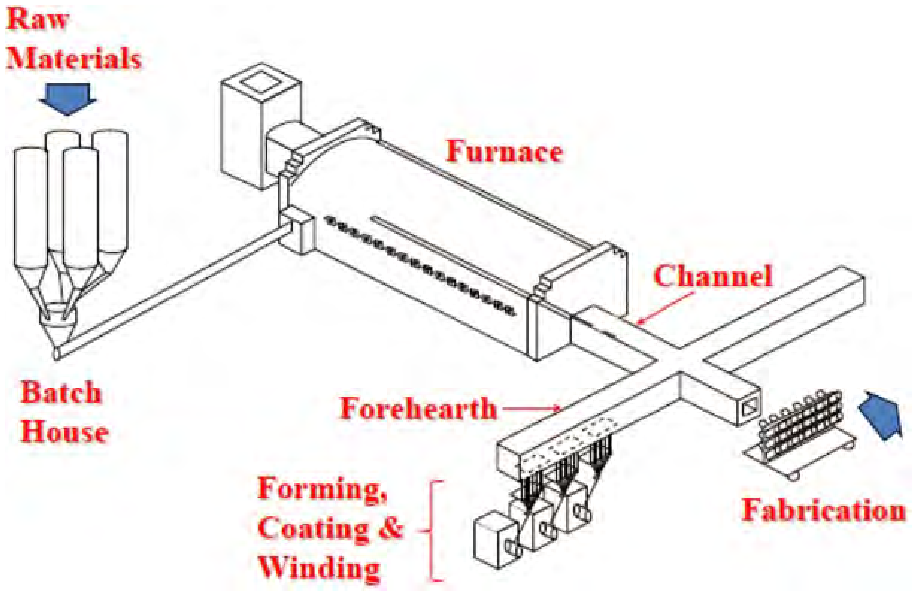

Figure 1.3: Glass fiber manufacturing principle. (Stickel and Nagarajan, 2012)

The process of producing glass fibers can be divided into four steps: preparation, melting, cooling and fibrillation. The most critical step is the fibrillation of the glass and the protection of the molded glass fibers after the fibrillation. This will directly affect its tensile strength. If the formed glass fiber has a good continuous state, its tensile strength will be higher than that of the chopped glass fiber Fig.1.3.

The main component of glass fiber is SiO_2, for example, E-glass contains 53% - 55% of this composition and C-glass has 60% - 65%. In addition to that there are CaO, Al_2O_3, B_2O_3, MgO, Na_2O, K_2O, TiO_2 and Fe_2O_3, etc (In order of the percentage of each component in E-glass) (Derradji et al., 2018). Among them, the content of SiO_2 is roughly in the range of 52% - 74%, which is not toxic to human body. Glass fiber is easy to cause allergic reactions on the body surface (the diameter is 5 - 25 µm (Middleton, 2016)). It cannot be decomposed in human body. Therefore, gloves, goggles and protective clothing must be worn when processing samples. Due to the different proportion of each component in the production process, the produced glass fibers are divided into the following categories 1.1 and exhibit different physical properties 1.2.

The primary types of glass fiber used in fiberglass is E-glass 1.4. It is the first major synthetic composite reinforcing material, originally developed for electrical insulation applications. E-glass is one of the most widely used of all fiber reinforcement materials. The principal reasons for this are their low cost and early development. The diametre of E-glass is 13 µm (Çuvalci et al., 2014). It is worth mentioning that a few air bubbles are observed in the glass fibers and these bubbles cause a reduction in the strength of the fibers here, where fracture is probable to occur in tensile tests. The reinforcing fibers are gathered together to form a yarn or a roving. The structure of the roving varies according

Fiber Category	Physical properties
E, electrical	Higher strength and electrical resistivity
C, chemical	Higher corrosion resistance
S_2	High strength, modulus and stability
A, alkali	Soda lime glass/ high alkali, higher durability, strength and electric resistivity
D, dielectric	Low dielectric constant
R	Higher strength and acid corrosion resistance
EGR	Long term acid resistance and short term alkali resistance
AR	Alkali resistance

Table 1.1: Common fiber categories and associated characteristic.(Sathishkumar et al., 2014)

Fiber	Density (g/cm^3)	Tensile strength (GPa)	Young's modulus (GPa)	Elongation (%)	Coefficient of thermal expansion (10^{-7}/°C)	Poison's ratio	Refractive index
E-glass	2.58	3.445	72.3	4.8	54	0.2	1.558
C-glass	2.52	3.310	68.9	4.8	63	-	1.533
S_2-glass	2.46	4.890	86.9	5.7	16	0.22	1.521
A-glass	2.44	3.310	68.9	4.8	73	-	1.538
D-glass	2.11-2.14	2.415	51.7	4.6	25	-	1.465
R-glass	2.54	4.135	85.5	4.8	33	-	1.546
EGR-glass	2.72	3.445	80.3	4.8	59	-	1.579
AR-glass	2.70	3.241	73.1	4.4	65	-	1.562

Table 1.2: Physical and mechanical properties of glass fiber. (Sathishkumar et al., 2014)

to the types of fibers used, but also the degree of mixing of these fibers within a roving (Bourban, 2004). Because of the wide application rate of E-glass, it was chosen to make one type of experimental samples in this thesis.

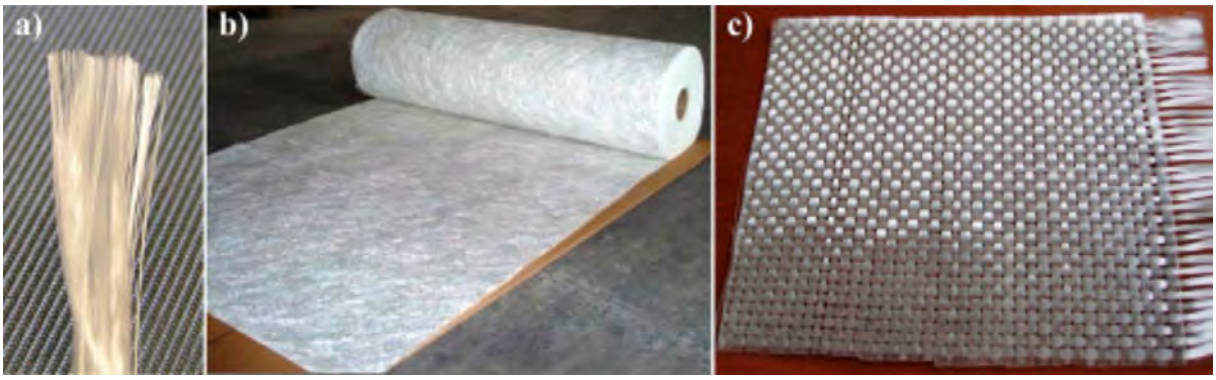

Figure 1.4: Examples of available forms of fiber reinforcements (Correia, 2023).

1.1.1.2 Carbon fiber

Carbon fiber is mainly composed of carbon atoms, which has the characteristics of high temperature resistance, friction resistance, electrical conductivity, thermal conductivity and corrosion resistance (Huang, 2009). The shape of carbon fiber is fibrous, soft, and can be processed into various fabrics, and it has high strength and modulus along the fiber axis due to its graphite microcrystalline structure which is preferentially oriented

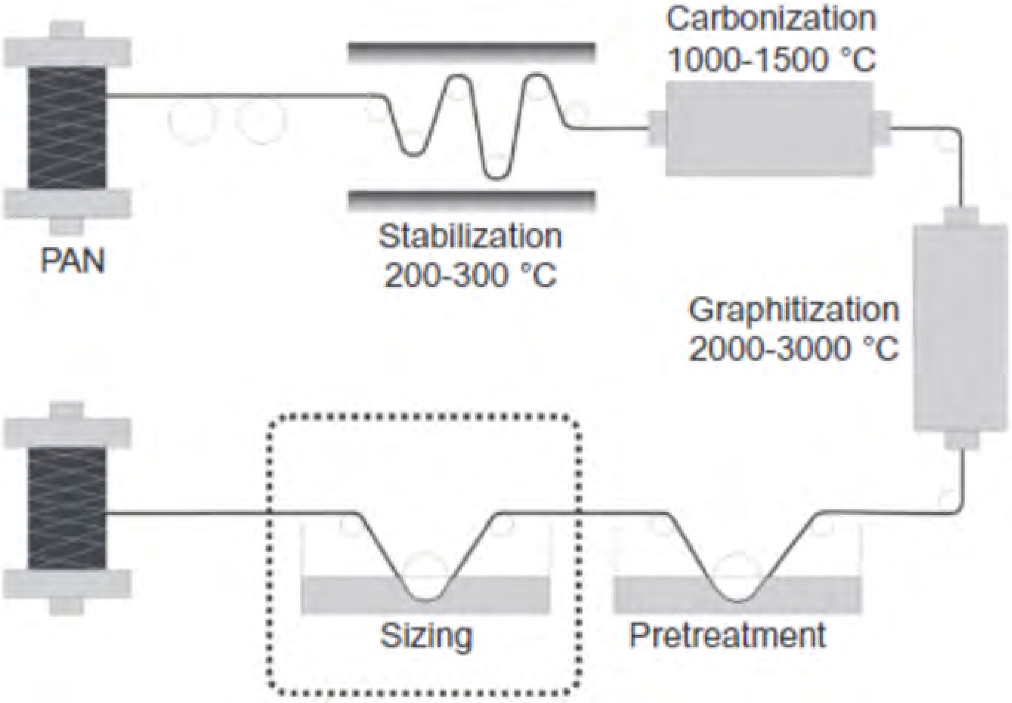

Figure 1.5: Schematic illustration of the carbon fiber production process out of polyacrylonitrile (PAN) fibers.(Sawaryn et al., 2011)

along the fiber axis. The density of carbon fiber is low, so the specific strength (the strength-to-weight ratio) and specific modulus (modulus of elasticity per unit density) are high. The main use of carbon fiber is as a reinforcing material compounded with resins, metals, ceramics and carbon to make advanced composite materials. Carbon fiber reinforced epoxy resin composites have the highest specific strength and specific modulus among existing engineering materials. The diameter of carbon fiber is only 5 μm - 10 μm (Bhatt and Goe, 2017), which is equivalent to one tenth to twelfth of a hair, but the strength is more than four times that of aluminum alloy.

Carbon fiber can be classified into polyacrylonitrile (PAN) based carbon fiber, rayon (viscose) based carbon fiber (Harry et al., 2007) or petroleum pitch-based carbon fiber (Singer, 1981) according to different raw materials. PAN-based carbon fibers are the most widely used in aerospace, sports equipment, and automotive industries, with a market share of more than 90% (Bhatt and Goe, 2017), due to their abundant raw material sources and superior tensile strength. Rayon-based carbon fiber and pitch-based carbon fiber are less used and less produced. Pitch-based carbon fiber have low strength and modulus, and are mainly used in the field of insulation materials; high-performance pitch-based carbon fiber are mostly used in aerospace engineering materials. Rayon-based carbon fiber is mainly used to make ablative corrosion resistant and thermal insulation materials.

With the PAN as the most widely used carbon fiber, its production process is also the most representative. Several researchers have described the production process in great detail in 1998 (Donnet and Bansal, 1998). The main process of producing carbon fiber, in general, is divided into three main processes : stabilization, carbonization and graphitization (Ramezankhani et al., 2019). (1) It is necessary to pre-oxidize the PAN filament in air first, so that the structure of PAN is transformed into a stable trapezoidal six-membered ring structure, it is not easy to melt. In addition, when heated long enough, there will be fiber oxygen absorption, PAN fiber molecules can form a stable chemical bonding. Pre-oxidation needs to be carried out in an oxidizing environment at 200°C - 300°C, with the original filament under tension (Ramezankhani et al., 2019); (2) Carbonization is the main stage of carbon fiber generation, which needs to be carried out in an inert environment from 1000°C - 1500°C. The main purpose of this step is used to remove a large amount of non-carbon elements such as nitrogen, hydrogen and oxygen, thus changing the structure of the original PAN fiber, which can produce raw carbon fiber yarn with about 99% carbon content. ; (3) Graphitization of carbon fibers needs to be carried out at a temperature of 2000°C - 3000°C, with inert gas protection. Placing the raw carbon fibers in a sealed device and applying constant pressure is able to transform the crystalline carbon in the fibers toward graphite crystals, narrowing their angle in the direction of the fiber axis. This step can effectively improve the modulus of elasticity of carbon fibers. Finally, fibers are coated and wound onto bobbins. These are then loaded onto spinning machines that twist the fibers into different size yarns.

Classification	Carbon fiber	Tensile strength (ksi)	Tensile strength (GPa)	Modulus (MSi)	Modulus (GPa)
Standard Modulus Carbon Fibers	T300	512	3530	33.4	230
	T700S	711	4900	33.4	230
	T700G	711	4900	34.8	240
Intermediate Modulus Carbon Fibers	T800H	796	5490	42.7	294
	T800G	853	5880	42.7	294
	T1000G	924	6370	42.7	294
	T1100S	1017	7000	47.0	324
High Modulus Carbon Fibers	M35J	654(6K) 683(12K)	4510(6K) 4700(12K)	49.8	343
	M40J	640	4400	54.7	377
	M46J	609(6K) 583(12K)	4200(6K) 4020(12K)	63.3	436
	M55J	583	4020	78.2	540
	M60J	554	3820	85.3	588

Table 1.3: Physical and mechanical properties of carbon fiber. (Toray, 2022)

For the classification of carbon fiber, the more accepted method worldwide is shown in the table below 1.3. The largest producer of carbon fibers, Toray (in Japan) (Toray, 2022) and Cytec (in US), both use carbon fiber classifications such as T300, T800H, M35J, etc. For example, T300 indicates a tenacity (tensile strength) of 300 ksi, which translated to about 2100 MPa. With precursor and process improvements, T300 grade now possesses a tenacity of almost 3530 MPa. The modulus of such fibers is typically 230 GPa, whereas the strain-to-failure is 1.5% – 2% (Inagaki, 2013). According to the different tensile modulus of carbon fibers, they can be broadly classified into three grades : standard modulus (**SM**), intermediate modulus (**IM**), and high modulus (**HM**) 1.6. According to the fiber size, carbon fibers can also be divided into continuous and discontinuous carbon fiber reinforced. Only long carbon fibers are discussed in this thesis. As carbon fiber T300 is the baseline carbon fiber used in aerospace applications and is known for balanced composite properties, high quality and consistency, reliability and availability of supply. In this thesis, a fabric made out of T300 fibres will be studied. Fig.1.7 shows the detailed observation of carbon fiber.

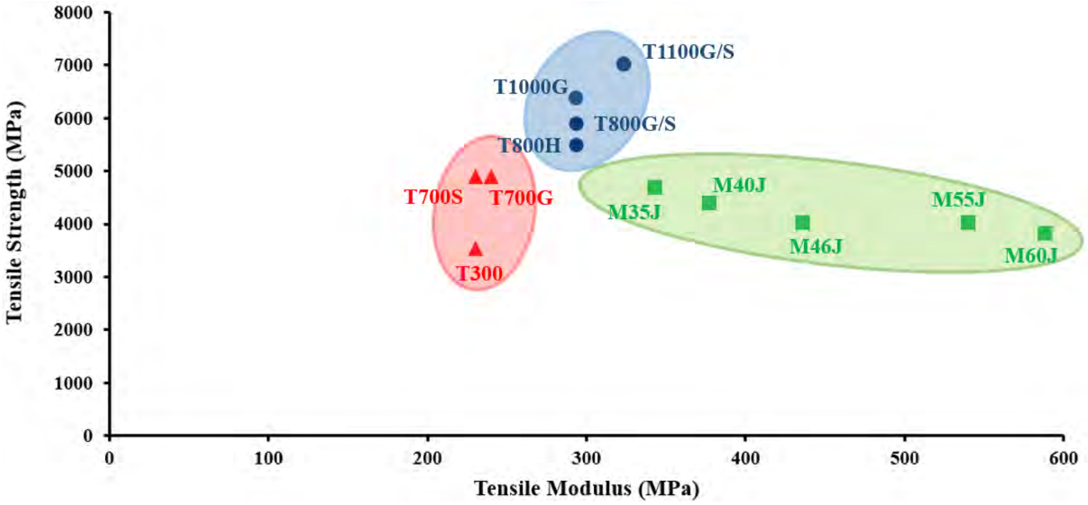

Figure 1.6: Classification of carbon fibers according to physical properties.

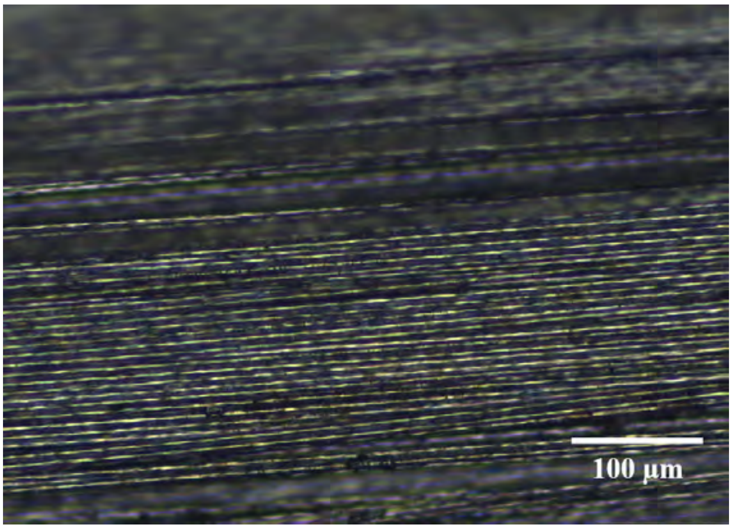

Figure 1.7: A detailed observation of carbon fiber.

1.1.1.3 Carbon/PPS fiber

In order to better conduct controlled experiments to study the deformation of woven reinforced materials, the carbon/PPS (Phenylene polysulfide) fabrics 1.9, a commingled composite (Patou et al., 2019), is introduced. PPS is a semi-crystalline thermoplastic (Lee et al., 2019). It has excellent thermal resistance, it is non-flammable and self-extinguishing, it has excellent resistance to chemicals, good mechanical properties, excellent dimensional stability, and is insensitive to moisture. As the name indicates, a commingled composite is a new roving made by combining the reinforcement filament and matrix filament in various ways during the production process (Asghar et al., 2021). The manufacture of commingled composites takes the following 4 main forms :

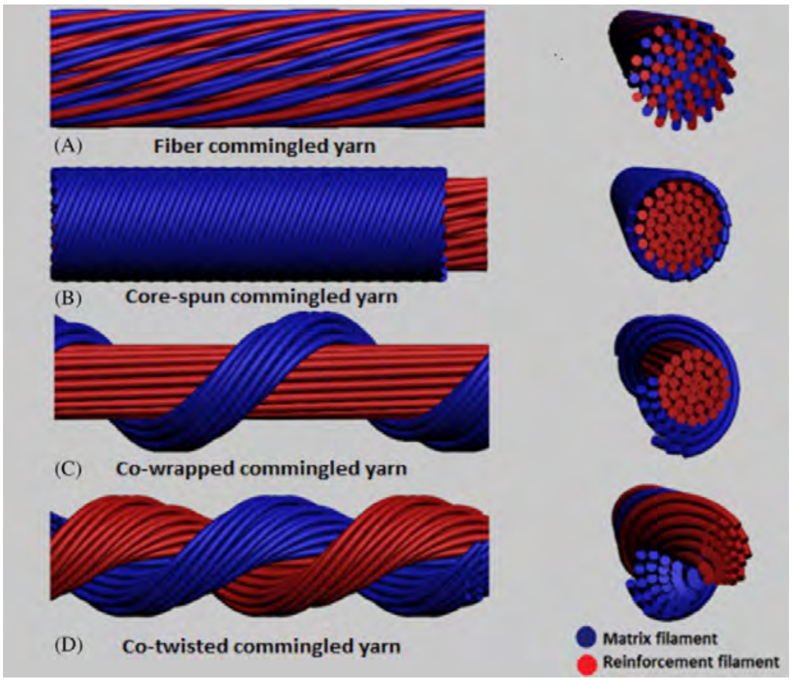

Figure 1.8: Various commingling techniques and hybrid yarn structures. (Choi et al., 1999; Asghar et al., 2021)

The analyzed prepregs are made of stretch broken carbon fibers comingled with PPS resins. The carbon fibers are commingled with thermoplastic polymer fibers (PPS filament) and are wrapped with a serving filament of the same polymer to stabilize the yarn for subsequent weaving processes (Wang et al., 2015). Through the fiber commingled and the co-wrapped commingled techniques, the main geometrical and physical properties are as show in 1.4.

	Material utilised	Carbon/PPS commingled prepreg
Reinforcement	Structure	5 harness satin
	Yarns (warp/weft)	313 tex / 313 tex
	Number of Yarns	7.5 X 7.5
	Areal density	281 $g/m^2 \pm 5\%$
	Fiber volume fraction	60%
Matrix	Type	PPS
	Melt temperature	280°C
	Areal density	188 $g/m^2 \pm 5\%$
	Volume fraction	40%
Prepreg	Areal density	469 $g/m^2 \pm 5\%$
	Thickness	0.3 mm

Table 1.4: Physical and mechanical properties of carbon/PPS. (Wang et al., 2015)

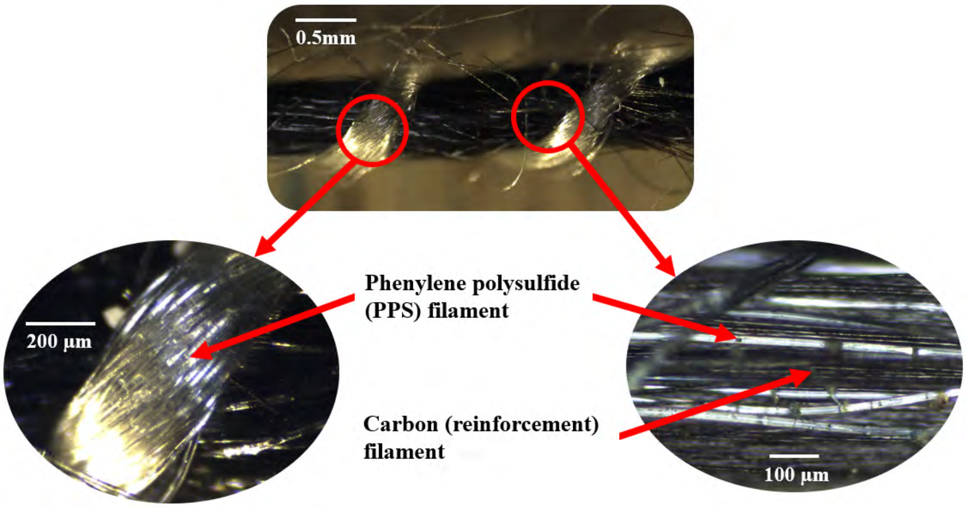

Figure 1.9: C/PPS structure observed under the microscope : roving made by the fiber commingled yarn techniques 1.8 (A), and the co-wrapped commingled yarn techniques 1.8 (C). (Patou et al., 2019)

1.1.2 Structure of textile reinforcement materials (2D)

The textile reinforcement fabric consists of two or more sets of yarns interlaced together to form a continuous 2D surface. The most common 2D textile reinforcement is the biaxial (orthogonal) fabric which is composed of longitudinal (warp) yarns and transverse (weft or filling) yarns interlaced at right angles (Lord, 1982). For the textile reinforcements, their structure and the way they are woven have an impact on their mechanical properties. Common weave types include plain weave, twill weave, and satin weave (Bloom, 2015). Plain weave is the simplest and the most common weave in the fabric. A complete plain weave cycle can be formed by using two warp and two weft threads. Twill construction consists of three or more consecutive warp and weft yarn structures. The fabric has a diagonal pattern. The satin weave is made of more than 5 consecutive warp and weft yarns. The basic characteristic of this weave is the discontinuity of the weave pattern.

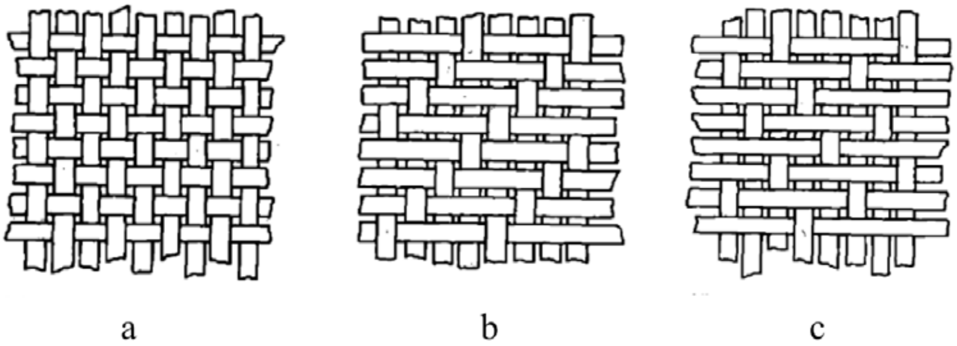

Figure 1.10: Common weave types: (a) plain weave; (b) twill weave; (c) 5 harness satin. (Bloom, 2015)

In this thesis, for the samples of the glass fabric and the carbon/PPS fabric, the studied weaves are satin of 5, and the estimated size of the pattern is approximately 6,7

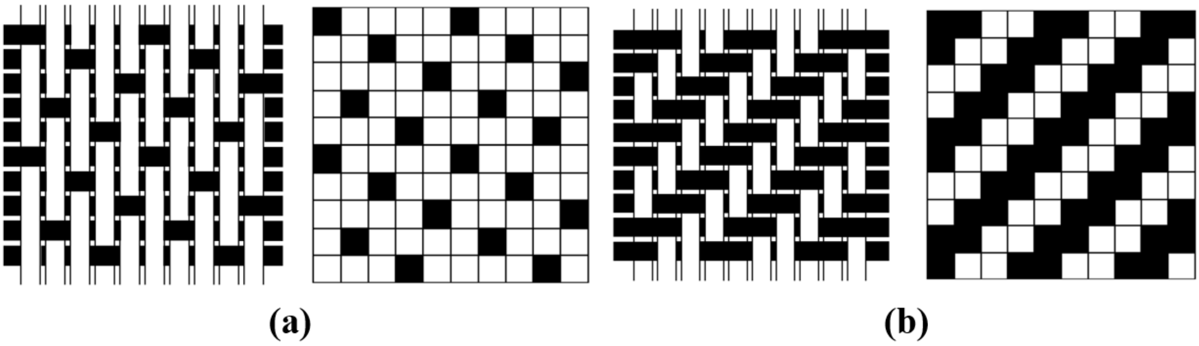

Figure 1.11: (a) The satin of 5 structure and (b) the twill 2×2 structure.

mm. For the samples of the carbon fabric, the studied weaves are twill 2×2, and the estimated size of the pattern is approximately 8 mm.

1.2 The composite molding process and effect of textile reinforcement molding

The composite molding process is the basis and condition for the development of the composite industry. With the broadening of the application field of composite materials, the composite material industry has been developed rapidly, the old molding process has been improved day by day, and new molding methods have emerged continuously, and there are more than 20 kinds of molding methods for polymer matrix composites, which are successfully used in industrial production. Compared with other material processing, the composite molding process has the following features :

(a) Material manufacturing and product molding are completed simultaneously.

In general, the production process of composite materials is also the molding process of products. The performance of materials must be designed according to the requirements of products, so the physical and chemical properties, structural shape, and appearance quality of products must be satisfied when selecting materials, designing ratios, and determining fiber lay-up and molding methods.

(b) Products are relatively easy to be molded.

The resin matrix of general thermosetting composites is a flowing liquid before molding, and the reinforcing material is soft fiber or fabric. The process and equipment required to produce composite products with these materials are much simpler than other materials, and only one set of molds is needed for some products.

1.2.1 Resin Transfer Molding (RTM)

Resin Transfer Molding (RTM) (Rudd et al., 1997; Rouison et al., 2004; Scarponi et al., 2009; Sozer et al., 2012) is a closed-mold technology that was developed in the 1950s as a modification of the hand-paste molding process to produce products with two sides. Resin Injection and Pressure Infection are also included in this process.

Fig.1.12 shows the basic principle of RTM (Long, 2005) : lay the glass fiber reinforcement material into the mold cavity of the closed mold, inject the resin into the mold cavity with pressure, soak the glass fiber reinforcement material, and then solidify and demold the molded products. From the previous research level, the research and development direction of RTM technology will include microcomputer-controlled injection unit, reinforcing material performing technology, low-cost mold, rapid resin curing system, process stability, adaptability, etc.

RTM technology has a wide range of applications (Kruckenberg and Paton, 2012) and is widely used in construction, transportation, telecommunications, health, aerospace, and other industrial fields. The products that have been developed include automobile shells and parts, recreational vehicle components, spiral slurry, 8.5m long wind turbine blades, antenna covers, machine covers, bathtubs, bathing rooms, swimming pool boards, seats, water tanks, telephone booths, electric poles, small yachts, etc.

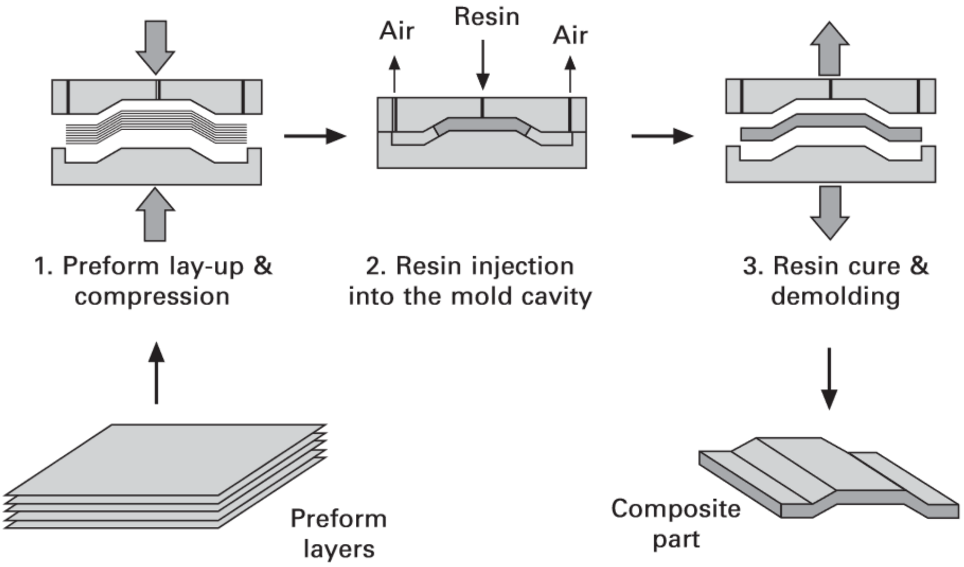

Figure 1.12: Double-belted press lamination used to produce thermoplastic composite lamination sheet and blanks.(Long, 2005)

(1) RTM process and equipment (Potter, 1999; Schmachtenberg et al., 2005; Laurenzi and Marchetti, 2012)

The entire production process of RTM is divided into 11 processes, with fixed positions of operators and tools and equipment for each process (Liu et al., 1996). The molds are transported by trolleys and go through each process in turn to realize flowing operation. The cycle time of the mold on the assembly line reflects the production cycle of the product. Small products generally take only ten minutes, and the production cycle of large products can be controlled to be completed within 1h.

RTM molding equipment is resin injection machines and molds.

The resin injection machine (Stark et al., 1998; Bickerton et al., 2001; Lawrence et al., 2002; Danisman et al., 2007; Tuncol et al., 2007) is composed of a resin pump and injection gun. The resin pump is a set of pistons reciprocating pumps, and the uppermost end is an air-powered pump. When the compressed air drives the air pump piston up and down, the resin pump pumps the resin in the barrel into the resin reservoir quantitatively through the flow controller and filter, and the lateral lever makes the catalyst pump move to pump the catalyst quantitatively to the reservoir. Compressed air fills the two reservoirs, generating a buffer force opposite to the pump pressure to ensure a steady flow of resin and catalyst to the injection gun head. There is a static turbulent flow mixer behind the injection gun, which can make the resin and catalyst mix evenly without air, and then inject into the mold through the gun. There is a cleaner inlet designed behind the mixer, which is connected to a solvent tank with 0.28 MPa pressure, and when the machine is used up, the switch is turned on and the solvent is automatically sprayed out to clean the injection gun.

RTM molds (Moore and Bland, 1999) are divided into 3 types: fiber reinforced plastics (FRP) molds (Schmachtenberg et al., 2005; Caba and Koch, 2015; Gauvin and Chibani, 2022), FRP surface plated metal molds (Wang et al., 2016), and metal molds (Tuncol et al., 2007; Yenilmez and Sozer, 2009). FRP molds are easy to manufacture and less expensive, polyester FRP molds can be used 2000 times, epoxy FRP molds can be used 4000 times. FRP molds with the metal-plated surface can be utilized more than 10,000 times. Metal molds are rarely utilized in the RTM process. The mold cost of RTM is only 2% to 16% of that of SMC.

(2) RTM raw materials

The raw materials used for RTM are resin system, reinforcing material, and filler.

Resin system: The resin used for the RTM process is mainly unsaturated polyester resin (Maazouz et al., 2000; Lee et al., 2002; Rouison et al., 2004).

Reinforcing materials: Generally, the reinforcing materials (Owen et al., 1990; Cai, 1992; Rouison et al., 2004; Sreekumar et al., 2012) for RTM are mainly glass fibers with 25% to 45% (by weight); commonly used reinforcing materials are continuous glass fiber mats, composite mats, and axial fabrics.

Fillers: Fillers (Um and Lee, 1991; Young, 1994; Lim and Lee, 2000) are important to the RTM process, not only to reduce costs and improve performance but also to absorb heat in the exothermic phase of resin curing. Commonly used fillers are aluminum hydroxide, glass beads, calcium carbonate, mica, etc.

1.2.2 Laminated and rolled tube forming process

(1) Lamination molding process.

Laminated molding (Himmer et al., 1999; Pillay et al., 2005; Toledo Filho et al., 2009) is the production process of cutting and stacking the prepreg according to the shape and size of the product, putting it between two polished metal molds, and forming the composite products by heating and pressing, as shown in Fig.1.13. It is an early and mature molding method in the composite molding process. This process is primarily used to produce electrical insulation boards and printed circuit boards. Nowadays, printed circuit boards are commonly used in radios, televisions, telephones and cell phones, computer products, various control circuits, and other products requiring flat integrated circuits.The lamination process is mainly used to produce various specifications of composite materials. It has the characteristics of mechanization, high degree of automation, and stable product quality. But the one-time investment is large, suitable for mass production, and can only produce plates. The specifications are limited by the equipment. The lamination process includes: Prepreg preparation, cutting and laminating, hot pressing, cooling, de-molding, processing, post-treatment, and other processes.

(2) Rolling tube forming process

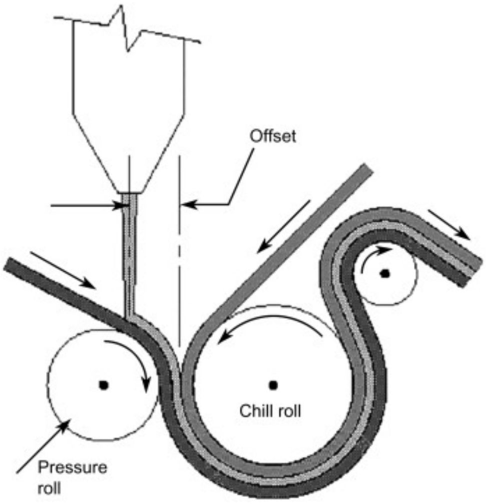

Figure 1.13: Double-belted press lamination used to produce thermoplastic composite lamination sheet and blanks.(Wagner, 2016)

The principle is to softening the tape and melting the resin on the tape with the help of the hot rollers on the tape rolling machine (Thostenson et al., 2001; Groche and v. Breitenbach, 2008; Li et al., 2022). Under a certain tension, the tape is continuously rolled onto the core tube with the help of friction between the rollers and the core mold, until the required thickness. Then cooled and shaped by the cold rollers, taken off from the rollers and sent to the curing oven for curing. After the tube is cured, take off the core mold, and the composite material rolled tube. The operation process is shown in Fig.1.14 :

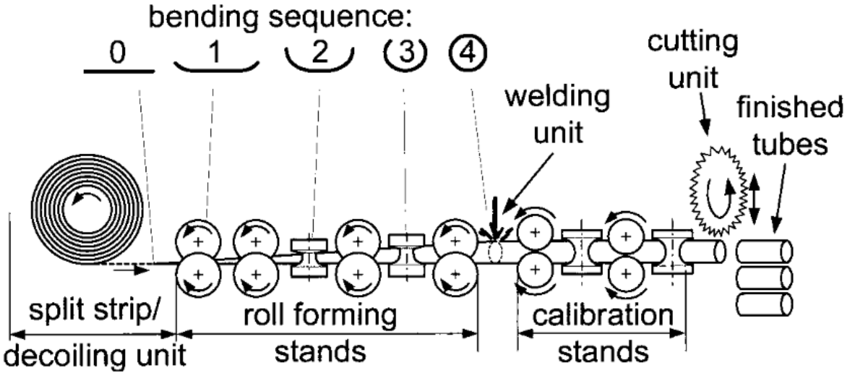

Figure 1.14: Principle of tube roll forming process.(Groche and v. Breitenbach, 2008)

1.2.3 Bag moulding, autoclave, hydraulic autoclave, and thermal expansion moulding

Bag moulding (Han et al., 2000; Summerscales and Searle, 2005; Jose and Joseph, 2012), autoclave or hydraulic autoclave (Boey and Lye, 1990; Nguyen et al., 2016; Grunenfelder et al., 2017), and thermal expansion moulding (Gusev et al., 2002; De Oliveira et al., 2008; Takenaka and Ichigo, 2014) are collectively referred to as low-pressure moulding processes. The molding process is to lay the reinforcing material and resin (including prepreg material) on the mold one layer after the other according to the design direction and sequence. After reaching the specified thickness, the product is obtained by pressing, heating, consolidating, demolding, and modifying. The only difference between the four methods and the hand-paste molding process is the process of pressurization and consolidation. Therefore, they are only the improvement of the hand-paste molding process, to improve the density and interlayer bonding strength of the products.

High-performance composite products made by low-pressure molding method with high-strength glass fiber, carbon fiber, boron fiber, aramid fiber, and epoxy resin as raw materials have been widely used in aircraft, missiles, satellites, and the space shuttle, such as aircraft hatch, fairing, airborne radome, bracket, wing, tail, bulkhead, wall panel, and stealth aircraft.

(1) Bag moulding

Bag moulding is divided into 2 types of pressure bag method (Visconti and Langella, 1992) and vacuum bag method (Williams et al., 1996; Summerscales and Searle, 2005).

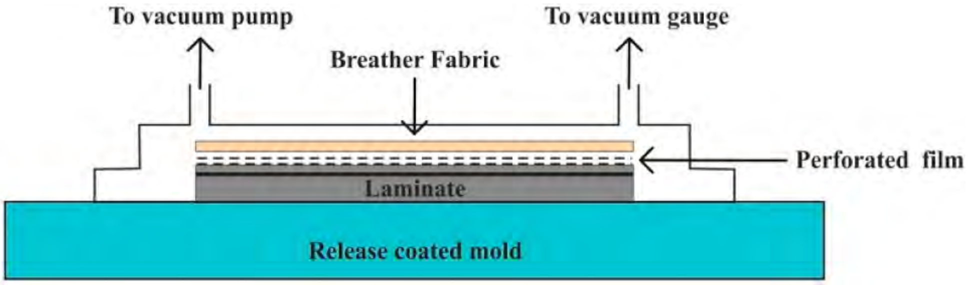

Figure 1.15: Vacuum bag molding process.(Rajak et al., 2019)

Bag moulding is to hand paste the uncured products, through the rubber bag or other elastic material to its gas or liquid pressure, so that the products under pressure are dense, curing, like Fig.1.15.

The advantages of the bag moulding method are: (1) The product is smooth on both sides; (2) It can adapt to polyester, epoxy, and phenolic resin; (3) The product performance is higher than hand paste.

The pressure bag method is to hand paste molding products not cured into a rubber bag, fixed cover, and then pass into the compressed air or steam (0.25 - 0.5MPa), so that the products are cured under hot pressure conditions.

The vacuum bag method is to cover the uncured products of hand-paste molding with a layer of rubber film, and the products are between the rubber film and the mold, sealed around, and vacuumed (0.05 - 0.07 MPa) so that the air bubbles and volatiles in the products are excluded. The vacuum bag forming method is only used for the wet forming of polyester and epoxy composite products because the vacuum pressure is small.

(2) Hot-press autoclave and hydraulic autoclave method

The hot-press autoclave and hydraulic autoclave method is a process of heating and pressurizing the uncured hand-paste products by compressed gas or liquid in the metal container to ensure that they are cured. For instance, the Fig.1.16 is the autoclave at Institute Clément ADER - Toulouse.

Figure 1.16: Autoclave at Institute Clément ADER - Toulouse (Patou, 2018).

Hot-press autoclave (Li et al., 2006; Mei et al., 2019) is a horizontal metal pressure vessel, uncured hand paste products, plus sealed plastic bags, vacuum, then together with the mold with a cart into the hot press autoclave, through the steam (pressure of 1.5 - 2.5MPa), and vacuum. The products are pressurized, heated, and discharged bubbles, so that they are cured under hot pressure conditions. It combines the advantages of the pressure bag method and the vacuum bag method, with a short production cycle and high product quality. The hot autoclave method can produce high-quality, high-performance composite products of large size and complex shape. The product size is limited by the hot press kettle. The products that have been developed and applied are wings, tail fins, satellite antenna reflectors, missile loading bodies, airborne laminated structure radomes, etc. The major drawback of this method is the large investment in equipment, large weight, complex structure, and high cost.

Hydraulic autoclave method (Johnston, 1997; Soutis, 2005b; Hubert et al., 2012) is an airtight pressure vessel, smaller in volume than the hot autoclave, placed upright, which is heated and pressurized to solidify the uncured hand-paste products by passing hot liquid under pressure during production. The pressure of the hydraulic autoclave can reach 2 MPa or higher, and the temperature is 80 to 100℃. With an oil carrier, the heat can reach 200 ℃. This method produces dense products, with a short cycle time, the disadvantage of the hydraulic autoclave method is a large investment in equipment.

(3) Thermal expansion moulding method

The thermal expansion moulding method (Gusev et al., 2002; De Oliveira et al., 2008; Takenaka and Ichigo, 2014) is a process used to produce hollow, thin-walled high-performance composite products. Its working principle is the use of different expansion coefficients of the mold material, the use of its heat volume expansion generated by the different extrusion pressure, and the construction of the product pressure. The upper mold of the thermal expansion molding method is a large expansion coefficient of silicone rubber, the lower mold is a small expansion coefficient of metal materials, hand paste uncured products placed between the upper and lower mold. When heated, due to the different expansion coefficients of the positive and negative molds, a huge difference in deformation is produced, so that the products are cured under hot pressure.

1.2.4 Spray forming

Spray forming technology (Srivatsan and Lavernia, 1992; Lawley and Apelian, 1994; Grant, 1995; Raju et al., 2008) is an improvement of hand-gluing molding, to a semi-mechanized degree. The proportion of injection molding technology in the composite molding process is large, as the United States accounted for 9.1%, Western Europe accounted for 11.3%, and Japan accounted for 21%.

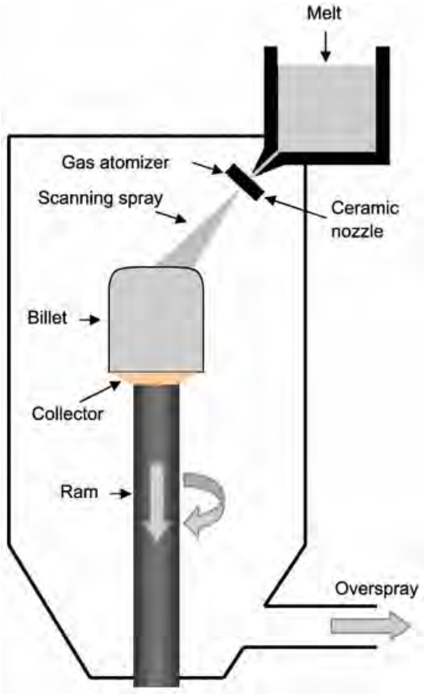

Figure 1.17: Schematic of the spray forming process for the manufacture of billets.(Grant, 2007)

The spray forming process is to spray two kinds of polyester mixed with initiator and accelerator from both sides of the gun. The cut glass fiber roving is sprayed out from the center of the gun, so that it is evenly mixed with resin and deposited onto the mold. When deposited to a certain thickness, it is compacted with a roller to make the fiber soak through the resin and exclude the air bubbles, and then cured into products. The schematic diagram is shown in Fig.1.17.

The advantages of spray forming (Singer, 1991; Schulz et al., 2008) are: i) the use of glass fiber roving instead of fabric can reduce the material cost; ii) the production efficiency is 2 to 4 times higher than that of hand gluing; iii) the product has good integrity, no seams, high interlayer shear strength, high resin content, good corrosion resistance, and leakage resistance; iv) the consumption of flying edges, cutting chips and remaining glue can be reduced; v) the size and shape of the product are not restricted. The disadvantages are: 1) the resin content is high and the product strength is low; 2) products can only be smooth on one side; 3) pollute the environment and endanger the health of workers.

The efficiency of spray forming reaches 15 kg/min, so it is suitable for large hull manufacturing. It has been widely used for processing bathtubs, machine outer covers, whole bathrooms, auto body components, large relief products, etc.

Other forming processes of polymer matrix composites mainly refer to the centrifugal molding process (Wannasin and Flemings, 2005), casting forming process (Vijayaram et al., 2006), elastomer storage resin molding process (ERM) (Palin-Luc et al., 2002), reinforced reaction injection molding process (RRIM) (Rudd et al., 1997; Kim and Macosko, 2000), etc.

1.2.5 Effect of textile reinforcement molding on the mechanical properties of composites

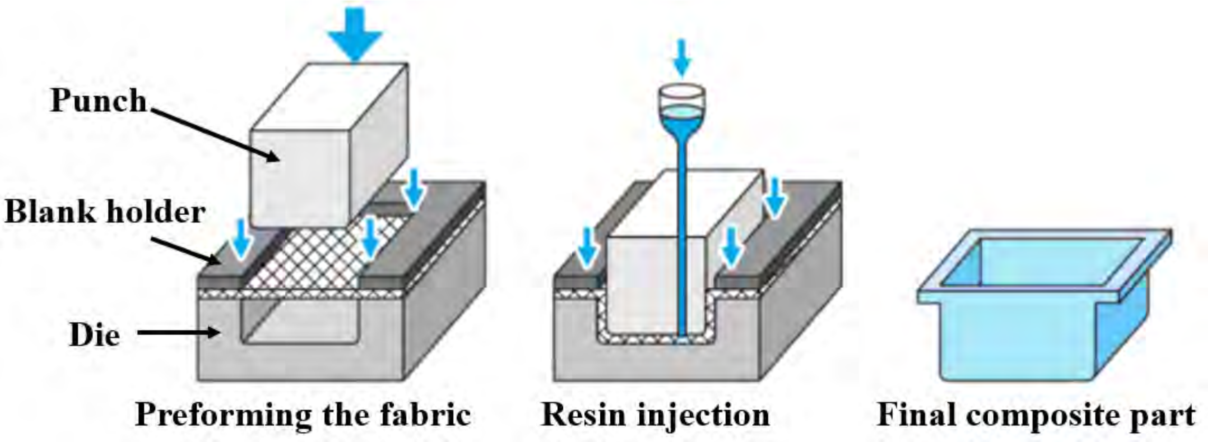

Figure 1.18: Schematics of performing and resin injection molding processes. (Boisse, 2004)

For composite materials with a thermoplastic matrix, the shaping of the textile reinforcement profoundly affects the mechanical properties of the composite materials at once consolidated 1.18. The deformation mechanisms of continuous, aligned fiber-based materials during the molding process are as indicated below : Intra-ply shear, intra-ply tensile loading, ply/tool or ply/ply shear, ply bending, and compaction/consolidation 1.19 (Long and Clifford, 2007).

The shear deformation of woven fabrics can be divided into four stages as follows: initial state, during shearing, further deformation, and deformation beyond locking angle (Rozant et al., 2000)(Syerko et al., 2015), where the deformation state of the textile reinforcement can be expressed by the shear angle between the yarns 1.20. As can be observed from the figure, the shear angle changes with the deformation of the reinforced fabric. Generally, at the first stage, the strands rotate at the intersection of the warp and the weft under a relatively small force. The degree of deformation is small, and the low stiffness comes from the friction of the strands between them. The second stage is

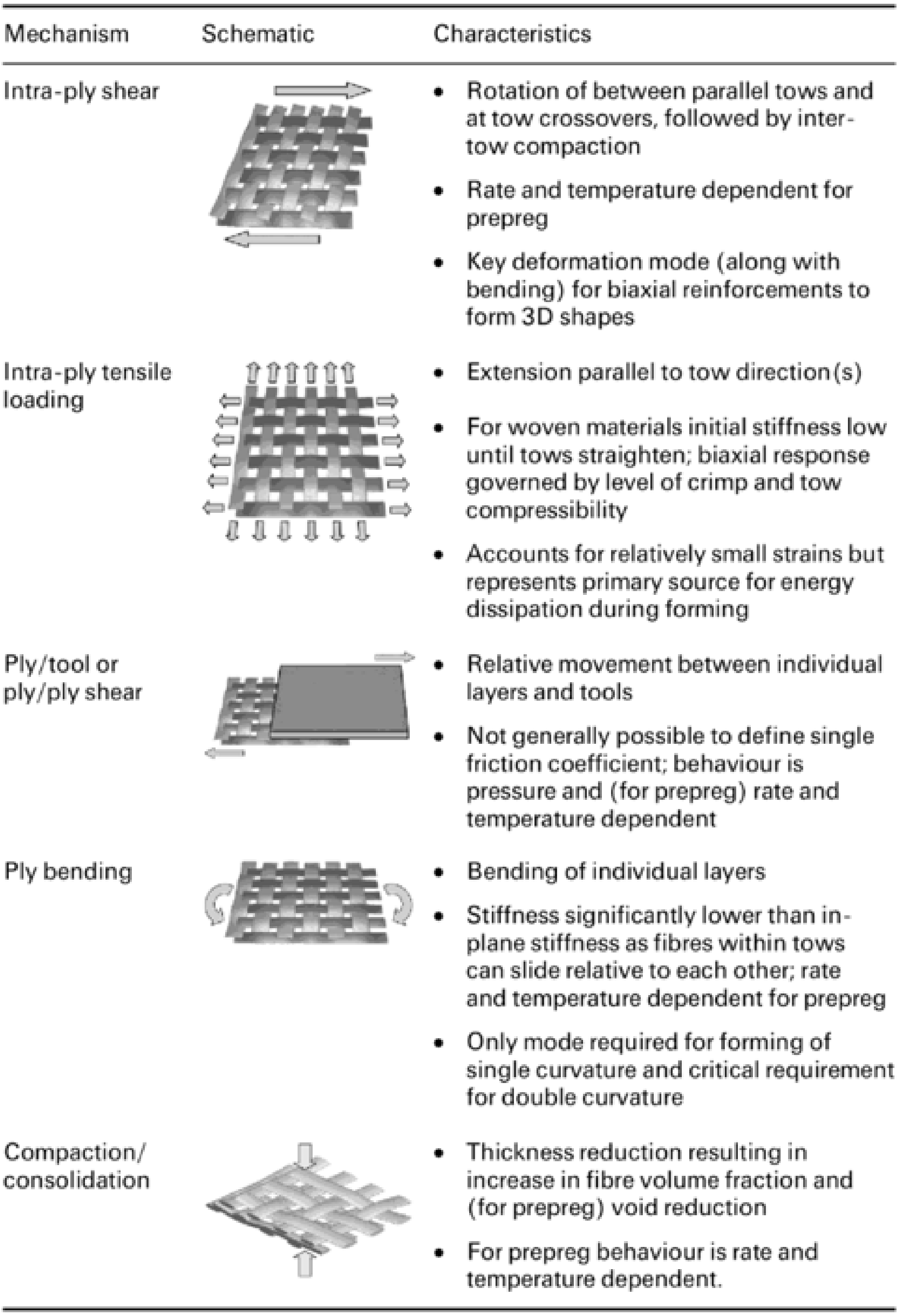

Mechanism	Schematic	Characteristics
Intra-ply shear		• Rotation of between parallel tows and at tow crossovers, followed by inter-tow compaction • Rate and temperature dependent for prepreg • Key deformation mode (along with bending) for biaxial reinforcements to form 3D shapes
Intra-ply tensile loading		• Extension parallel to tow direction(s) • For woven materials initial stiffness low until tows straighten; biaxial response governed by level of crimp and tow compressibility • Accounts for relatively small strains but represents primary source for energy dissipation during forming
Ply/tool or ply/ply shear		• Relative movement between individual layers and tools • Not generally possible to define single friction coefficient; behaviour is pressure and (for prepreg) rate and temperature dependent
Ply bending		• Bending of individual layers • Stiffness significantly lower than in-plane stiffness as fibres within tows can slide relative to each other; rate and temperature dependent for prepreg • Only mode required for forming of single curvature and critical requirement for double curvature
Compaction/ consolidation		• Thickness reduction resulting in increase in fibre volume fraction and (for prepreg) void reduction • For prepreg behaviour is rate and temperature dependent.

Figure 1.19: Deformation mechanisms of continuous, aligned fiber-based materials during forming. (Long and Clifford, 2007)

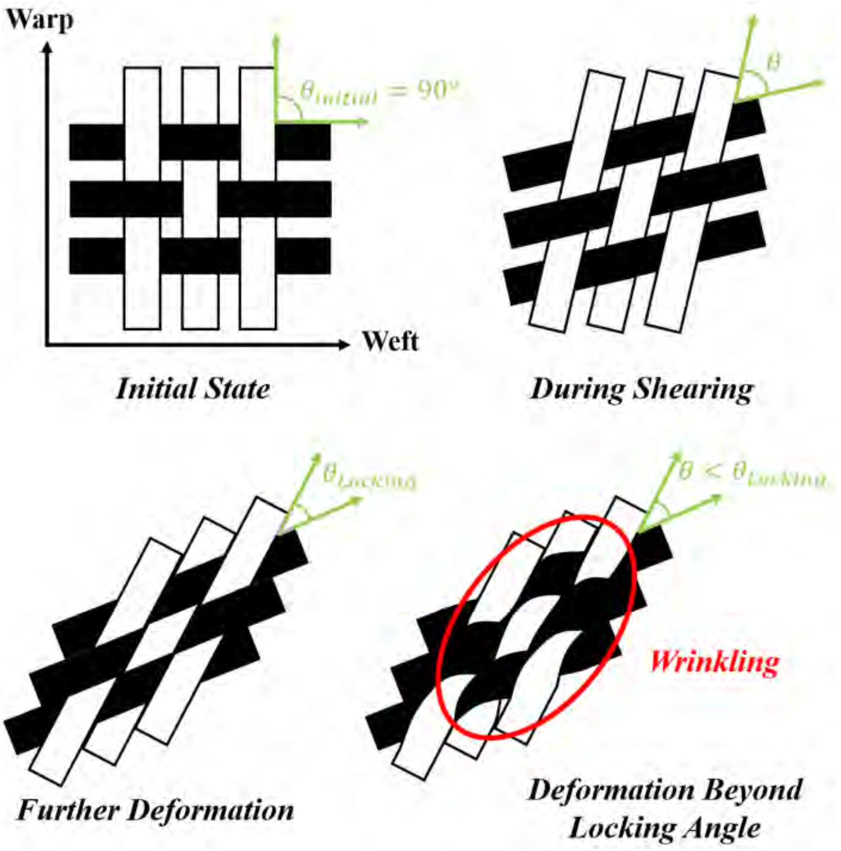

Figure 1.20: Schematic representation of shear deformation of woven fabrics.

the shear blocking phenomenon. Adjacent strands in the same direction contact each other and produce lateral compression. This phenomenon can be observed by measuring the shear angle between the warp and weft networks. In the final stage, the lateral compaction of the strands gains in intensity and is added to the friction of the fibers causing the stiffening of the fabric. Depending on the nature of the fibrous reinforcement, this phase is generally accompanied by wrinkling of the reinforcement. The wrinkle is the main defect. The shear in some areas exceeds the limit of in-plane deformation, resulting in wrinkles; while other areas with relatively low shear have no wrinkling. In RTM, for example, during the preforming of composite material, the fabric reinforcement is subjected to forces exerted by the mold: (1) the orientation of the warp and weft yarns is transformed; (2) the state of the warp and weft yarns changes from almost unstressed and bent to stretched and taut.

As mentioned above, wrinkles may occur in the final state and fiber breakage will greatly affect the mechanical properties of the composite material after molding, causing irreversible consequences. Molding a fabric reinforced material in this state, there is a certain possibility that air pores exist at the wrinkles. This means there is no perfect contact between the resin and the fabric reinforcement material, and there are likely be gaps between them. In the case of the finished product being subjected to external forces, the defective areas are more likely to have: (1) the slippage between the fiber and resin; (2) the inter-layer movement; (3) the fiber rupture; (4) the weakening of toughness and strength; and (5) the cracking of the resin, which leads to the fracture of the finished product.

The overall objective of the work presented is to develop innovative tests and measurement methods to study the mechanical properties of this type of composite in situations representative of their shaping. For the measurement part, the idea is tantamount to moving towards the finite elements approach to digital images correlation formulated in the world reference (Pierré et al., 2017). The latter should open many perspectives in terms of dialogue or take into consideration the underlying kinematics of tissue.

1.3 Characterization methods for mechanical properties of textile reinforcement

The deformations of reinforcements (Boisse, 2004) are complex and are a combination of several phenomena: biaxial tension, plane shear, tension between strands, but also compaction and friction during tests of performing multi-ply and bending. So, generally, accepted methods for studying the link between the mechanical properties of the composite and the characteristics of textile reinforcement include bias-extension test (Buckenham, 1997; Taha et al., 2013; Wang et al., 2014; Boisse et al., 2017), picture frame test (Mohammed et al., 2000b; Lebrun et al., 2003; Harrison et al., 2004; Peng et al., 2004; Launay et al., 2008; Cao et al., 2008), and punch test (Toloczko et al., 2000; Guduru et al., 2006; Wakeman et al., 2006; Egan et al., 2007; Boisse et al., 2011).

1.3.1 Bias-extension test

The bias extension test is a classical method for characterizing the shear deformation of a woven reinforcement (Buckenham, 1997; Boisse et al., 2017). A simple rectangular fabric sample whose edges are aligned with the bias is conventionally loaded into a tensile machine (for a woven material, the weft and warp threads must be oriented at ±45° with respect to the tensile direction). We note L its length and W its width. Let's imagine that we stretch the fabric from L to L + d. If L is at least twice as large as W, three zones can be distinguished during the deformation process: a zone an where no shear is observed, a semi-shear zone, and a pure shear zone (Bel et al., 2012; Gereke et al., 2013), as shown in Fig.1.21. In zone A, both the warp and weft yarns have indeed clamped ends, and the forces acting on the yarn in this zone are balanced. Therefore, the yarn in this zone does not deform. In zone B, one yarn direction is clamped at its end while the other direction is free. This means that during the stretching process, the yarns in this zone will be stretched towards the fixed side. Zone C is the pure shear zone. In this region, both the warp and weft yarns have free ends, and theoretically, there is no relative movement of the crossover point between the warp and weft yarns during the stretching process. There is only rotation around the crossover point. Due to this deformation state between the warp and weft yarns, zone C is stretched in the direction of the force by a distance of d. According to several researchers, the shear strain on the yarn in zone B is half of that in zone C (Boisse et al., 2017).

$$\gamma = \frac{\pi}{2} - 2arccos(\frac{H+d}{\sqrt{2}H}) \tag{1.1}$$

As a consequence of this property, the deformation state of the zone C can be expressed

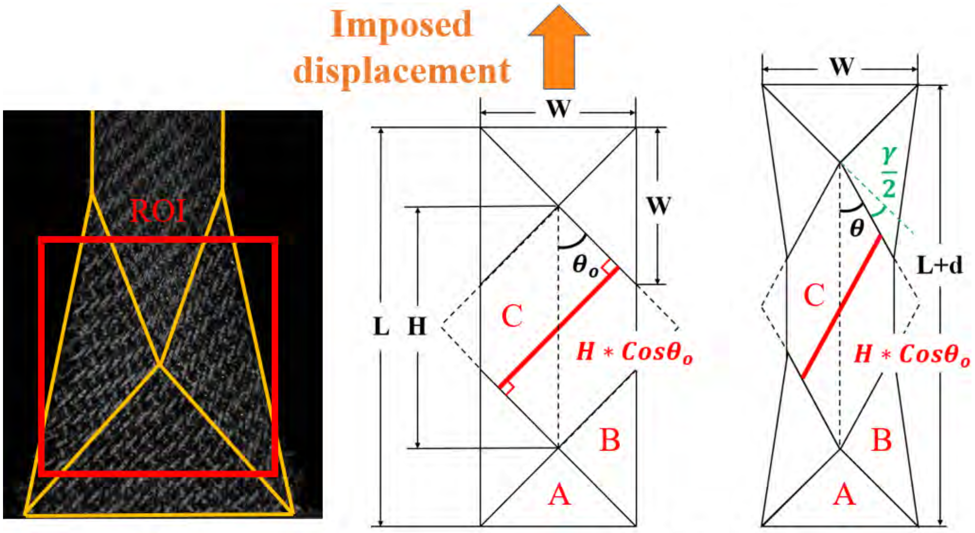

(a) (b)

Figure 1.21: (a) Fabric sample subjected to a bias extension test. The region of interest (ROI) selected in the present work is illustrated by the red rectangle. This region enables the study of the three classical zones (noted A, B and C) but also of the transition layers (b) Classical zoning observed in the Bias extension test: A zone without shear, B semi-shear zone, C pure shear zone (from (Cao et al., 2008))

in terms of the shear angle γ (Cao et al., 2008). The most common method for calculating the shear angle of textile reinforcement material during a bias extension test is attributed to Gilbert Lebrun (Lebrun et al., 2003). In zone C, if the partition lines of the region are extended (dashed lines indicate extension lines), a square is obtained as shown in Fig.1.21 (b). In the initial state, the side length of the square can be easily calculated. During the second stage of stretching, for the fabric sample, adjacent yarns of the same direction touch each other and compress laterally, as shown in Fig.2.4 (b). The shear angle consequently changes, resulting in the shear blocking phenomenon. At this stage, the main role of tension is to promote the warp and weft yarns to rotate around the intersection, and the tension in the direction of the extended fiber is not very large, so the fiber elongation in the stretching process can be ignored. In other words, the edge length of the diamond will not change during the shear angle change and can be calculated based on the initial state $H * Cos\theta_0 = \frac{H}{\sqrt{2}}$. Assuming that the elongation of the textile reinforcement material is d, the formula for the shear angle γ can be obtained from the geometric properties of the rhombus, as shown in Equation 1.1:

1.3.2 Picture frame test

Shear deformation is the main mode of deformation in woven fabric forming (Launay et al., 2008). Another experimental approach similar to the bias test is the picture frame test, but with a significant difference (Lebrun et al., 2003; Harrison et al., 2004; Taha et al., 2013; Hosseini et al., 2018). When performing the picture frame test, the sample is theoretically subjected to a homogeneous pure shear strain field. As shown in Figure 1.22, a square hinged frame with four equal length bars is designed in the tensile testing machine. One corner of the picture frame device is fixed to the tensile testing machine and the direction of tensile force is applied vertically upward along the diagonal direction of the picture frame device. During the experiment, two cameras equipped with telecentric lenses are mounted symmetrically on either side of the sample. They are used to measure the displacement field at the surface of a yarn.

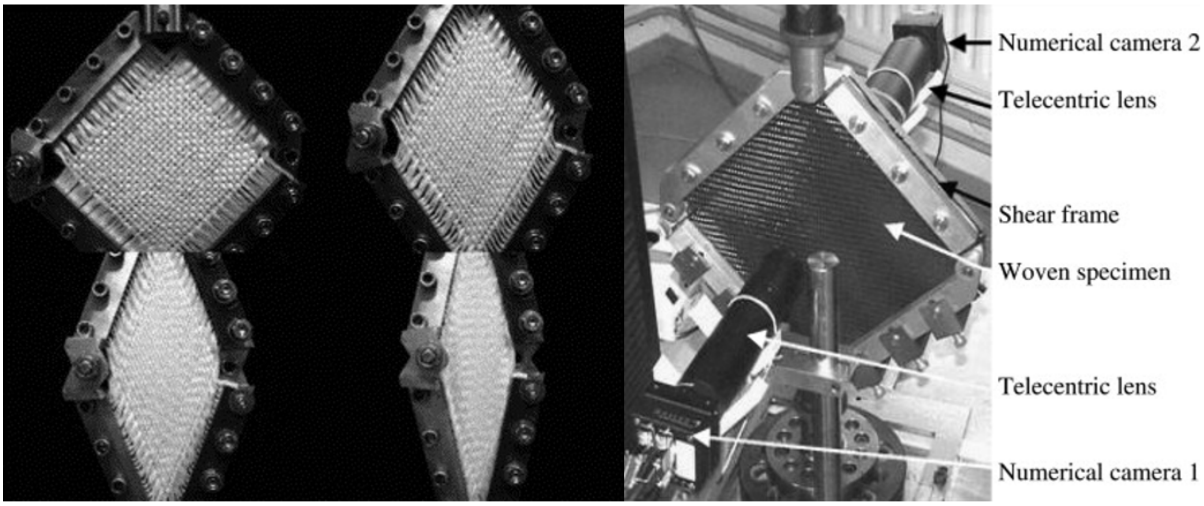

Figure 1.22: Images taken at various stages of loading during a picture frame test (Zhu et al., 2007a) and DIC instrumentation for monitoring deformation locally at yarn scale (Launay et al., 2008)

Due to the very high tensile stiffness of the fabric, the yarn is installed parallel to the side of the frame in order to avoid not being stretched during the test. In order to ensure that the fabric in the test effective area occurs pure shear (Zhu et al., 2007a), the boundary yarns are removed to prevent the wrinkle phenomenon due to extrusion in the near side frame 1.22.

Similar to the bias test, the shear deformation of the reinforced material can also be divided into 3 stages (McGuinness and ÓBrádaigh, 1998; Mohammed et al., 2000b; Peng et al., 2004). The first stage is the elastic deformation stage, the fabric shear force is less than the friction resistance at the crossover point. The second stage is the yarn rotation stage, the yarn in the fabric around the crossover point rotation. When the yarn rotation to interlocking compact, the fabric shear process into the third stage, that is, the yarn extrusion stage. At this moment, the yarn is locked and compressed with each other until the wrinkle is produced, what one seeks to avoid in a forming process. The angle between the warp and weft yarns in the fabric when adjacent yarns are in contact with each other is called the fabric locking angle. In the ideal state (1) the sizing agent is evenly distributed in the yarn; (2) the relative slip of warp and weft yarns in the shearing process is ignored; (3) there is no elongation of the yarn in the length direction; (4) the thickness of the fabric in the shearing process remains unchanged.

There are significant differences in the shear strain field in the fabric samples observed during the bias extension test and the picture frame test (Harrison et al., 2004; Hosseini et al., 2018). A large part of the reason for the difference in the observed results is due to the difference in the boundary conditions on the fabric when the two experiments were performed. For the boundary conditions of the bias test, the shorter two sides are fixed and the other two sides are free ends. During the experiment, the sample of the bias test is divided into three regions: the zone without shear, the semi-shear zone, and the pure shear zone, which can better reflect the shear deformation state of the reinforced fabric in its natural state. For the frame experiment, the yarn is clamped to the rigid bars of the frame, and ideally the entire fabric plane is considered to be a pure shear region, which is difficult to achieve for other types of experiments. The bias test makes it much easier to observe the shear angle. However, for the picture frame test, the parallelism between the yarns and the sides of the frame is difficult to accomplish, and a certain initial tension (Lebrun et al., 2003; Launay et al., 2008) will be applied when the fabric is installed. As the initial tension is too small, the initial tension is regarded as zero, and the effect on the results is negligible. And usually, the in-plane shear stress depends only on the shear angle. For picture frame tests, the shear angle can be calculated from the frame displacement or measured by optical measurements. The theoretical shear angle is related to the elongation of the diagonal of the frame 1.23:

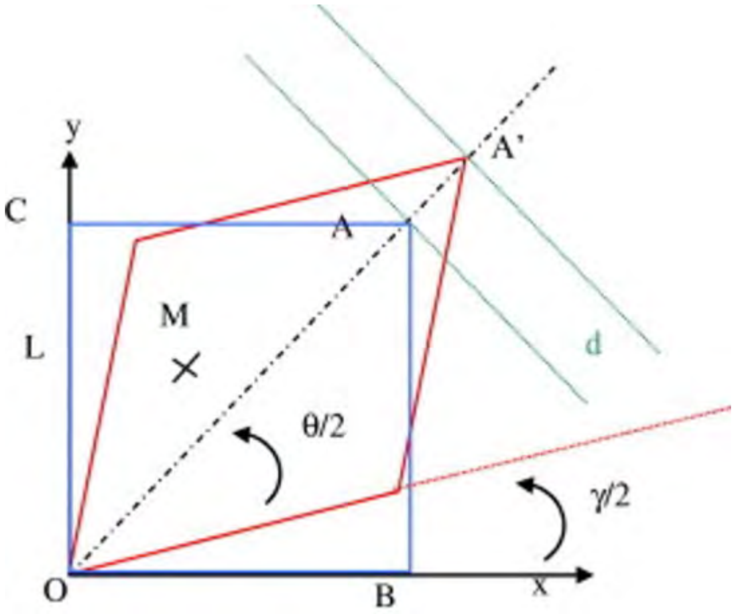

Figure 1.23: Pure shear kinematics. (Launay et al., 2008)

where the side length of the picture frame ABOC is L and the elongation of the diagonal OA is d. During the stretching process, the angle of the frame is θ and the shear angle is γ. According to the characteristics of isosceles triangle, it is easy to get the expression equation of the shear angle γ :

$$\gamma = \frac{\pi}{2} - 2arccos(\frac{\sqrt{2}L + d}{2L}) \tag{1.2}$$

According to Equation 1.2, the trend of the shear angle is only related to the length L of the picture frame. Fig.1.24 shows the variation curve of the shear angle with respect to the stretch length for L of 150 mm, 175 mm, and 200 mm. For the 3 curves, it can be seen that the trend of the shear angle is approximately the same. The picture frame experiment also has some limitations. Since image frames are non-standard and each frame test device is a unique device developed by the research institution or company itself, there is no comparability between different test devices. And small changes in the test device can cause substantial changes in the results.

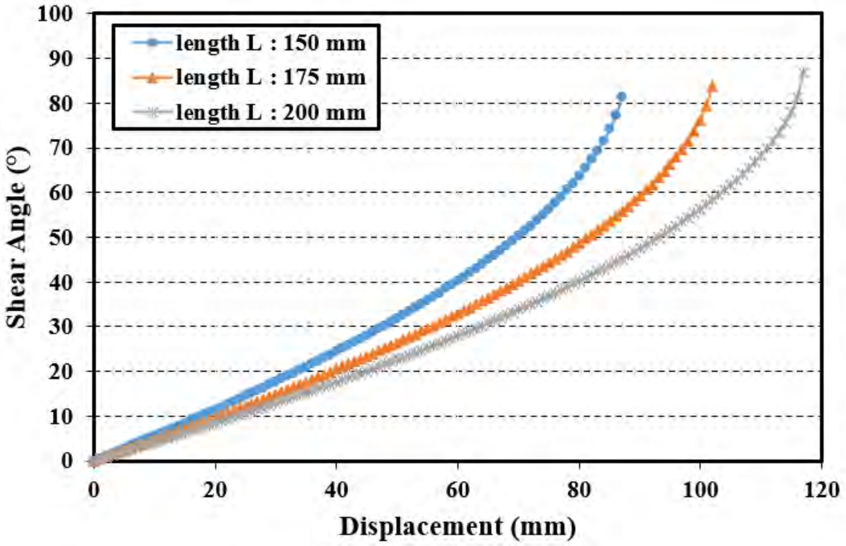

Figure 1.24: Theoretical shear angle obtained from the formula 1.2.

1.3.3 Draping experiment

The purpose of the draping experiment is to provide information on the local deformation of fabrics and yarns, as shown in Fig.1.26. The characteristic local deformations of yarns are warpage and slippage of the yarn. Yarn flexion out of plane causes a change in yarn orientation and gaps between the upper and lower plies of the yarn. When resin is applied with compression and impregnation, these areas flatten out, leading to significant local fiber misalignment, which reduces the local stiffness and strength of the composite. By the same reason, in the transverse direction, yarn slippage can cause large gaps between adjacent yarns, and after the composite is formed, can result in high resin content here but low yarn percentage. No matter which defect is present, these areas are likely to become the initiation point of matrix cracking when external forces are applied, as this is the case with non-crimp fabrics (Truong et al., 2005; Mikhaluk et al., 2008).

It is well known that defects in composite materials are to a large extent generated during the manufacturing process. The wrinkling (Mohammed et al., 2000a; Boisse et al., 2018a; Guzman-Maldonado et al., 2019) is one of the most common defects during the textile composite reinforcement molding process. The other is the large slippage that can occur during the molding of preforms (Boisse et al., 2016). As mentioned before, in-plane shear deformation is generally studied by bias test and picture frame test. Shearing can cause fiber disorientation. It can lead to localized rigid orientations of the final part that deviate significantly from the original design and expose the base material. It also results in increased the stress in these areas, and causes unacceptably high tensile forces in the part. This eventually leads to premature part damage. For textile composite reinforcement, shear behavior is the most important draping mode. If situations such as wrinkles or fiber misalignment occur during the preforming process, this can lead to resin enrichment in these draping defect areas during the infiltration process. These resin-enriched areas then become the starting point for fracture. In order to study more directly the deformation of the textile composite reinforcement during preforming, the draping experiments is used.

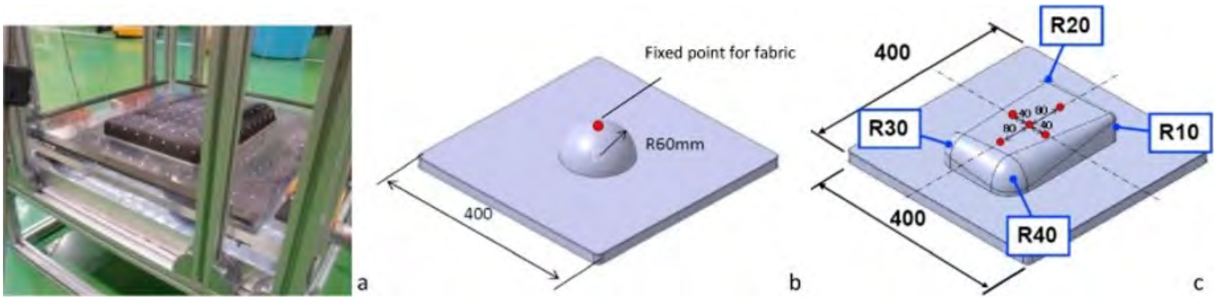

Figure 1.25: The draping experiment: (a) setup, moulds; (b) hemispherical; (c) box-shape. (Iwata et al., 2019)

More and more researchers are using this method to study the deformation of fabrics. (Breen et al., 1994a) describe two experiments conducted to evaluate the approach. Different deformed shapes or drape patterns may appear when repeating the same draping experiment for the same piece of fabric. (Hu et al., 2000) explore the possibility of using numerical techniques to reproduce this complicated but interesting fabric drape behavior. (Yin et al., 2014) investigate the complex fiber reorientation and redistribution of plain woven carbon fabrics draping over a double-curvature mold through experimental and numerical approaches. (Engelfried et al., 2017) deal with a method to describe the inter-ply friction of preforms that consists of carbon fibre yarns joined by a thermoplastic binder. (Iwata et al., 2019) report results of such combined meso-macro modelling for a plain weave carbon fabric with spread yarns. Computationally viable meso-level simulation is achieved by coupling continuous macro draping simulation with a local meso-modeling in the location where the defects are expected to occur.

As shown in the Fig.1.25, the most common mould is hemispherical mould and box-shaped mould. The draping experiments are performed into three steps (Breen et al., 1994b; Han and Chang, 2018) : (1) First, the fabric is placed over the mould with fixed corner points, and the fabric is fixed with double-sided tape, ensure that the state of the fabric before the start of the experiment; (2) after that, the plate over the fabric was moved down with steps of 10 mm; (3) the final step is to capture the fabric deformation at each step with a camera.

The first 2 steps of the draping experiment process are basically completed, after which the full-field 3D deformation of the formed fabric is measured by an optical measurement system. For the optical measurement, there are two important points worth noting. One is to make regular dots on the surface of the fabric for tracking the deformation field before the experiment is conducted. Second, the experimental samples are photographed with a camera at different positions after the samples are fixed in the experimental equipment. The 3D coordinates of each dot can be derived by a photogrammetric algorithm. The

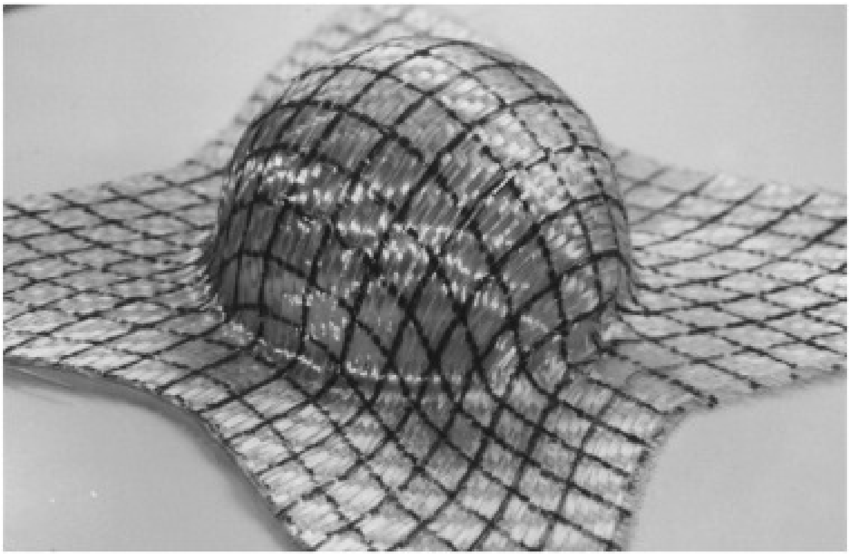

Figure 1.26: Draping of a woven reinforcement on a double-curved surface. (Bai et al., 2022)

images before and after deformation are analyzed to obtain the deformation field as well as the surface strain tensor in space and also to analyze the local shear angle.

Here is a material that must be mentioned : non-crimp (multi-layered warp-knit stitched) fabrics (NCFs) (Creech and Pickett, 2006; Sirtautas et al., 2013; Krieger et al., 2018). NCFs have attracted much attention in the composite industry and its usage is growing rapidly. As NCFs are deformed mainly due to shear deformation, they are difficult to be formed in three dimensional shapes. NCFs enable relatively high mechanical properties by keeping the reinforcement tows straight. Handling of those fabrics is improved by stitching the reinforcement tows together. While the stitching has little structural influence on the final part, it highly affects the NCFs capability to shear and drape over a mold duruing preforming. High tensile strain in the stitching yarn has been correlated to the NCFs resistance to shearing and even adverse drape defects such as tow undulations. Furthermore, stitching causes the shear behavior of the fabric to be anisotropic, with different behavior in positive and negative shear. Fig.1.27 shows the example of two representative biaxial NCFs configurations with their respective layer orientations (Colin et al., 2020). The basic process of NCF's draping experiment is slightly different from the traditional one (Krieger et al., 2018). This experimental procedure is closer to the experiment conducted by (Khan et al., 2010).

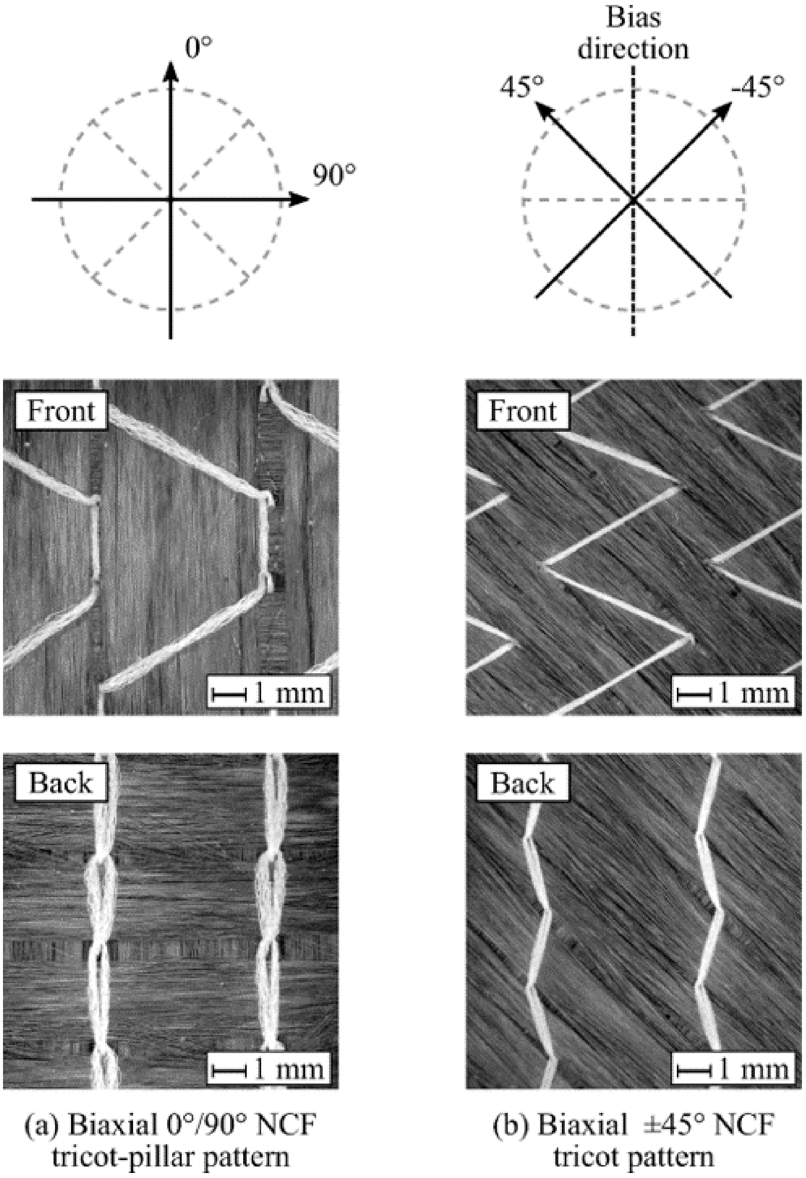

(a) Biaxial 0°/90° NCF tricot-pillar pattern

(b) Biaxial ±45° NCF tricot pattern

Figure 1.27: Example of two representative biaxial NCF configurations with their respective layer orientations. (Colin et al., 2020)

1.4 Characterization of textile reinforcements using optical measurements

Many optical methods have been developed to study the displacement and deformation of textile reinforcements during (or after) an experiment to in order to establish a link between the mechanical properties of composites and the deformations of their reinforcement (Vanclooster et al., 2009; Mallach et al., 2017; Dufour et al., 2018; Kunze et al., 2020). Digital image correlation (DIC) technique is the most commonly used method today (Launay et al., 2002; Lomov et al., 2008; Willems et al., 2008).

1.4.1 Digital image correlation (DIC)

1.4.1.1 DIC principle

Digital Image Correlation is an optical measurement method that gives access to the displacement field on the surface of an object from a speckle pattern deposited on the surface of an object. The idea is to match points of the surface in the images captured in the initial state then after deformation. The displacement field obtained following this pairing is often post-processed to provide a strain field.

2D DIC originated in the 1980s. Early work in the field of experimental mechanics is attributed to Peters and Ranson (1982). With the development of personal computers, digital cameras and processing methods, DIC then very quickly developed and imposed itself in research laboratories (Sutton et al., 1983; Chu et al., 1985; McNeill et al., 1987; Lyons et al., 1996; Sutton et al., 2009). The method gave rise to extensions called Stereo DIC (Helm et al., 1996) or Digital Volume Correlation (Bay et al., 1999). For DIC and Stereo DIC, more specifically, the three key steps to determine a displacement field are (Pan, 2018):

1. **Speckle Pattern Fabrication.** This is often a necessary and always a crucial step. A texture suitable for correlation must be created on the surface of the object: it must follow the deformation of the object, not alter its behavior and not generate parasitic reflections. The relevance of the image formed on the sensor (distribution of gray levels) of the camera will directly depend on this. This point will be dealt with in the section on 1.4.2.

2. **Digital Image Acquisition** When one is interested in "quasi 2D" displacements on "planar" surfaces, 2D DIC is an option. Only one camera, carefully arranged, is then required (see Fig. 1.29). The use of a calibration target, although it is rarely reported, may be useful to correct for distorsions (Pierré et al., 2016). The knowledge of an optical resolution is however necessary to go from measurements in pixels to measurements in mm. Stereo-DIC requires 2 cameras. In this case, the stereo bench should be calibrated. Many images of calibration targets are usually captured in order to identify the intrinsic and extrinsic parameters of the camera models.

3. **Displacement and Strain Field calculation.** The sample surface displacement field could be obtained by image registration in the acquired set of images (2D-DIC). For stereo-DIC, the 3D coordinates of all measured points are usually obtained (by

"triangulation") from the disparity maps calculated by the DIC algorithm knowing the intrinsic and extrinsic parameters of both cameras. After that, a series of algorithms can be used to determine the strain field.

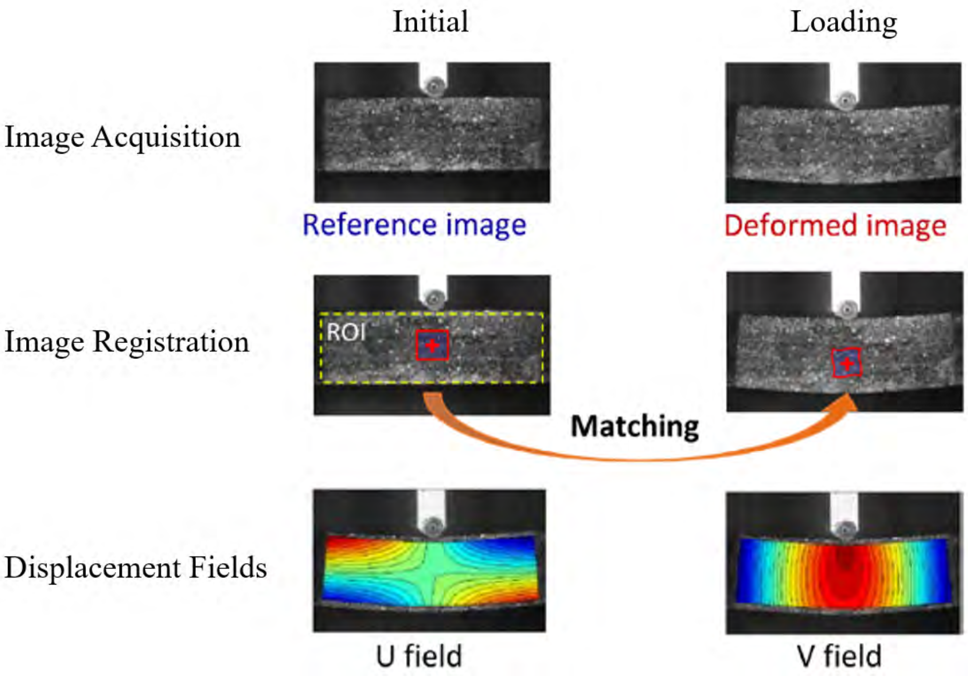

Figure 1.28: Implementation procedures of 2D-DIC. (Pan, 2018)

Fig.1.28, taken from (Pan, 2018), explains the principle for 2D DIC. This technique is very convenient because of the simplicity of its implementation. Fig. 1.29 shows the few necessary elements and precautions. However, it should be borne in mind that, without special precautions, the transformation identified by analysing the images has little chance of representing the true transformation seen by the object (the one we are interested in). With a standard macro lens, even if care is taken to orient the optical axis correctly with respect to the specimen ("fronto-parallel" set up, as shown in Fig. 1.29), (Sutton et al., 2008) show that the out-of-plane displacements can cause significant errors in the in-plane displacement measurement. The same authors show that if a telecentric lens can partially remedy this for small out-of-plane displacements, stereo DIC should be adopted in the presence of significant out-of-plane displacements.

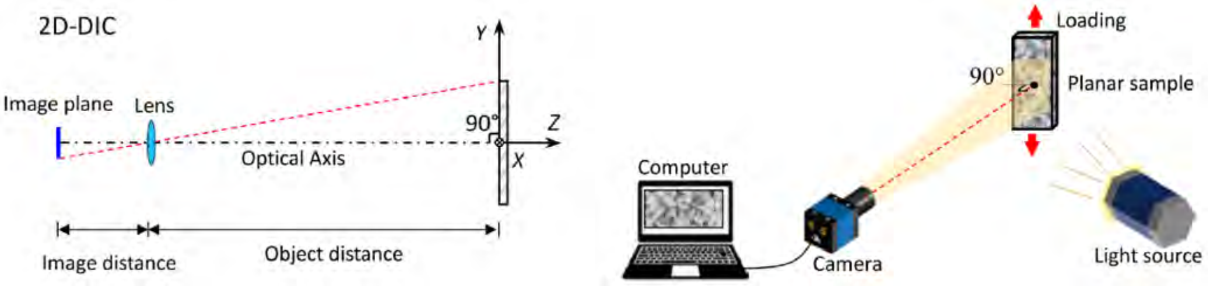

Figure 1.29: Schematic diagram of the principle of 2D-DIC. (Pan, 2018)

DIC is based on the assumption of relies on a so-called luminance or grayscale conservation equation. It usually consists in searching for the displacement field $\underline{u}$ in a given region Ω that minimize, in the least squares sense, the following functional:

$$\Phi^2(\underline{u}) = \int_{\Omega} [f(X) - g(X + \underline{u}(X))]^2 dX \tag{1.3}$$

where X is the position vector of a point in an image (in pixels), f and g represent the images captured in the reference and the deformed states respectively, and $\underline{u}$ is the sought-after displacement field.

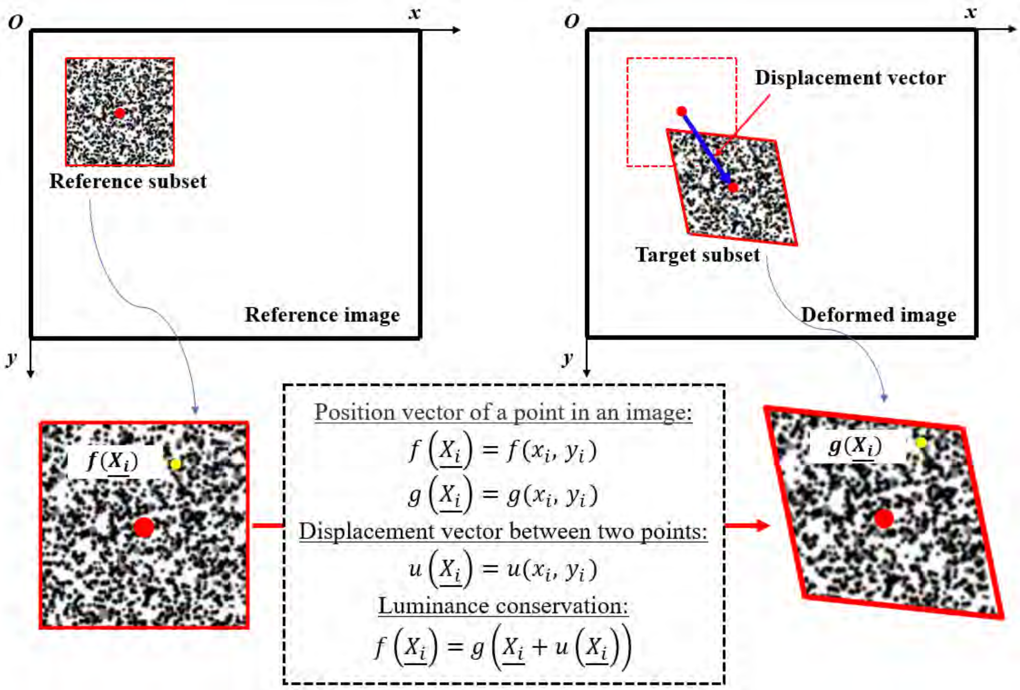

Figure 1.30: Principle of the common local approach to DIC, known as subset-based DIC. The approach is to treat the problem piece by piece in a number of image portions, called subsets. An i th subset is taken from the reference image f (on the left) at position (x_i, y_i). Taking into account a given transformation, the subset that best matches it in the image g is searched for. The likelihood criterion used is generally based on the hypothesis of gray level or luminance conservation. The recorded displacement vector $\underline{u}_i$ is usually calculated at the centre of the subset (Pan, 2011).

The problem being ill-posed, the displacement field is sought on a previously defined kinematic basis. For common approaches, referred to as local, the field is described in a small Zone Of Interest (or Subset - Ω=ZOI in Eq. 1.3) of the Region Of Interest (ROI) (Sutton et al., 1983). The principle of such an approach is depicted in Fig.1.30 taken from (Pan, 2011). In contrast, when the displacement field is described in the entire ROI (Ω=ROI in Eq. 1.3), it is referred to as a global method. In this thesis, a finite element formulation for a digital image correlation method (FE-DIC) (Sun et al., 2005; Besnard et al., 2006; Pierré et al., 2017) is used.

By its great simplicity of implementation, its robustness, DIC is essential in a large number of applications every day increasing. This method indeed plays an indelible role in many fields, for instance such as experimental mechanics (Orteu, 2009; Pan et al.,

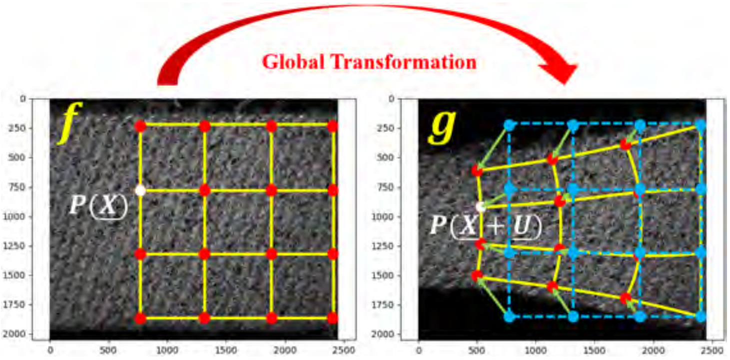

Figure 1.31: FE-DIC principle. The sought-for displacement field is described on a FE basis (Sun et al., 2005; Besnard et al., 2006). In this case, a uniform quadtree structured mesh is selected. The red and light blue dots represent the position of mesh nodes in the current and deformed states respectively. Green arrows represent identified nodal displacements. In practice, the problem is treated in physical space as described in (Pierré et al., 2016), using the Pyxel (Passieux, 2021) library. P stands for the projector allowing to project one point $\underline{X}$ on the sample surface into the image ($\underline{x} = P(\underline{X})$) and $\underline{U}$ for the displacement in the physical space.

2013; Ye et al., 2015; Engqvist et al., 2016), biomechanics (Bay, 1995; Huang et al., 2009; Brunon et al., 2010; Huang et al., 2016), composite mechanics investigation (Périé et al., 2002; Boisse et al., 2017; Pierré et al., 2017; Bai et al., 2020), and, even now structural health monitoring (Reagan et al., 2018).

1.4.1.2 FE-DIC

The most famous approach to global DIC, called FE-DIC, consists in decomposing the displacement field on a Finite Element basis (Sun et al., 2005; Besnard et al., 2006). Fig.1.31 illustrates the principle behind this technique.

FE-DIC problem resolution

A Gauss-Newton iterative method is used to solve this problem numerically. Suppose we know the displacement $\underline{u}_i$ at the i th iteration. In practice, we are looking for the correction $\delta\underline{u}$

$$\underline{u}_{i+1} = \underline{u}_i + \delta\underline{u} \tag{1.4}$$

which allows us to minimise Eq. 1.3. The correction is assumed to be small. A Taylor expansion of $g(\underline{X} + \underline{u}_i + \delta\underline{u})$ allows us to rewrite the equation 1.3 :

$$\Phi^2(\underline{u}) = \int_\Omega [g(\underline{X} + \underline{u}_i) + \delta\underline{u}\nabla g(\underline{X} + u_i) - f(\underline{X})]^2 d\underline{X} \tag{1.5}$$

In practice, we will not use $g(\underline{X}+\underline{u}(\underline{X}))$ (the gradient of the deformed image advected by the displacement), which should be updated at each iteration, but we will approximate it by the gradient of the reference image $f(\underline{X})$ (Neggers et al., 2016; Passieux and Bouclier, 2019). The new functional to be minimised is now:

$$\Phi^2(\underline{u}) \approx \int_\Omega [g(\underline{X} + \underline{u}_i) + \nabla f(\underline{X})\delta\underline{u} - f(\underline{X})]^2 d\underline{X} \tag{1.6}$$

The displacement correction is then decomposed on a FE basis as follows

$$\delta \underline{u}(\underline{X}) = \sum a_i \underline{N}_i(\underline{X}) \tag{1.7}$$

where a_i represent the degrees of freedom (the components of the nodal correction displacement field) and $N_i(x)$ are finite element shape functions. Eq. 1.7 is finally injected in the equation 1.6. The minimization of the scalar residual $\Phi^2(\underline{u})$ leads to the solution of linear systems of the type $\mathbf{M}\underline{a} = \underline{b}$. The displacement is then updated, and a new correction is sought. Several types of stopping criteria are used (stagnation, number of iterations, etc.). The following 1D example illustrates how the correlation matrix $\mathbf{M}$ and the right-hand side vector are constructed.

1D FE-DIC problem resolution

We consider a one-dimensional displacement field. We consider a bar of length L. We know the gray level distribution along the bar $f(X)$ at the start (reference image). We look for the displacement field u in the bar that explains which leads to the distribution $g(x)$ (Assumption: the texture is passively advected by the displacement). We mesh the bar uniformly. We use n linear elements. The length of each element is assumed to be equal to h ($h = L/n$). Each element domain is defined as $\Omega_e = [x_{e-1}, x_e]$, where $x_k = (k-1)h$ with $e = 1, ..., n$. u^i is the displacement field obtained in step i. In each element, two shape functions ϕ_n and ϕ_{n+1}

$$\phi_n = 1 - \frac{X - x_n}{h} \quad et \quad \phi_{n+1} = \frac{X - x_n}{h} \tag{1.8}$$

are used to interpolate the displacement field correction:

$$\delta u(X) = a_n \phi_n(X) + a_{n+1}\phi_{n+1}(X) \tag{1.9}$$

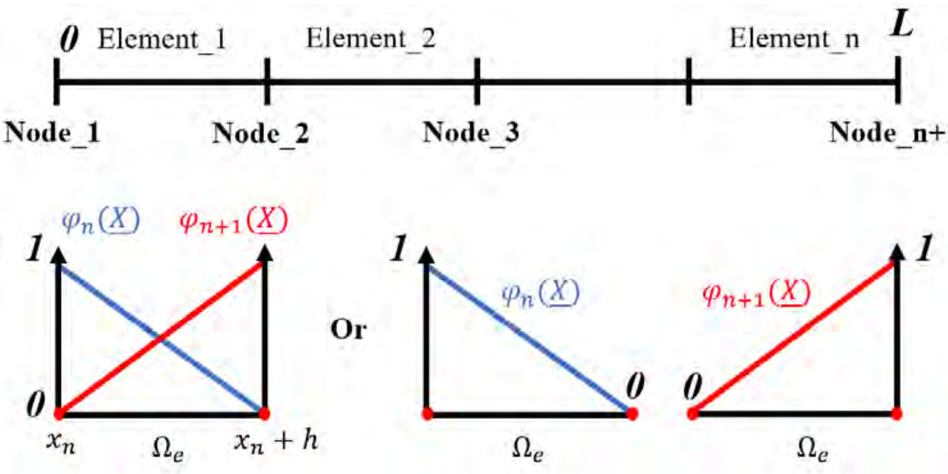

Figure 1.32: 1D shape functions ϕ_n and ϕ_{n+1}.

Eq. 1.6, for the e^{th} element $\Omega = \Omega_e$, reads

$$\Phi^2(\underline{u}) \approx \int_\Omega [g(X + u^i) + \nabla f(X)(a_n\phi_n(X) + a_{n+1}\phi_{n+1}(X)) - f(X)]^2 dX \tag{1.10}$$

We can then derive Eq. 1.10 with respect to the two nodal displacements a_n and a_{n+1}. The notations are simplified below: $g(X + u^i) = g_u$, $\phi_n(X) = \phi_n$ and $\nabla f(X) = \nabla f$. This gives:

$$\frac{\partial \Phi^2}{\partial u_n} = 2\int_{\Omega_e} [g_u + \nabla f(a_n\phi_n + a_{n+1}\phi_{n+1}) - f]\nabla f \phi_n dX = 0 \tag{1.11}$$

$$\frac{\partial \Phi^2}{\partial u_{n+1}} = 2\int_{\Omega_e} [g_u + \nabla f(a_n\phi_n + a_{n+1}\phi_{n+1}) - f]\nabla f \phi_{n+1} dX = 0 \tag{1.12}$$

i.e. the following system:

$$a_n \int_{\Omega_e} \phi_n^2 \nabla f^2 dX + a_{n+1}\int_{\Omega_e} \phi_n\phi_{n+1}\nabla f^2 dX = \int_{\Omega_e} [(f - g(X + a_i))\phi_n \nabla f] dX \tag{1.13}$$

$$a_n \int_{\Omega_e} \phi_n\phi_{n+1}\nabla f^2 dX + a_{n+1}\int_{\Omega_e} \phi_{n+1}^2 \nabla f^2 dX = \int_{\Omega_e} [(f - g(X + a_i))\phi_{n+1} \nabla f] dX \tag{1.14}$$

A system $[M]^e * [a] = [b]^e_n$, where $[M]^e_n$ and $[b]^e_n$ are respectively the elementary correlation matrix and the right-hand side vector for the considered element e, is finally obtained. It reads:

$$[M]^e_n = \begin{bmatrix} M^e_{11} & M^e_{12} \\ M^e_{21} & M^e_{22} \end{bmatrix} = \begin{bmatrix} \int_{\Omega_e} \phi_n^2 \nabla f^2 dX & \int_{\Omega_e} \phi_n\phi_{n+1}\nabla f^2 dX \\ \int_{\Omega_e} \phi_n\phi_{n+1}\nabla f^2 dX & \int_{\Omega_e} \phi_{n+1}^2 \nabla f^2 dX \end{bmatrix}$$

$$[b]^e_n = \begin{bmatrix} b^e_1 \\ b^e_2 \end{bmatrix} = \begin{bmatrix} \int_{\Omega_e} [(f - g(X + u_i))\phi_1 \nabla f] dX \\ \int_{\Omega_e} [(f - g(X + u_i))\phi_2 \nabla f] dX \end{bmatrix}$$

To determine the Hessian matrix of the global problem $[M]_{global}$ and the right-hand side vector $[b]_{global}$, we need to assemble the elementary matrices $[M]^e_n$ and the elementary vectors $[b]^e_n$ in the following form:

$$\begin{bmatrix} M^1_{11} & M^1_{12} & 0 & \dots & 0 \\ M^1_{21} & M^1_{22} + M^2_{11} & & & 0 \\ 0 & M^2_{21} & M^2_{22} + M^3_{11} & & 0 \\ \vdots & & & \ddots & \vdots \\ 0 & 0 & 0 & \dots & M^n_{22} \end{bmatrix} * \begin{pmatrix} a_1 \\ a_2 \\ a_3 \\ \vdots \\ a_n \end{pmatrix} = \begin{pmatrix} b^1_1 \\ b^1_2 + b^2_1 \\ b^2_2 + b^3_1 \\ \vdots \\ b^n_2 \end{pmatrix}$$

Generalisation to any mesh, and of course extension to 2D and 3D, requires some further development. However, the main task is to assemble the correlation matrix and the right-hand side vector. The 'Pyxel' library, developed by Passieux (2021), is designed to do just that.

Specific features of the approach developed at the ICA

In the following, we follow the route proposed in (Pierré et al., 2016). The main change is that the DIC problem is formulated directly in the physical coordinate system. The problem's unknown becomes the displacement $\underline{U}$ (expressed in mm in the physical coordinate system), and no longer $\underline{u}$ in the image (in px). This requires the introduction of a projector model P (a 3D point $\underline{X}$ is projected in the image plane at x, *i.e.* $\underline{x} = P(X)$).

The latter must be calibrated. There are several arguments for adopting such a FE-DIC scheme. The method makes it possible to impose the continuity of the displacement field, and by relying on the same kinematic basis as that usually adopted for the simulation, it makes it possible to connect simply to these tools, even in stereo DIC (Pierré et al., 2017).

1.4.1.3 Bi-telecentric lens

In this work, a bi-telecentric lens (Hu et al., 2022) is used to perform 2D FE-DIC measurements. These lenses have two major advantages for monovision measurements:

1. Unlike the macro lenses traditionally used in DIC, a telecentric lens keeps the principal rays parallel to the optical axis of the lens. As a result, the size of the object remains unchanged in the event of (moderate) out-of-plane movements.
2. Telecentric optics offer very low distortion and provide extremely precise geometric information

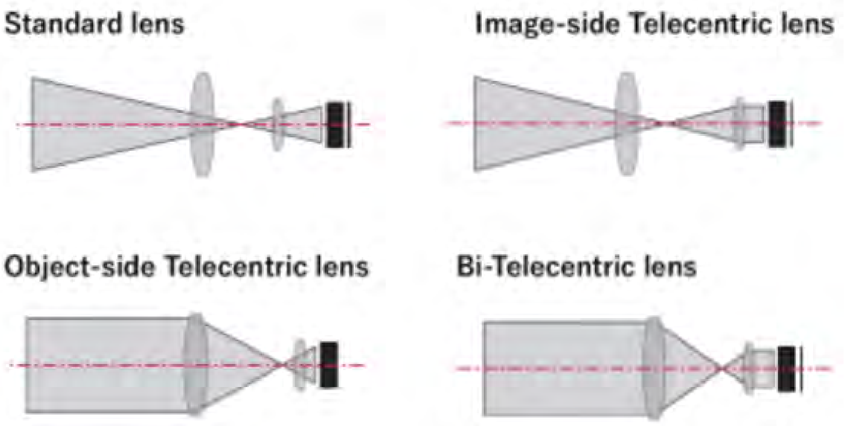

Figure 1.33: Four different types of lens, and their principles of performance. [Taken from VS Technology website]

In addition, this type of lens enables (Mei et al., 2016):

- An increase in the depth of field;
- A homogeneous illumination of the CCD sensor;
- Constant magnification, even if the sensor is not perfectly positioned.

A bi-telecentric lens is composed of two sets of lenses called object-side lens and image-side lens, respectively, as Fig.1.34 shows (Hu et al., 2022). The object-side lens's rear focal plane coincides with the front focal plane of the image-side lens at a common plane where an aperture stop is placed. This aperture stop cooperates with the object-side lens to form telecentricity in the object space and cooperates with the imaging lens to form telecentricity in the image space. The magnification of the bi-telecentric lens is determined by the focal lengths of the two sets of lenses together, so no matter the working distance or the camera sensor's position changes, it will not change the optical

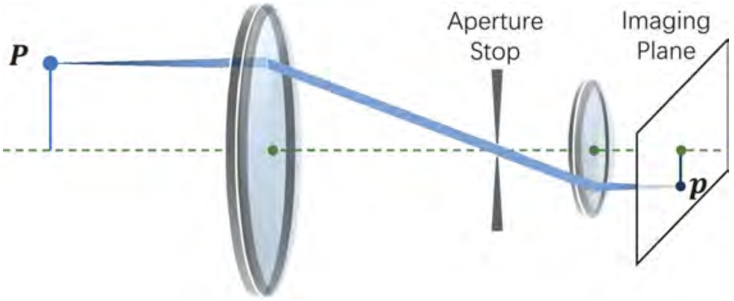

Figure 1.34: The optical model of a bi-telecentric lens. (Hu et al., 2022)

magnification. However, a specific working distance (depends on the model of the lens) should be satisfied when applying bi-telecentric lenses to minimize imaging distortion and maintain "perfect" telecentricity.

1.4.1.4 Stereo-digital image correlation

Based on the principle of binocular stereovision, stereo DIC (Genovese et al., 2013; Goidescu et al., 2013; Shao et al., 2016; Pierré et al., 2017; Pan et al., 2018) is commonly used to measure 3D shape and is often preferred for assessing deformation of both planar and curved surfaces where significant out-of-plane displacements are expected (Sutton et al., 2008). The principle of operation for the stereo-DIC technique is similar to 2D-DIC.

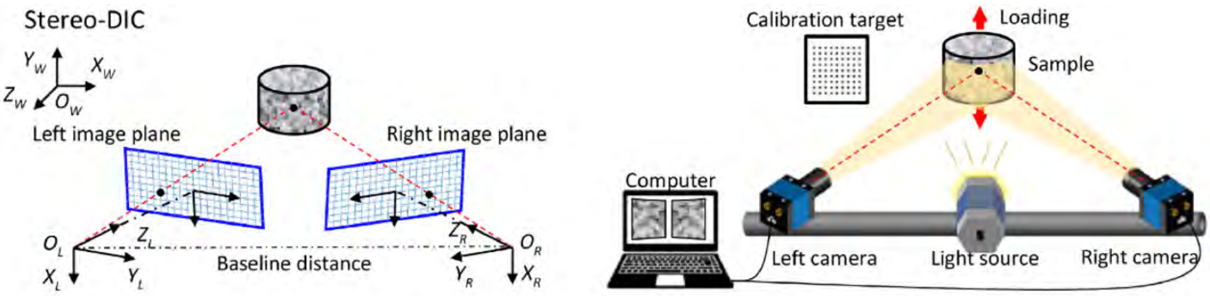

Figure 1.35: Schematic diagram of the principle of stereo-DIC. (Pan, 2018)

For the stereo-DIC technique, the main components are the two cameras, the control and image acquisition software, the calibration target, and the light source, as shown in Fig.1.35. Fig.1.36 shows the main steps involved in stereo-DIC: calibration target image acquisition, camera calibration, experiment image acquisition, image registration, displacement measurements and calculation of strain fields. Before starting the experiment, the cameras must indeed be calibrated to obtain the magnification factor and the intrinsic and extrinsic parameters of the imaging systems. VIC-3D (Patou, 2018), the subset based Stereo-DIC software used in this work, also controls the system and performs image acquisition. This kind of Stereo-DIC approach uses disparity fields measured by DIC between one master camera (say the left) and the others (say the right for shape measurement, and the deformed ones for tracking the displacement) (Sutton et al., 2009). The spatial position of a point M can then be calculated from the difference in position of its projection m_L and m_R respectively in the left and right camera and the knowledge of the projectors P. Here, the parameters obtained from the stereovision calibration are used. The 3D point cloud obtained at one stage of the deformation process gives access to the shape of the part. The displacement field is finally deduced by subtracting the position of the points in the deformed state from that obtained in the reference state (see Fig.1.36).

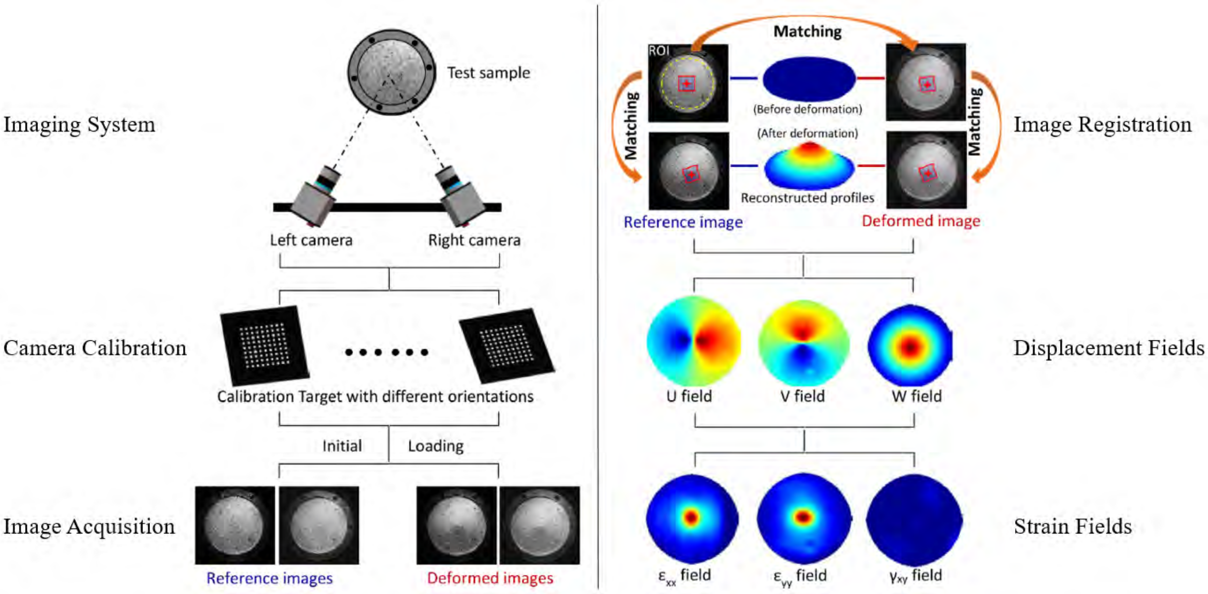

Figure 1.36: Implementation procedures of stereo-DIC. (Pan, 2018)

1.4.2 Speckle pattern fabrication for textile reinforcements

DIC can track a selected point on the reference images in the "distorted" images (images captured in the distorted states) provided that a sufficient distribution of gray levels (i.e. gradients) is available in its vicinity. When the surface of the material is not adapted for obtaining a suitable image (poor natural texture, reflections, etc.), it is necessary to apply markings to the part. The idea is to create a distribution of 'colour' on the surface of the samples so that the image formed is informative. This phase is called "Speckle pattern fabrication" (Dong and Pan, 2017). The literature provides a number of recommendations for this process (Lecompte et al., 2007; Pan et al., 2010; Su et al., 2016). On a given scale, the three characteristics expected for a speckle pattern to be acceptable are:

1. The distribution of speckles is random and disorderly (isotropic behaviour, make the matching robust, etc.). Dots of random size and position with strong contrast to the background are often the chosen solution.

2. The size of the speckles is reasonable, taking into account the resolution of the image acquisition camera. These dots must be large enough to avoid aliasing, but its maximum diameter must be controlled to improve spatial resolution (The iDICs Good Practices Guide for DIC (Jones et al., 2018) consider that the optimal feature size is 3-5 pixels once imaged by the camera).

3. The density of the speckles is appropriate and uniformly distributed. Speckle pattern does not contain too much black or too much white (The iDICs Good Practices Guide for DIC (Jones et al., 2018) consider that the pattern density should be arround 50 %)

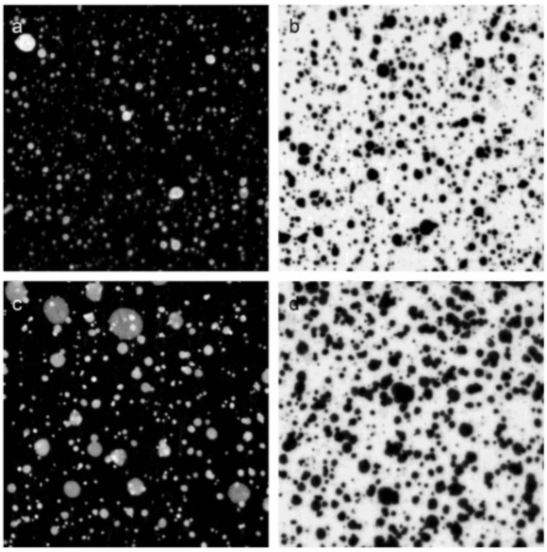

Figure 1.37: Example of images obtained for speckles deposited in different ways: (a) and (b) come from a deposition with an airbrush; (c) and (d) result from a more conventional spraying of paint (Crammond et al., 2013)

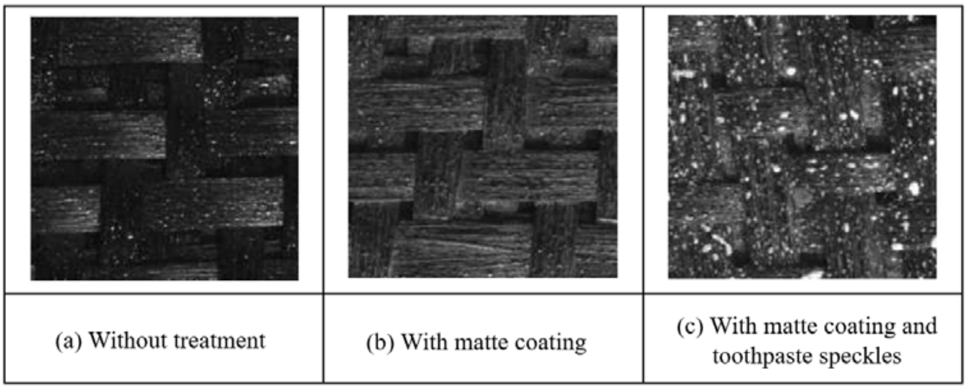

(a) Without treatment

(b) With matte coating

(c) With matte coating and toothpaste speckles

Figure 1.38: Treatment of a carbon fabric with matte coating and toothpaste speckles. (De Luycker, 2009)

Based on the above three considerations, different techniques are developed. Airbrush or Spray speckle pattern are the most common. Black matte paint speckles of random size are then usually sprayed on a white background (matte paints to avoid reflections). White speckles on a black background are also possible, as shown in Fig.1.37. Although this technique is by far the easiest to implement, dot size and density control require experience, and the repeatability of the process is not guaranteed. Other techniques such as printing or laser marking are developing (Liu et al., 2015; Pierré et al., 2017). It is indeed very tempting to digitally synthesize the "ideal" pattern (Orteu et al., 2006; Sur et al., 2018; Fouque et al., 2021; Su and Zhang, 2022) and "print" it directly on the part.

Several methods and specific tools have been developed to qualify speckles once deposited and imaged (Su and Zhang, 2022). David Lecompte (Lecompte et al., 2007), for instance, proposed a way to calculate the cumulative percentage of speckles within a given radius interval. In other words, the size of the speckles is divided into several intervals in pixel, and then the number and percentage of speckles in each interval are calculated. The percentage of each interval is plotted as a curve, and the more the curve tends to be straight, the more uniform the size and distribution of the speckles are. Another more common and simple evaluation method consists in plotting the grayscale histogram of the speckle pattern (Pan et al., 2010; Hua et al., 2011; Wang et al., 2012; Liu et al., 2015), as shown in Fig.1.39. Other indicators are presented in (Dong and Pan, 2017).

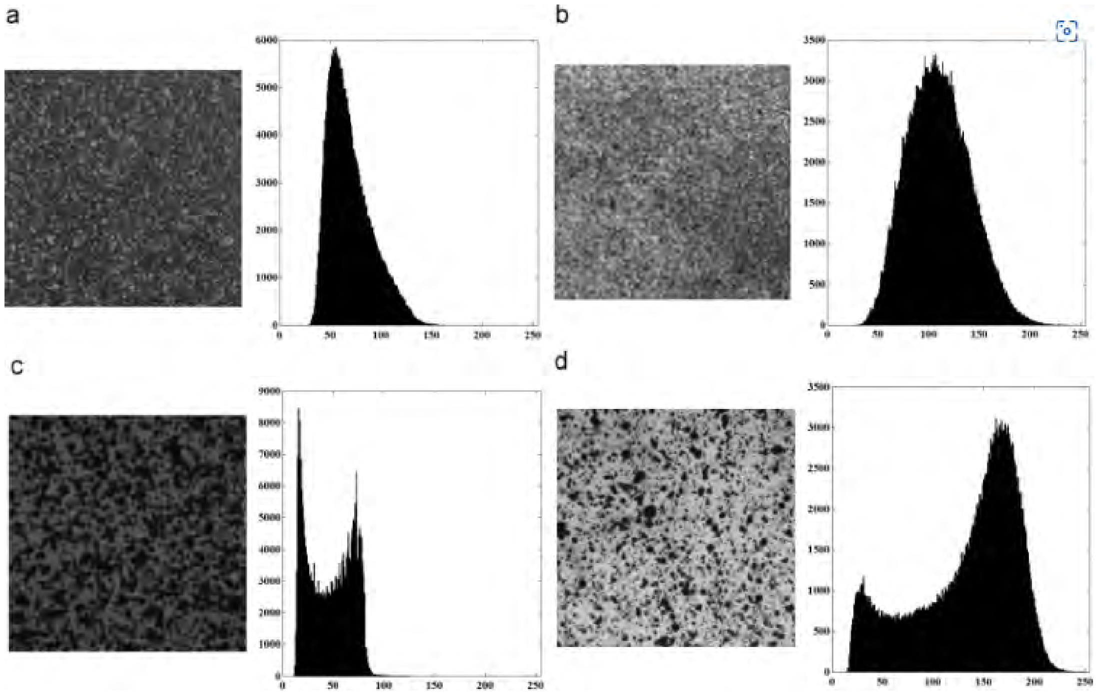

Figure 1.39: Example of grayscale histograms of different speckles to be qualified (Hua et al., 2011)

Speckle pattern fabrication for textile reinforcements is even more challenging. Due to the physical properties of fabric, like the reflectivity, impregnation and uneven surface of fabric, it is more difficult to make speckle on this kind of materials than metallic or composite materials. In particular, the reflective characteristics of the fabric can interfere for image correlation tracking. The most common method is to paint a matte coat and then to spray speckles (De Luycker, 2009), as shown in Fig.1.38.

1.5 X-ray tomography

A radiograph essentially provides a contrast map of the attenuation of radiation as it passes through a sample. Tomography, on the other hand, aims to identify the local attenuation at any point in the sample. The basic principle is to collect a large number of 2D projections to reconstruct a 3D image.

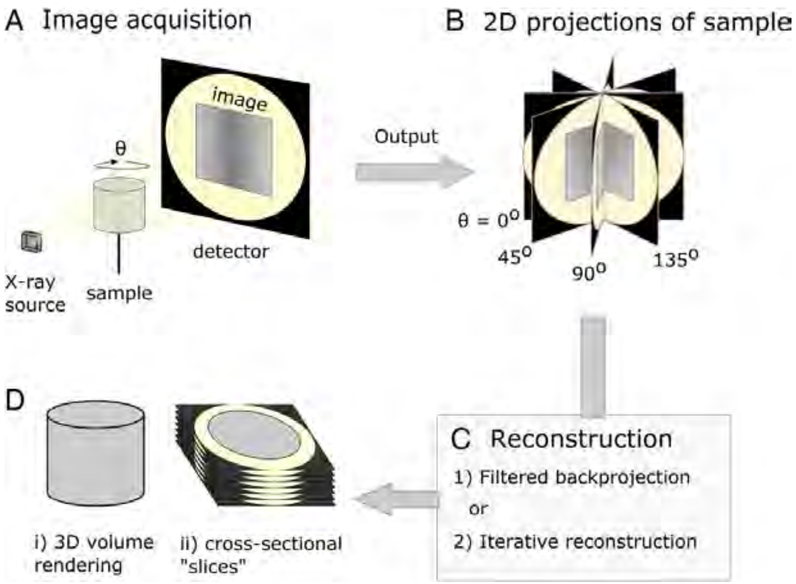

Figure 1.40: Diagrammatic representation of X-ray micro-computed tomography workflow. (O'Sullivan et al., 2018)

Fig.1.40 shows the workflow of X-ray micro-CT with lab (cone beam) equipment as described by (O'Sullivan et al., 2018). For each angle θ, several radiographs are taken (typically 5 to 10). Frame averaging is then used to produce a single, less noisy 2D projection, which is recorded (A). The procedure is repeated for another angle. Typically, more than 1000 projections are recorded per rotation (B). An inverse problem must be solved to go from the 2D projections to a 3D volume. Several reconstruction algorithms have been developed (C). The reconstructed image is often stored as an image stack. It can later be visualised and processed using software such as Dragonfly or Fiji ImageJ (D).

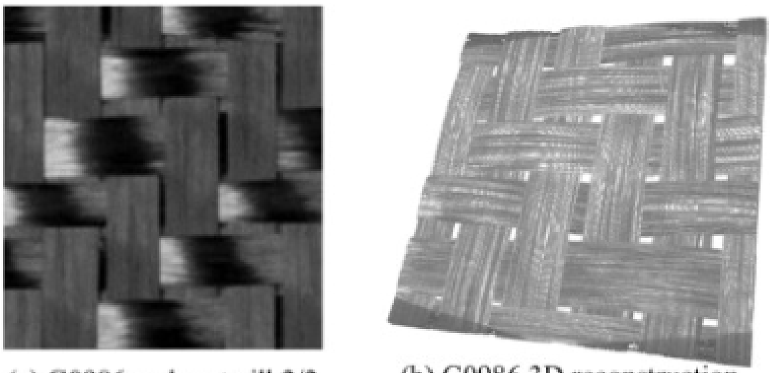

(a) G0986 carbon twill 2/2

(b) G0986 3D reconstruction from µCT

Figure 1.41: Meso-scale FE analyses of carbon twill based on X-ray computed tomography. (Naouar et al., 2014)

The technique is still mainly used today for non-destructive evaluation of parts. It allows 3D imaging of microstructures, detection of defects and damage in materials (Seibert, 2014; O'Sullivan et al., 2018). However, laboratory equipment now provides high sensitivity and high resolution images. Laboratory μCT can currently go down to about 0.7μm/vx (note that the actual resolution depends on the spot size of the X-ray source, but more importantly on the distance between the object and the source. The smaller the object, the closer the source can be, the smaller the voxel size can be). It is therefore conceivable that reconstructed images could be used to build a high fidelity finite element model representing the actual microstructure of the material (Guldberg et al., 1998). In addition, X-ray CT can be used in conjunction with *in-situ* testing (Buffiere et al., 2010) to monitor damage (Toda et al., 2003) or to measure 3D displacement fields (Bay et al., 1999).

For composite materials, X-ray tomography thus allows quantitative segmentation and analysis of reinforcement, matrix and porosity (Morales-Rodriguez et al., 2009; Bonnaire et al., 2019; Tretiak and Smith, 2019). X-ray micro-CT is also more and more widely used for the study of textile reinforcement materials. It can perfectly provide images with sufficient resolution to go down to the fibre scale, while imaging a region larger than a unit cell. (Naouar et al., 2014), for example, build mesoscale FE models of textiles from μCT images. They simulate the behaviour of a carbon fabric (shown in Fig.1.41). These authors have also studied a 3D orthogonal non-crimp woven fibre architecture.

In this thesis, X-ray tomography is chosen to study the behaviour of fabric samples at the yarn scale or below. We aim to develop both digital image based models and at the same time measure their deformation during an *in situ* testing.

1.6 Reminder of the roadmap

The following chapters cover three topics:

1. In order to make develope yarn-scale test/calculation exchanges, chapter 2 first proposes the development of the FE-DIC method to measure the displacement field. Three materials are studied: glass, carbon and CPPS fabrics. The influence of mesh size and mesh orientation on the measurement performance is discussed.

2. Chapter 3 deals with the delicate issue of the measurement of large deformations in DIC. An incremental approach using specific features of FE-DIC is proposed. The idea is to transform the problem of measuring large deformations of fabrics into a problem of tracking multiple small deformation fields.

3. Chapter 4 considers the potential of X-ray tomography combined with in-situ testing to eventually move towards data assimilation based on image-based models and full-field measurements. An in situ bias extension test is developed in a laboratory X-ray μCT to investigate the mechanical behaviour of yarns at the yarn scale.

CHAPTER 2

Parametric study of the performance of FE-DIC

Sommaire

Background: *For composite materials with a thermoplastic matrix, the shaping of the textile reinforcement affects the mechanical properties of the composite materials at once consolidated. Many experiments are available to simulate the process of fabric preforming. The most typical one is the bias extension test. Presently, a variety of nondestructive measurement techniques are used to study textile reinforcement materials, particularly Digital Image Correlation (DIC). However, when measuring the deformation field of these materials, significant measurement errors could arise due to their large deformation and more complex kinematics as a result of their physical characteristics and structure.*

Objective: *The objective of the proposed work is to reduce the measurement error of the displacement field by studying the mesh in the analysis phase. This includes studying the influence of mesh size and orientation. In a second part, the accuracy of the FE DIC method through numerical simulations was evaluated.*

Methods: *In terms of experiments, bias extension tests are performed on several typical reinforcing materials, including glass fabric, carbon fabric, and carbon/PPS fabric. The displacement field is measured using "global" digital image correlation by finite elements (FE-DIC) to regularize the displacement field and facilitate its exchange with simulation. In the analysis of the results, the ultimate error and residuals are calculated and compared while varying the mesh size and the mesh orientation to find the most suitable parameters. The evaluation of the accuracy for numerical simulations was performed by the "Ground Truth" method.*

Results: *A comparison of the analysis results reveals that for the influence of mesh size, there is a specific size that minimizes the error for the same fabric, which is related to the width of the yarn. Regarding the influence of mesh orientation, most of the experimental samples demonstrate that the residuals are minimized with the mesh parallel to the yarn direction, with the minimum value appearing in a certain range of the mesh orientation (which varies according to fabric type). The FE DIC method is effectiveness in tracking the displacement field of the fabric.*

Conclusions: *As a result, this regularized method reduces the error in measuring the deformation field of fabrics and provides a theoretical basis for studying their large deformation. This is of great interest for the use of the FE-DIC method in studying the shaping of textile reinforcement.*

Besides the algorithmic aspects, the physical properties of the fabric and its architecture may also affect the capability of DIC in presence of significant shear deformation. For instance, since the scattered speckles are attached to the yarns, changes in speckle distribution may be correlated with the size or rotation of the yarns (Lomov et al., 2008). In addition, apart the issue of large deformations (which will not be considered in this chapter), the speckle pattern recorded by the camera during testing (even for moderate extensions) may be quite different from what should be recorded if the initial recorded pattern was simply advected by the displacement field. Inter-yarn kinematics may indeed cause changes in speckle distribution, such as shedding, deformation, covering, or hiding. Small parts of the speckles can also peel off. Finally, specular reflections can appear and strongly modify the recorded texture. A careful preparation of the specimen is therefore suggested. Last but not least, to avoid applying deformations to the sample before the test, but also to make sample mounting in the traction machine more repeatable and easier, we imagined to stabilize the sample as soon as the speckle is applied. The idea is to use a frame. An original procedure is proposed.

This chapter is divided into five sections. The 'Methodology' section begins with a reminder of the principles of the bias extension test. The initial preparation of the coupons (generation of specific speckles and re-preparation) is then described. Finally, the principle of FE-DIC is briefly recalled. In the "Results" section, the influence of mesh size and orientation is analysed in detail. Two indicators are used: the final error and the correlation residuals. The third section proposes a first step towards the generation of synthetic images to evaluate the metrological performance in a representative but controlled situation. This is followed by a "Discussion" and "Conclusion and Outlook".

2.1 Methodology

2.1.1 Material and patterning

Three materials are investigated in the sequel: a classical glass fabric, a classical carbon fabric and a carbon/PPS fabric (Patou et al., 2019). The materials, fabric structures and pattern (unit cell) sizes were chosen to provide a clear contrast in the experimental results. The yarn structure of the three fabrics used in this study is shown in Fig.2.1. Table 2.1 lists the main characteristics of the fabrics.

Material name	Weave	Pattern size [mm]	Sample size [mm]	Number of samples
Glass Fabric	5 Harness Satin	6.25	150×50	3
Carbon Fabric	2×2 Twill	8	150×50	3
Carbon/PPS (C/PPS)	5 Harness Satin	6.7	150×50	3

Table 2.1: Main characteristics of the specimens and number of tests performed.

The C/PPS fabric is produced by Porcher Industries. Its commingled weft and warp yarns are made of cracked carbon fibers with PPS yarns. Specifically, a covering is made around the carbon fibers by the yarns in each yarn, as shown in Fig.2.1. The roving is made using the fiber commingled yarn techniques and the co-wrapped commingled yarn techniques (Asghar et al., 2021).

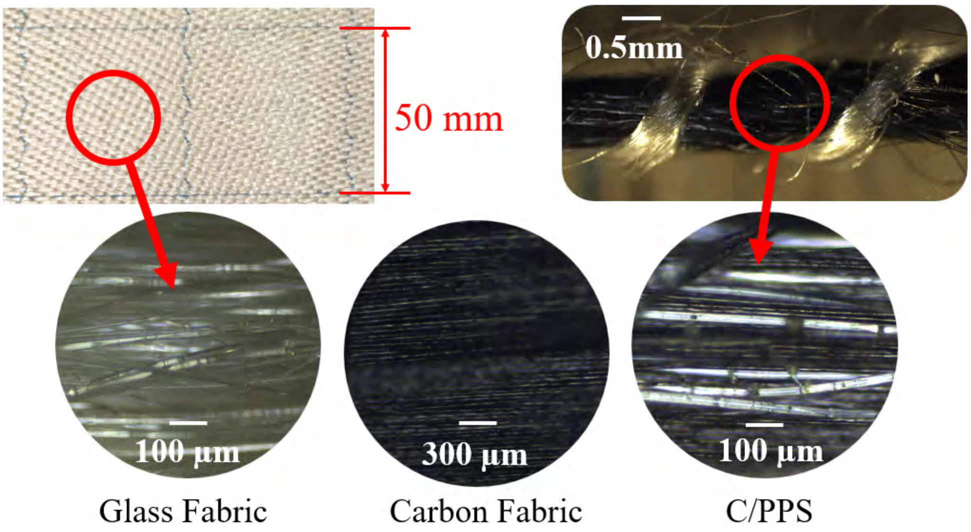

Figure 2.1: Microscopic observation of the structure of the samples : (a) glass fabric, (b) carbon fabric and (c) C/PPS fabric.

It should be noted that in the production of glass fabrics, blue glass fine yarns are mixed in. These yarns are oriented in the same direction as the warp and weft yarns. These are spaced 50 mm apart and form squares on the surface. This helps during sample preparation to ensure that the warp and weft yarns are oriented at ±45°.

To track the displacements of the fabric using DIC, speckles must be deposited on the fabric. Numerous preparation techniques have been proposed, depending on the nature of the material (Lionello et al., 2014), the temperature (Berke and Lambros, 2014) and the scale under consideration (Helm, 2008; Stinville et al., 2016).

In most cases, the aim is for the coating to be softer than the substrate, but speckle can also be obtained from rigid features that adhere to the surface (Barranger et al., 2012). In the conditions we are interested in, the classic method is to use paint projection. However, it is difficult to create good speckles on the surface of woven materials due to their high absorbency (we want to minimize the impact of the - *a priori* surface - treatment on yarn behavior) and geometry. Furthermore, due to their architecture and the type of fibers, these fabrics in their delivered state are prone to multiple specular reflections. As these reflections change throughout the test (without being directly correlated to the displacement), the speckle recorded by the cameras will therefore be strongly interfered with. Finally, if we want to be able to resolve displacements at yarn scale, we need to be able to create multiple spots across the width of a yarn. The process of making speckle patterns thus involves three steps: matifying the fabric to get rid of specular reflections, creating an attachment surface and, finally, spraying scattered speckles. Two procedures, which are the result of numerous trials, were finally retained.

- For the glass and C/PPS fabrics used in this study, the first step involves spraying white mat lacquer homogeneously on the surface of the sample. The second step involves applying a high viscosity white watercolor uniformly to the upper surface of the fabric with a paint roller after the mat lacquer had dried. The purpose of this step was to reduce impregnation of the fabric. In the final step, black mat lacquer was sprayed at a distance of 20-30 cm from the sample to obtain uniformly distributed and appropriately sized speckles.

- For the carbon fabric samples, the thinness of the architecture proved to be a significant obstacle when applying watercolor. The correct amount of paint had to be carefully determined, as an excessive amount could stiffen the fabric and later alter significantly its mechanical properties.

Fig.2.2 illustrates the three typical speckle patterns recorded for the materials under consideration. The latter obviously have an impact on the resolution and the spatial resolution of DIC measurements (Lecompte et al., 2006). In practice, it is recommended that spots be between 3 px and 7 px in diameter (Sutton et al., 2009; Jones and Iadicola, 2018). In this respect, the previous deposition methods have produced satisfactory results. Spot size was thus examined in more detail. For glass and C/PPS fabrics, spot sizes are mainly in the range [0.1 mm, 0.35 mm] ([3.2 px, 11.4 px] measured in the image), with a maximum diameter of 1.8 mm (58.6 px), while for carbon fabric they are mainly in the range [0.1 mm, 0.3 mm] ([3.2 px, 9.8 px] in the image), with a maximum diameter of 1.1 mm (35.8 px). The difference between these two distributions can be attributed to the higher permeability and impregnation of the glass fabric compared to the other fabrics. In addition, the resulting pattern on the yarns is mat, random, presents a wide variety of spot sizes, and there is usually more than one spot across the width of a yarn. Such speckle patterns should thus enable spatial resolutions of the order of the yarn width to be approached. However, a number of potential improvements have been identified. The size of the spots, especially the larger ones, could be reduced and the density increased using an airbrush. In addition, the impact of speckling on fabric behavior should be studied in greater detail. While the effects for the samples tested in this chapter appear to be minimal (Patou et al., 2019), we were able to observe an effect on smaller samples.

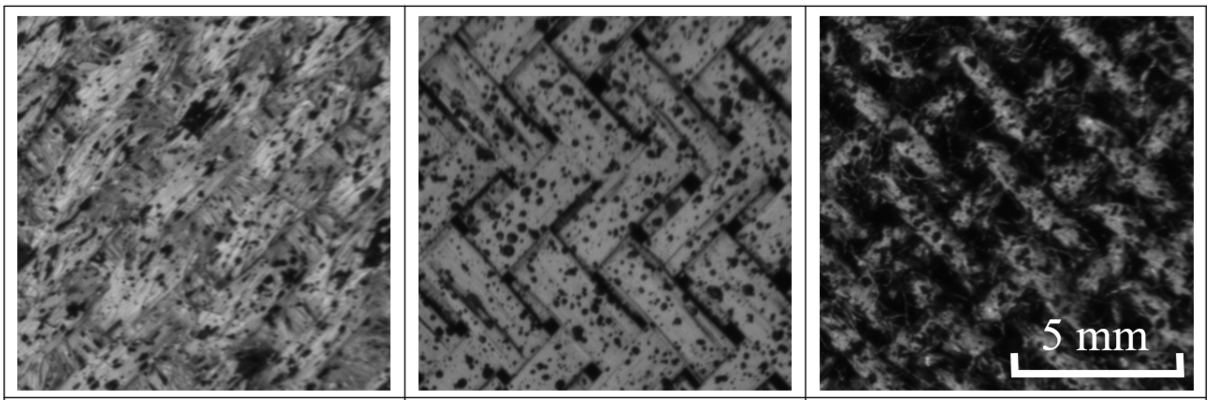

(a) Glass fabric | (b) Carbon fabric | (c) C/PPS

Figure 2.2: Aspect of speckle patterns obtained on the three types of fabrics studied with the procedures proposed in this work.

2.1.2 Coupon preparation

The aspect ratio of the fabric part is next fixed at 3. In this study, the dimensions of the textile part between the grips are 150 mm × 50 mm. One of the main contributions of this work concerns the preparation of the specimen once speckled. We suggest gluing a 2-piece aluminum frame that sandwiches the fabric. The primary motivation for this proposal is to simplify the pre-test handling and the specimen installation in the tensile machine. Indeed, the frame maintains the fibers in position during the whole manipulation, and also allows to align simply and precisely the specimen in the machine. In addition, this aluminium frame, once the temporary lateral members cut, will later acts as tabs. The latter will prevent the fabric from sliding in the grips, which is sometimes observed during the test (Boisse et al., 2017).

The main steps involved in preparing the samples are illustrated in Fig.2.3: (a) A piece of fabric larger than the one to be tested is first cut off. Its dimensions, 180 mm × 70 mm in the present work, correspond to those of the aluminium frame. Particular attention is paid to the angle between the yarns, and between the cutting template and the yarns (warp and weft yarns being oriented at ±45°). Only one side is then speckled (DIC side) by following the procedures suggested in the previous section. (b) Two 1 mm thick aluminum plates are laser pre-cut. The external dimensions of these plates are 180 mm × 70 mm. Four 2 mm wide notches are also cut out. They prevent adhesive from being squeezed in the fabric to be tested during the future bonding phase. Two of them are made perpendicular to the axis of traction. They precisely delimit longitudinally the region of the fabric to be tested (L=150 mm). Two triangular notches are cut out on both sides of the aluminum plates to facilitate the release of fixation on the left and right

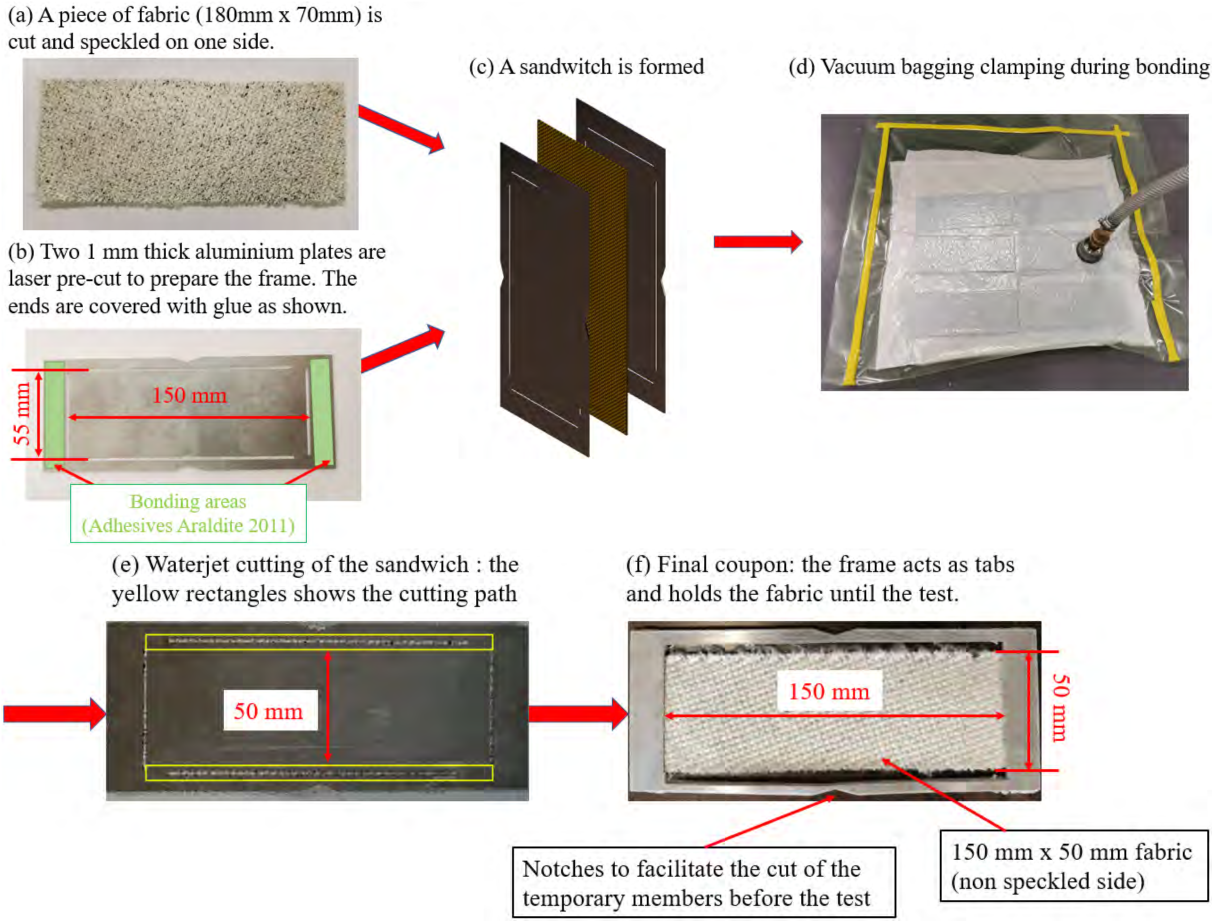

Figure 2.3: Proposed bias test specimen preparation procedure. An aluminum frame is added to the fabric piece so that the warp and weft remain well oriented at ±45° throughout the test preparation. The end portions will then serve as tabs during the test.

sides of the sample before the experiment starts, so that the fabric would be in a free state. (c) An adhesive "Araldite 2011" is carefully deposited around the frames. The sandwich is then formed. After a final check of the angle between the warp and weft directions (external marks on the cutting table are used), one of the plates is carefully glued to the fabric, once the test specimen is upside down, the second plate is glued (d) The sandwich is held in place during the bonding phase by vacuum bagging. (e) The sandwich is water-jet cut to remove two rectangles with dimensions of 150 mm × 5 mm, as shown in Fig.2.3. Spaced 50 mm apart across the width of the test specimen, they are used to delimit the width of the piece of fabric to be tested (W=50 mm). The small sides of these rectangles coincide with the laser pre-cuts and allow to clear the central part of the useless aluminium piece. (f) The end parts will be placed inside the jaws. They will later act as tabs. Once the grips are tightened, the temporary elements of the frame are cut to keep only the fabric between the grips. Two notches have been added to simplify cutting.

2.1.3 Experimental setup

Fig.2.4 shows the experimental setup. It contains the following components:

(1) An electromechanical tensile testing machine 3R Instrumentation (Remy Research & Realizations) MEG20 TT equipped with a 10 kN load cell is selected. The manufacturer's software is used to control the machine and acquire load/displacement data. The crosshead speed is set to 10 mm/min. (2) A stereo correlation bench (Two 5Mp cameras equipped with macro lenses) is used to estimate the global deformation of the samples and to verify the absence of significant out-of-plane displacement. A commercial software (Vic 3D, Correlated Solutions) was used to perform those stereo DIC measurements.

(3) A 5 MP camera (Allied Vision Pike) equipped with a Opto Engineering TC ZR 072-C telecentric lens (Bi-telecentric zoom with motorized controls, magnifications, × 0.125, × 0.250 , × 0.500 and × 1.000) is preferred to perform FE-DIC measurements in the region of interest (ROI). It is mounted on a tripod equipped with a 3-Axis translation stage. This camera-lens assembly could eventually be used to carry out multi-scale acquisitions while following the region of interest. It is carefully positioned so that the optical axis is perpendicular to the sample surface. These precautions make it possible to limit the impact of out-of-plane displacements on the in-plane measurements. For this study, a single, fixed field of view is selected (70.4 mm along the tensile direction × 52.8 mm), and is located near the lower wedge grip (fixed).

The camera cluster is mounted in front of the tensile testing machine and faces the speckled side of the specimen as shown in Fig.2.4. The VicSnap acquisition software (Correlated Solutions) is used to grab the images during the experiment. A led lighting allows to reduce exposure time (20 ms), reduce noise and sensitivity to variations in ambient light. The image acquisition rate is set to 1 frame/second.

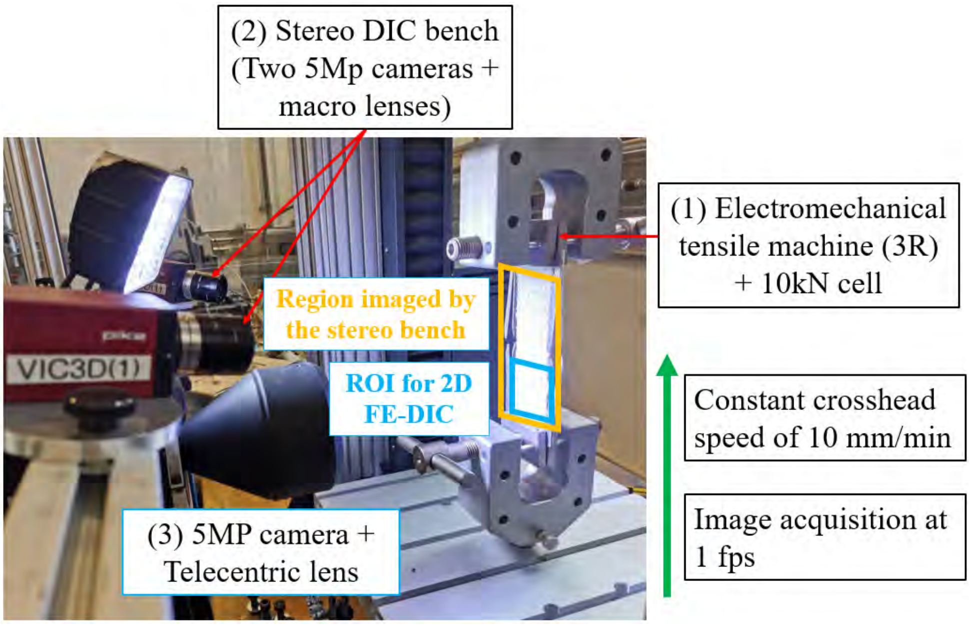

Figure 2.4: Experimental setup for the bias extension test. A stereo-DIC bench allows measuring the global fabric deformation. A 5 Mp camera equipped with a telecentric lens zooms on a smaller ROI to perform 2D FE-DIC measurements.

2.1.4 FE-DIC

In this work, the images captured during the tests are processed using Pyxel (Passieux, 2021), which is an open-source library for FE-DIC developed at the Clement Ader Institute (see section 1.4.1.2 for more details). Here, we just analyse the images grabbed by the camera equipped with the telecentric lens, and we perform a 2D DIC measurement. A simple uniform quadtree structured mesh is then generated using the Gmsh software (Geuzaine and Remacle, 2009). It is made of Q4 linear elements (see Fig.1.31). In practice, we measure an in-plane macro 2D displacement field (the stereo DIC measurements show that the fabric remains flat for the images considered). In our case, the adoption of a telecentric lens and a "quasi-plane" kinematics greatly simplify the calibration phase. The magnification is indeed known, and distortions can be neglected. Only one rotation and one translation must be entered to position the mesh with respect to the image.

Thereafter, we study the impact of the mesh size and the orientation of the mesh (with respect to the orientation of the fabric) on the measurements. A "Subpixel Translations" method is first applied to investigate the impact of mesh size on the ultimate error (Bornert et al., 2009, 2018). The reference image is artificially translated in successive steps of 0.05 pixels from 0 to 1 pixel, and each generated image is then considered as a new "deformed" image. The displacement field is finally measured and compared to the imposed displacement. Two parameters are subsequently introduced (Fouque et al., 2021):

- The systematic error:

$$e_u = \frac{1}{N}\sum_{n=1}^{N}\sum_{\alpha\in(x,y)}(U^m_{\alpha n} - U^{imp}_{\alpha n}) \tag{2.1}$$

- The random error:

$$\sigma_e = \sqrt{\frac{1}{N}\sum_{n=1}^{N}\sum_{\alpha\in(x,y)}(U^m_{\alpha n} - U^{imp}_{\alpha n} - e_u)^2} \tag{2.2}$$

where N represents the number of nodes in the mesh, $U^m_{\alpha n}$ the displacement measured at node n, where α indicates the component under consideration ($\alpha \in (x, y)$) and $U^{imp}_{\alpha n}$ is the corresponding imposed displacement

From another perspective, at convergence, From another point of view, the quality of a real image registration at algorithm convergence is revealed by the grayscale residual map. Two indicators are then exploited:

- global residuals

$$residuals = \frac{f(P(\underline{X})) - g(P(\underline{X} + \underline{U}(\underline{X})))}{\eta} \tag{2.3}$$

- the standard deviation of the global residuals R

$$R = \sqrt{\frac{1}{N}\sum_{n=1}^{N}\sum_{\alpha\in(x,y)}(\mu_n - \overline{\mu_n})^2}\ /\eta \tag{2.4}$$

where $\eta = Max(f) - Min(f)$ stands for the range of gray-levels in the ROI and $\mu_n = f(P(\underline{X})) - g(P(\underline{X} + \underline{U}(\underline{X})))$ for the residual correlation field at convergence.

A low residual R (relative to the noise in the images) indicates that the displacement field obtained by the FE-DIC method is consistent.

2.2 Results

2.2.1 First observations and conventional data processing

The specific procedure proposed in this chapter to prepare the specimens gives very satisfactory results. The added frame plays its role perfectly. The orientation of the warp and weft yarns in the reference image captured at the very beginning of the bias test have been measured. For all the specimens manufactured, the absolute values of the angles between the yarns (warp or weft) and the tensile axis are in the following range [44.6°, 45.2°]. Moreover, while this procedure may seem complex, it greatly simplified later testing. Last but not least, no slippage between the sample and the jaws was observed.

The load/displacement curve for a C/PPS fabric sample is presented Fig.2.5. Similar to the shear deformation of classical woven fabrics, the bias extension test can be divided into three main phases:

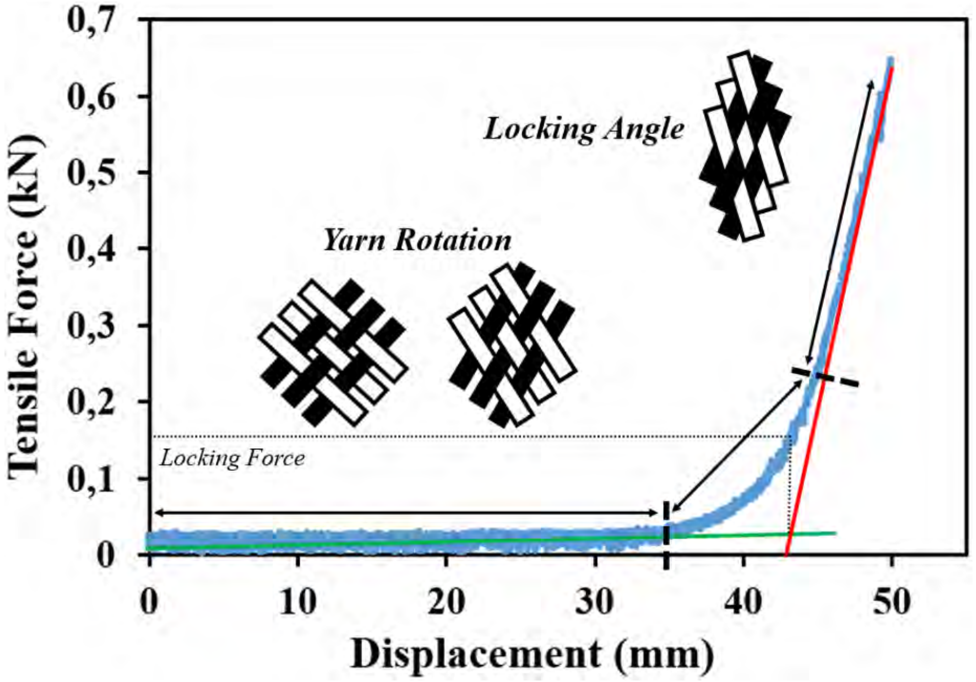

Figure 2.5: Example of Load[kN]/Displacement[mm] curve for a bias extension test performed on a carbon/PPS fabric studied in this paper. As with more conventional fabrics, three phases of deformation can be clearly distinguished.

Phase I: The yarns rotate at the warp and the weft crossover point under a relatively small force (<15 N). The degree of deformation is small, and the low stiffness is due to friction of the yarns between them;

Phase II: The second phase is characterized by the shear locking phenomenon, where adjacent yarns in the same direction come into contact and produce lateral compression. This phenomenon can be observed by measuring the shear angle between the warp and weft yarns, and the locking angle can be observed;

Phase III: In the final phase, the lateral compaction of the yarns gains in intensity and is added to the friction of the fibers, causing the stiffening of the fabric. Depending on the nature of the fibrous reinforcement, this phase is generally accompanied by wrinkling of the reinforcement.

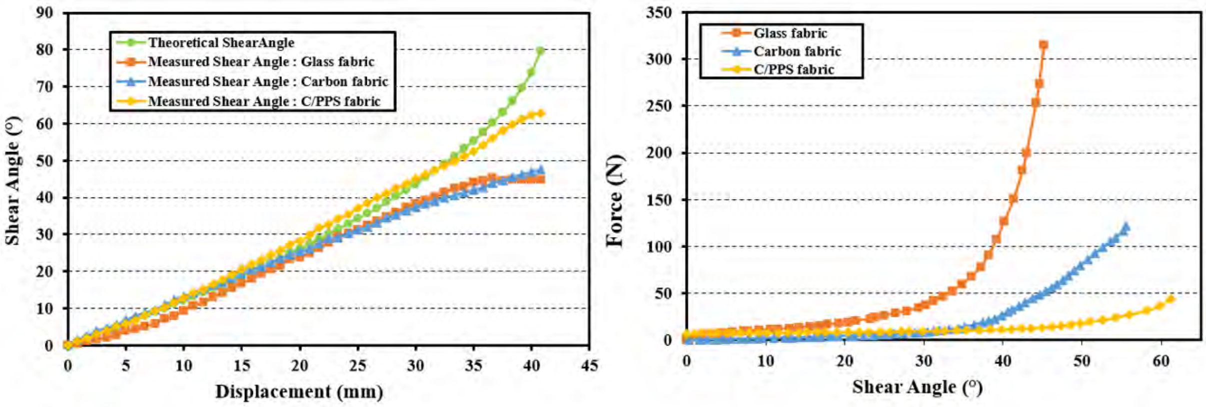

(a) **(b)**

Figure 2.6: Comparison of (a) theoretical of shear angles obtained from the formula 1.1 and measured and of (b) the load/shear angle curves for the three fabrics studied in this chapter (carbon fabric, glass fabric, and C/PPS fabric)

Fig.2.6 (a) displays the shear angle variation curves for the tested samples. The green curve represents the theoretical shear angle variation curve derived from equation 1. The remaining curves illustrate the shear angle variation of the experimental samples, including one glass fabric, one carbon fabric, and one C/PPS fabric sample. According to the formula, the maximum theoretical elongation of the sample is 41.4 mm, which indicates that the sample will enter the third stage before it is stretched by 41.4 mm. The shear angle variation curve indicates that the shear angle of the test sample no longer changes significantly when the glass fabric is stretched by 35.8 mm and the C/PPS fabric is stretched by 39.2 mm. This result indicates that the experiment will enter the third stage, and the shear angle at this point is the locking angle mentioned in Fig.2.5.

The previous shear angle estimation allows for the derivation of the Force/Shear-Angle curve (Fig.2.6 (b)). Due to the variation in fabric structure, the tensile force applied to the samples at the same shear angle showed a significant difference. Several factors influence tensile strength, including the material, production process of the fibers, and warp and weft yarn winding method.

The images acquired during the test are subsequently used to measure the in-plane displacement field using FE-DIC. As planned, we propose to investigate the effect of 2 key parameters, namely element size and mesh orientation, on the ultimate error and the correlation residual R.

2.2.2 Influence of mesh size

Table 2.2: Mesh size in mm and approximate number of pixels used by an element.

Number of elements	36	24	18	12	9
Mesh size [mm]	0.982	1.473	1.964	2.946	3.928
Approximate number of pixels used by an element	32×32	48×48	64×64	96×96	128×128

The choice of mesh size is indeed the result of a tricky compromise. A large element size allows us to benefit from a large amount of information (large number of pixels covered), thereby reducing measurement uncertainties, while at the same time reducing the chances of being able to describe the underlying kinematics correctly (a bi-linear interpolation certainly can't describe the movement of multiple warp and weft yarns of the textile reinforcement).

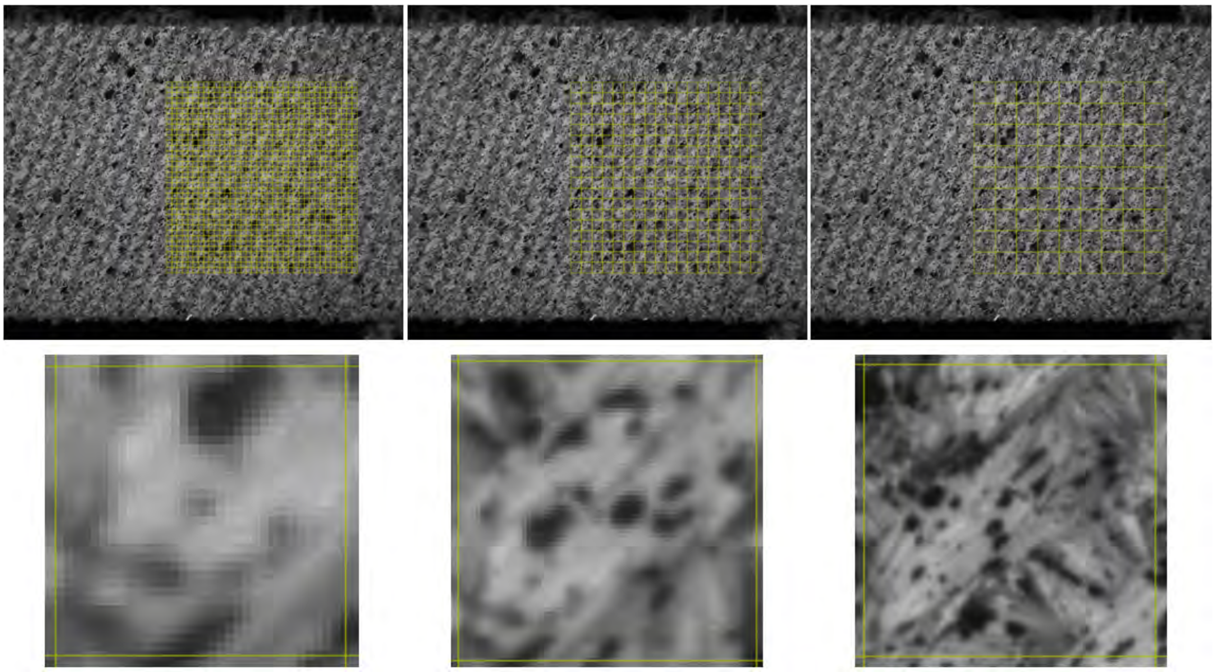

Figure 2.7: Typical reference image of a glass fabric captured by the 5Mp camera equipped with the telecentric lens (optical resolution: 3.07×10^{-2} mm/px). The tensile axis X is horizontal (sample width=50mm). 3 meshes covering the same ROI are shown here in the first row. The three corresponding element sizes are (a) 0.98 mm (approx. 32x32 px^2 available for correlation calculation), (b) 1.964 mm (64x64 px^2) and (c) 3.928 (128x128 px^2). The second row shows a zoom on a finite element.

As a first step, we therefore propose to study the evolution of the ultimate error as a function of mesh size using the procedure introduced in Section 2.1.4. The element size is varied while fixing the size of the ROI (see Fig.2.7). The same number of nodes is used in both horizontal and vertical directions. The resulting numbers of elements are specified in table 2.2.2. The optical resolution in our case is around 3.07×10^{-2} mm/px. As the number of pixels used by each element is a non-integer value, an integer value is chosen to indicate approximately the number of pixels that each element uses during the correlation process (so that it can be compared with more traditional subset based approaches).

It should be noted that the FE-DIC algorithm no longer converges when the element size is less than approx. 0.982 mm (approx. 32×32 px^2) due to speckle deficit on certain yarns and/or in inter-yarn regions. As usual, the size of the speckle combined with the optical resolution sets a kind of lower limit to the spatial resolution (Sutton et al., 2009; Bornert et al., 2009). The displacements measured by FE-DIC are then compared with the imposed displacement. The evolution of systematic e_u and random errors σ_e is shown in Fig.2.8. Measurement errors are of the same order of magnitude for all three fabrics. We note that the measurement bias is generally smaller than the random error. In the following, we will therefore focus on random errors σ_e. The latter are small in relation to the size of the yarns (only a few hundredths of a mm), but they are almost ten times greater than those observed in more common situations (they reach values representing several tens of pixels in the image). To better illustrate the relationship between mesh size and random error σ_e, we propose a new parameter, namely the median of the random error (noted MRE in the following). The MRE simply corresponds to the value of σ_e obtained for a reference image translation of 0.5 px (along the X-axis direction). Figures 2.9 (a), (c) and (e) show the evolution of MRE as a function of element size for various samples of the 3 materials studied. Classically, for small element sizes, the MRE starts to decrease as the element size increases. After a certain value, however, it increases. Surprisingly, for all the fabrics tested, there appears to be an element size that minimizes the ultimate error. We believe that speckle patterning largely explains the first part of the curves (more informative gray-level gradients, better resolution), and that the second part of the curves stems from the strong anisotropy of the recorded pattern induced by the material architecture (yarn structure clearly visible) and its effect on speckle patterning (large, elongated spots). For the glass fabric samples, the MRE are the smallest for mesh sizes between 1.47 (approx. 48×48 px^2 in each element) and 1.96 mm (approx. 64×64 px^2 in each element). The variation within the samples is likely due to the difference between speckle patterns, and this variability highlights the importance of this study. The findings are similar for the C and C/PPS fabris: the smallest MRE is obtained for a mesh size of approx. 1.96 mm. As a reminder, the width of one yarn of glass fabric, carbon fabric, and C/PPS fabric are around 1.25 mm, 2 mm, and 1.34 mm, respectively. The optimum size for minimizing the ultimate error is therefore larger than the yarn width, with the exception of carbon fabric, for which they coincide.

We are now interested in real experiments. FE-DIC measurements are carried out during the bias extension tests in the ROI specified in Fig.2.7 (overlapping the 3 usual zones presented in section 1.3.1). The results for a displacement d=2 mm are presented in Fig.2.9. The measured displacement field u_x (along the tensile loading direction X) is completely in line with the expectations (cf. Section 1.3.1). The triangular zone A (min. displacement in dark blue) is clearly visible, as are the beginnings of the other

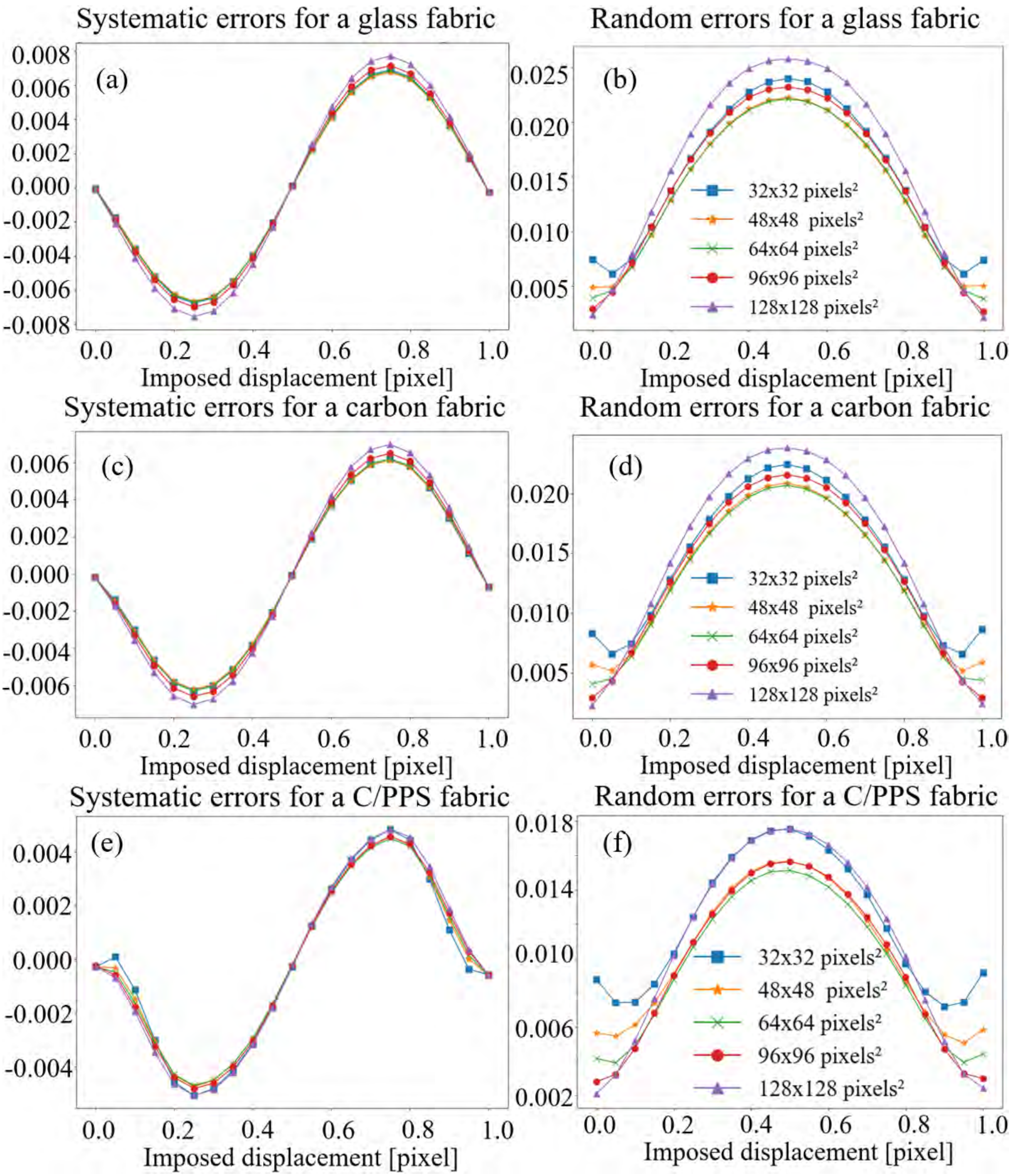

Figure 2.8: Artificial "deformed" images are created by applying sub-pixel translations to the reference image. An error, known as the ultimate error, between the displacements measured by FE DIC and those imposed (Bornert et al., 2009). The left-hand column shows the evolution of the systematic error e_u, while the right-hand column shows the random error σ_e (in mm). From top to bottom: (a) and (b) are the curves obtained for a glass fabric sample, (c) and (d) for a carbon fabric sample, (e) and (f) for a C/PPS fabric sample. In the same graph, the different curves correspond to different element sizes.

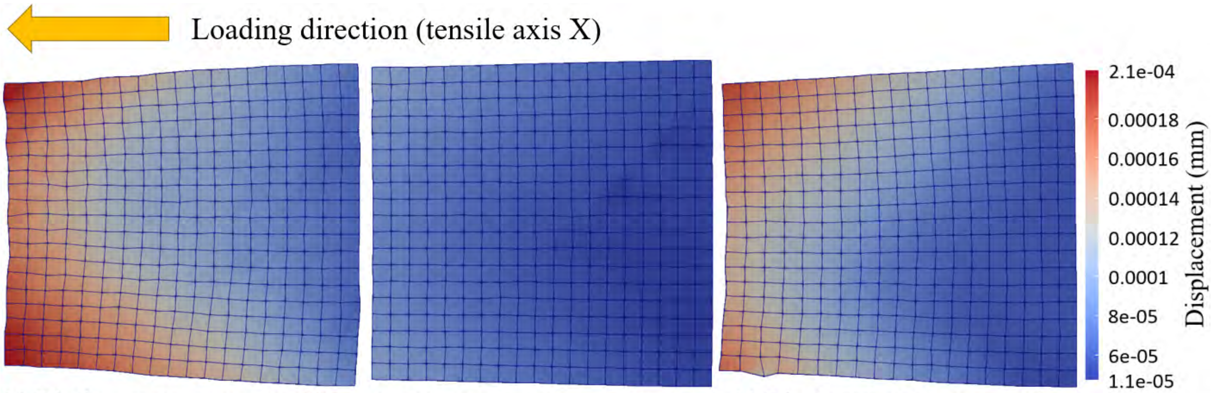

(a) Displacement u_x measured for a glass fabric sample

(b) Displacement u_x measured for a carbon fabric sample

(c) Displacement u_x measured for a C/PPS fabric sample

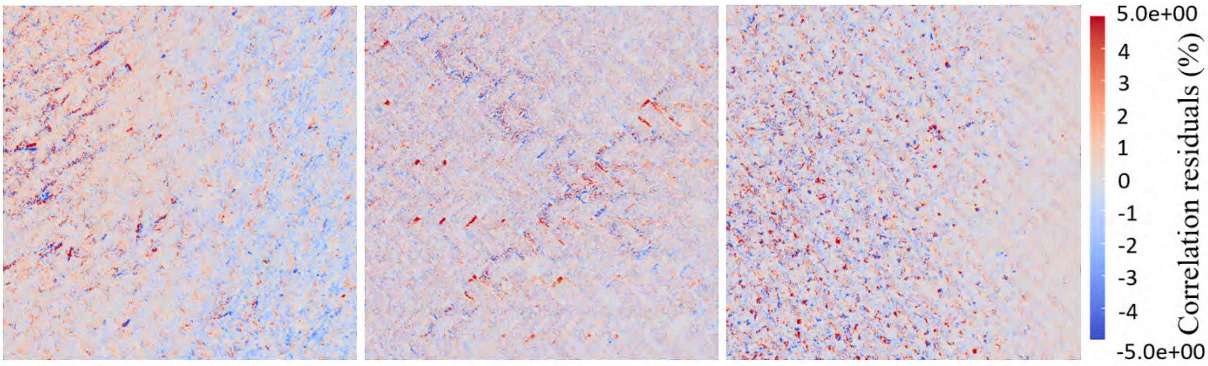

(d) Correlation residual field for a glass fabric sample

(e) Correlation residual field for a carbon fabric sample

(f) Correlation residual field for a C/PPS fabric sample

Figure 2.9: FE-DIC results obtained using Pyxel (Passieux, 2021) and displayed with ParaView (Ahrens et al., 2005). Distribution of the measured horizontal displacement field u_x (along the loading direction, in mm) in the deformed configuration (×10) and corresponding correlation residual maps (in %). The ROI studied is shown in Fig.9. The element size is set at 1.964 mm (approx. 64 × 64 px). The samples were stretched by 2 mm. Results for 3 samples are presented: for a glass fabric sample ((a), (d)), for a carbon fabric sample ((b), (e)) and for a C/PPS fabric sample ((c), (f)).

zones. However, there are significant differences in terms of maximum values and gradients depending on the fabrics studied. Fig.2.9 also features residual maps, a strength of FE DIC, for different fabrics. As explained earlier, these maps are used to estimate the quality of the image registration performed. A structure clearly appears, in particular in the case of carbon fabrics: we observe more important residuals at the level of the inter-fiber regions and crossings. For glass and C/PPS fabrics, correlation residuals are greater on the left, i.e. where the displacements are greater.

To better explain those residual maps, we studied in more detail the first 12 images obtained during the tests for each material (12th image: 2 mm extension). For glass fabrics (Fig.2.9 (d)), the main source of residuals is the specular reflection that evolves during the experiment. Although our method of speckle creation clearly improved the results, the deformation of the sample resulted in the mat coating on the surface splitting or peeling off, giving rise to some reflections and a slight variation in speckle distribution. Regarding carbon fabric (Fig.2.9 (e)), the speckle deposited on the wires doesn't seem to be too altered by the deformation, and there's very little specular reflection. The singularly higher residual levels in the inter-yarn and cross-yarn regions clearly reveal the model error linked to a too poor kinematical description. Each carbon yarn is indeed flattened and the frictional forces between yarns are relatively low, facilitating inter-yarn movement. The yarns kinematics is correctly captured, but, as expected, the linear interpolation adopted inside such a large element (in comparison with the inter yarn distance) associated with the imposed continuity of the displacement field cannot describe the underlying complex kinematics. The kinematics of the wires are correctly captured. But, as expected, the linear interpolation adopted, the size of the element (far too large in relation to the inter-wire distance), added to the imposed continuity of the displacement field mean that the underlying complex kinematics cannot be captured. This results in high correlation residuals concentrated at yarns crossings and between yarns. For C/PPS fabric (Fig.2.9 (f)), the distribution of points with large correlation residuals is more diffuse. The reason for this is that C/PPS fabric is manufactured using fiber commingled yarn techniques and co-wrapped commingled yarn techniques, as shown in Fig.2.1 (c). The speckle deposition procedure is therefore not sufficient to get rid of the specular reflections caused by the PPS yarns. The gray-level values of these reflective spots change constantly in the various images recorded, resulting in a flickering of the speckles, which in turn leads to a salt-and-pepper appearance of the residual map. The effect is most pronounced in regions that experience the most displacement.

We will now examine in greater detail the impact of mesh size on correlation residuals. More specifically, we evaluate the influence of mesh size on the standard deviation of the global residuals R (introduced in Section 2.1.4: see Equation (2.4)), later named correlation residual, for a given stretch (d=10 mm). Fig.2.10 (b), (d), and (f) show the same trend for all samples, whatever the material considered. The correlation residual increases with element size. This observation can largely be related to the increase in model error when the size of the elements becomes large in relation to the yarn width (*i.e.* the interpolation of the displacement field, here linear by elements, is clearly too poor to represent the deformation of a fabric). Conversely, if we reduce the size of the elements to better describe the kinematics, we become more sensitive to spurious variations in the recorded pattern, whether induced by kinematics (for example, masking effects linked to the movement of a yarn covering/discovering speckle on the yarn below) or by changes

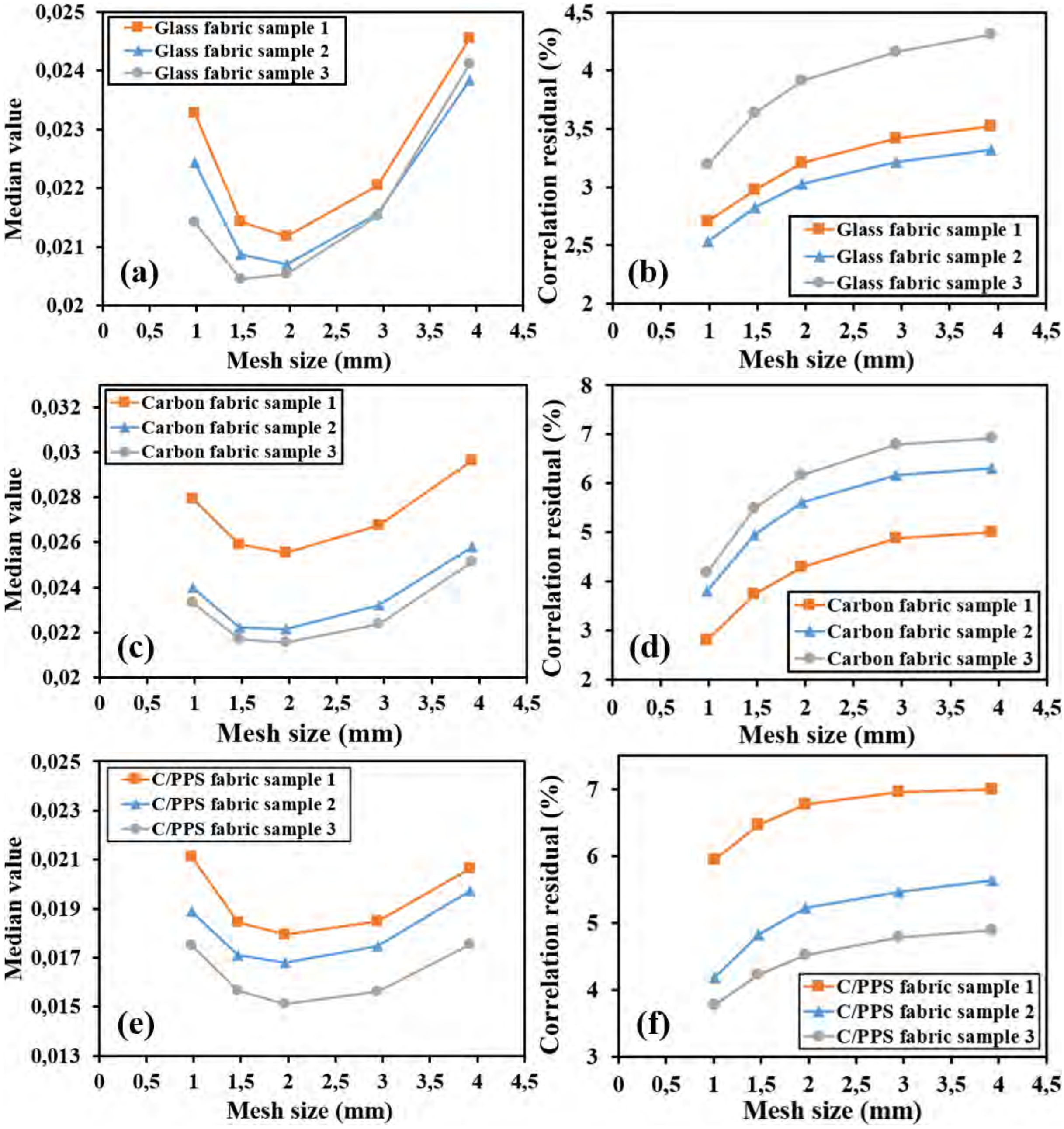

Figure 2.10: Evolution of MRE, the median random error (left-hand column), and of R, the correlation residuals (right-hand column), as a function of the mesh size. Results for 3 samples of each fabric (from top to bottom: glass, carbon, and C/PPS) are presented. The sample was stretched by 10 mm.

in gray levels (for example, associated with specular reflections or speckle degradation). The previous study also clearly showed that decreasing the size of the elements below a certain value will be accompanied by greater measurement uncertainties (cf. Fig.2.10). For all the fabrics tested, an element size of between approximately 1.5 and 2 mm seems to provide an interesting compromise between resolution and spatial resolution. In what follows, we focus on the effect of mesh orientation, and only element sizes 1.47 and 1.96 mm are examined.

2.2.3 Influence of mesh orientation

In the literature, to the best of our knowledge, subset-based local DIC processing of bias extension tests is always carried out using square subsets, one side of which is substantially aligned with the tensile direction (due to the orientation of the image with respect to the specimen). In this work, we propose to study the impact of mesh orientation, and therefore of its elements, on FE-DIC measurements. We compare the quality of the image registration performed using the global residuals, and in particular the correlation residual R. We use again a uniform quadtree structured mesh rotated by an angle θ with respect to the tensile axis X as shown in Fig.2.11. The diagonal of this square mesh is set to 50 mm, to match the width of the sample. To objectively compare the results obtained for different angles, we propose to extract information only from the common circular region common to all meshes defined in Fig.2.11.

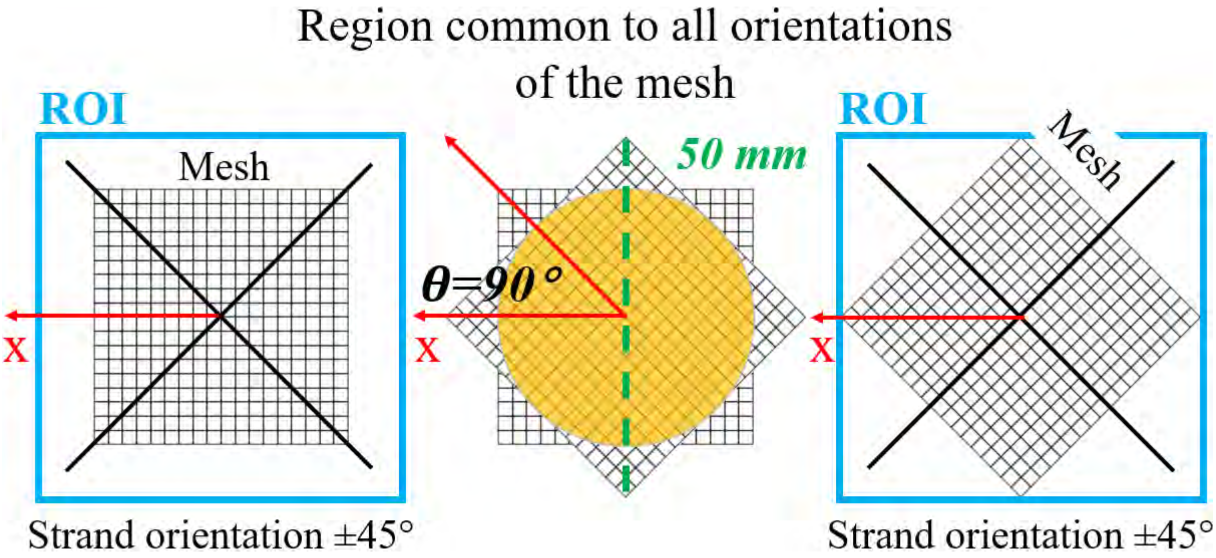

Figure 2.11: A uniform square structured mesh is again used. It is now rotated through an angle θ with respect to the tensile direction X. The diagonal of the square mesh matches the width of the useful region. FE DIC measurements are made for angles ranging from 0° to 90°. The correlation residuals R obtained (standard deviation of correlation residuals) are compared only in the circular region common to all mesh orientations (in yellow).

The influence of mesh orientation on R is examined from two perspectives: (1) the effect of mesh orientation for the 2 element sizes selected (1.47 and 1.96 mm: approx. 48×48 px^2 or 64×64 px^2 used) at a given stretch (d=5 mm); and (2) the impact of mesh orientation when the mesh size is fixed at 1.96 mm (approx. 64×64-px^2 used), but for different stretches (d=5 mm, 10 mm, 15 mm, and 20 mm). Fig.2.12 illustrates for the 2 analyses considered the evolution of R as a function of the mesh orientation θ for all three materials, more precisely for a glass fabric sample ((a) and (b)), a carbon fabric sample ((c) and (d)), and a C/PPS fabric sample ((e) and (f)). Rotation angles θ ranging from 0° to 90° in steps of 5° are studied. When the mesh is rotated by 45°, the edges of the elements are theoretically parallel to the warp and weft yarns.

For the glass fabrics, all the curves $R(\theta)$ obtained look similar. They all feature a valley where residuals are significantly lower than on the surrounding plateaus and virtually constant. Changing the mesh size basically causes the curve to shift vertically. Fig.2.12 shows that R goes from about 3% in the valley to about 3.8% on the plateaus and from 3.2% to 4% for an element size of 1.47 mm and 1.96 mm respectively. The larger the element size, the larger the residuals. The difference between the residuals obtained for the 2 element sizes at a given θ is in line with the observations made in the previous paragraph (around 0,2 % - see Section 2.2.2). The valley extends over a range of θ angles from approximately 20° to 60°. Fig.2.12 (b) shows that the shapes of the $R(\theta)$ curves are similar for the 4 stretching lengths examined. However, the difference between the residual levels observed in the valley and on the neighbouring plateaus becomes increasingly marked with stretching. In addition, the width of the valley decreases slightly with increasing stretching length: its extent varies from around [20°, 60°] to [25°, 60°]. We haven't been able to verify this, but we're leaning towards a clear modification of the pattern linked to both kinematics and specular reflections. For example, as the yarns are brought close together, the spacing between adjacent yarns is reduced until they touch, resulting in a smoother sample surface in the second stage, a slightly higher reflectivity, and a slightly higher density of speckles.

For the C/PPS fabric sample (Fig.2.12 (e) and (f)), the curves have usually the same aspect as those obtained for glass. The influence of mesh orientation is also significant. Smaller residual values are concentrated in the range of mesh orientation of [30°, 50°]. We assume that the same reasons as above are behind these observations. This range is clearly narrower than that observed for glass fabrics (see Fig.2.12 (a) and (b)). This is probably due to the presence of co-mingled fibers, which are potential sites for specular reflections. It is interesting to note that for some samples, the influence of mesh orientation is no longer observed. This is attributed to regions where the speckle on the yarns is too coarse (large regions without gradients of gray-levels). Figure 2.13 shows the speckle pattern when the influence of mesh orientation is observed (a) and not observed (b).

For the carbon fabric sample (Fig.2.12 (c) and (d)), the situation is different. Correlation residuals are approximately within the ranges [3.9, 4.2] and [4.4, 4.6] % respectively for these two different mesh sizes. No clear valleys or plateaus emerge. The influence of mesh orientation on the residuals is not significant: changing the mesh orientation has here no obvious positive/negative effect on the quality of image registration. Our interpretation is that the speckle is theoretically dense and thin enough to obtain well-resolved displacement measurements, but that most of the residuals are due to the poor kinematic description (see previous section: continuity of displacement imposed by the FE description, and element size too large compared to the inter-yarn size). In fact, the carbon yarn is less prone to specular reflections, and the architecture of the fabric leads

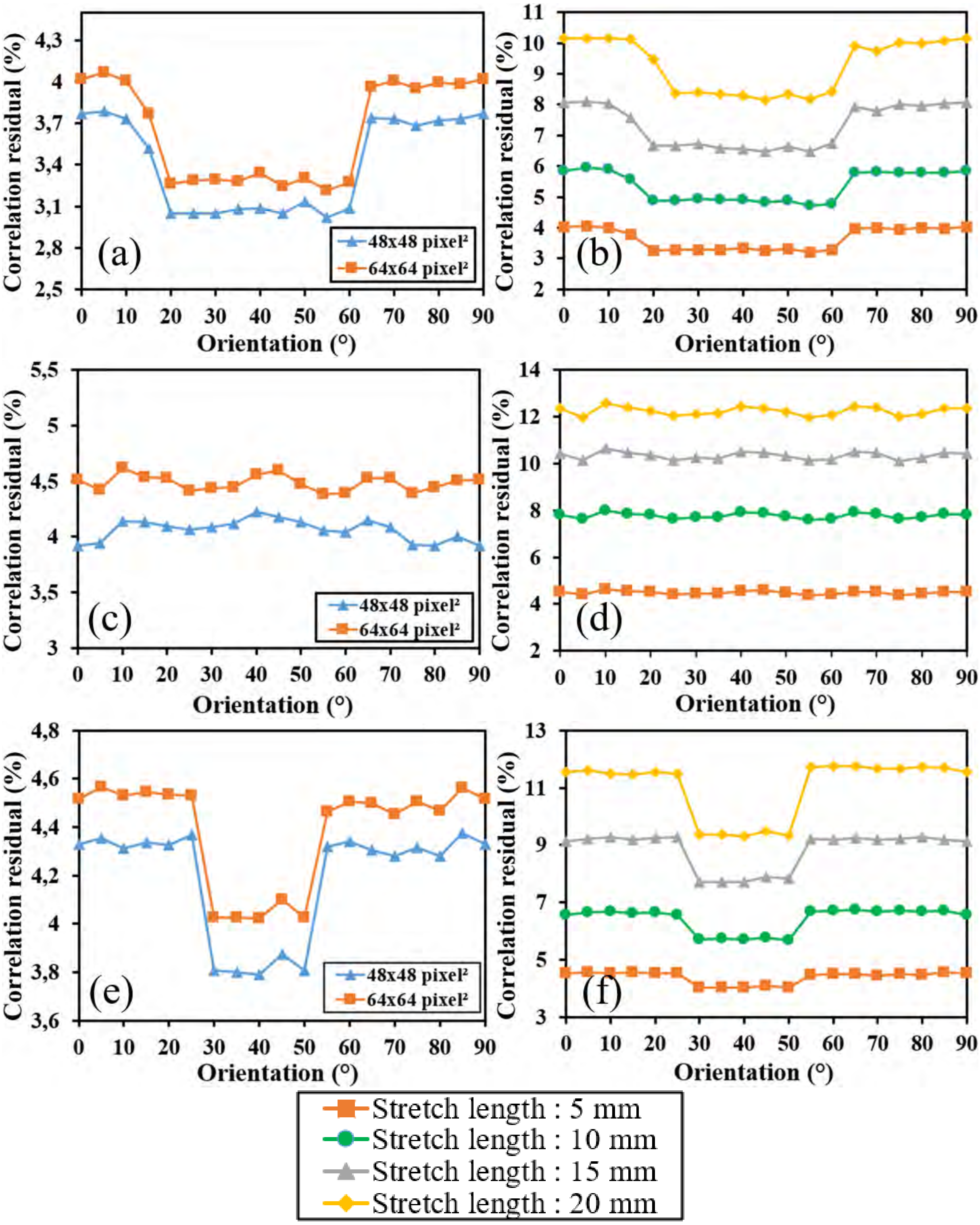

Figure 2.12: Evolution of the standard deviation of the overall residuals R as a function of the relative mesh orientation/tensile direction θ for a glass fabric sample ((a) and (b)), a carbon fabric sample ((c) and (d)), and a C/PPS fabric sample ((e) and (f)).

to much better speckle coverage. Fig.2.12 (d) shows that the model error increases with extension.

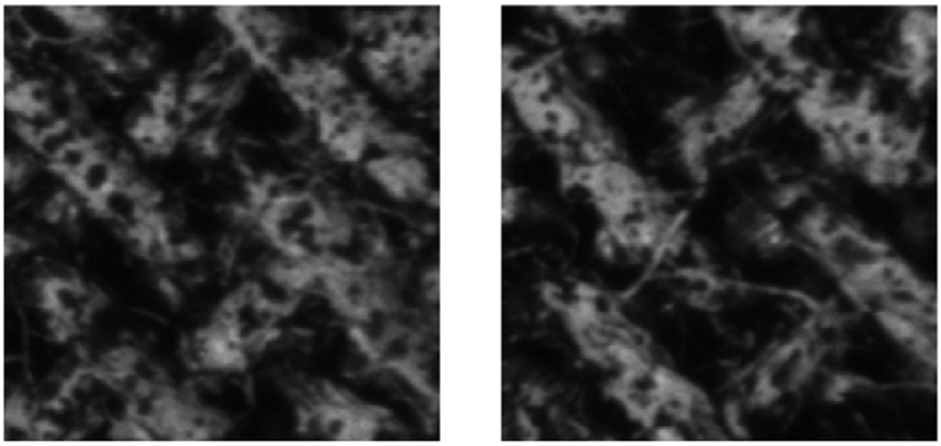

(a) Dots are relatively large (in relation to yarn width), but are fairly uniform and well distributed across the yarns

(b) Numerous large dots are present, some completely covering the strands

Figure 2.13: Comparison of speckle patterns for experiments where the influence of mesh orientation (a) can be observed and (b) is not observed. A clear difference in terms of dots density and distribution is observed.

2.2.4 Interim report

One of the delicate points of the previous analysis is that the evolution of the correlation residuals is multi-factorial. As mentioned on several occasions, the increase in the latter may in fact be due to flaking of the speckle, a variation in the reflected light, poorly described kinematics, and so on. On the other hand, the analysis of a sub-pixel translation can in no way account for the influence of kinematics in the real performance of an FE-DIC measurement.

In the following section, we present the first initiated works aimed at producing synthetic data representative of the product test, but where the displacement field is known.

2.3 A first step towards synthetic ground truth data to challenge (FE-)DIC

The work described below is part of a more general approach to develop "ground truth" data to better evaluate the performance of DIC algorithms. The idea is to advect a predetermined speckle applied to an object's surface from a known displacement field (Reu et al., 2022) to better understand the effect of mesh selection on measurement error. It is now possible to move the approach to 3D and exploit a calculated field (Balcaen et al., 2017; Rohe and Jones, 2022). This type of approach makes it simpler to study the influence of certain parameters, and to evaluate a priori the performance of the algorithm in more representative situations (field mimicking the expected experimental field, and not a simple translation, effect of lighting and shooting, etc.), but with perfect knowledge of the displacement field . We propose to initiate such a procedure for our case study.

2.3.1 Generation of synthetic images

Modelling of a micro-bias extension test is thus used to generate synthetic images.

2.3.1.1 Reference displacement field based on FE simulations

The geometry selected is intended to be representative, but the aspect ratio of the ROI is just 1.5. The CAD model is created using Texgen and updated with tomography data as described in Chapter 4. Volumetric meshing is performed in Abaqus from an STL mesh generated by TexGen. The resulting mesh is shown in Fig. 2.14 (a). FE calculations performed in Abaqus consider elastic yarns, but frictional contacts between them. The whole simulation is divided into 200 steps.

2.3.1.2 Boundary conditions

Boundary conditions simulating gripping are applied to the ends. A uniform horizontal displacement is applied to the left edge while the right edge is clamped. No out-of-plane displacement is allowed on the "free edges". For more details on this aspect, one could again refer to Chapter 4.

2.3.1.3 Creating an artificial speckle on the mesh

The speckle can be mimicked by marking the skin of the FE model element by element. A simple method is proposed here. We start from a white background. Then, a gray level is assigned to each element visible from above so as to produce a believable speckle. In practice, several pixels are manually and randomly assigned to an element set. Here, 4 element sets are defined. Each of them is assigned its gray level. Fig.2.14 shows three groups of different speckle distributions, and four sets of "elements" are defined in each group. The whole surface of both yarn and weft yarns are here speckled. Three speckles have been produced following this procedure in Fig. 2.14 (b-d).

2.3.1.4 Image synthesis

Images corresponding to "top views" are then generated at all stages of mesh deformation (*i.e.* 200 images) directly in Abaqus. They mimic the acquisition by the camera+telecentric device. The reference image and the deformed images are simply taken from screenshots. The corresponding image resolution is 1150 x 661 pixels². The corresponding pixel size is approximately 0.019 mm.

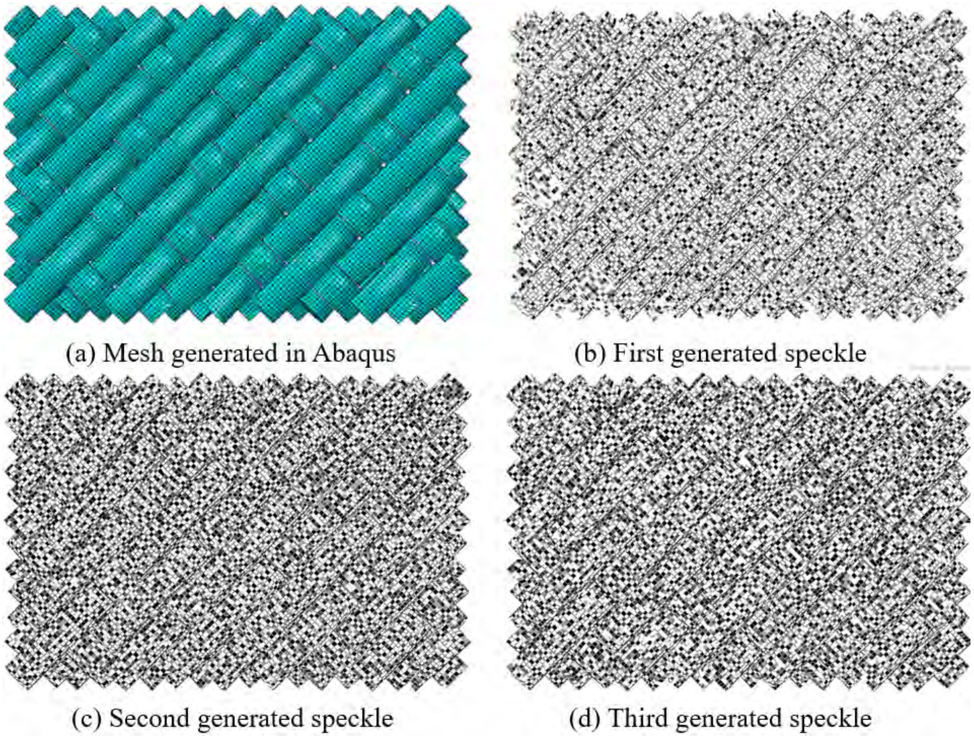
(a) Mesh generated in Abaqus
(b) First generated speckle
(c) Second generated speckle
(d) Third generated speckle

Figure 2.14: Mesh of a "micro" bias extension test specimen generated from the X-ray tomographies performed in Chapter 4 (a). Three speckles were manually generated on the surface of the specimen by randomly colouring the elements (b-d). Synthetic images were generated by taking a 'top view' (a view similar to that provided by the telecentric) screenshot mimicking the scanning process carried out by the sensor.

2.3.2 *a priori* evaluation for FE-DIC mesh size choice

As with real experiments, we want to evaluate the ultimate error in our situation in order to select a correct element size before proceeding further. The ROI here covers the entire surface of the model. The element size is 0.673 mm, 0.904 mm, 1.250 mm, 1.673 mm, and 2.038 mm, to use about $35 \times 35\ pixel^2$, $47 \times 47\ pixel^2$, $65 \times 65\ pixel^2$, $87 \times 87\ pixel^2$, and $106 \times 106\ pixel^2$ respectively in the DIC process.

The evolution of the systematic error and random error is shown in Fig.2.15. As in Section 2.2.2, the reference image is translated horizontally in the x-direction by successive steps of 0.05 pixels between 0 and 1 pixel.

The evolution of the systematic error according to the displacement is classical (S-shaped). The maximum amplitudes range from 0.012 to 0.017 mm for the different element sizes considered. We attribute these higher amplitudes than those observed in real tests

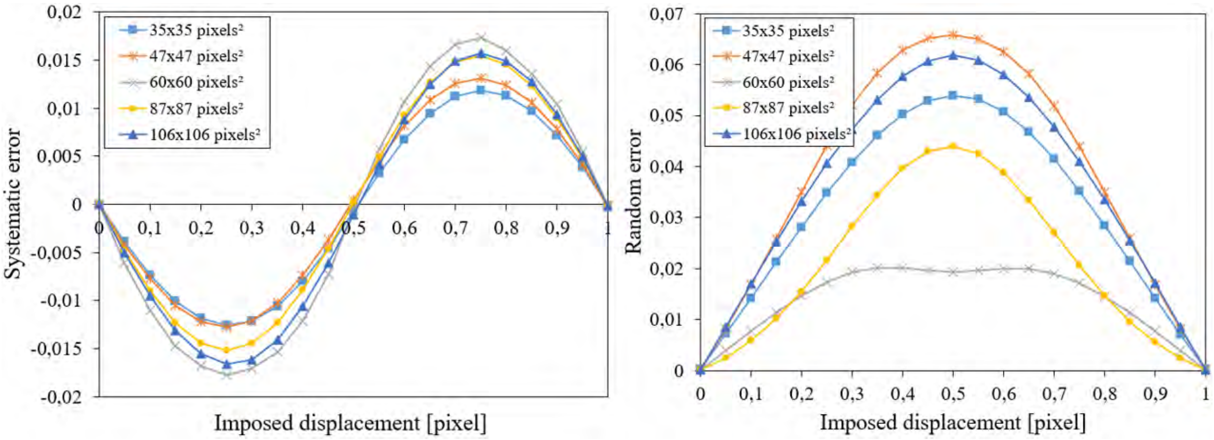

Figure 2.15: Evolution of systematic and random errors for the synthetic images generated using Abaqus simulations

(0.006 to 0.008 mm) to the low image resolution, as well as to the excessive simplicity of the speckles (too uniform size, too sharp texture). In the same way, the random errors have a bell shape and the levels are again higher than those observed in the real experiments. Once again we see that the random errors are more important than the systematic errors. However, their level depends much more on the size of the element. Consequently, we are again interested in the evolution of MRE (median value of the random error) as a function of the element size plotted in Fig. 2.16. Fig.2.16 shows that the random error is somewhat minimal when the mesh size is around 1.250mm. This value is retained for subsequent analyses. It is worth noting that the yarn width in the model is close to 1.14 mm.

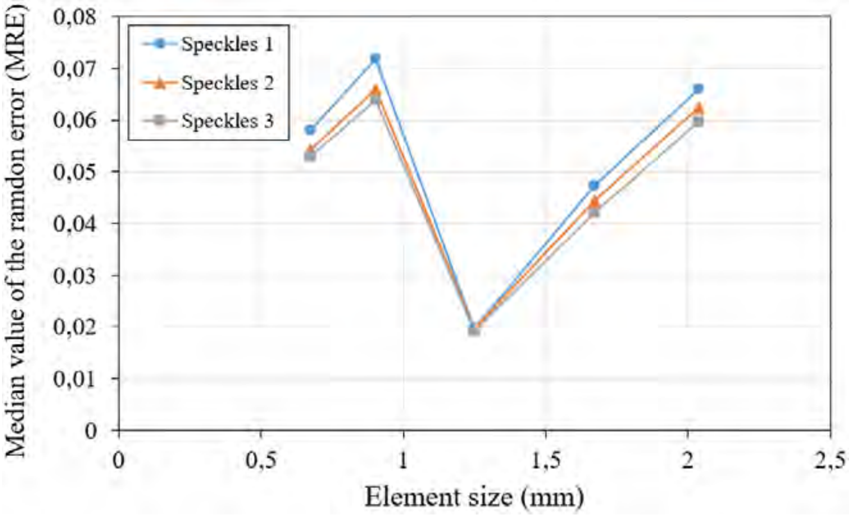

Figure 2.16: Evolution of the median value of the random error (MRE) for the synthetic images generated using Abaqus simulations

2.3.3 FE-DIC diplacements and residuals for the selected mesh size

We are interested in the displacement field between the reference image and the last synthesised image. As a reminder, the left part of the sample then moves by 2mm. The element uses around 65 × 65 ($pixel^2$) gray levels values.

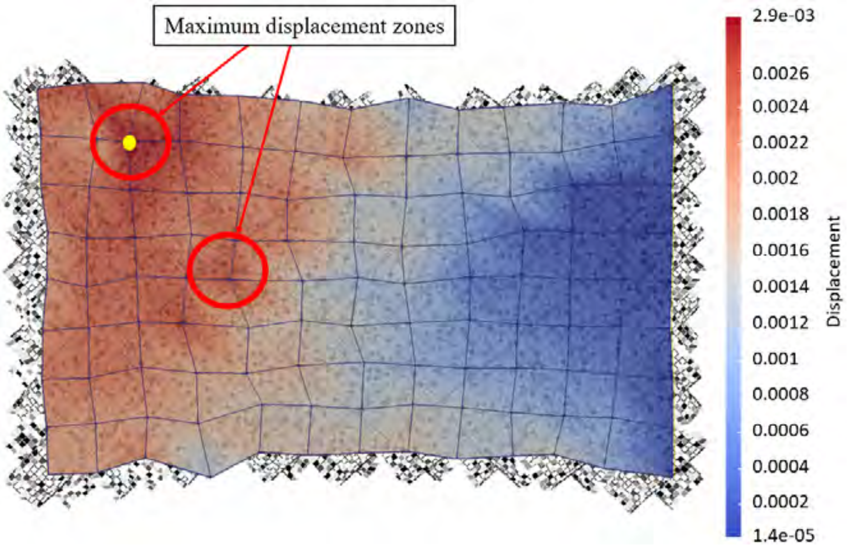

Figure 2.17: Displacement field measured by FE-DIC from synthetic images (unit m). The yellow dot indicates a point where the displacement is particularly important and will be investigated.

Fig.2.17 shows the corresponding displacement field calculated with Pyxel. This field should be compared with Fig.4.25 (a). Non-shear and semi-shear zones are clearly observable. In order to better compare subsequently the imposed displacement with the measured displacement, a node is selected in the region of extreme values indicated in Fig.2.17. The displacement curves as a function of time for this node are plotted in Fig. 2.18. As we are performing 2D DIC, only the displacement components (along the X and Y axes) and their magnitude are available in the planes. Their maximum values are -2.878 mm, -0.361 mm and 2.900 mm respectively.

The quality of the correlation can be assessed from the correlation residuals shown in Fig.2.19. It shows that the high residuals are mainly located

1. at the edges of the strands and at the level of the crossings between strands
2. on yarns where significant relative slip occurs in the simulation (Fig.4.25).
3. at the edges of each Abaqus element mesh. There are two main reasons for this. Firstly, the creation of the speckle pattern is based on the Abaqus mesh, knowing that this mesh is very regular (same size and ordered). The other reason is that the speckle is sharp and contains only few gray values.

We now focus on the global residual R defined by Eq.2.3 (see section 2.2.2). Fig.2.20 shows the evolution of R according to different mesh sizes for 3 different speckle patterns.

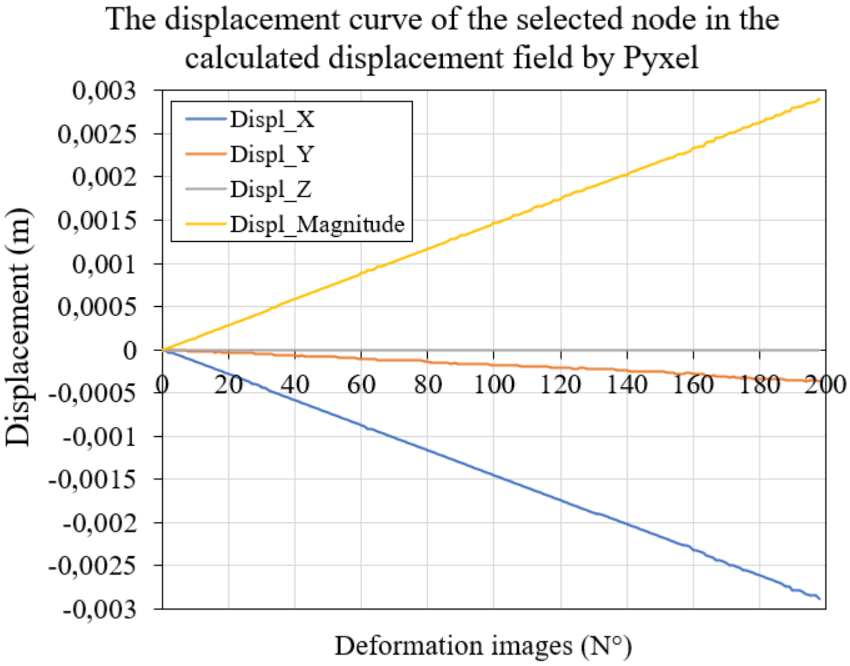

Figure 2.18: Evolution of the measured displacement (Pyxel) of the node selected in Fig. 2.17 according to the number of the processed image.

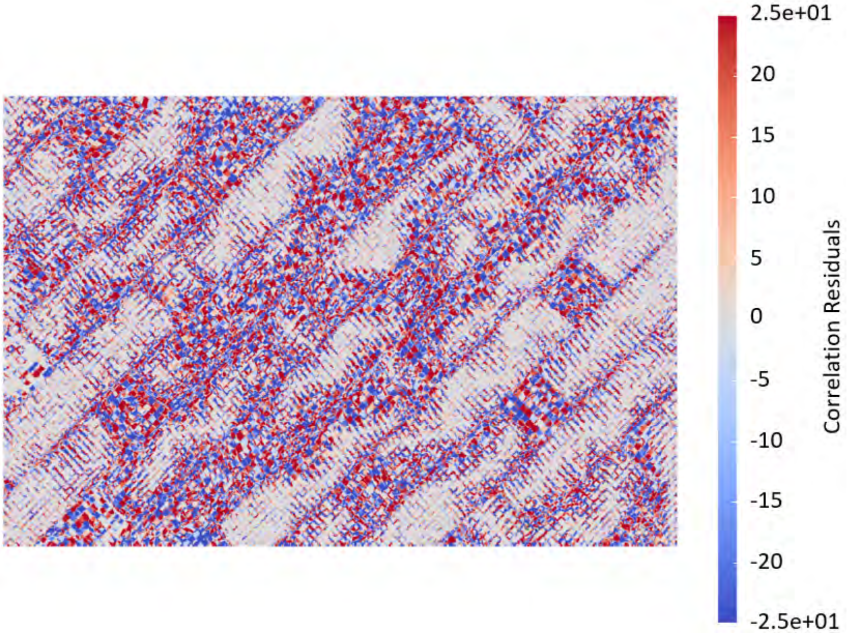

Figure 2.19: Correlation residual map obtained from the synthetic images for the last loading step.

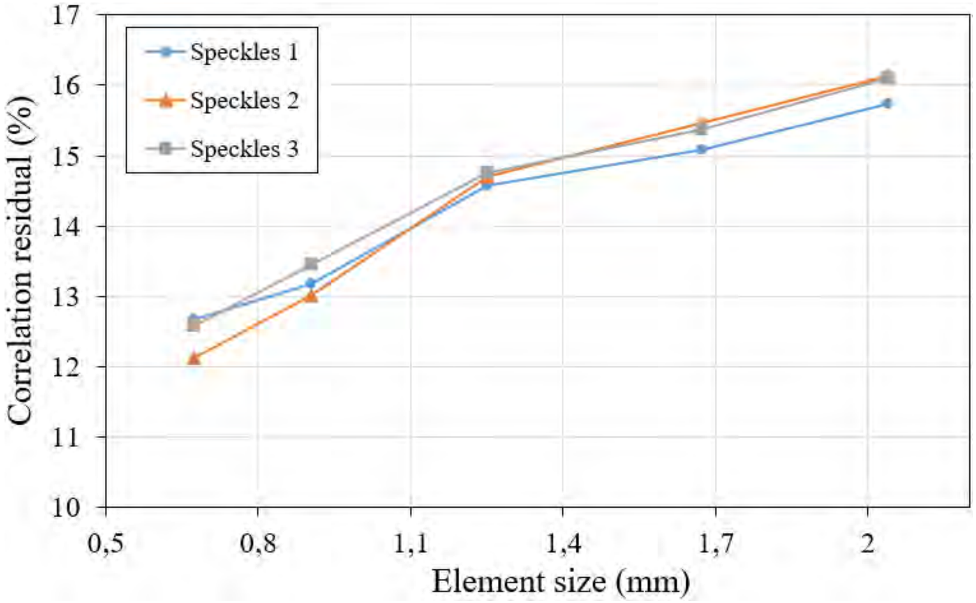

Figure 2.20: Evolution of the global correlation residual R as a function of mesh size, obtained for 3 different speckle distributions.

There is no significant difference between the three curves. In fact, the dot size and density are almost identical. As expected, we observe that the larger the size of the elements, the larger the residuals. This is largely due to an increasingly poor representation of the underlying kinematics. However, there is a slight bend in the curve at the value chosen for the FE-DIC measurement shown above.

2.3.4 Comparison in between Abaqus computed displacements (ground truth) and FE-DIC measurements for a given mesh size

The most important difference between the simulation and the real experiment in this section is that the imposed displacement field is known. Therefore, the ability of the FE-DIC algorithm to track the displacement field could be evaluated by studying the imposed displacement field.

Firstly, the parameter is proposed as the relative displacement error E which is based on the imposed displacement field, as follows :

$$E = \frac{u_{Abaqus}^{imposed}(\underline{X}) - u_{Pyxel}^{measured}(\underline{X})}{\sigma} \tag{2.5}$$

where $u_{Abaqus}^{imposed}(\underline{X})$ is the computed displacement used to generate the synthetic images; $u_{Pyxel}^{measured}(\underline{X})$ is the FE-DIC displacement measured from those images; and $\sigma = Max(u_{Abaqus}^{imposed}(\underline{X})) - Min(u_{Abaqus}^{imposed}(\underline{X}))$ is the range of imposed displacements.

The evolution of the displacement $u_{Abaqus}^{imposed}$ with respect to the frame number for the node selected in Fig. 2.17 is shown in Fig. 2.21. The maximum displacement $u_{Abaqus}^{imposed}$ reaches -2.349 mm, -0.571 mm and 0.906 mm along the X, Y and Z axes respectively. The

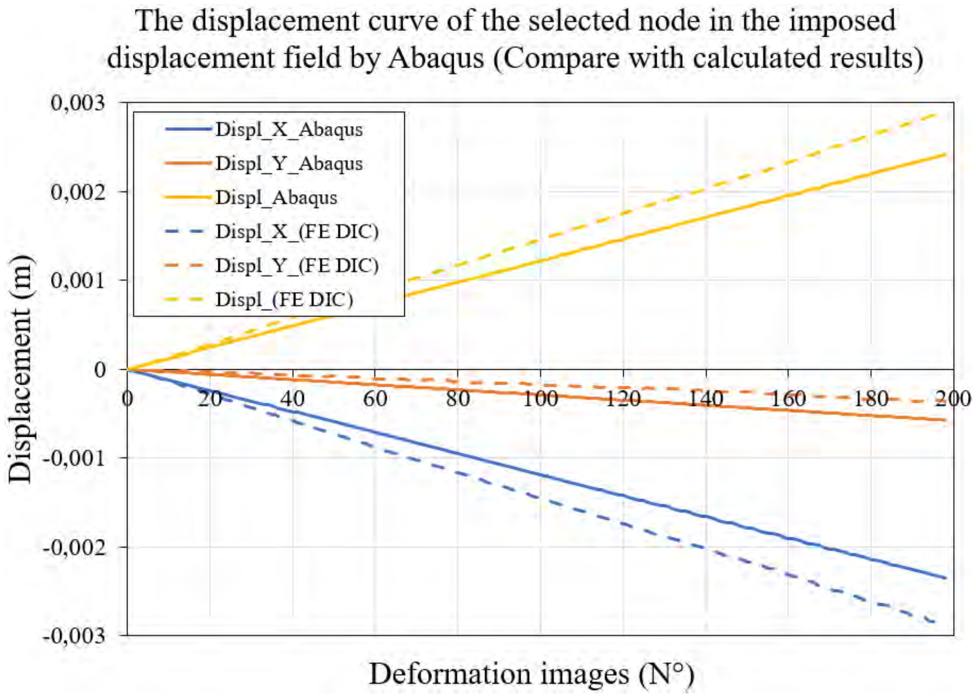

Figure 2.21: Evolution of the imposed displacement (Abaqus calculation) of the node selected in Fig.2.17 according to the number of the synthesized image. The displacement measured by FE-DIC at the same point is shown in dotted lines for comparison.

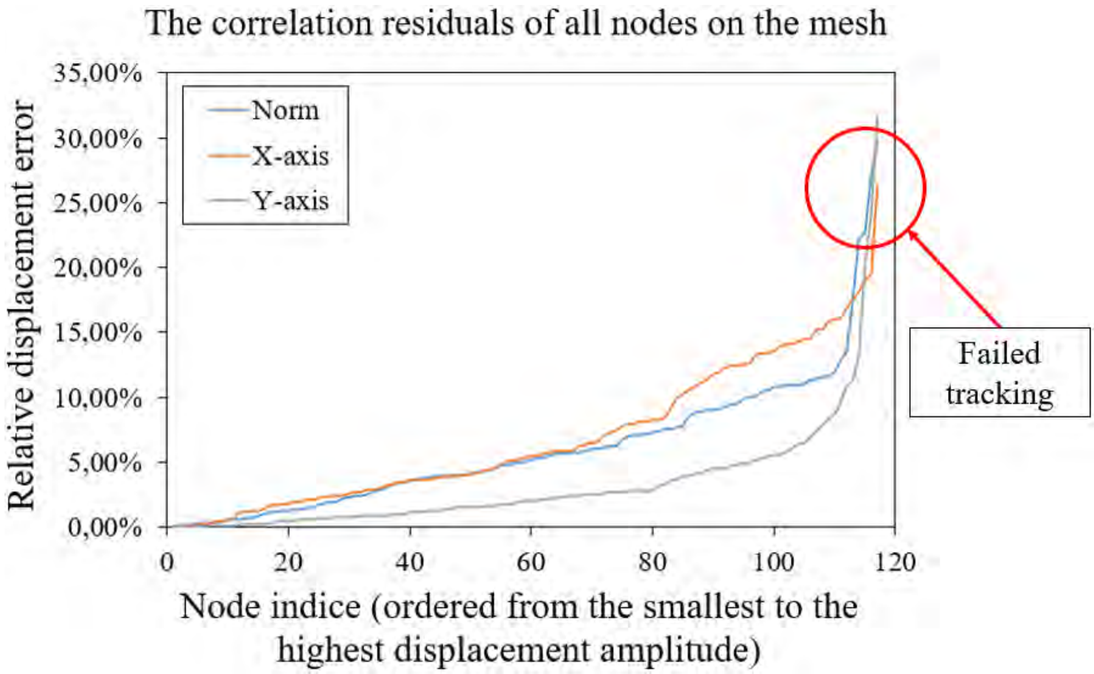

Figure 2.22: Distribution of the relative error between measured displacements and imposed displacements for all the nodes of the mesh (mesh of Pyxel). The results are listed here from smallest to largest.

difference in displacement between the displacement imposed and measured by FE-DIC $u^{imposed}_{Abaqus} - u^{measured}_{Pyxel}$ is therefore at most 0.529 mm on the X-axis, 0.211 mm on the Y-axis and -0.48 mm in norm (in the X,Y plane). The corresponding relative error E for this node is 19.4% along X, 5.4% along Y and 20% in norm (see Fig.2.21).

Fig.2.22 shows the relative error level for all mesh nodes. In practice, the nodes are arranged so that they go from the smallest residual levels to the largest. The total number of nodes is $13 \times 9 = 117$. It can be seen that the residuals of the nodes moving along the X-axis (stretching direction) are larger than the residuals of the nodes moving along the Y-axis. In other words, when tracking the displacement field, the measurement error in the stretching direction is greater than that in the other directions. It is also evident that there are several nodes where the E error is excessive, causing the motion tracking to fail. After analysis, it was found that these faulty nodes are mainly concentrated at the upper and lower boundaries of the mesh.

2.3.5 Comparison of FE-DIC measurements for different mesh sizes

We now want to compare FE-DIC measurements errors as a function of mesh size. To do this, we now introduce the unscaled standard deviation of the displacement errors:

$$SD_u = \sqrt{\frac{1}{N}\sum_{n=1}^{N}\sum_{\alpha\in(x,y)}(\xi_n - \overline{\xi_n})^2} \;/\sigma \tag{2.6}$$

where $\xi_n = u^{imposed}_{Abaqus}(\underline{X}) - u^{calculated}_{Pyxel}(\underline{X})$ is the displacement error, and $\overline{\xi_n}$ is its mean.

For an element size of 1.25 mm (using around 65 $\times 65 pixels^2$), the unscaled standard deviation SD_u is 7.691 % along X, 5.485 % along Y and 7.285 % (in norm). This latter value can be considered acceptable for tracking large strain displacement fields. We now perform the same type of analysis for the other mesh sizes, but with the same speckle pattern.

Fig.2.23 shows the evolution of the unscaled standard deviation SD_u as a function of the size of the elements. The red crosses in the figure indicate the standard deviations SD_u of the norm of the displacement. The upper and lower limits represent the SD_u along the X-axis (upper limit) and the Y-axis (lower limit). This analysis shows that the mesh size has a significant effect on the quality of the tracking performed by 2D FE-DIC. When the mesh size is smaller than the strand width (1.1 mm), SD_u is smaller than when the mesh size is larger than the strand width. The scaled standard deviation SD_u is smallest (7.285 %) when the mesh size is close to the strand width. This finding supports the choice of element size suggested in section 2.2.2.

2.3.6 Comparison of FE-DIC measurements for a given mesh size but different speckles

This time we are interested in the effect of different speckle patterns, but with a fixed element size of 1.25 mm ($65 \times 65 - pixel^2$).

Fig.2.24 shows the unscaled standard deviation of the displacement errors SD_u for the three speckle patterns (shown in Fig. 2.14), but with the same mesh (element size = 1.25

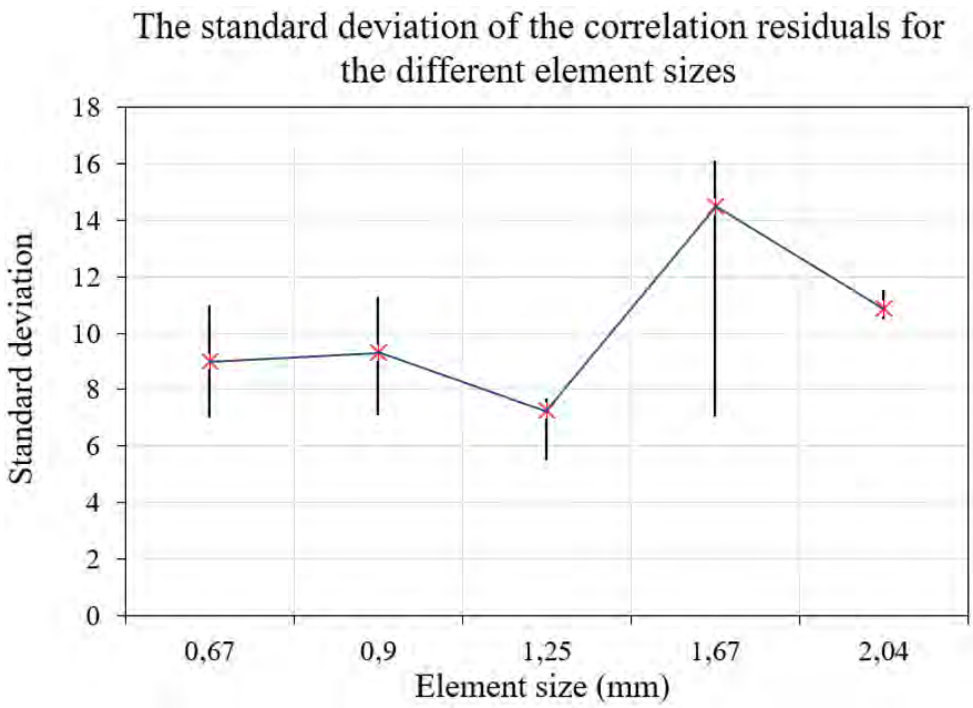

Figure 2.23: Unscaled standard deviation of the displacement errors for different mesh sizes with the same speckles distribution. The red crosses correspond to the displacement norm deviations, while the top and bottom of the bars indicate the displacement deviations along X and Y, respectively.

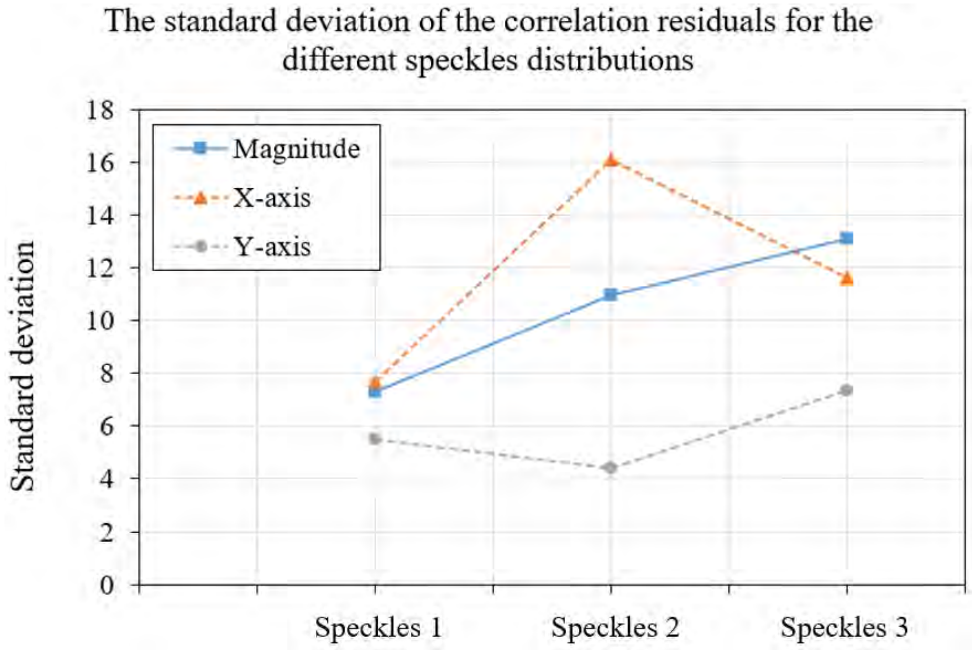

Figure 2.24: Unscaled standard deviation of the displacement errors for the three speckle patterns (shown in Fig. 2.14). The FE-DIC element size is set to 1.25 mm ($65 \times 65 pixel^2$).

mm). This figure shows that generated pattern has a direct effect on the tracking of the displacement field. The first speckle seems to give better results overall. A refinement of the mesh (what about the calculation time?) and/or another procedure for creating the speckle pattern could make it possible to improve the latter.

2.4 Discussion

The aim of this work is to initiate work on FE-DIC in the context of fabric testing, with a view to eventually developing test/calculation exchanges at yarn scale. Because the classic bias extension test was chosen, we therefore decided to carry out FE-DIC measurements in only a part of the specimen (region close to the heels which includes the 3 regions of uniform deformation, but above all interesting gradient zones). We are interested here in the impact of the mesh selected on the FE-DIC measurement.

For subset based approaches, subset size and shape function are clearly identified by DIC users as the two key parameters. The resolution and spatial resolution of the DIC, for a given speckle pattern, result from this parameterization (Pan, 2018). It is ideal for the subset size to be large enough to contain sufficient information to mitigate random errors caused by image noise, and for the shape function to accurately approximate local actual deformations in the target subset region. For FE-DIC approaches, the same concerns prevail: one must also be interested in the effect of the size of the element and the FE shape function. Here, the FE-DIC (formulated in physical space) is conducted with a uniform structured QUATREE mesh (using bilinear quadrilateral element). All the elements therefore have the same size, which makes it possible to derive statistics. With this approach to DIC, it even becomes very simple to orientate the elements with respect to the tensile direction (here, we simply rotate the mesh). In this work, we therefore look at the effect of both element size and orientation. The results suggest that if we are unable to obtain an adequate speckle pattern and must therefore work with an element size larger than the yarn width, it is preferable to align the elements approximately with the yarn directions. This precaution considerably reduces the level of correlation residual. Our interpretation is that when a large part of the correlation residual is linked to alterations/changes in the speckle pattern, then orienting the mesh along the yarns should make it possible to take advantage of the continuity of the displacement introduced by the EF description (regularizing effect). Conversely, when the speckle pattern is passively advected, but its characteristic size does not allow the adoption of small enough elements, most of the residuals come from the model error.

The previous study makes it possible to envisage several ways of improvement. First, despite our best efforts, reflection from the surface of the fabric was observed during the tests, through the speckle detachment or poor coverage of certain elements (e.g. PPS strands). Secondly, the size of the dots (especially the larger ones) should be reduced and their density increased. We plan to explore other ways of speckling. Furthermore, only three fabrics were studied. Other fabrics could be tested to support our conclusions. This kind of parametric study could be carried out for any new fabric study. Nevertheless, we think it would be interesting to carry out a similar study using synthetic images generated from simulations, in order to have an objective ground truth (controlled images and displacement fields). Such a study would certainly give us a better idea of the various sources of uncertainty in such a situation. This work is currently in progress. Finally, the proposed method does not address the challenges caused by the complex kinematics between yarns and defects in shear deformation. This question is part of future work. An outlook on this work includes:

1) Optimizing FE-DIC for the measurement of less biased displacement fields during large fabric transformations. In fact, as observed in this chapter, the correlation residual increases significantly as the extension increases. In addition to the problems associated with poorly approximated kinematics, and despite all efforts to improve the speckle, the evolution of the recorded pattern clearly cannot be neglected. We are considering 2 avenues:
    a) The first involves adopting an incremental approach. This could be achieved by decomposing the problem into several consecutive FE-DIC problems. One advantage of the FE-DIC method presented is that it allows us to simply update the reference image (*e.g.* image n) and the mesh for subsequent calculations (*e.g.* we can exploit the deformed mesh obtained for image n). Different strategies can be envisaged. The correlation residual is an invaluable ally for comparing the performance of the latter. This work is presented in the nex chapter.
    b) Eventually, we plan to use an FE mesh that conforms to the real architecture (Rouwane et al., 2022, 2023a). For example, it would be interesting to use a mesh for each yarn. Our initial tests, with a single element across the width of the yarn, show that this approach is feasible but that the uncertainty levels associated with the measured displacements are not reasonable. The challenges to be overcome in order to make this measurement exploitable include (i) improving the speckle (ii) constructing a conformal mesh (iii) devising a suitable regularization (Chapelier et al., 2021) (iv) addressing the tricky question of visibility.
2) Studying the mechanical behavior of fabrics during *in-situ* testing performed in a X-ray micro-CT. The goal is to investigate the fabric structure and kinematics at the yarn scale. This question will be the subject of the last chapter of this document.

Assessing the resolution of the FE-DIC measurement in such a context is, as we have seen, particularly complex. An *a priori* study, although it seems to help in the choice of an element size more adapted to a speckle pattern and probably to an architecture, allows even less than usual to anticipate the "true" level of the expected uncertainties. Furthermore, the evolution of the correlation residual during the test depends on a large number of parameters. The effects of kinematics, speckle degradation, specular reflections, etc. come to mind. The idea of generating synthetic data, as proposed in this chapter, seems attractive in this context. Indeed, it would make it possible to test the 2D FE-DIC algorithm in representative situations, knowing exactly the displacement used to deform the images. In this first work, we modelled a glass fabric and performed a simulation of a kind of bias extension test on a very small scale. In order to evaluate the ability of the FE DIC method to follow the displacement field of the fabric, we generated synthetic images from the FE simulations in which the elements were manually coloured. This type of image can then be used to estimate displacement errors (Passieux et al., 2015), correlation residual maps (here without reflection and without speckle degradation) and to evaluate separately the influence of the main parameters (mesh size, speckle pattern). The main limitation of the presented work concerns the marking technique. For the time being, this technique is essentially manual, the marking shows strong variations in gray level and is too crenellated (depends on Abaqus mesh size), it covers all the strands (it would be interesting to speckle only the visible parts of the yarn) and it is non-parametric (Shi et al., 2022)). Lastly, we did not have time to study the influence of the orientation of the measurement mesh on the results.

2.5 Conclusion and outlook

In this work, new procedures for carrying out bias extension tests are proposed. They meet 2 objectives.

On the one hand, we suggest a new sample preparation procedure to facilitate sample handling and installation in the tensile testing machine. The fabric is initially speckled: a specific speckling procedure, adapted to the 3 types of fabrics studied (glass, carbon, and co-mingled C/PPS), is proposed. A two-part frame is then glued to the fabric. A water-jet cutting precisely delimits the lateral borders of the piece of fabric to be tested, while clearing the unnecessary part of the frame. The frame allows easy alignment of the sample and good respect of orientations. The order of magnitude of the maximum deviation on yarn orientation is about one degree. The side posts of this frame are cut just before the test, while its ends act as tabs that prevent slippage in the jaws.

On the other hand, we propose to make FE-DIC measurements in order to make them directly comparable with the simulation results. To our knowledge, this is the first time that such measurements have been carried out on this type of fabric. The presented study investigates the influence of mesh size and mesh orientation on fabric deformation measured using the FE-DIC method. The study uses images acquired during bias extension tests performed on the 3 types of fabrics. The first part, based on the analysis of artificially translated images, determines the evolution of the ultimate error as a function of the mesh size. It demonstrates that it is advisable to adopt sufficiently large elements to allow the convergence of the algorithm. Measurement uncertainty initially decreases with increasing element size, but, contrary to usual observations, increases above a certain element size. For the chosen speckling procedure and the fabrics studied, a kind of optimal element size for measurement is therefore apparent. Here, to minimize measurement errors, it would be desirable to use elements at least as large as the yarn width. This analysis shows that the speckle could be a little finer to hope to go down to the yarn scale or below. We plan to use an airbrush to better control the size of the spots and increase their density. The second part of this study concerns the evolution of correlation residuals during bias extension tests for different mesh sizes and orientations. Regarding the influence of mesh size, as the element size decreases, the residuals diminish. However, the displacements obtained for small elements do not seem to better describe the kinematics (erratic oscillations) but simply compensate for some experimental artifacts (reflections, speckles, etc.). Concerning the influence of the mesh orientation on the correlation residuals, the work reveals that it is preferable to orient the quadtree mesh in the direction of the yarns rather than in the direction of extension. Only the C fabric seems insensitive to this parameter. We explain this by the fact that the element sizes considered are close to or smaller than the yarn width. We believe that the kinematics of yarn deformation can be captured correctly with such meshes and speckle. In this case, most of the residuals arise from the inability of the kinematic model (linear interpolation of displacement) to describe what happens in the inter-yarn voids and at inter-yarn crossings related to inter-yarn movement.

All these observations confirm our decision to focus on yarn-scale measurements, generating a finer speckle pattern and using a FE mesh conforming to the actual architecture, *e.g.*, derived from a Digital Image Based Model (Rouwane et al., 2023a). Such a model could perfectly be obtained from tomographies as will be detailed in the last chapter of this document. Such a model could obviously be used to perform FE simulations incorporating ad-hoc behavior models of yarns and interfaces. Incidentally, this type of simulation could make it possible to generate synthetic images allowing us to test our algorithms and better understand the origin of the errors we have observed.

The last part of this chapter was precisely devoted to a first attempt to generate synthetic images from simulated data. A FE micro-bias extension virtual test was performed. The generated images were first subjected to an a priori analysis in order to propose an appropriate mesh size for the next FE-DIC analysis. In a second step, given this mesh size, the evolution of the residuals during the test, but also the displacement error between the displacement fields ("ground truth") and the displacement fields measured by FE-DIC could be evaluated. Finally, the effect of the element size or the speckle used is studied. Such an approach would make it possible to better define the kinematic part of the increase in residuals. All of the essential elements have been put in place. However, the speckle part can still be improved. The speckles should be more realistic and the generation process should be automated. But above all, only the 'visible' elements should be speckled to better represent experiment conditions.

The following chapter examines the delicate question of the large deformations which are expected during this type of test.

CHAPTER 3

FE-DIC to study the large deformation of textile reinforcements.

Sommaire

Background: *Large deformations combined with complex underlying kinematics lead to large DIC measurement errors, making it tricky to accurately track fabric deformation even during a simple bias extension test. Changes in the recorded speckle pattern, whether due to degradation of the speckle, its deformation, reflections or occlusion of part of the speckle by an overlying yarn, are largely responsible.*

Objective: *In this part, the idea is to seek to improve the DIC algorithm in order to reduce the measurement uncertainties of the displacement field during such tests.*

Methods: *In terms of experiments, bias extension tests were conducted on two distinct reinforcement materials, namely glass fiber fabric and carbon/PPS (phenylene polysulfide) fiber fabric. The measurement of displacement fields is again based on Finite Element Digital Image Correlation (FE-DIC). An initial classical analysis is proposed. The reference image is not questioned. A sequential analysis, more conventional in this situation, is then proposed. As the test progresses, the reference image is updated. The distorted mesh that is obtained when the reference image is updated will be used for the next FE-DIC measurement. Several strategies are compared. Updating the reference image with each new correlation is the first strategy. The second strategy is to update the reference image only when the correlation is estimated to be questionable. The correlation residual, which provides global information about the quality of the image registration performed, can be used for this purpose.*

Results: *The results indicate that the new algorithm method provides a displacement field that corresponds more closely to the actual experimental results and reduces measurement error to some extent. Additionally, the method provides a way to identify the best partition conditions of the "residual values", thereby improving the accuracy of the obtained displacement field. We can see that, despite all the efforts made, the measurement is affected by a significant error at high levels of deformation.*

Conclusions: *This analysis once again shows the benefits of using FE-DIC measurements. The correlation residual is a real plus in this type of analysis. In addition, this work confirms our desire to move towards regularised measurements at yarn scale based on information collected on the surface as well as the volume.*

As mentioned at the beginning of this manuscript, the deformation of textile reinforcements during forming has a direct impact on the properties of consolidated composites (Boisse, 2004; Patou et al., 2019). Textile reinforcements generally have complex structures which give rise to complex deformation mechanisms (Bel et al., 2012; Nosrat-Nezami et al., 2014; Nishi et al., 2014; Liang and Boisse, 2021), which in turn make it particularly difficult to simulate their behaviour (Badel et al., 2007; Boisse et al., 2011; Rios-Soberanis et al., 2012; Boisse et al., 2018b; Liang and Boisse, 2021). They also undergo large deformations during forming (Zhu et al., 2007b; Badel et al., 2008a).

In this context, optical measurement techniques (Willems et al., 2008; Lomov et al., 2008; Willems et al., 2009) and X-ray tomography (Naouar et al., 2014, 2015, 2020) have proven to be important allies. Nevertheless, the processing and analysis of data for the characterization of displacement and deformation fields can be difficult. In the previous chapter, we showed for example that it is not easy to correctly measure the deformation of the fabric with the DIC in particular because of the complex movements between the threads and the modifications of the recorded speckle pattern. In this chapter, we now wish to address the issue of measuring large deformations by FE-DIC. Our case study is still the bias extension test. Glass fabrics (5 HS satin) are studied here. An aluminum frame is again used to control and facilitate the placement of the sample in the machine. The good flatness of allows to delay the appearance of folds (see chapter 2).

In "classical" (FE-)DIC, the displacement measurement is performed between the reference state and the deformed state. However, for large deformations, the considered kinematics may be completely surpassed. In addition, the appearance of the speckle pattern may change due, for instance, to stretching (e.g. what was initially seen as a small dot may appear as a population of dots as the object is stretched) or due to its degradation or even specular reflections. Decorrelation thus appears. Furthermore, in the case of fabrics, the fabric is far from a continuum (complex movements between the yarns and within the yarns). As a result, image registration becomes less efficient with increasing deformation. It is therefore necessary in this case to adopt an incremental approach (Pan et al., 2012). The idea is to update the reference image periodically. In subset-based DIC, the position of the reference subset in the new reference image is then determined according to the previous measurement (itself subject to uncertainty), and the displacement of a point is the sum of incremental displacements, each subject to uncertainty. The multiplication of these updates makes it possible to go further in the monitoring, but at the cost of an increasing measurement error (Anwander et al., 2000). It is therefore essential to limit the number of updates. To do this, it is necessary to have objective criteria that allow the image registration carried out to be questioned (Pan et al., 2012).

In what follows, we are interested in an incremental approach to FE-DIC (see Fig.1.31). First, we show the limitations of "classical" measurements. We then examine the performance of different approaches to incremental methods. In FE-DIC we can rely natively on a valuable indicator, the correlation residual. Furthermore, the mesh obtained in the update stage can simply be used as a starting mesh in the new reference image.

3.1 Non incremental FE-DIC measurements

3.1.1 Data and settings

The data obtained from the bias extension experiments in the previous chapter has been reused in this study. Three experiments carried out on glass fabric speckled samples are examined. Unlike carbon fabrics, glass fabrics have narrower yarn cross-sections and experience more friction between yarns, resulting in simpler kinematic behaviour between warp and weft yarns. The test is monitored by a camera equipped with a telecentric lens. It is worth remembering that the travel speed is set at 10 mm/minute and the frame rate is 1 frame/second. The field of view chosen for this study is shown in Fig.1.21.

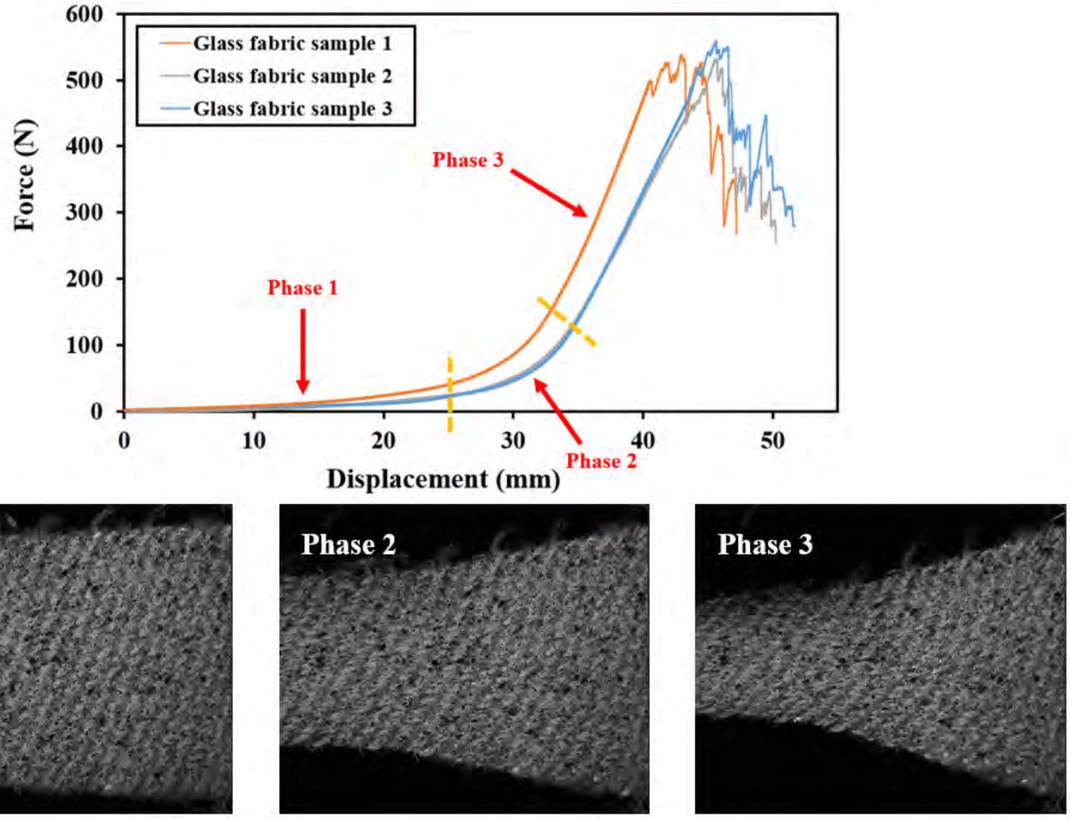

Figure 3.1: Force[N] vs Displacement[mm] curves for three bias extension tests performed on glass fabric samples (top). The images shown below were captured during the 3 phases indicated on the curve. The images shown below were taken during the 3 phases indicated on the curve. From left to right, the displacement corresponding to the image shown is 10 mm (image 60), 26 mm (image 160) and 34 mm (image 200).

Fig.3.1 shows the force vs displacement recorded for the 3 speckled specimens. As mentioned earlier in Section 2.1.3, the shear deformation process of textile reinforcement materials can be divided into three phases: shearing, deformation after shearing before the locking angle, and deformation beyond the locking angle. The transition points between the three phases can be clearly seen in Fig.3.1. The simple shear deformation ends when the imposed displacement reaches between 25 mm and 33 mm. It can be concluded that the first phase of the stretching process is from 0 to about 150 frames, the second phase is from 150 to about 195 frames and the third phase starts after 195 frames. The 60 (10 mm), 160 (26 mm) and 200 (34 mm) images are then studied in particular in order to estimate the potential of FE-DIC in each phase.

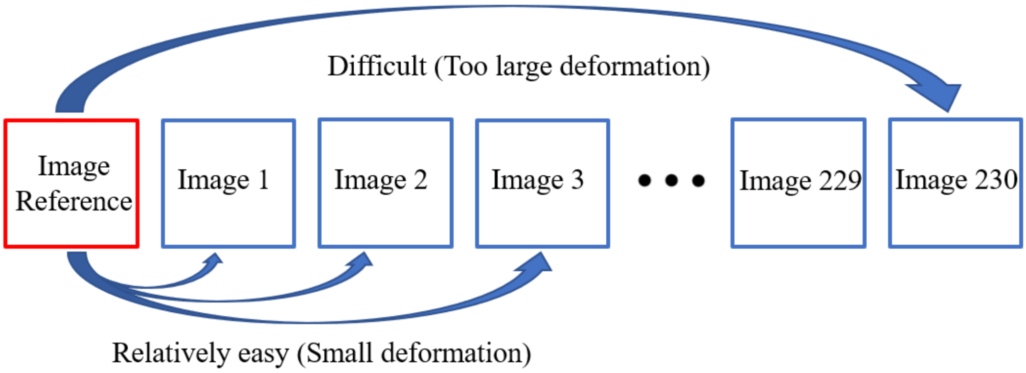

Figure 3.2: Diagram of the "classic" FE-DIC algorithm. The reference image is not updated. Moving to the previous step initialises the next measurement. If the deformation between two images is significant, the initialisation and consequently the measurement can become difficult.

In this first section, the reference image is never updated. In this case, the loading is monotonic. As a result, the displacement obtained at the nth image is theoretically a very good initialization for identifying the displacement for image n+1. The schematic diagram of the "classic" procedure is shown in Fig.3.2.

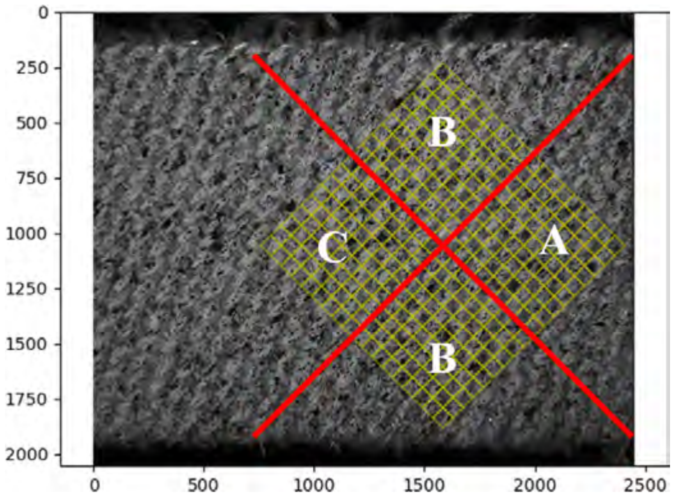

Figure 3.3: Reference image of a glass fabric sample prior to the bias extension test. The mesh selected for the FE-DIC measurements covers the 3 zones shown (non-shear zone A, semi-shear zone B and shear only zone C). The yarn directions are indicated in red.

Based on our preliminary observations, the uniformly structured square mesh used for the FE-DIC measurement is oriented at 45° with respect to the tensile axis. Fig.3.3 shows the position of the mesh in the reference image. The latter includes: the non-shear zone A, the semi-shear zone B and the shear-only zone C. Measuring the displacement field is particularly challenging, not only due to the large deformation that may result in significant measurement errors but also because of the intricate kinematic behavior between warp and weft yarns. The marking of the lower yarns by the yarn passing over them makes measurement in this area impossible. The analysis software used in this section is Pyxel, as in chapter 2. Gmsh is used to generate the mesh. The mesh size is chosen based on the analysis described in chapter 2. For glass fabrics, the latter analysis indicates that an element size of 1.964 mm (using 64×64 pixels^2) allows the ultimate error to be minimised. We choose this size in the following.

3.1.2 Limits of FE-DIC in the presence of large deformations

To estimate the accuracy of the measured displacement field, this study proposes three methods: observation of the global displacement field, analysis of the correlation residuals, and a local comparison of the measured and visually estimated nodal positions. The figures shown are for only one of the three glass fabric samples to make the illustrations as clear as possible, but the results obtained for the other glass fabric samples are comparable in every respect.

3.1.2.1 Global displacement field

The displacement fields obtained using the general FE-DIC method are presented in Fig.3.4. By importing the displacement field results obtained from Pyxel's calculations into ParaView, a clearer view of the displacement field in the ROI is achieved. Pyxel still tracks the displacement field very well at an elongation of 10 mm. However, as the stretch length increases, the adjacent warp and weft yarns in the sample approach each other, making the deformation in the semi-shear zone and pure shear zone more complex. As shown in Fig.3.4 (f), the area with the largest deformation probably represents a part of the zone B and/or C. In this area, the algorithm's inability to track the displacement field becomes first apparent. The likely boundaries of the ROI after deformation (blue dotted lines) are shown in Fig.3.4 (g-i). They were obtained by tracking points on the boundary of the initial ROI. Fig.3.4 (c) indicates that the algorithm is unable to track and measure the displacement field at all, due to the excessive deformation. Figures (g), (h), and (i) show that at the macroscopic level, there are significant differences between the "actual" visually estimated and the FE-DIC measured displacement fields. Note, for example, that the deformed mesh obtained at the highest level of deformation does not even have its top and bottom corners above the fabric.

These macroscopic observations lead us to conclude that the 'classic' FE-DIC method, which never questions the reference image, cannot provide correct measurements in the presence of major deformations such as those involved in a bias extension test.

3.1.2.2 Correlation residual map

To better illustrate the limits of the image registration achieved, the parameters defined in chapter 2, namely the global residual (equation 2.3) and the standard variance R of the global residual (equation 2.4), were used.

The Fig.3.5 displays the residual maps of the FE-DIC measured displacement fields for the three phases. The darker color in the graph indicates a larger absolute value of the residuals, which means that the measured displacement fields can not provide a nice image registration. It can be seen that the residuals increase in intensity as the load progresses. Only the less sheared part, as expected, continues to show low residuals. The

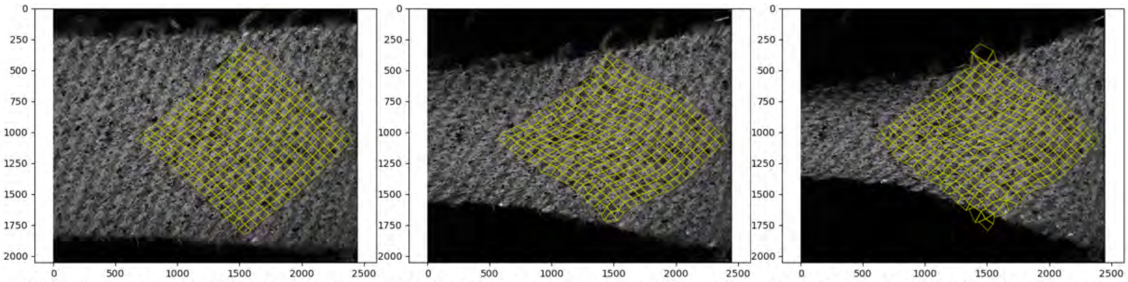

(a) Deformed mesh given by Pyxel for the 60th frame (b) Deformed mesh given by Pyxel for the 160th frame (c) Deformed mesh given by Pyxel for the 200th frame

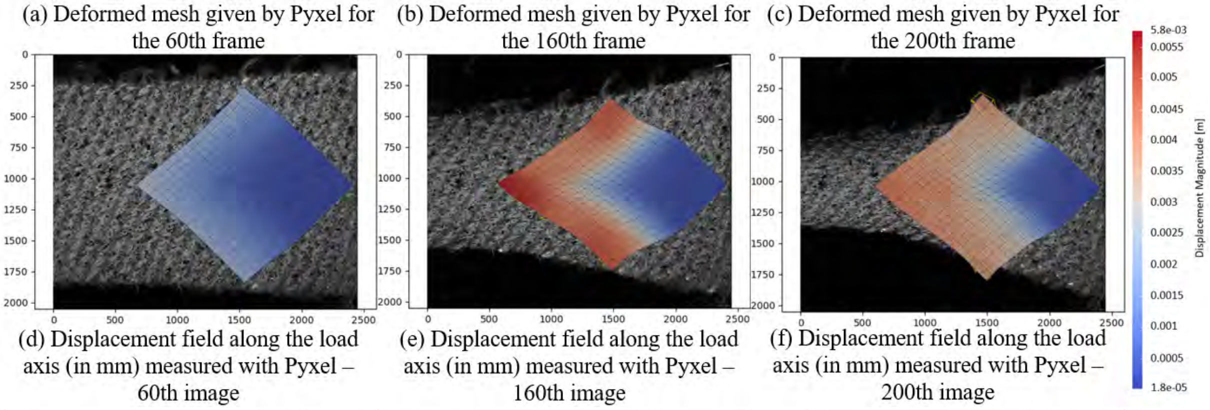

(d) Displacement field along the load axis (in mm) measured with Pyxel – 60th image (e) Displacement field along the load axis (in mm) measured with Pyxel – 160th image (f) Displacement field along the load axis (in mm) measured with Pyxel – 200th image

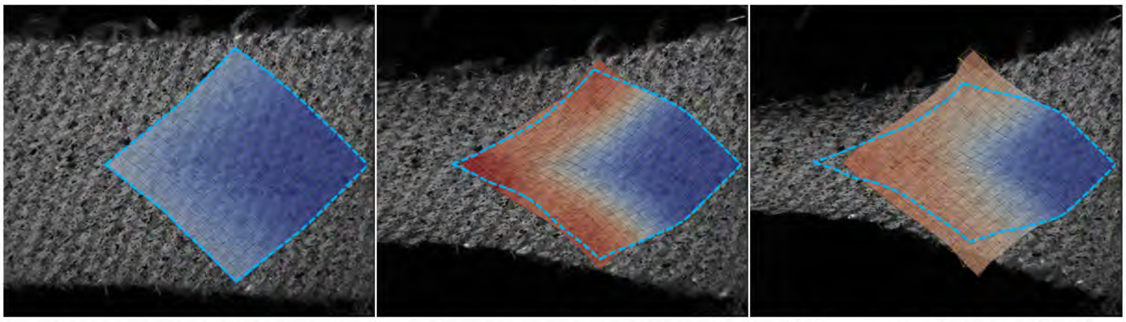

(g) Comparison of deformed mesh contour obtained by FE-DIC with visual contour tracking (dotted lines) – 60th image (h) Comparison of deformed mesh contour obtained by FE-DIC with visual contour tracking (dotted lines) – 160th image (i) Comparison of deformed mesh contour obtained by FE-DIC with visual contour tracking (dotted lines) – 200th image

Figure 3.4: The displacement fields measured with Pyxel for the (a) 60th, (b) 120th and (c) 200th frames and plotted with ParaView (d, e and f). (g), (h) and (i) are plots comparing macroscopically the visually estimated "real" displacement field (dotted blue square) and the FE-DIC measured one.

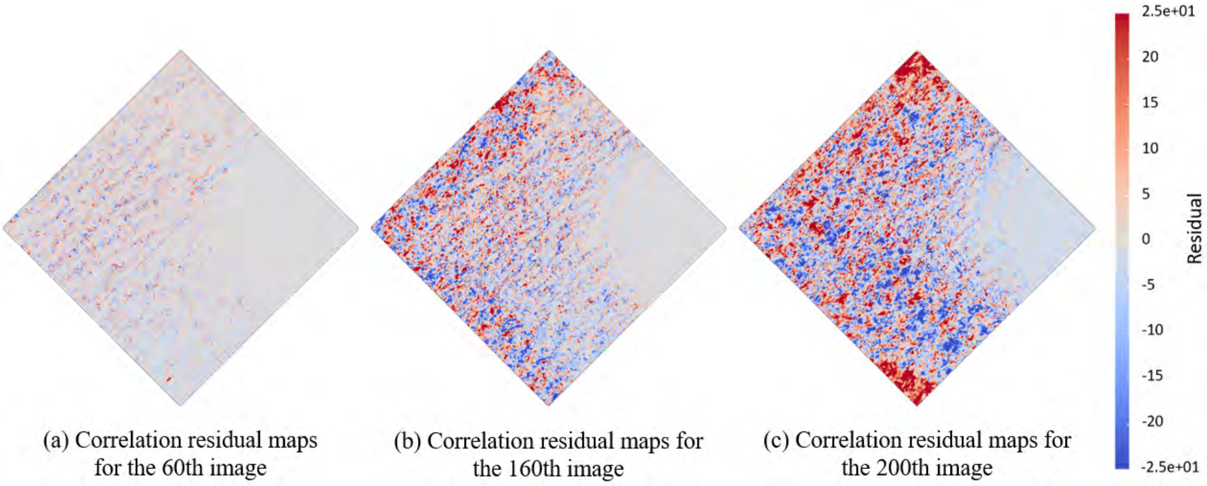

(a) Correlation residual maps for the 60th image

(b) Correlation residual maps for the 160th image

(c) Correlation residual maps for the 200th image

Figure 3.5: Correlation residual maps in the selected ROI for (a) the 60th, (b) the 120th and (c) the 200th image obtained with Pyxel and plotted with ParaView.

maps shown in Fig.3.5(b and c) show, on the other hand, that decorrelation is very marked in the sheared regions. Fig.3.5(b and c) shows that the residuals are naturally greatest where the deformed mesh has even emerged from the fabric. The corresponding global residual R for the displacement fields in the three maps are approximately 4.94%, 11.62%, and 14.94% respectively. Such high levels of residuals, for the last 2 states, illustrate that it is illusory to claim to have correctly estimated a displacement field.

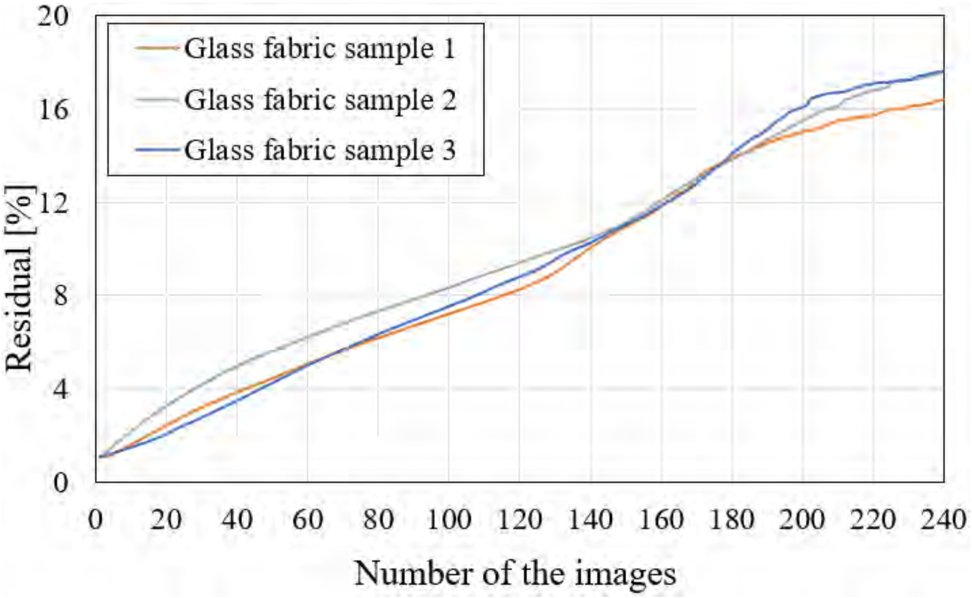

Figure 3.6: Evolution of correlation residuals R (%) for the three glass fabric samples during loading.

Fig.3.6 shows the evolution of R for the three glass fabric samples. This figure shows that R increases continuously with the stretching length, indicating that the measurement error also increases with the stretching length.

3.1.2.3 Local comparison

Three regions, named zone 1, 2 and 3, were selected to compare the measured displacement field with the "actual" visually identified displacement field, as illustrated in Fig.3.7.

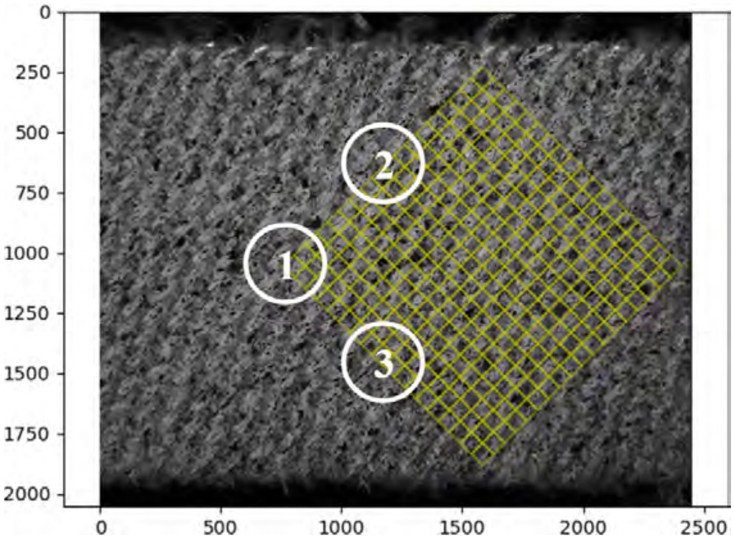

Figure 3.7: Three areas are selected in the refernce image for a more local assessment of FE-DIC performance in the presence of large deformations

Figure 3.8 shows the distorted mesh in the 3 regions shown in Fig.3.7 for comparison with visual estimates. In this case, the yellow mesh was created by Gmsh and calibrated on the reference image. The red points in the reference images represent the initial positions of the mesh nodes. As the sample is stretched, the positions of the red dots change, and the positions of the mesh nodes (yellow mesh) measured by FE-DIC deviate from the positions of the red dots. The actual displacement field or experimental displacement field in the region can be obtained by connecting the red dots (in blue). This figure demonstrates that the FE-DIC algorithm is still relatively effective in tracking the displacement field in the 60th image. However, the algorithm fails when the stretch length reaches the position of the 160th image. There are two main reasons for the inability to track displacement fields:

1. The first and primary reason is excessive deformation, which could be addressed by modifying the algorithm.

2. The second reason is the more complex kinematics between the warp and weft yarns at this deformed stage. During the stretching process, the fibers in the yarn tighten due to the traction and shear forces. Then, the warp and weft yarns rotate at the intersection, causing two outcomes: the black dye attached to the fibers squeezes and deforms or even falls off; and when the yarn rotates, it exposes the position where the speckle is not sprayed. These phenomena generate a lost of information, resulting in erroneous measurements of the displacement. New concept to avoid these problems will be proposed.

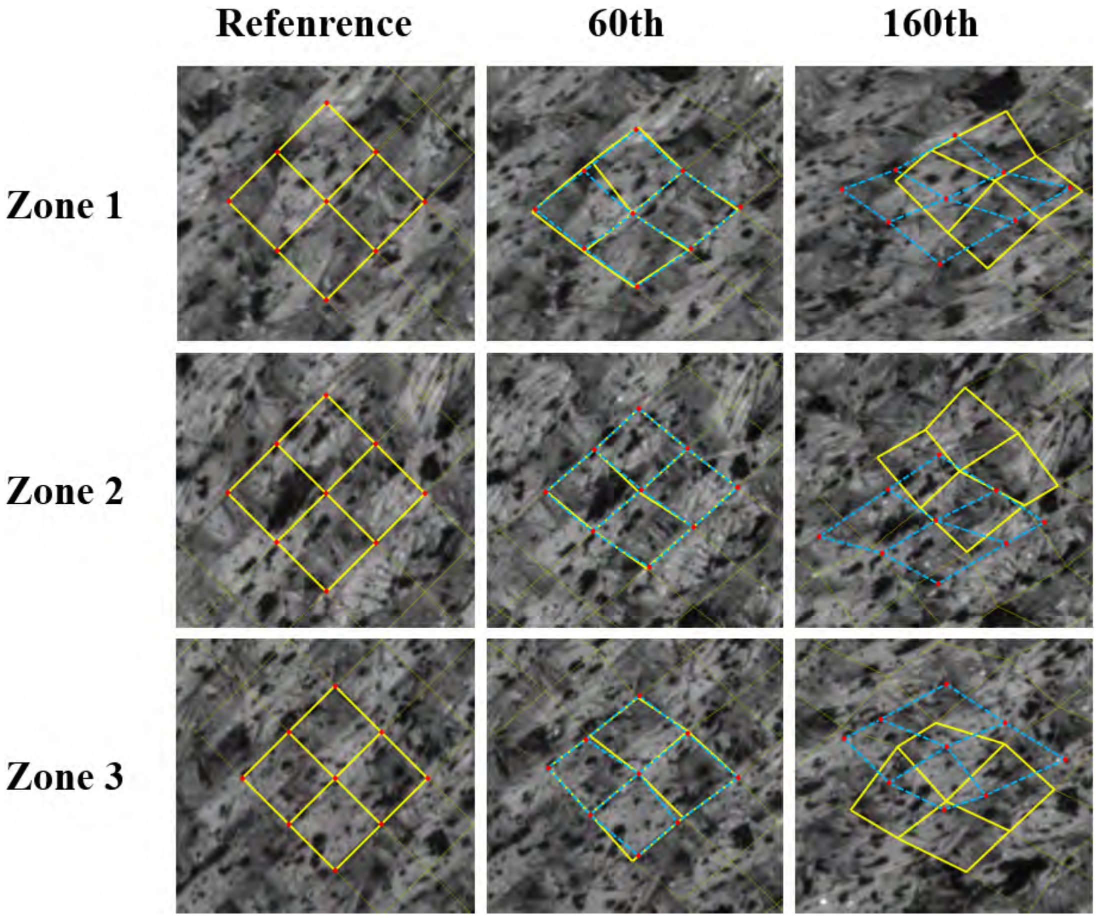

Figure 3.8: Comparison between the displacement field measured by "conventional" FE-DIC and the "real" displacement field (estimated visually by tracking points on the specimen surface) in the three regions shown in Fig.3.7

3.2 Incremental FE-DIC for studying large deformations of textile reinforcement

As shown in the previous section, a "classical" FE-DIC algorithm cannot be effective for tracking displacement fields in the large deformation regime in the present situation. Under these conditions, we propose to resort to an incremental FE-DIC method. In other words, the reference image is now regularly updated so as to limit the deformation field between the reference image and the deformation image. The problem of measuring large deformations is thus transformed into a succession of problems measuring small deformations (Pan et al., 2012; Tang et al., 2012).

The new proposals will be developed on the basis of the glass fabric, and will then be tested with the C/PPS fabric.

3.2.1 Unconstrained FE-DIC incremental algorithm

In this first version, we choose to update the reference image with each new image processed. Fig.3.9 shows the principle of this incremental approach to FE-DIC, which does not require the setting of constraints. In the present case, all the acquired images are used:

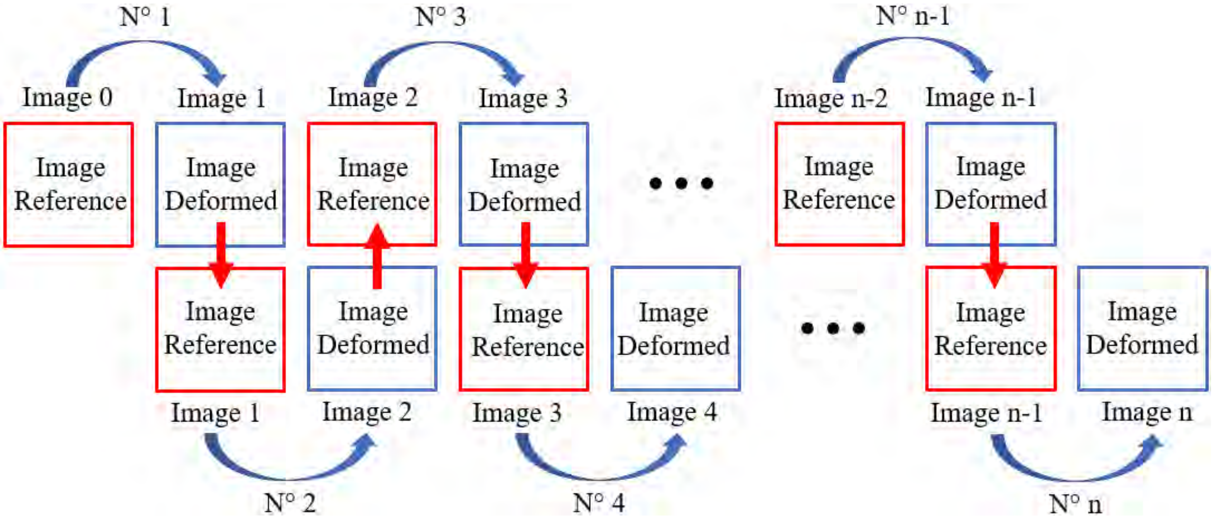

Figure 3.9: Diagram of the operation of the unconstrained incremental FE-DIC algorithm. In this case, all captured images are processed.

the deformation between two successive images is very small and the residual correlations are minimal. Based on the chosen stretching speed and frame rate, the stretched length of two adjacent images is approximately 0.167 mm. Therefore, as long as the "distorted" image $(N + 1)$ is not the last one (n), the procedure is simply to repeat the following sequence:

1. update the reference image. The reference image is image N.
2. use the deformed mesh obtained in the previous step as the new measurement mesh
3. compute the displacement field between the reference image N and the following image $N + 1$

Fig.3.10 compares the contour of the deformed mesh obtained for the 3 key images with the expected visually identified contour. From a macroscopic point of view, the displacement field obtained with this algorithm appears to be much more relevant than that obtained previously. At a stretching length of 26 mm (160th image), the FE-DIC measurements are still convincing and we no longer observe pb of mesh dropout for certain nodes, contrary to the classical FE-DIC approach. Even at a stretch length of 34mm (200th frame), the algorithm is still efficient, albeit with reduced accuracy, as shown in Figs.3.10 (f) and (i). However, the increase in measurement error is not only due to the main reasons mentioned in the previous section, but also due to this new algorithmic issue. Although the new algorithm has a strong tracking capability for displacement fields, each operation changes the reference image, which weakens the correlation between the calculated displacement field and the initial reference image. So the next direction for improvement is to ensure tracking capability while increasing the correlation of the results with the initial reference image.

The Fig.3.11 shows the standard deviation of the global residual R for all the increments. It can be observed that R in between two adjacent images are around 1%. There were two instances where the standard residuals became slightly larger, near the 70th and 170th images, respectively. Upon observing the original images, it was discovered that

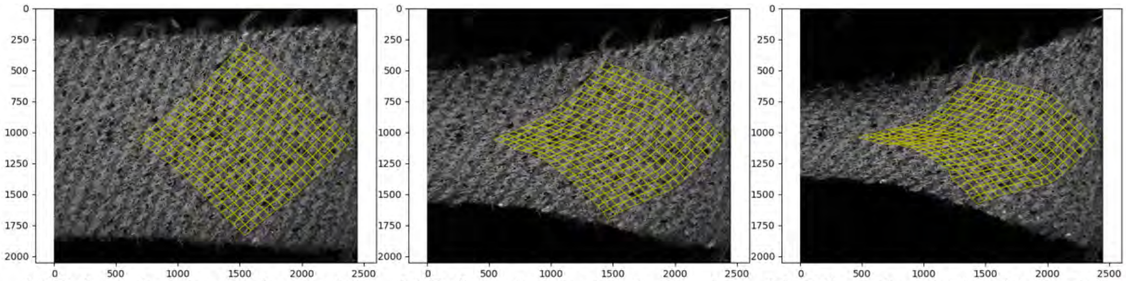

(a) Deformed mesh given by Pyxel for the 60th frame (b) Deformed mesh given by Pyxel for the 160th frame (c) Deformed mesh given by Pyxel for the 200th frame

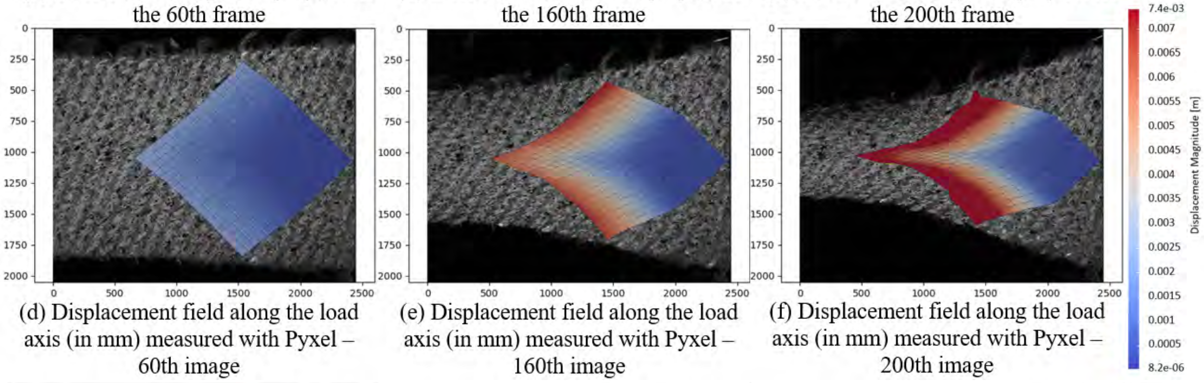

(d) Displacement field along the load axis (in mm) measured with Pyxel – 60th image (e) Displacement field along the load axis (in mm) measured with Pyxel – 160th image (f) Displacement field along the load axis (in mm) measured with Pyxel – 200th image

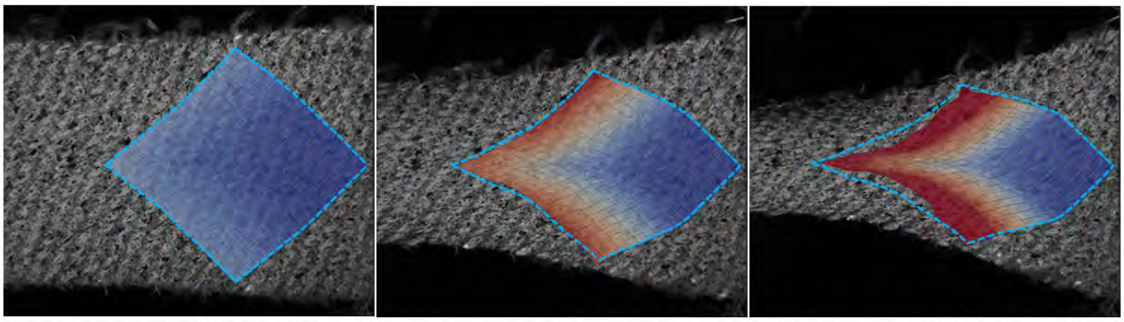

(g) Comparison of deformed mesh contour obtained by FE-DIC with visual contour tracking (dotted lines) – 60th image (h) Comparison of deformed mesh contour obtained by FE-DIC with visual contour tracking (dotted lines) – 160th image (i) Comparison of deformed mesh contour obtained by FE-DIC with visual contour tracking (dotted lines) – 200th image

Figure 3.10: Measured displacement fields for the (a) 60th, (b) 120th and (c) 200th image measured using an unconstrained FE-DIC incremental approach and plotted in ParaView (d, e and f). (g), (h) and (i) allow comparison of the deformed mesh position with the "real" ROI boundaries (blue dotted quadrilateral, visually identified).

the distribution of scattered speckles had suddenly changed slightly due to changes in the glass fibers on the sample surface, such as peeling off from the surface, squeezing and deforming each other, etc. This issue could be addressed by cleaning the excess fibers on the surface of the sample before creating the scattered speckles. In the middle and late stages of the third phase of deformation (deformation after the lock angle, after image 220), the distribution of scattered speckles changed considerably due to the compression between the warp and weft yarns and the interaction between the fibers within the yarns, resulting in a larger correlation residual.

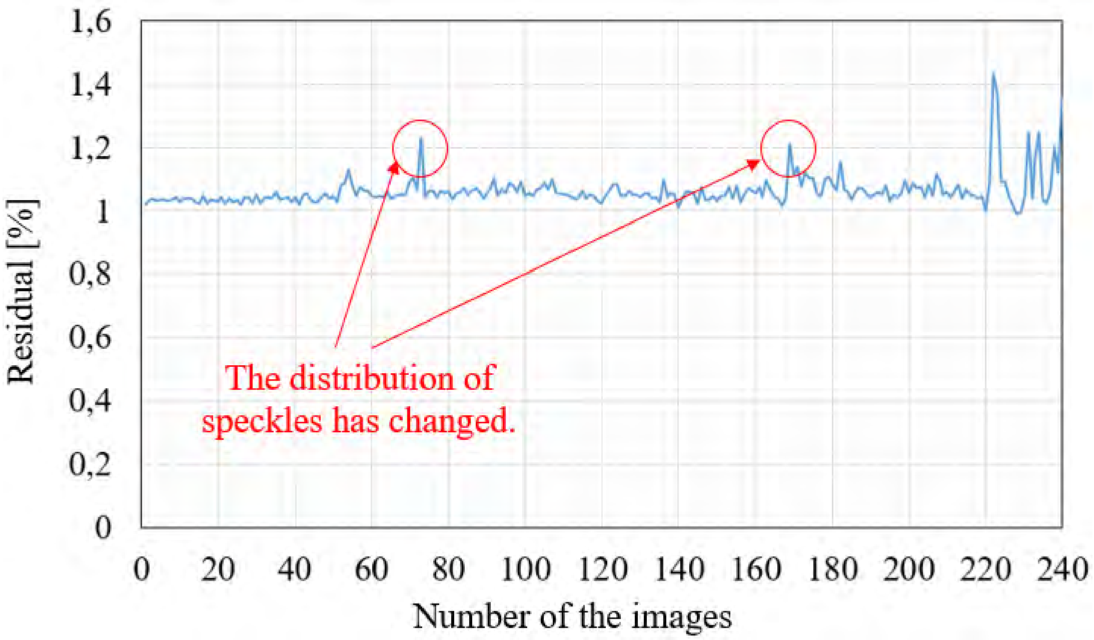

Figure 3.11: Correlation residual obtained at each increment for a glass fabric using the unconstrained incremental FE-DIC method.

The accuracy of this algorithm could be assessed by examining the local displacement fields. Fig.3.12 shows a detailed comparison of local displacement fields calculated by this algorithm. For the 160th image, analysis of the results for the three zones defined in Fig.3.7 indicates that the displacement field is tracked more accurately than with the general method for most zones. For the 200th image, significant errors are observed in the calculations for zones B and C, although they still attempt to track the displacement field.

The error can be estimated directly by calculating the norm of the vector between the measured position of the mesh node and what should be its "real" position. As an example, we consider zone A of the 160th image, which contains four elements and nine nodes. We compute the vectors between the actual nodes and the nodes obtained from the FE-DIC calculation in pixels. The average of the norms obtained for all the nodes can be used to describe the measurement error in this zone. After calculation, this mean displacement error in this zone ranges from 17.8 pixels to 47 pixels, with an average value of 28.8 pixels. When the analysis reached the 200th image, the average modulus of the vectors increased to 33.4 pixels. In zone B, the average modulus of the vectors changes from 23.5 pixels to 57.4 pixels when going from the 160th image to the 200th image. Although this new algorithm improves the measurement of the displacement field to a

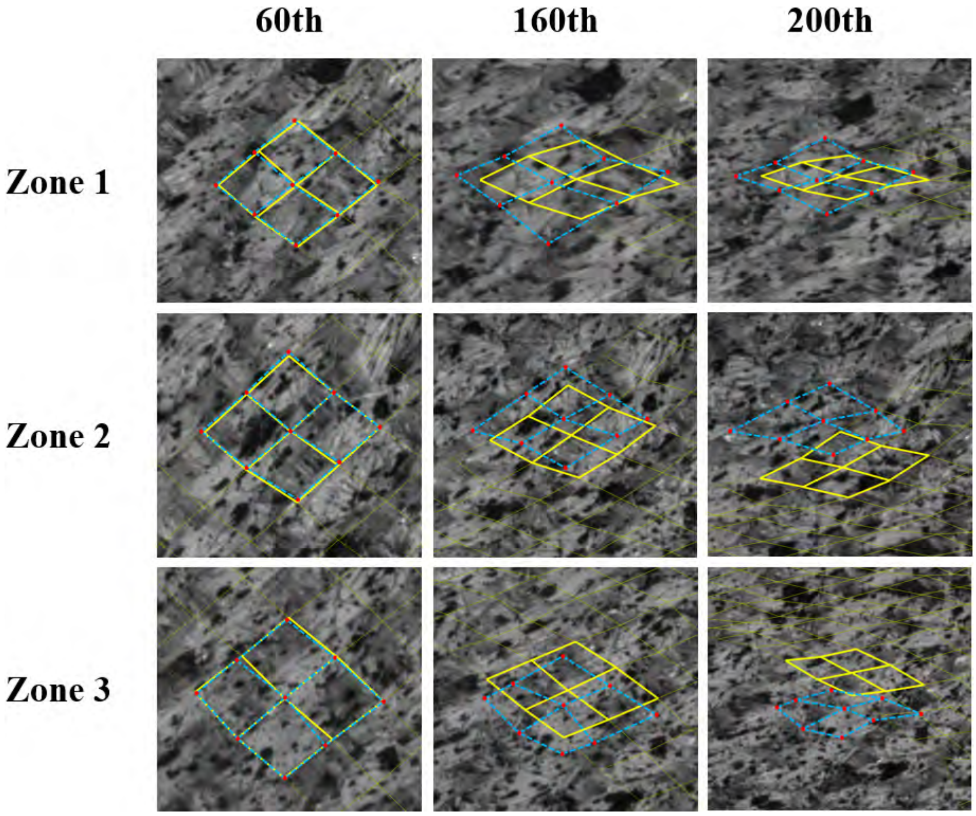

Figure 3.12: Local comparison of displacement fields measured by an unconstrained incremental FE-DIC approach. Here all the images have been used and the displacement between two images is of the order of 2 tenths of a mm, and the correlation residual R of the order of %.

large extent, the error is still considerable. This indicates that there is still room for further development of this algorithm.

We believe that a large part of the problem comes from cumulative measurement uncertainties. Indeed, at each step, the deformed mesh is not "perfectly" placed on the following image. Rather than questioning the reference image systematically, nothing would for instance prevent us from "arbitrarily" processing only one image every p images. Another approach is to keep a reference image as long as the level of decorrelation with the deformed image under consideration is acceptable. The idea is to find a compromise between a systematic approach (accumulation of uncertainties) and an approach where the interval between images becomes inappropriate (effect of significant changes in texture and poorly described kinematics). This is the subject of the next section.

3.2.2 Residual constrained incremental FE-DIC algorithm

3.2.2.1 Definition of operational procedures

Thus, we suggest to update the reference image only when the decorrelation between the two images becomes 'critical'. This takes advantage of a datum that is directly available at the end of a FE-DIC measurement, namely the correlation residual R. When the latter exceeds a predetermined value, the reference image is updated, as shown in Fig.3.13.

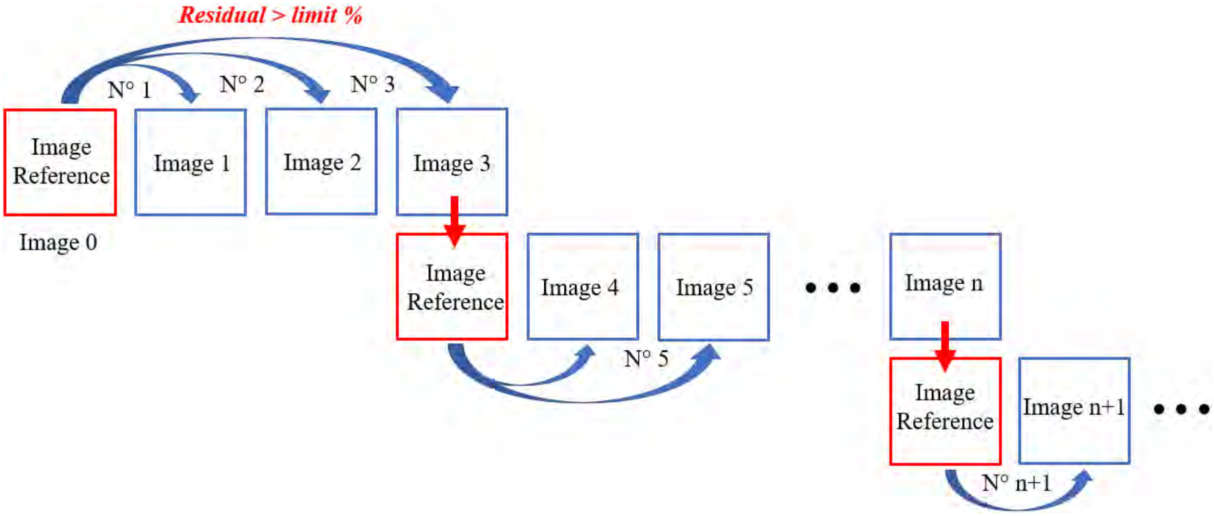

Figure 3.13: Diagram of an incremental FE-DIC measurement process using correlation residuals as constraints for reference image update.

Fig.3.14 shows an example of correlation residual evolution obtained for a sample of glass fabric with either a residual $R < 3\%$ or $< 5\%$. Figures 3.15 show a comparison of displacement fields measured with constrained incremental (with different thresholds), unconstrained and "classical" FE-DIC. Several observations can be drawn from this:

- The constraints effectively reduce the number of iterations. For instance, when the constraints are set as $R < 3\%$ and $< 5\%$, there are only 11 and 6 iterations, respectively, before entering the third phase of deformation (after lock angle). Moreover, the first iteration occurs at the 30th and 65th images, respectively. Fig.3.15 shows that a better match between the FE-DIC measured displacement field and the "real" displacement field could be obtained by setting constraints.
- However, the larger the value of the constraint R, the greater the chance that the error in the displacement measurement at each iteration will be large. Therefore, the value of the fixed constraint R results from a compromise: we do not want large uncertainties at each increment (the fact that R is small indicates a good registration), but we do not want to have too many increments to limit the uncertainty on the final field (accumulation of many uncertainties).
- As the operation progresses to later stages, the reference image updating rate becomes faster, indicating that the calculation error gradually increases as the operation progresses.

3.2.2.2 Research of the optimized threshold of R to minimize computational errors

In order to determine the optimal constraint value that minimizes the calculation error, two methods were used: macroscopic observation of the overall displacement field and local detailed view comparison. From a macro perspective, Fig.3.15 shows a comparison between the actual displacement field (blue dotted line region) and the displacement field calculated by other methods (yellow meshes). The displacement fields are calculated

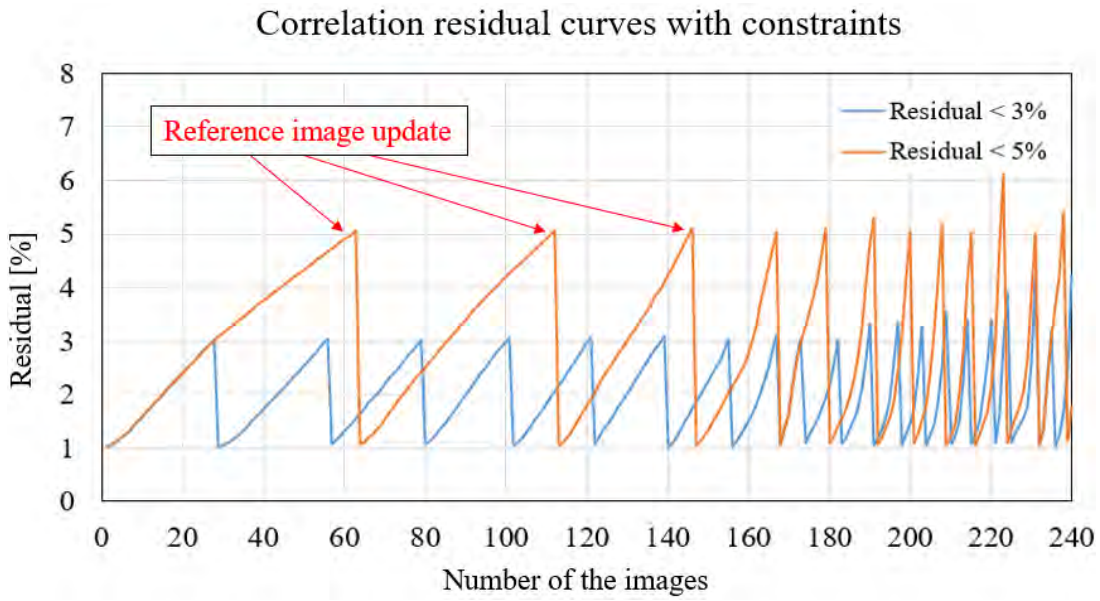

Figure 3.14: Bias extension test on a glass fabric. Example of the evolution of the correlation residual provided by a constrained incremental FE-DIC with 2 different constraints ($R < 3\%$ or 5%).

using three different methods: the general FE-DIC algorithm, unconstrained FE-DIC incremental algorithm, and incremental FE-DIC algorithm with different constraint values.

As shown in figures (a) through (f), when the sample is stretched by 26 mm (160th image), the two new algorithms (unconstrained FE-DIC incremental algorithm, and incremental FE-DIC algorithm with constraint) allow for good tracking of the displacement field. However, when the constraint condition reaches a certain value ($residual < 6\%$), the operation fails again due to the influence of large deformation and the resulting error. When comparing figures 3.15(e) and (f), it can be seen that the pure shear zone C is the first to fail. In comparison to other zones, zone C not only undergoes the largest deformation, but the yarns in this zone also gather more tightly during the stretching process, leading to a more concentrated and variable distribution of scattered speckles in zone C. Therefore, this may explain why the method first fails in this area.

When the fabric is stretched to the third stage of 34 mm (200th image), the difference between the calculated and actual displacement fields becomes more obvious. (1) A comparison of Fig.3.15 (g) and (h) shows that the unconstrained FE-DIC incremental algorithm has strong tracking ability for the displacement field. However, as the sample is gradually stretched, the discrepancy or distortion between the calculated and actual displacement fields becomes increasingly larger. This distortion is mainly concentrated in the semi-shear region B and the pure shear region C, especially at the intersection of the two zones, where the deformation is the largest and the kinematics is the most complex. The yarns at the intersection experience two different force cases and are more prone to distortion during the tracking of the displacement field. (2) The incremental FE-DIC algorithm with different constraint values gradually attenuates this distortion by changing the constraint conditions. When $R < 6\%$, the inability to track the displacement field appears again. Thereby, for measuring the displacement field of the glass fabric in this study, the best constraint condition is $R < 5\%$.

The comparison of the 160th image

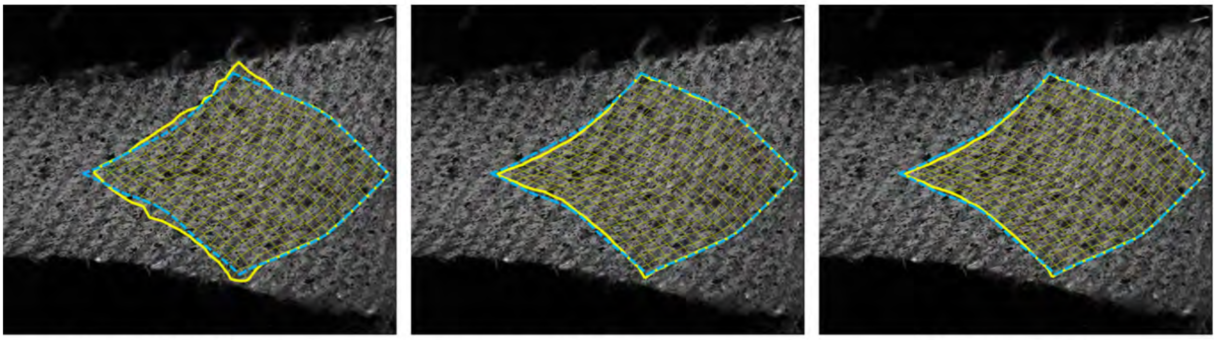

(a) General DIC-FE algorithm. (b) Unconstrained DIC-FE iterative algorithm. (c) Residual < 3%.

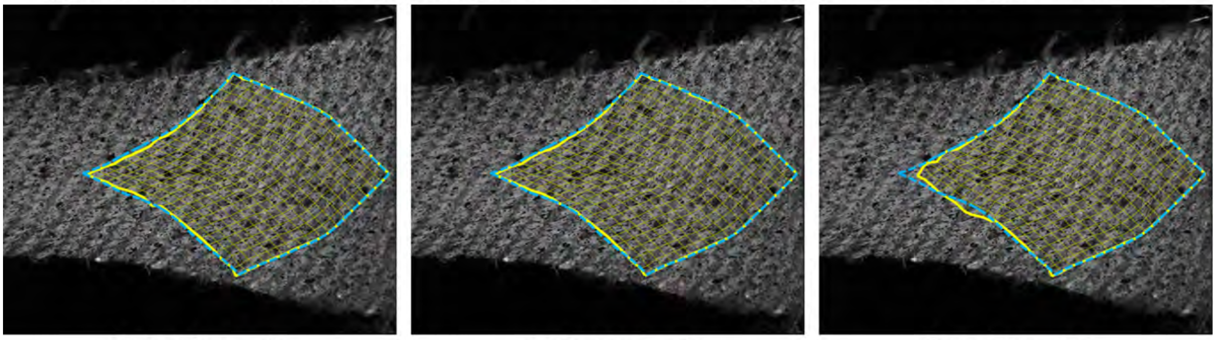

(d) Residual < 4%. (e) Residual < 5%. (f) Residual < 6%.

The comparison of the 200th image

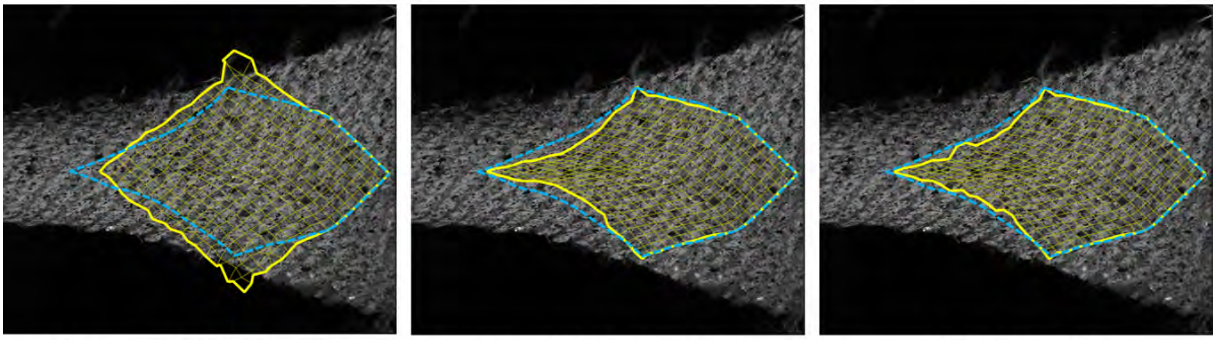

(g) General DIC-FE algorithm. (h) Unconstrained DIC-FE iterative algorithm. (i) Residual < 3%.

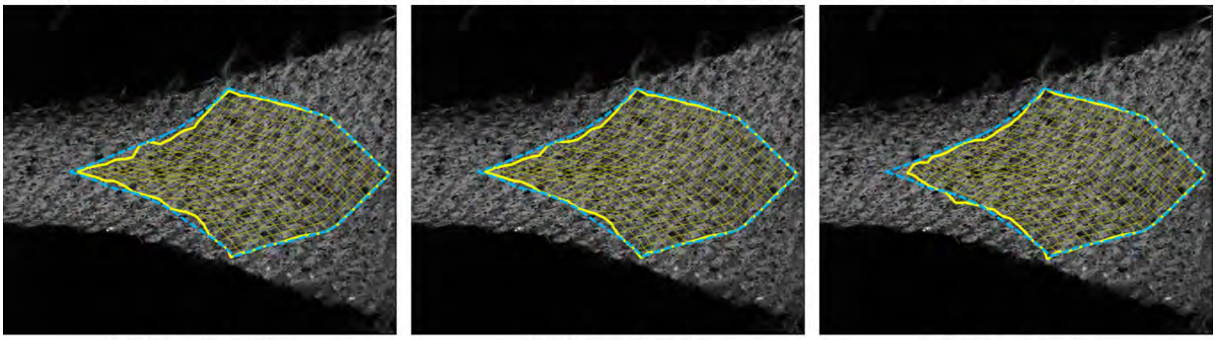

(g) Residual < 4%. (k) Residual < 5%. (l) Residual < 6%.

Figure 3.15: Bias extension test on a glass fabric. Comparison between the "real" displacement field (blue dotted line region - visually identified) and the FE-DIC displacement field measured by different methods (yellow meshes).

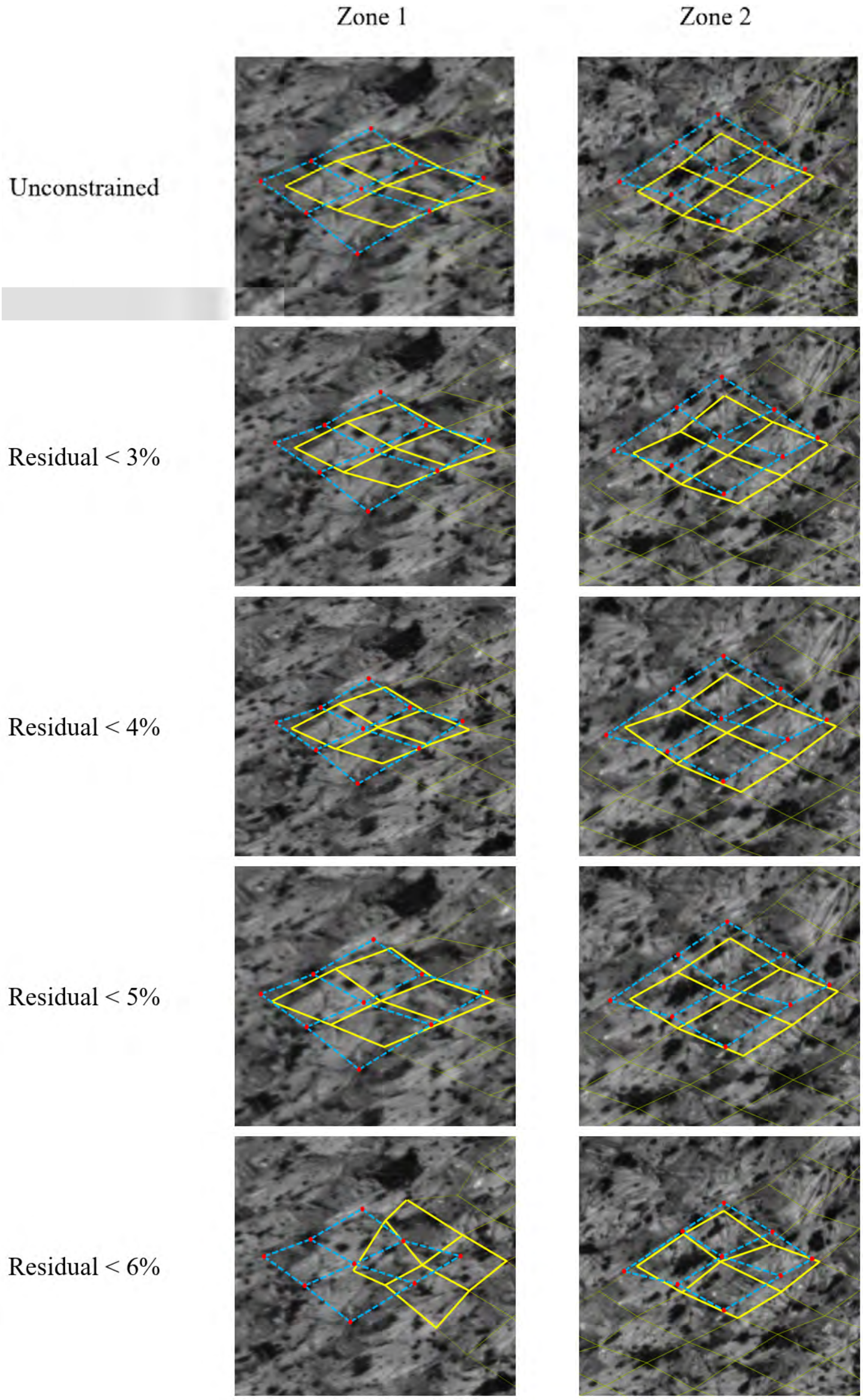

Figure 3.16: Bias extension test on a glass fabric. Comparison of the displacement field measured by the different incremental FE-DIC approaches proposed with the "real" displacement field in zone 1 and zone 2.

Zone 1 :

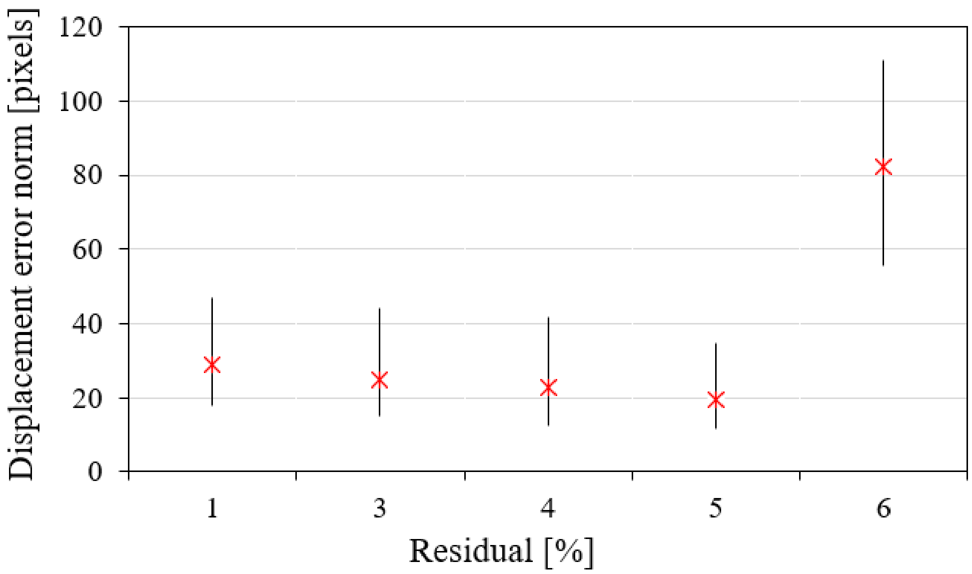

Zone 2 :

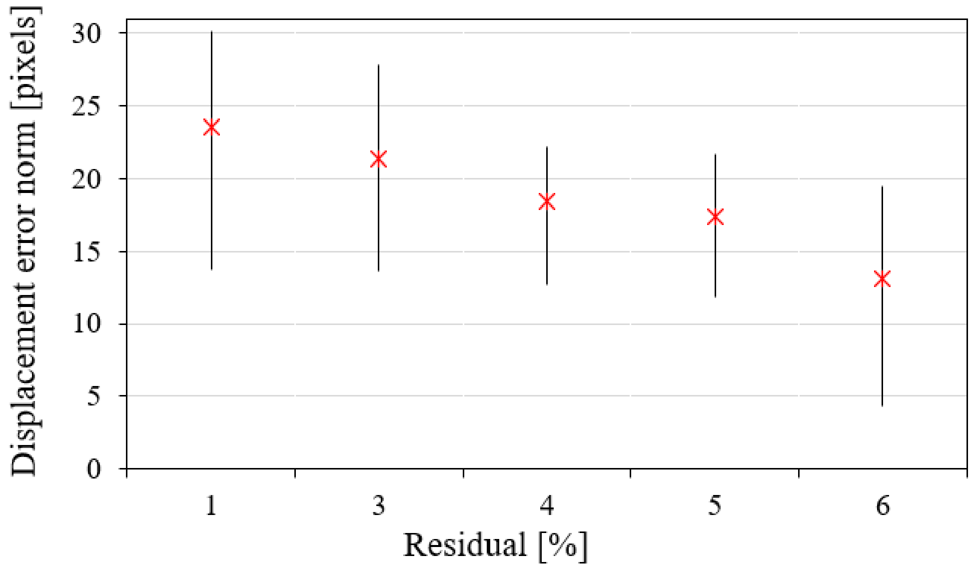

Figure 3.17: Bias extension test on a glass fabric. Average of the vector norm between nodes of the measured deformed mesh and their "real" (visually identified) homologs in zone 1 and zone 2 for different thresholds.

Fig.3.16 presents a local comparison of deformed meshes obtained by FE-DIC and visual tracking in regions 1 and 2 for different R thresholds. This zoom facilitates the observation of the effect of this parameter on the measured displacement field. It is observed that as the value of the constraint conditions increases, the calculated results correspond more closely to the actual displacement field. Similar to the conclusions obtained from the macroscopic approach, when $R < 6\%$, the obtained displacement field fails due to the excessive error caused by the large deformation between the reference and deformed images. Therefore, as shown in Fig.3.16, when the threshold on R is set to 5%, the measurement error appears to be minimal.

To better describe this trend and to identify the most appropriate constraints on the residuals, the parameter proposed at section 3.2.1 is reused: it is proposed to calculate the average of the standards of the vectors connecting the nodes of the measured deformed mesh and their "real" positions (by visually tracking the points). Fig.3.17 makes it possible to follow the evolution of this average displacement error as the constraint on R increases. In addition to the results corresponding to the 4 thresholds already studied (3, 4, 5 and 6 %), we find results for a threshold of 1 %. In fact, as shown in Fig.3.11, the residual values of two adjacent images are in the range [1, 1.06], which explains why the unconstrained incremental FE-DIC algorithm is considered here as an incremental approach with a constraint on R less than 1%. If the measurement error initially decreases in the 2 regions studied, the analysis of the results confirms that R must be kept below 5%.

An intermediate conclusion at this stage is that the measurement of a displacement field by incremental FE-DIC makes it possible to significantly reduce measurement errors in the presence of large deformations. The solution adopted consists in using the correlation residual R as a threshold triggering the updating of the reference image. In this case, it seems that 5% is a good precision-efficiency compromise. We now propose to apply this method to study other fabrics in large deformations.

3.2.3 Incremental FE-DIC displacement field measurement in C/PPS fabric

We now study namely a C/PPS fabric. In this case, we know that new problems such as specular reflections are likely to make our task even more difficult. Fig.3.18 shows the force vs displacement curves recorded during two bias extension tests on C/PPS fabrics. The C/PPS fabrics can be elongated more than the glass fabrics because the C/PPS yarn is woven using the fiber commingled and co-wrapped commingled techniques. The gap between adjacent yarns is greater than that of the glass fabric, resulting in a greater elongation. In this study, the displacement field of the 200th image, when the sample is stretched by 34mm, is analyzed.

Regarding the bias test of C/PPS fabric for locating the displacement field, it is evident from Fig.3.19 that the general FE-DIC algorithm fails before the stretching length reaches 34mm. The failure region remains concentrated in the semi-shear and pure shear zones. However, the unconstrained FE-DIC incremental algorithm performs well in tracking the displacement field, as depicted in Fig.3.20, showing accurate results. Nevertheless, residuals are important.

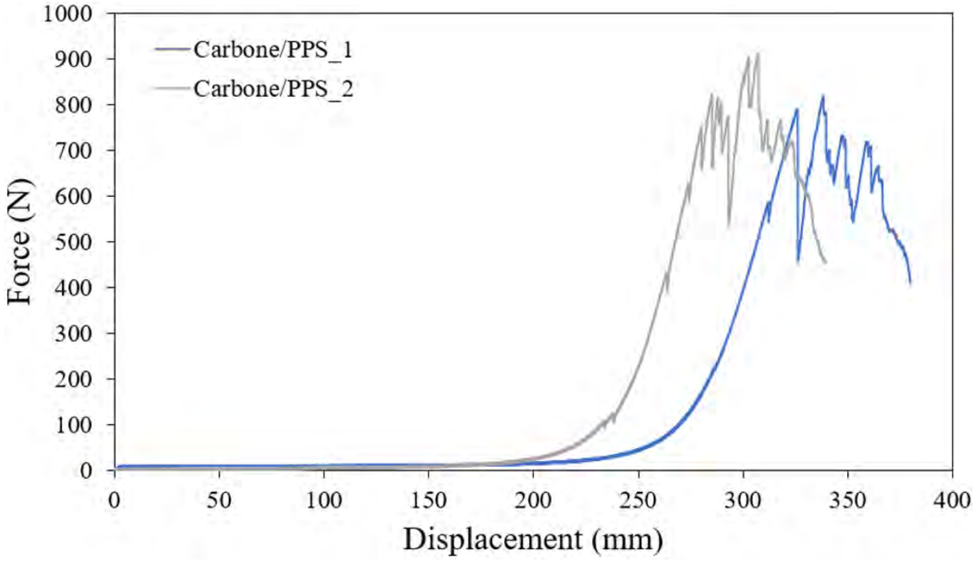

Figure 3.18: Force [N] vs Displacement [mm] curves recorded during two bias-extension tests performed on C/PPS fabric samples.

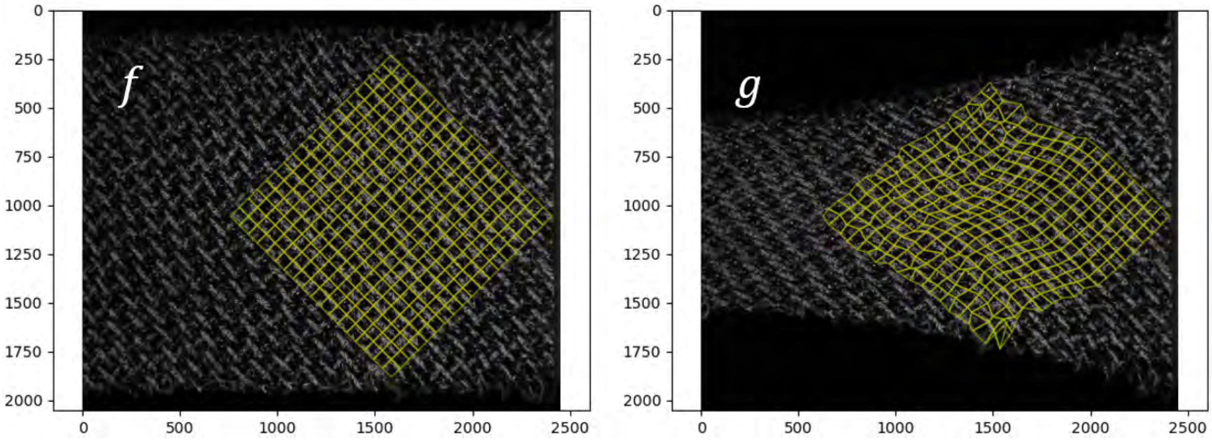

Figure 3.19: Result of a "classical" FE-DIC analysis on a C/PPS fabric. Reference and deformed mesh superimposed on reference image f (left) and deformed image g (right - 34 mm stretch).

By adding constraints to the algorithm for tracking the displacement field, improved results were achieved, as shown in Fig.3.21. In this figure, the displacement field was measured without constrain or with residual as constraint as it was propose on the glass fabric. The tracking of the C/PPS fabric displacement field with the new algorithm is similar to analyzing the kinetic motion of the glass fabric. The obtained displacement field closely corresponds to the real situation as the associated residual R, which serves as a constraint, gradually increases. This trend is evident in Fig.3.22, on which we can see the evolution of the average modulus in function to the residual R parameter. Effectively, the average modulus decreased this the residual R, when it is less than 5. However, when the value of R exceeds a certain threshold (in this experiment, the specific value is 6), the algorithm fails due to excessive deformation, resulting in increased measurement errors. Therefore, it can be concluded that the new algorithm is highly effective in tracking the

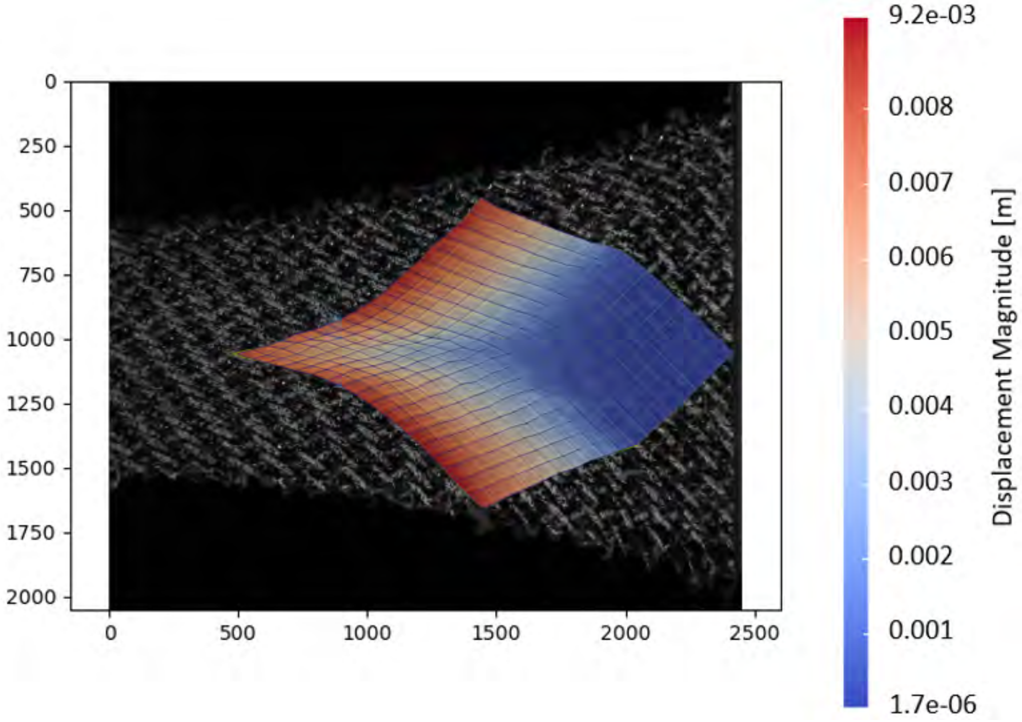

Figure 3.20: Deformed mesh and displacement field along the load axis measured in a C/PPS specimen by unconstrained incremental FE-DIC, plotted by ParaView.

displacement field of the fabric and significantly reduces computational errors caused by large deformations.

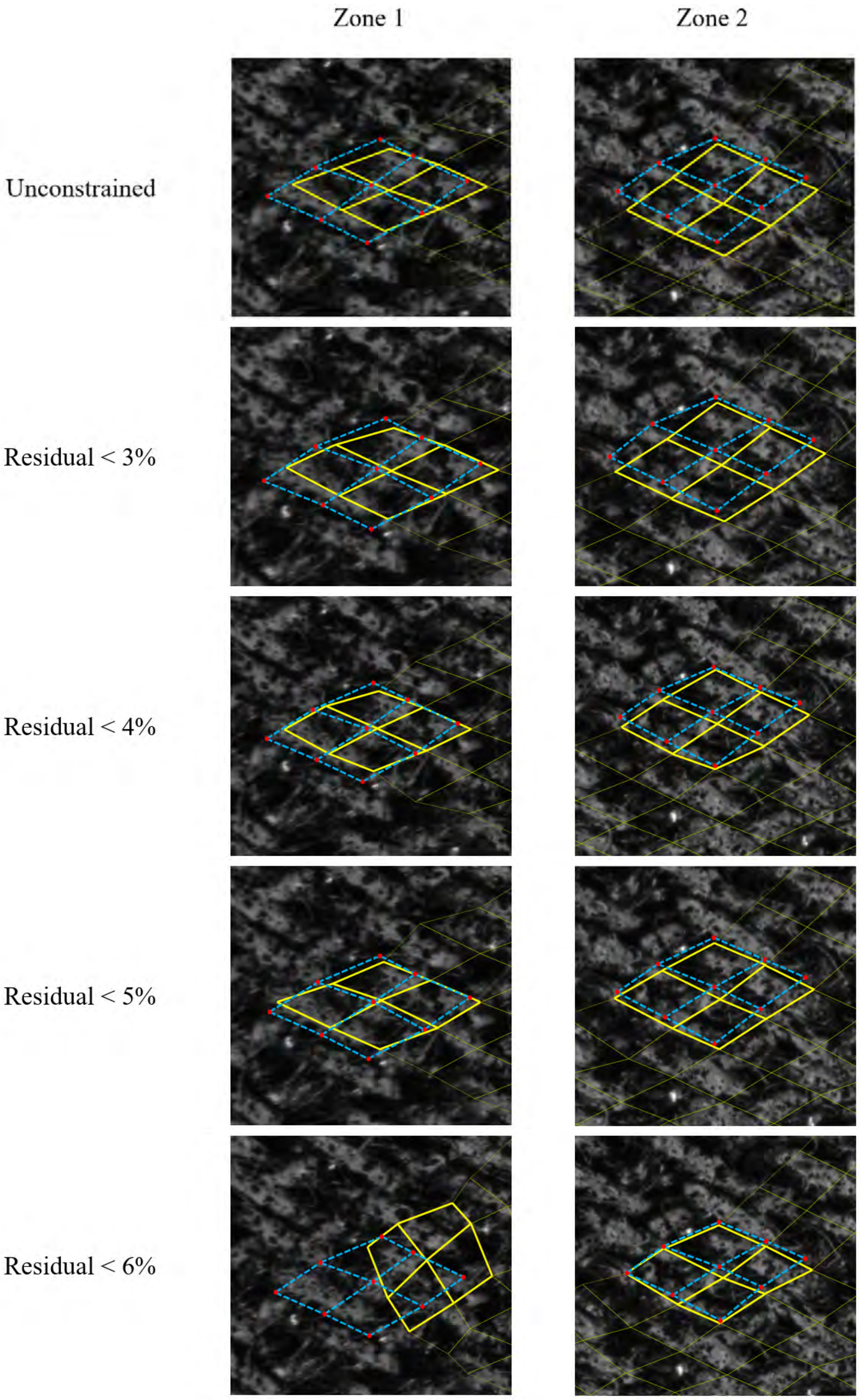

Figure 3.21: Bias extension test on a C/PPS fabric. Comparison of the displacement field measured by the different incremental FE-DIC approaches proposed with the "real" displacement field in zone 1 and zone 2.

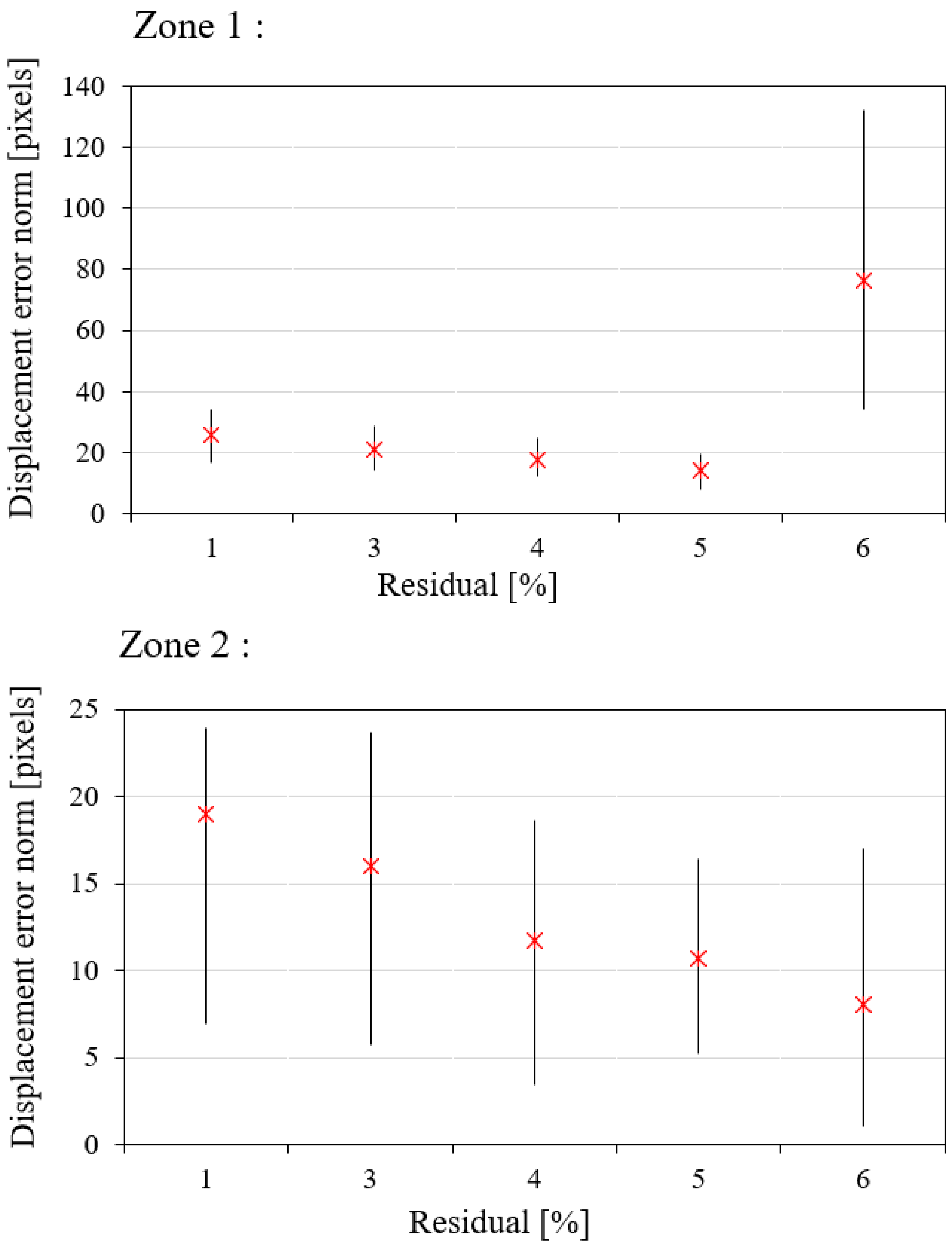

Figure 3.22: The average modulus of the vectors between the mesh nodes and the actual positions for C/PPS fabric sample in zone 1 and zone 2 for different limits.

3.3 Application example: Mechanical behavior of carbon fabrics under the action of shear forces

The shear deformation of carbon fabrics under tensile load is more complex compared to glass fabrics, and the defects that can be observed are more pronounced. This is attributed to the physical properties of carbon fabric and its weave structure. Carbon fabrics have a smooth surface, which causes reflection issues and poses challenges in measuring the displacement field accurately. The shear deformation of carbon fabric can be studied through bias extension tests, where the sample is subjected to tensile forces resulting in three distinct zones: no shear zone (zone A), semi-shear zone (zone B), and pure shear zone (zone C). The defects that occur in the carbon fabric during the experiment are often concentrated along the partition line of these regions.

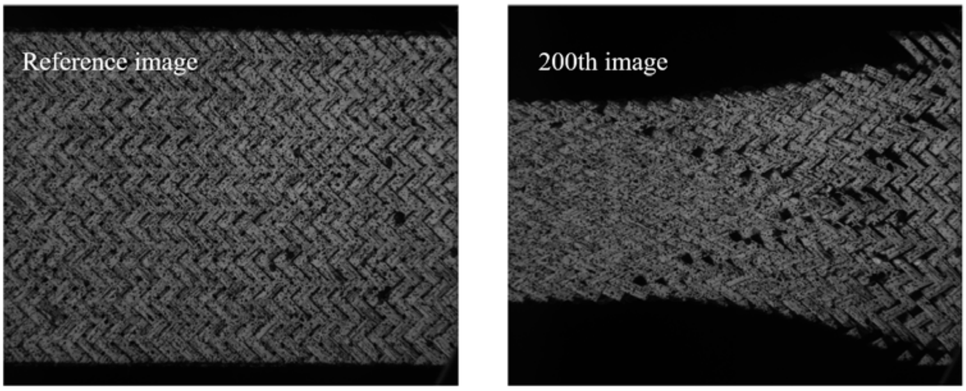

Figure 3.23: Bias extension test of a carbon fabric sample: reference image (left) and 200th image (right)

Fig.3.23 displays the reference image and the 200th image obtained during the bias test on the carbon fabric. A comparison of the two images reveals that, as the experiment progresses to a certain stage, yarns start to pull away at the boundaries of the regions due to differential forces acting on them in the three zones limit. The yarns at the border exhibit different kinematic behavior compared to the yarns in the three regions, resulting in a more complex deformation pattern. This complex kinematic behavior is particularly obvious at the intersections of the three regions.

Fig.3.24 illustrates that tracking the displacement field on the surface of the carbon fabric through calculations is challenging due to the presence of huge inter yarns movements, particularly yarns that have pulled off at the boundaries. The main reason for this difficulty is that, in the woven and layered structure of the fabric, some yarns are not exposed to the surface of the sample. Moreover, during the process of applying scattered speckles, only the surface of the fabric is typically coated, while the yarns in the lower layers retain their strong reflective properties. As a result, during the experiment, the areas where defects occur may cause lower yarns to come to the surface, leading to a significant alteration of the original surface layout. This irreversible transformation hinders the tracking of the displacement field on the surface. These defective areas are also clearly visible in the residual map shown in Fig.3.24. Furthermore, it is evident that the main errors in the calculated displacement field are concentrated in these reflective regions.

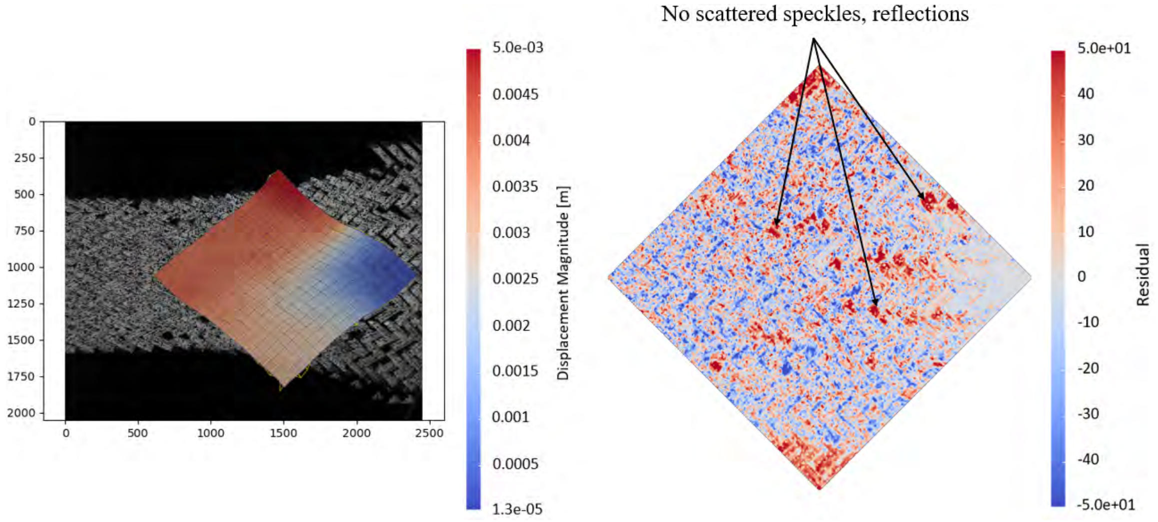

Figure 3.24: Bias extension test of a carbon fabric sample. Displacement field in the direction of loading measured by "classical" FE-DIC and corresponding residual map.

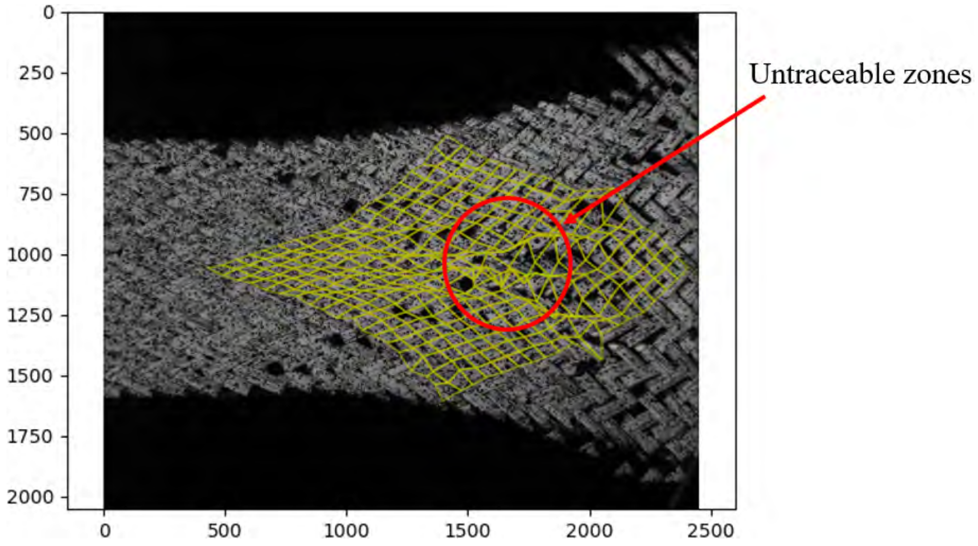

Figure 3.25: Deformed mesh given by incremental FE-DIC with an update constraint based on correlation residuals ($R < 5\%$).

The FE-DIC incremental algorithm with residuals as constraints has proven effective in reducing computational errors arising from large deformations, as demonstrated in Fig.3.25. However, errors resulting from experimentally induced defects are challenging to eliminate using this method. In regions where the fabric has defects, nodes may struggle to accurately identify corresponding points using the algorithm. This is obvious in Fig.3.26, where the algorithm fails to accurately track the displacement field in the defective area due to the substantial measurement error caused by sample-generated defects during the experiment.

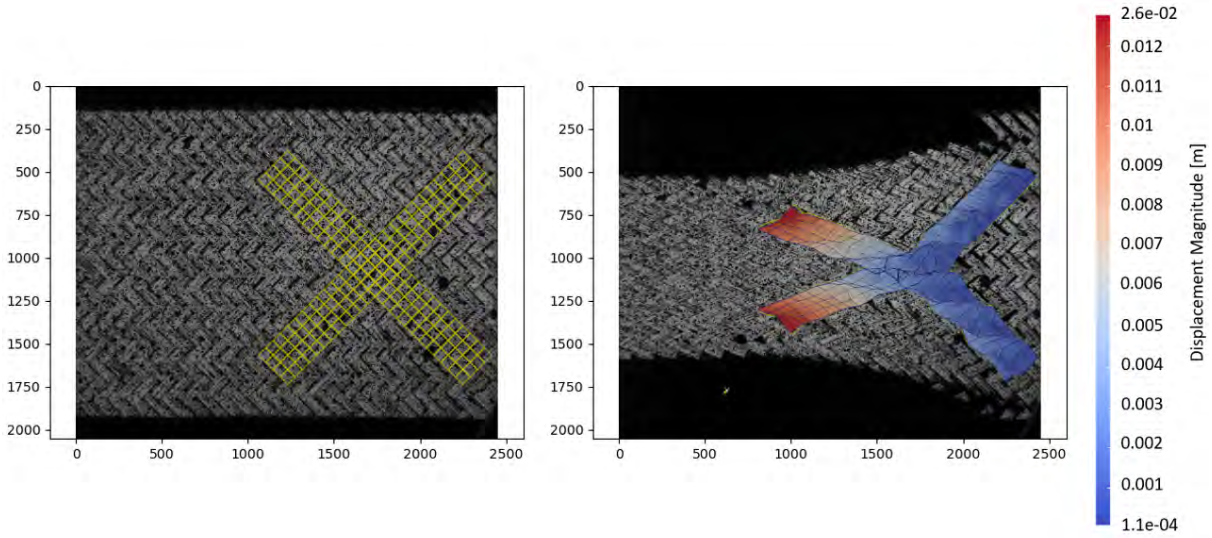

Figure 3.26: Tracking of the displacement field in the area where the defect occurs.

3.4 Discussion

When using the FE-DIC algorithm to track the shear deformation of textile reinforcement, two main sources of measurement errors were identified:

- large deformations
- complex kinematics between yarns

The majority of defects observed during the preforming of textile reinforcement materials can be attributed to this intricate mechanical behavior between the yarns. The measurement error arising from large deformations can have a significant impact on the study of defects in the fabric forming process, thus reducing the measurement error of the deformation field is of great value.

It is widely acknowledged that FE-DIC has strong tracking ability for moderate deformations. When the deformations are small, it is the resolution of the FE-DIC which poses a problem. When the deformations are large, in addition to the poor representation of the kinematics, the very hypothesis on which the technique is based is questionable (can we just write the conservation of gray levels to find the displacement?). In this work, we proposed a method for transforming the large deformation problem of textile into multiple moderate deformation problems, using glass fabric and testing it on C/PPS fabric. We explored a way to reduce measurement errors by optimizing the operation mode of FE-DIC. In contrast to the general FE-DIC algorithm (e.g. based on the cross correlation product to evaluate the decorrelation Pan et al. (2012)), our approach uses the correlation residual R as a constraint. When R becomes greater than a specific value, the calculated displacement field is used as the initial value for the next operation, and the deformed image of the previous operation is defined as the reference image. The effectiveness of the FE-DIC incremental algorithm was confirmed through both macroscopic and local detailed observations, ensuring both the correlation between the calculated displacement field and the initial reference image, and greatly improving the ability to track the displacement field.

The incremental FE-DIC algorithm is more efficient, but this method still has its limitations. This method mainly reduces measurement errors caused by large deformations and cannot completely eliminate measurement errors caused by complex kinematics (yarn rotation, slippage, wrinkling, etc.) or texture changes (whether related to speckle degradation, reflections, relative movements, etc.). The analysis of the results for the carbon fabric shows the way to go to measure the displacement field correctly at the end of the test in the transition regions. Modifications of thresholds cannot compensate for the lack of kinematic description. In these regions, significant shifts and rotations between warp and weft yarns are observed. To date, few studies have been able to bring these movements to light. To enable metrological studies in such regions, it therefore seems necessary to work on new descriptions of kinematics ("conformal mesh") and speckle generation.

The main limitation of this study is that the "real" data is obtained by "visual" tracking. In addition to stains, "visual" tracking exploits knowledge of the architecture of the fabric. This task, eminently time-consuming and very texture dependent, is not conducive to a generalization of the proposed methods.

3.5 Conclusion of the chapter and outlook for the future

In this chapter, bias extension tests performed on glass fabrics and C/PPS fabrics are used, and images acquired up to very high macroscopic strain levels are exploited to measure the diplacement field. As expected, it is observed that the traditional FE-DIC method cannot follow the displacement field correctly in any case. Incremental approaches to FE-DIC have been proposed to reduce measurement errors induced by large deformations. It is proposed, rather than updating the image and the mesh at each step, to wait for the correlation residual to reach a predefined threshold value. Encouraging results were obtained for bias extension tests on glass fabrics and C/PPS fabrics. A threshold set at 5% seems to give the most satisfactory results in these cases.

The research presented in this paper greatly reduces the measurement error in tracking the displacement field. It provides strong theoretical support for studying the mechanical properties of textile reinforcement and for further improving the performance of composite materials after molding. The calculation errors caused by large deformations could be further reduced by optimizing the speckling and by improving the resolution of the device.

However, and despite all our efforts, the differences observed between the results provided by the FE-DIC and the displacement field actually observable, remain significant at the highest deformation levels. In addition, all the results obtained are based on references obtained by visual tracking which does not allow generalizations.

Here again, synthetic data such as those generated in Section 2.3 would be welcome to propose a convenient setting for a given speckle. Above all, this work strengthens our conviction that our idea of moving towards regularised measurement using a model of the architecture (Rouwane et al., 2023b) of the material would be a real way forward.

To achieve these further research objectives, in the following chapter we propose using X-ray tomography to both model the tissue and study its deformation *in situ*.

CHAPTER 4

Study of the deformation of a textile reinforcement at the yarn scale: towards the assimilation of visible and X-ray image data

Sommaire

Background: *The implementation of an experiment/simulation dialogue down to the yarn scale requires a good knowledge of the architecture of the fabric and an adaptation of the measurement. An image data assimilation approach associated with an in situ test conducted in an X-ray micro tomograph could constitute an ideal framework for this, and eventually allow the identification of constitutive parameters.*

Objective: *In this section, we propose to set up the main ingredients of such an approach and to show its feasibility in the case of a miniaturized in situ bias extension test.*

Methods: *A specific sample preparation procedure is proposed. As in previous chapters, a frame (which also acts as tabs) is again used to stabilize the fabric during handling and to simplify the mounting of the sample. Under conditions similar to those that will be encountered during the in situ test, the satin glass fabric samples are first scanned. Once segmented, the resulting images are used to build digital image-based models (DIB) in TexGen. The most representative model is then used to simulate a mini-bias extension test. An in-situ tensile machine is then used to test this type of miniature specimen. This machine is specially designed to accommodate the large displacements expected in such experiments. In this machine, tests on specimens, both speckled and unspeckled, are first performed ex situ. They were aimed at validating the design of the machine and specimens, evaluating the effect of the patterning technique, anticipating the experimental protocol in situ and defining the different load levels at which tomographies will be acquired. Surface 2D FE DIC measurements are performed on speckled samples. Finally, an in situ bias extension test is performed. A reference scan of the fabric is acquired at rest. It is segmented and used to "directly" build a DIB model. 3 further scans to follow the deformation of the fabric are taken at different stages of loading. First analyses concerning the evolution of the architecture and an attempt to measure FE DIC based on radiographs are proposed.*

Results: *The preparation of the sample fulfilled its mission perfectly. The in-situ tensile testing machine has given us full satisfaction. A 2D displacement field of the surface of the speckled fabric could be measured by image correlation ex situ through the PMMA tube by means of a telecentric lens. For the samples considered, the deposited speckles have a significant influence. Under the experimental conditions presented, μCT can perfectly be used to retrieve the architecture of such fabrics down to the yarn scale and to build relevant DIB models. The developed tensile testing machine combined with the proposed specimen preparation allows for in situ bias extension tests up to significant deformation levels. The DIB model generated here directly from the segmented image does not capture the architecture well. This underlines the interest of the work proposed above.*

Conclusions: *Multi-instrumented in situ bias tests are perfectly feasible in X-ray micro computed tomography. The joint exploitation of volume images and surface images collected should make it possible to improve the measurement of the complex kinematics of fabrics. The idea would be to use global image correlation to carry out architecture-assisted measurements. However, the speckle deposition procedure could be rethought (to limit its effect on the mechanical part), the type and size of samples could be adjusted and the cutting improved. Finally, the optical instrumentation inside the tomograph needs to be developed.*

The use of X-ray micro computed tomography (µCT) has become widespread in research laboratories and industries. It has established itself as an essential tool in the study of materials and structures. This imaging modality has been widely used in particular for the characterization of composite materials. Uses range from initial defects and damage characterization (Schilling et al., 2005; Mendoza et al., 2019) to architecture studies (Desplentere et al., 2005; Requena et al., 2009), including Digital Image Based models generation (Delerue et al., 2003; Czabaj et al., 2014; Naouar et al., 2015; Sencu et al., 2016; Mazars et al., 2017; Sinchuk et al., 2019; Ai et al., 2021). *In situ* tests have been developing over the past twenty years (Buffiere et al., 2010), including for investigating the manufacture (Vilà et al., 2015; Larson and Zok, 2018) and the behavior (Schilling et al., 2005; Moffat et al., 2008; Scott et al., 2011; Chai et al., 2020) of long fiber composite materials. µCT thus appears to be an invaluable element for studying effect of defects (Wang et al., 2018a). If *in situ* testing often require complex compromises (weight and footprint, loading, region of interest, image definition, etc.), it has the advantage of not requiring delicate assembly/disassembly of the sample. By making it possible to keep the sample loaded, they make it possible in particular to examine damage processes in detail (the cracks remain open). Only a few works report the use of digital volume image correlation (DVC (Bay et al., 1999)) with (Brault et al., 2013; Gomes Perini, 2014; Schöberl et al., 2020) or without (Mazars et al., 2017; Mehdikhani et al., 2021) the introduction of additional constrast particles to access information on internal damage and kinematics.

Concerning more precisely the study of the behavior of fabrics, µCT has already enabled great progress. It allows in particular to investigate the actual geometry (Desplentere et al., 2005), to build more representative models (Green et al., 2014; Naouar et al., 2015; Blusseau et al., 2022; Ali et al., 2022) and even to validate partly meso models (Barburski et al., 2015) by scanning deformed sample. However, few studies report analyzes of *in situ* tests (Yousaf et al., 2021), and, to our knowledge, no 3D measurements at this scale has been reported to date. The measurement of 3D displacement fields by DIC at the fabric architecture scale, in particular in the presence of large deformations, faces major pitfalls. As presented in (Lomov et al., 2008) for 2D measurements, one can speckle the sample and try to monitor its deformation by reducing the field of view and performing a dense stereo DIC on both sides. However, these measurements would still be complicated to link to the actual deformation of the yarns. If we rather try to retrieve the displacement on a reduced kinematic basis (for example, by relying on an element covering a unit cell during a FE approach), a usual interpolation will not be able to represent all the complexity of the deformation of the cell (cf. 2D studies: see chapter 3). Moreover, visibility (for example, a part of the speckle masked following the movement of a yarn) and lighting issues are expected. The latest work at ICA on stereo digital image stereo correlation, namely Photometric DIC (Fouque et al., 2022), would potentially allow to alleviate some of the identified issues. Another avenue being considered would be to conduct an *in situ* bias test in a µCT and to use DVC to assess 3D volumetric displacements. The reference image would provide valuable information for a digital image based (say FE) modeling. The images collected would allow to characterize the geometry of the fabric at various stages of its deformation. However, the texture (anisotropic at least) present in such images would not allow to retrieve a displacement field in the yarns. One solution might then be to use a mechanical model to regularise DVC (Rouwane et al., 2022, 2023b). The work presented hereafter aims at initiating an approach which would consist in exploiting jointly photometric DIC (Fouque et al., 2022) and architecture driven

DVC (Rouwane et al., 2023b) during the very same *in situ* test.

In what follows, we therefore put in place the essential ingredients that would make it possible to jointly grab tomographic and surface images during an *in situ* mechanical test to identify some constitutive parameters of a meso (FE) model. At first, the point is to make sure that the selected material, the sample and its environment enable exploitable images for the construction of digital image-based models (DIB) to be obtained. In a second step, the main building blocks that allow to perform an *in situ* bias extension test in a µCT are presented. The final section presents the initial results of an *in situ* test carried out in a lab CT.

4.1 Feasibility of image-based model construction

In this section, we first propose to scan samples under conditions close to those that will be encountered for the *in situ* bias extension test. These first CT scans were actually taken before the test machine was finalized. The fiberglass fabric studied in chapter 2 (5-harness satin weave) is here selected. The higher X-ray attenuation coefficient of glass fiber (compared to carbon fiber) and the large cross-section of the yarns (yarn width close to 1.25 mm), which facilitate the observation of the architecture by CT scan, are the main reasons for this choice. The width of the gage region of the future coupon must be small enough to obtain a satisfactory image (for cone beam microtomography, the smaller the diameter of the machine - and therefore the sample width - the better the resolution) and large enough to ensure that the test carried out is representative (the wider the sample, the greater the number of unit cells involved). The width of the specimen is later set at 20 mm. This means that, in this case, the sample contains just over 2 unit cells across the width. The gauge length is then set at 60 mm to maintain the same aspect ratio as in the previous chapters. Even more than in the tests carried out in the previous chapters, preparing the sample, handling it and placing it in the scanner and then in the *in situ* machine (see next section), are a real challenge. We therefore first propose to sandwich again the sample in between two frames. It is then proposed to verify that the architecture of the glass fabric can correctly be resolved by X-ray tomography. Then, from these images, we will try to develop the first models based on the image. Here we will follow a classic approach. We will first segment the image so as to identify each yarn. Then we will use the segmented images to build the model of a unit cell using an *ad hoc* tool.

4.1.1 Preparation of samples

As mentioned earlier, we are here adopting the same type of "frame" as was used in the previous experiments. The idea is to maintain the correct orientation/position of the fibres when handling the small and fragile samples, but also when placing them in the CT, and later in the machine. The main difference is the type of material used to make the frame. We use cardboard rather than a metal frame to avoid the reconstruction artefacts that would result. The side posts are cut after the jaws have been clamped to free the fabric, while the upper and lower parts act as tabs.

Contrary to what was done in the previous chapters, and due to a lack of time, a rectangular piece of fabric is here pre-cut to the width of the sample to be tested (i.e. 20mm). A simple scalpel is used. The reason for this is essentially linked to the fact that water jet cutting is not viable here. The architecture of the glass fabric simplifies the task of cutting. It is indeed woven with blue glass strands mixed in as auxiliary yarns. The size of the squares formed by these blue yarns is 50 mm × 50 mm. The fabric can therefore be easily planed once flattened, if required, and the pieces of fabric used to make the test specimens can be precisely cut (the aim being to guarantee the orientation ±45° of the warp and weft yarns with respect to the edges). In our case, the sample taken is 90 × 20 mm. A typical cutting pattern is shown in Fig.4.1. Despite all the care taken, the yarns at the edges are frayed. We plan to develop the protocol further in the future. We are considering, for example, testing laser cutting.

The sample manufacturing process here comprises three main steps: (1) Cut the glass

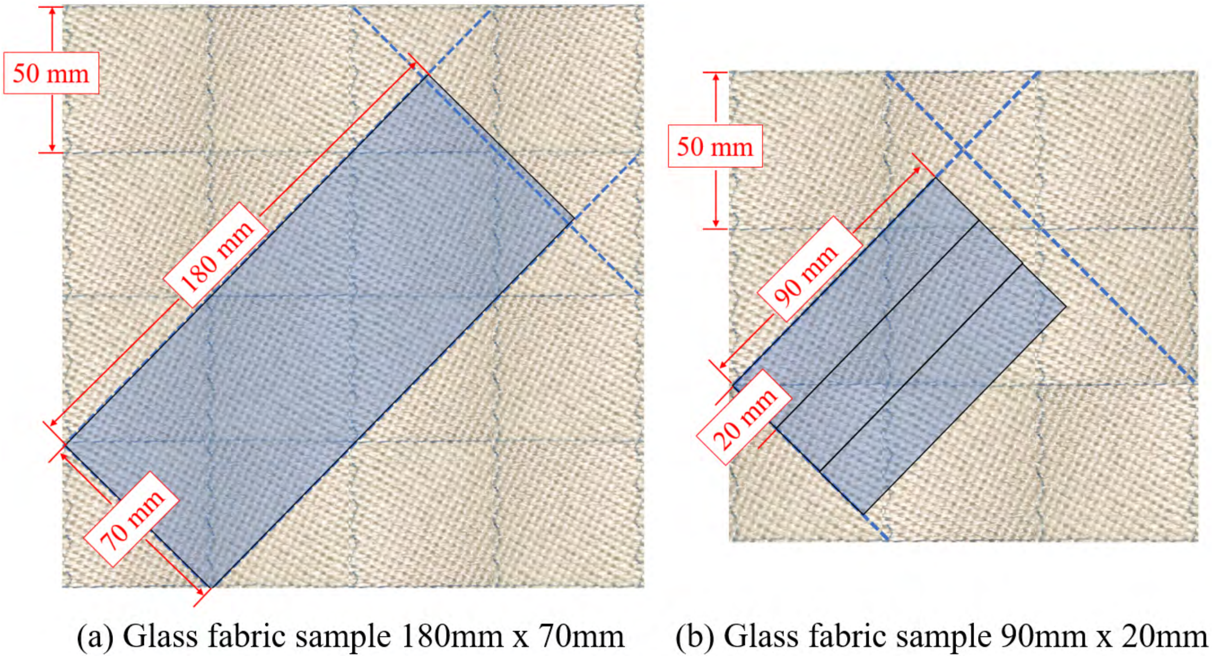

(a) Glass fabric sample 180mm x 70mm (b) Glass fabric sample 90mm x 20mm

Figure 4.1: Glass fabric (5-harness satin weave) from which samples are taken. The blue auxiliary wires are aligned with the yarns spaced 50 mm apart. The rectangles on the left and right correspond respectively to the cutting patterns for the specimens studied in previous chapters and here, in tomography.

fabric as previously described (2) Four cardboard rectangles of 30 mm × 20 mm and two long strips of 90 mm × 4 mm are cut. The glass fabric is sandwiched between the four cardboard rectangles and bonded to them using Araldite 2011 adhesive, as shown in Fig.4.2 (a). Next, the two long strips of cardboard were also glued to the four cardboard stubs on either side of the glass fabric to complete the frame (3) Two rectangles of plastic plate, measuring 60 mm × 30 mm, were cut using a laser cutter and adhered to the long strips of cardboard. This only served to stiffen the specimen to simplify handling (particularly for mounting in the holder), but also to flatten it. Fig 4.2 (a) shows a final sample.

Although the sample is stiffened, the specimen remains too flexible to consider a tomography without additional support. The idea here is to place ourselves in acquisition conditions very close to those of the *in situ* test. A PMMA tube (identical in all points to the tube that will be used in the *in situ* machine - see paragraph 4.2.2.1) with a height of 100 mm was thus cut out and the sample is placed in its center. The inner and outer diameter of this tube are respectively 32 mm and 38 mm. Fig. 4.2 illustrates the two methods that have been tested to hold the specimen. The first, illustrated in Fig 4.2 (a), consists in attaching the sample to plastic plates (1 mm thick) which are taped to the ends of the tube. The second, shown in Fig. 4.2 (b), involves sliding the sample between two parallel sheets of PMMA (1 mm thick), 3 mm apart, previously glued to the inside of the tube. The 2 techniques gave excellent results in terms of stability during X-ray tomography. The second technique proved more difficult to implement.

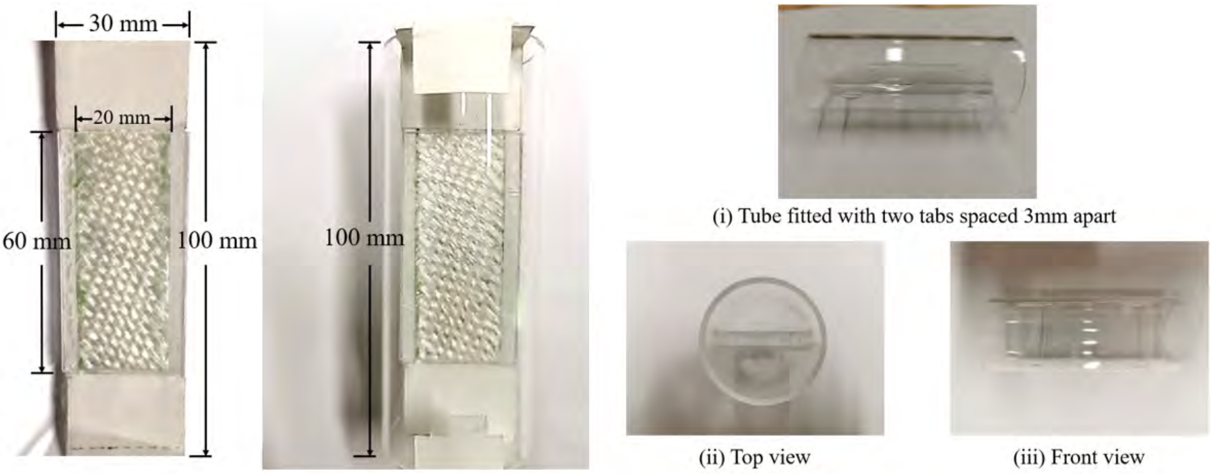

(i) Tube fitted with two tabs spaced 3mm apart

(ii) Top view

(iii) Front view

(a) Schematic diagram of the dimensions of each part of the sample, and the final sample

(b) PMMA tube with clapboards

Figure 4.2: First samples produced to test the manufacturing protocol for future test specimens and produce the first CT scans: a cardboard frame holds the fabric in place. However, the sample are still too flexible for tomography (a tomography scan takes about 48 minutes) without developing a specific support. The idea here is to use the same type of tube that will be used for the frame of the in situ tensile testing machine. Two options have been tested : (a) the sample is held by the ends (b) the sample is inserted between two PMMA tabs, themselves glued to the tube

4.1.2 X-ray micro tomography on glass fabric samples

Fig.4.3 shows the lab micro-CT (RX Solutions Easytom 130 located at the Clement Ader Institute, in Toulouse facilities) that is used. Its main components are: a Hamamatsu 130kV microfocus X-ray source (40 kV to 130 kV - Maximum Output: 39 W), a CsI planar imager (1024 × 1024 px^2, 127 µm pixel pitch), a computer running proprietary software (X-Act 2.0) for controling the X-ray source, the CT axes and collecting radiographs. The X-ray beam emitted by the source is polychromatic, divergent (conical). For such a cone beam CT, the focal spot size plays an important role in the sharpness of the images. The used source proposes 3 possible focusing modes. In the following, we use the large focus mode and the focal spot size is estimated to be around 8 μm (min 5 μm at 4W). Another computer (with graphics cards and huge amount of memory), not visible in Fig.4.3, is used for masked-time reconstruction using proprietary software (UniCT module). It should be noted that the manipulator can support loads of up to 20 kg. The tomograph was also placed in a large radio protection cabin (see Fig.4.3 (a)). As a result, large parts/assemblies can be imaged, and the space available around them makes it possible to simplify the assembly and the development of in situ experimentation.

The samples are mounted in their holders (PMMA tube) on the tomograph's sample manipulator as shown in Fig. 4.4. A simple glue gun is used to immobilize the different elements together. Two acquisitions were made on the same sample in order to obtain two images at different magnifications (ratio around 5): one covering practically the height of the future gauge length (resolution around 47,5 μm/vx), the other one corresponding to a zoom covering just the width around (approximately the lower third of the sample - 10,3 μm/vx). The table 4.1 presents the parameters retained for the tomography. The

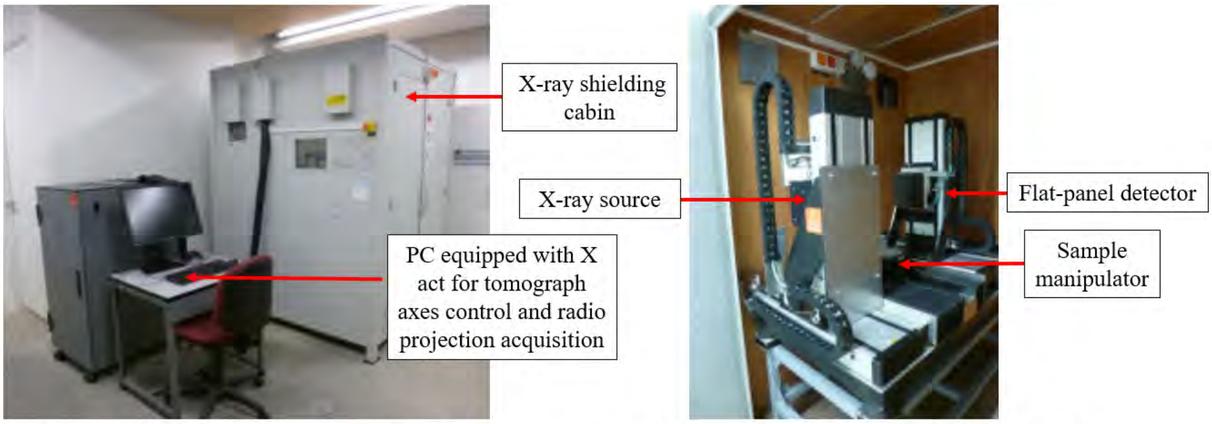

(a) X-ray shielding cabin + PC equipped with X act software for controlling the X-ray source and axes, as well as the acquisition of X-ray projections

(b) Interior of the X-ray shielding cabin. The CT scanner occupies only part of the available space, providing a large volume for in-situ tests

Figure 4.3: RX Solutions Easytom 130 μCT scanning system (located at Clement Ader Institute, Toulouse).

parameters used to obtain the "macro" and "zoomed" images are respectively summarized in the columns identified "Set (a)" and "Set (b)". For both magnifications, volumetric CT images are reconstructed from 1,440 projections acquired when the object is rotated through 360º. In practice, each of these projections corresponds to an average of 8 images acquired at a given angle.

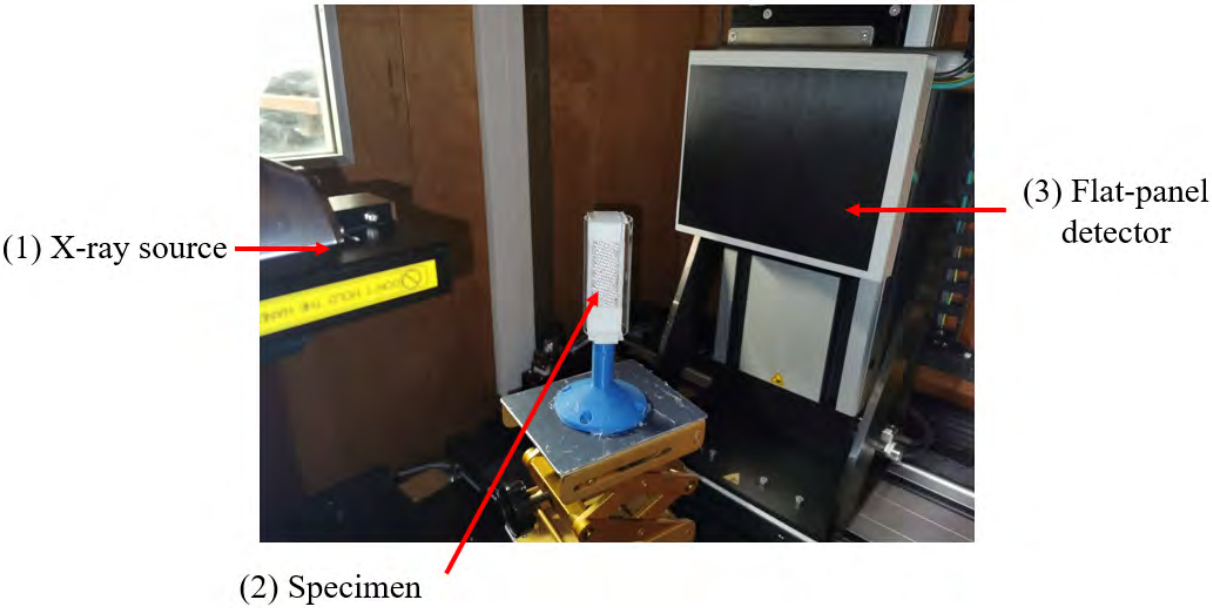

Figure 4.4: Experimental setup for X-ray tomography of the fiberglass fabric sample

At the end of the reconstruction, the UniCt module of the X-act software provides stacks of images spaced one voxel apart. In our case, one of these is a stack of slices in planes roughly parallel to the sample plane. Another stack provides slices in planes roughly perpendicular to the "sample axis". Based on this data, software such as ORS DragonFly or Fiji ImageJ can be used to visualize the volume image, generate further slices and, of course, process the image. The 3D reconstructed images for both resolutions visualised using DragonFly are respectively presented in the upper left of Fig.4.4(a) and Fig.4.4(b) (surrounded by a red frame). New slices are also presented: one generated roughly in the mid-plane of the fabric sample (bottom left) and two perpendicular to this plane and oriented at ± 45° (right-hand column). For information, the diameter of a glass fiber is close to 10 μm/vx and it may be useful to remember that the width of the glass fabric sample is close to 20 mm.

We did not observe any reconstruction artefacts in any of the reconstructed images (which could interfere with segmentation). Fig.4.6 makes it possible to compare in a common zone the two 3D reconstructions obtained. The 2 images make it possible to give a good account of the reality of the architecture of the weaving. Unsurprisingly, the high-resolution image makes it much easier to identify the orientation of the fibers inside the yarns (you can almost guess the individual fibers). In what follows, we will therefore use the HR image to construct an image-based model.

	Parameters	**Set (a)**	**Set (b)**	**Unit**
X-ray focal spot size	Tube power	21	/	W
	Tube voltage	70	/	kV
	Tube intensity	300	114	μA
Imager	Mode	1×1 0.5pF VG1	/	
	Frames per second	4	3	
	Calibration	128	/	
	Digital gain	1	/	
	Rotate/mirror	Normal	/	
	Average	8	/	
Control	Generator H	206.8728	211.8606	mm
	Generator V	-236.0117	0.0000	mm
	Imager H	204.8294	211.8606	mm
	Imager V	-238.0529	2.0412	mm
	Imager Zoom	0.0000	-2.0413	mm
	Rotation	-0.4425	-15.0548	°
	Zoom	0.0000	210.0353	mm
Acquisition	Total number of images	1440	1440	
	Geometrical Zoom	2.67	12.29	
	Optical Zoom	1.00	1.00	
	Voxelsize	47.52	10.33	μm
	Volume height	63.6	13.8	mm
	Volume diameter	86.3	18.8	mm
	Slices	1339	1339	
	Estimated time	0:48	0:48	hh : mm

Table 4.1: Main acquisition parameters for tomography. The data sets (a) and (b) were used to obtain respectively the wide and zoom images shown in Fig. 4.6

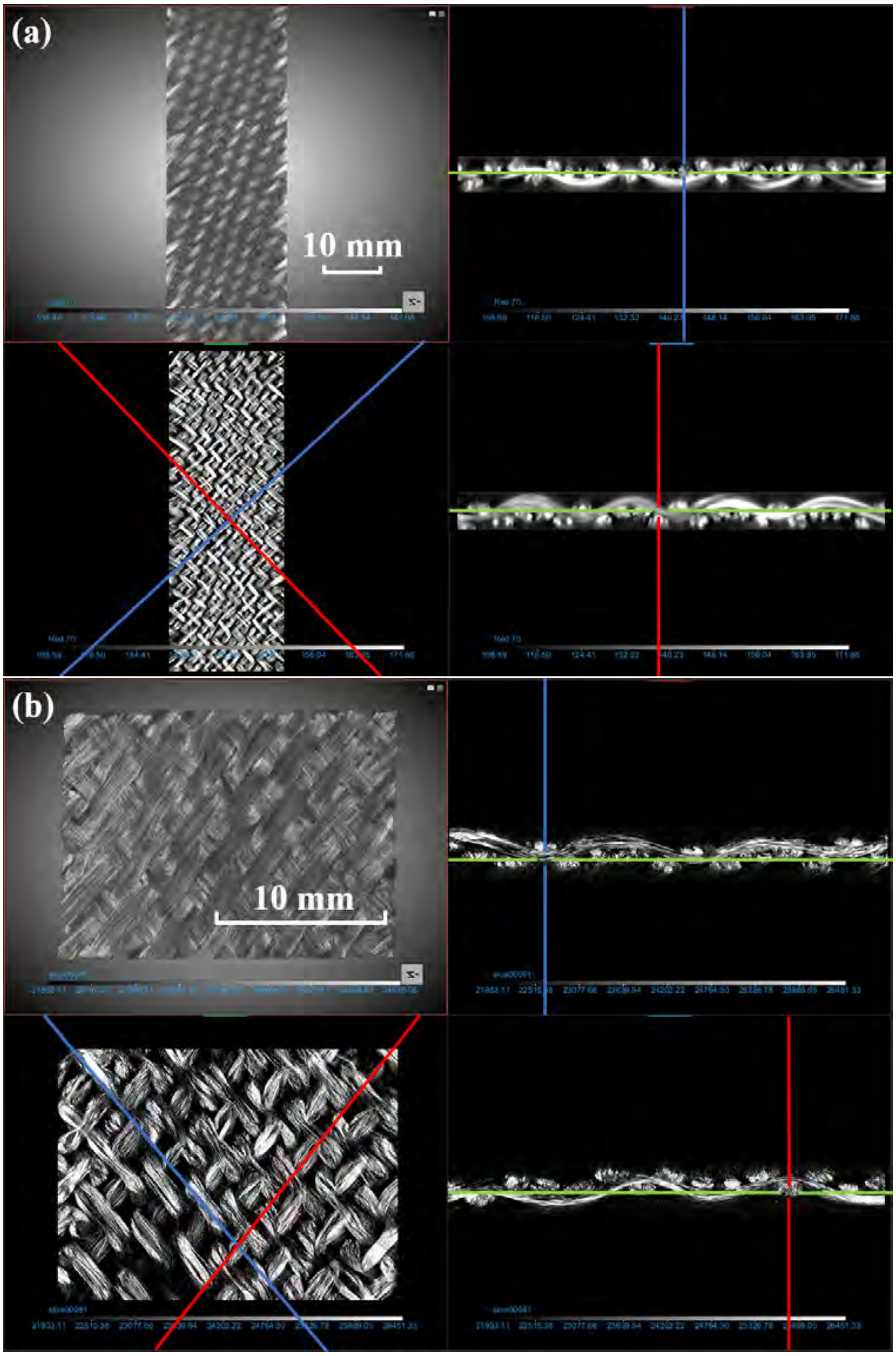

Figure 4.5: Visualization with DragonFly software of reconstructed tomographic images of the glass fabric sample. The image batch (a) corresponds to an acquisition covering a good part of the sample (at approximately 47.5 μm/vx), while the batch (b) corresponds to a zoom on the lower part (at approximately 10.3 μm/vx). For each batch, a realistic 3D rendering of the reconstructed image (top left), a cut in the mid-plane (bottom left), and two cuts in planes perpendicular to the previous one and oriented at 45° to the sample axis are displayed.

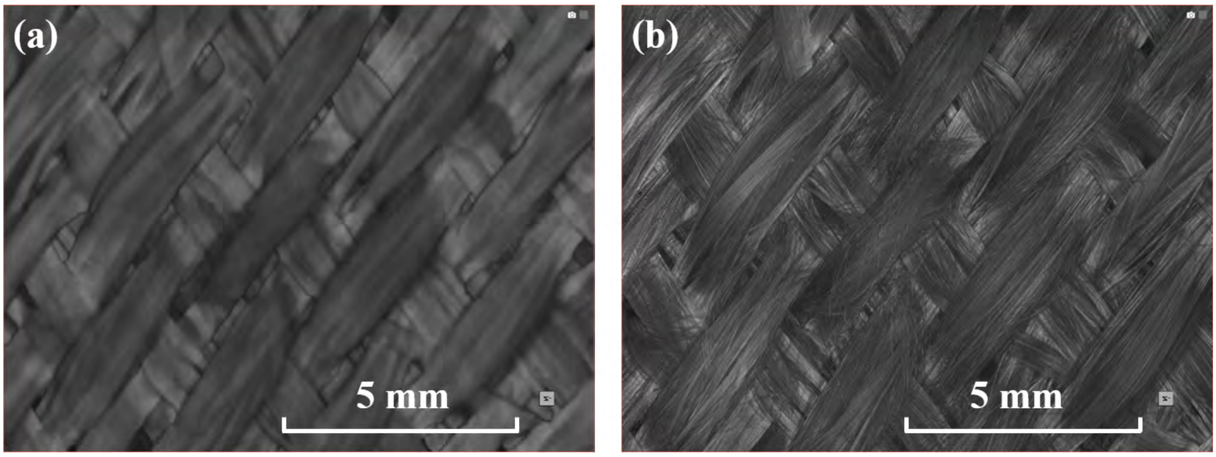

Figure 4.6: Qualitative comparison of volume images reconstructed at resolutions of 47.5 μm/vx (a) and 10.3 μm/vx (b) in a common zone. It shows that tomography at the higher resolution reveals the architecture, and even the fibers arrangement, much better. As a reminder, the glass fibers diameter is around 10 μm.

4.1.3 Image based Meso Modelling of a unit cell

In what follows, the open source software TexGen (Brown and Long, 2021) is used to develop CAD models of the fabric. As a reminder, the studied sample is a 5-Harness Satin weave fiberglass fabric. The warp and weft yarns are woven in the same way. A typical theoretical unit cell for such a fabric is shown in Fig. 4.9(a). Next, we try to model the unit cell shown in blue dotted lines. The width of the yarn is denoted by w. The horizontal distance between adjacent strands is denoted by L. The resulting clearance (gap) is therefore $g = L - w$. According to manufacturer data, we know that the size of the pattern is approximately 6.25 mm, *i.e.* $L \approx 1.25$ mm. We also know the nominal yarn width: $w \approx$ 1,25 mm. The D-D section proposed in Fig.4.9 (b) makes it possible to specify the dimensions h and s of the yarns at the crossings. Here we first assume that $h = s$. If the fabric is considered "almost flat", one can assume that $h = s \approx thickness/2$, *i.e.* $h = s \approx$ 0,65 mm. By providing Texgen with all this information, this handy tool can automatically generate a CAD model of an idealized geometry. This first "naïve" model is presented in Fig.4.7. A qualitative comparison of this model with the tomographic slices presented in Fig. 4.8 clearly shows that this CAD is largely perfectible.

Our objective, in the following, is thus to try to propose a more realistic geometric model of the unit cell using tomographic data. Starting from a high resolution image of our fabric (cf. Fig. 4.8, the idea is thus to extract the key weaving parameters which will make it possible to build new unit cell models still using TexGen (Brown and Long, 2021).

4.1.3.1 Segmentation for extracting key architectural parameters

The architecture analysis proposed thereafter is essentially based here on tracking the evolution of the cross-section of the yarns (in the warp or weft direction) in the reconstructed 3D image. Initially, the mid-plane (in green in Fig.4.5) is positioned as best as possible (halfway between two planes which best frame the fabric). The orientation of the 2 planes perpendicular to the previous (at approximately ± 45° with respect to the

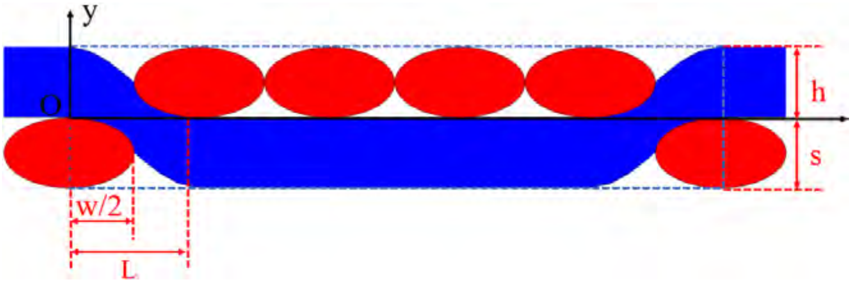

Figure 4.7: The first theoretical CAD model of glass fabric, "naive", obtained automatically with TexGen by providing only a few basic geometric parameters.

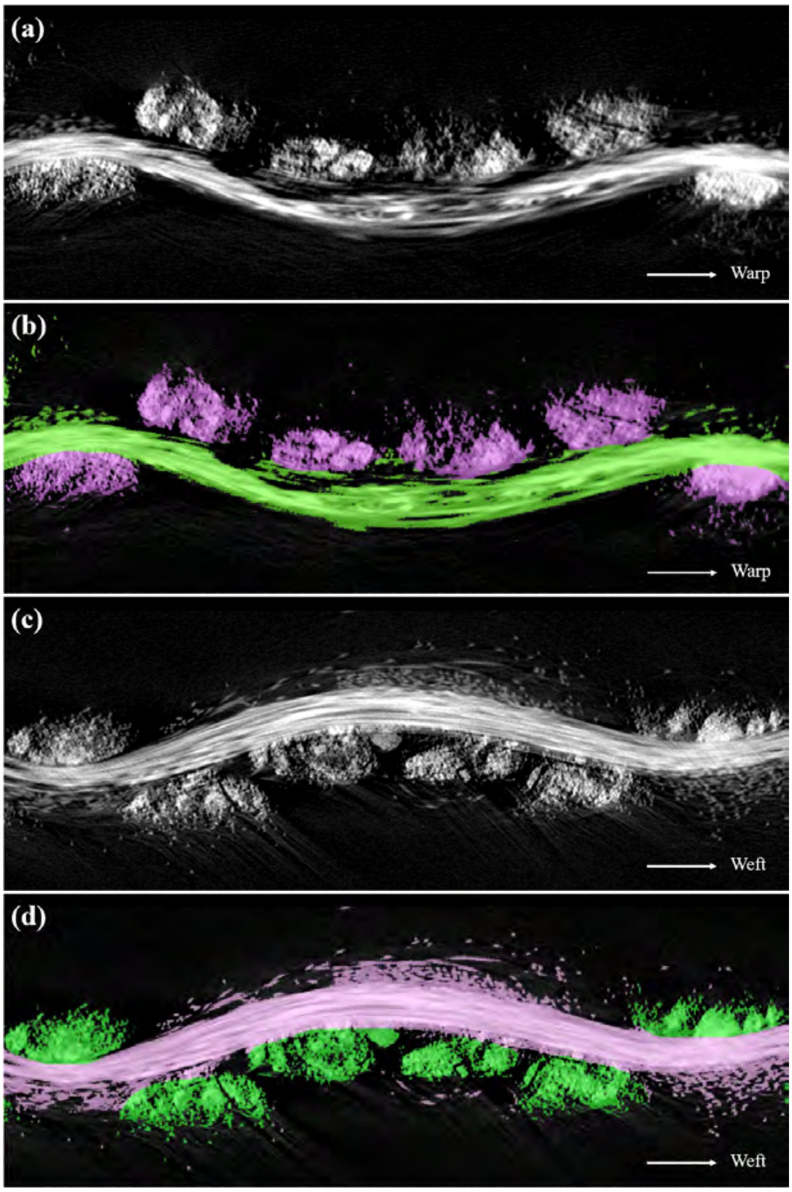

Figure 4.8: Slice views obtained in the warp (a and b) and weft (c and d) direction when the cutting plane passes approximately threw the middle of the yarn. (a) and (c) correspond to raw grayscale images used for sementation; (b) and (d) are the segmented images. Warp and weft strands appear green and purple respectively.

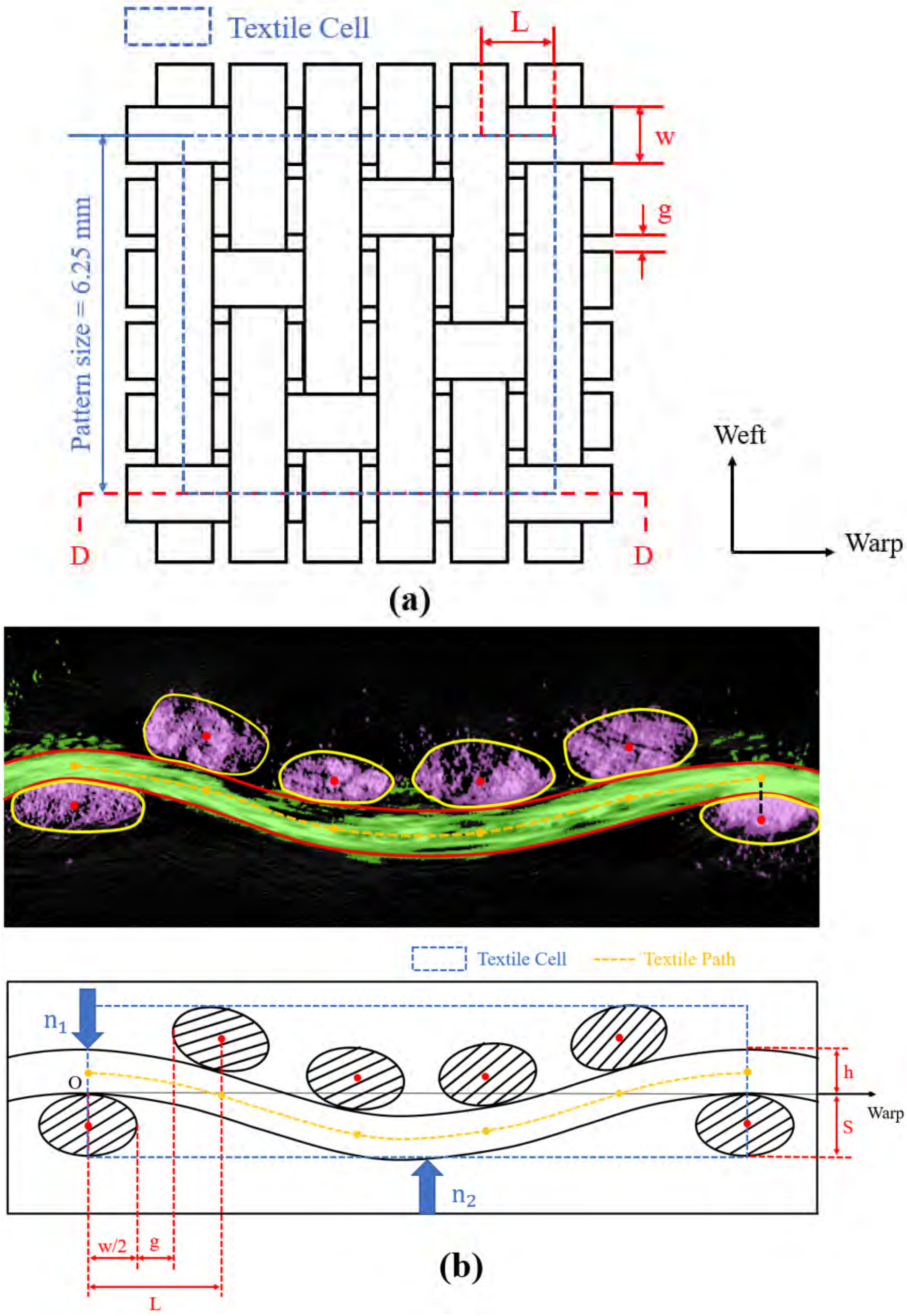

Figure 4.9: (a) Scheme of the studied fabric with the main dimensions useful for modelling. The square area indicated by the blue dotted lines corresponds to a unit cell; (b) DD tomographic slice obtained after segmentation (top) and schematic diagram of the corresponding image-based model (bottom) aimed at

edges of the sample - red and blue lines in Fig.4.5 (b)) is then adjusted so that they were as much as possible parallel to the yarns. Various cross sections are then obtained by translating these planes. For the new Texgen modeling proposed in the next section, it is necessary to extract from those images

1. the master nodes which later allow defining the yarn path. In practice, they are defined where the warp and weft yarns cross (red points in Fig.4.9 (b)). In our case, 6 nodes per yarn must be defined. A smooth curve (C^1 continuity) will be used to interpolate the path in between those master nodes.

2. the shape and dimensions of the yarn sections. These sections are in the later considered elliptical. It is therefore necessary to identify two dimensions (the semi axes) and an orientation.

The cross-sectional slices shown in Fig.4.7 along the warp (a) and weft (c) direction show the arrangement of the weft and warp yarns respectively. We decided to segment the images to better distinguish the warp and weft fibres and to better identify the shape and position of the yarns. Fig.4.8 (b) shows the result of a manual image segmentation, taking advantage of the information available on adjacent slices. Fibers belonging to the warp yarns are colored green, while those belonging to the weft yarns are colored purple. About 130 slices were processed. For each slice, 2 to 3 minutes of manual processing were necessary. Thus, the manual segmentation operation presented requires about 5 hours for a unique unit cell. We have also tried automatic approaches, without much success. Fig.4.8 (b) perfectly illustrates the challenge that this image represents for an automated segmentation procedure based on a single slice. It is indeed tricky to distinguish cut fibres (elipses with low eccentricity?) belonging to the warp or weft in a single slice. At the end, the segmentation enables the cross-section of the strands to be discerned more objectively.

Fig.4.8 (b) actually present a transverse slice made in the warp direction and passing approximately threw the middle of the warp yarn. The same type of processing is carried out in the weft direction. From these data, we were able to verify that the distance between the yarns was on average close to 1.25 mm for the unit cell considered. In the following, L is still set to 1.25 mm. For each segmented weft yarn, the "out of plane" position of its center is estimated. Using these data, we first define the set of needed master nodes as illustrated in Fig. 4.9 (b).

Regarding the section of the wires (see Fig.4.9 (b)), the geometry delivered by the segmentation process is very complex, highly variable and irregular. In this work, as indicated, we nevertheless model the yarn section as an ellipse. In practice a mean width w is calculated from the measurements taken on each segmented yarn. Note that all of these manual measurements are made within in Dragonfly. In the present case, the average yarn width w is 1.14 mm and the resulting gap between yarns g is 0.11 mm. The thickness of the yarn (h and s respectively for weft and warp yarns) is never constant. As shown in the warp yarn in Fig.4.9 (b), yarn is thinnest at position n_1 and yarn is thickest at position n_2. This is due to the interaction between warp and weft yarns, and the warp yarn is subjected to a greater bending at n_1 than at n_2. It also results in a smaller gap between the fibers. However, to simplify the modeling, we will consider that $h = s$ and we will assign it an average value deduced from all the measurements made on the segmented yarns. h and s are thus set to 0.51 mm.

Beyond the aspect ratio variation, the section of the strand rotates due to the interaction with the perpendicular strands. Fig.4.10 shows for example the evolution of a weft

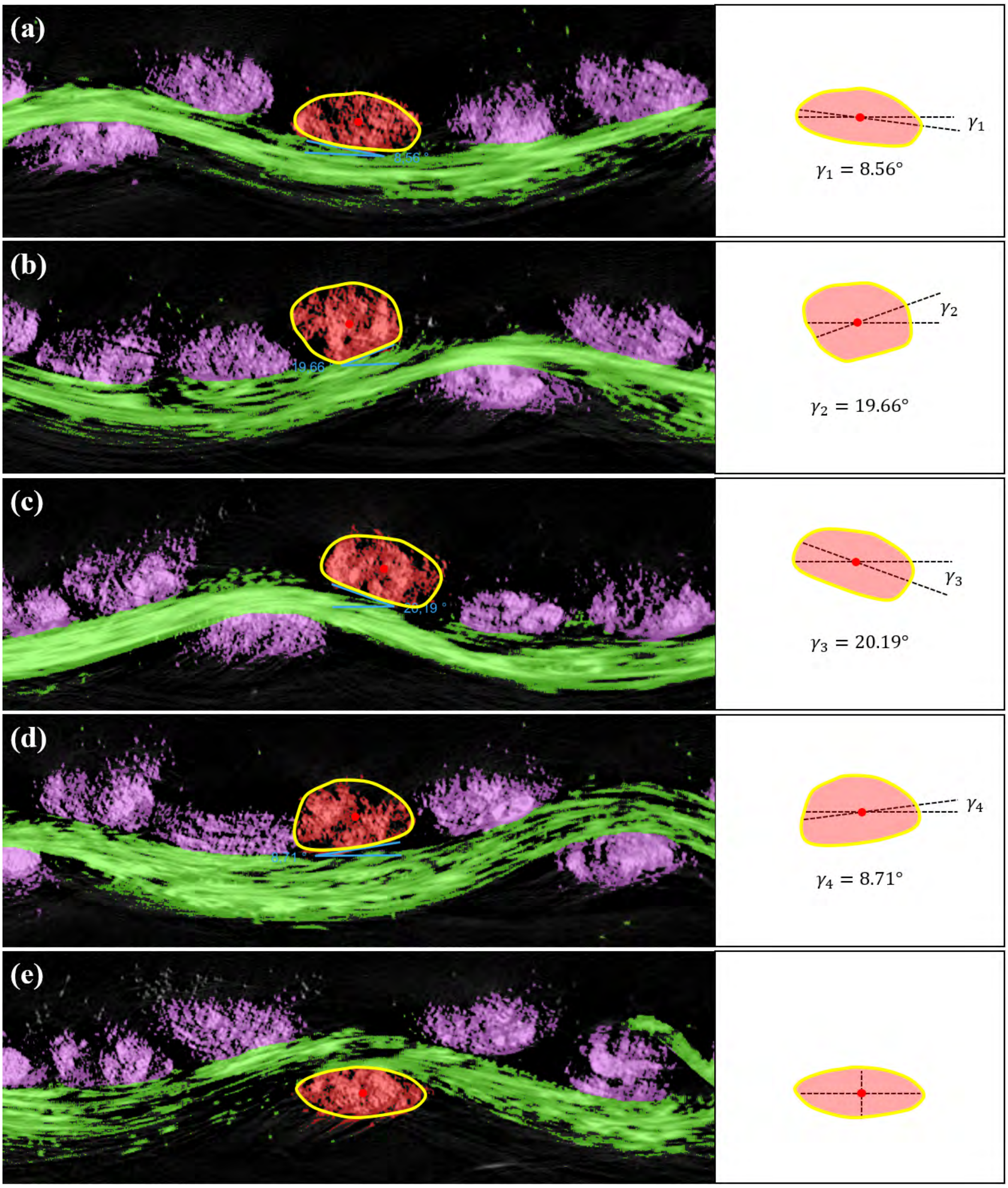

Figure 4.10: Evolution of the section of the same weft yarn at the 5 crossings; the "rotation" angle is measured at the level of the contact (angular sector in blue) and reported on the segmented section (on the right)

strand (in red) at the crossing with the 5 successive warp strands. Seen from afar, it shows a slight change of shape, but above all it reveals the rotation of the cross section. Once again, the angle between the median (horizontal) plane and the line of contact can be estimated directly using Dragonfly. For Fig.4.10, the measured rotation angles of this yarn are estimated to be around (a) $\gamma_1 = -9°$, (b) $\gamma_2 = -20°$, (c) $\gamma_3 = 20°$, and (d) $\gamma_4 = 9°$. By analyzing and measuring the angles for all the strands present in this unit cell, it is possible to confirm that the evolution is similar: practically identical and periodic. The previous values will therefore be used later.

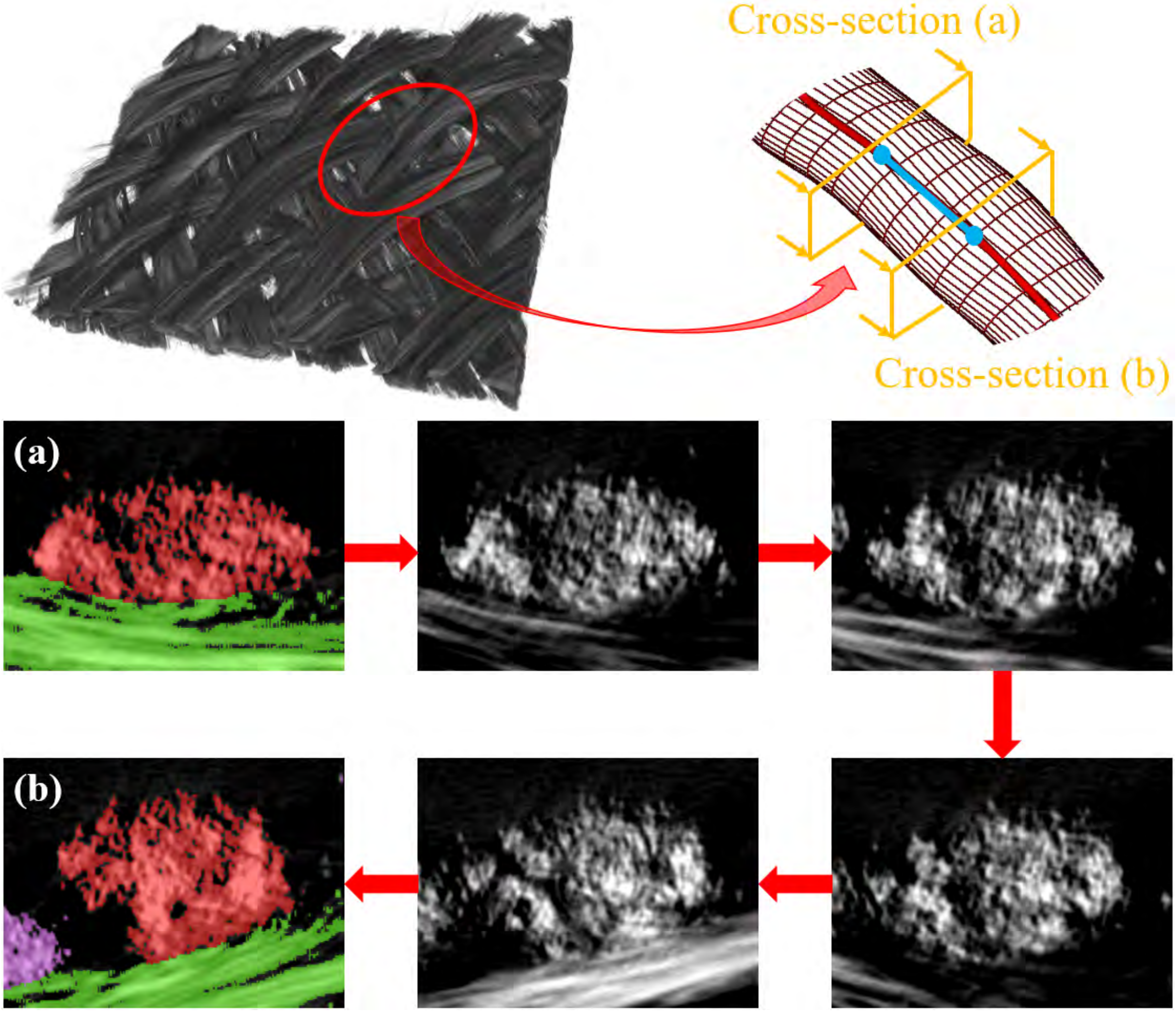

Figure 4.11: Weft yarn from state (a) to state (b): the change of fiber distribution is obvious.

Microscopically, the reason for the variation in yarn shape can be more clearly observed in Fig.4.11: it is a schematic representation of the transition of a selected weft yarn from state (a) to state (b). Due to the compression from the warp yarn, the fibers in the weft yarn are moving. There are pores between the glass fibers, and larger pores transform into larger cracks. When subjected to compression from the warp yarn, the fibers are extruded inward to reduce the squeezing pressure by reducing the pores. From state a to state b, the weft yarn is subjected to different directions of force from the warp yarn. This also leads to a slight rotation of the weft yarn as a whole. However, the main reason for this visual rotation is the deformation of the yarn. The variation of position of the fibers in the yarn, in particular due to the transverse compression, remain a main challenge for modeling (Durville, 2010; Sibellas et al., 2020).

4.1.3.2 Updated Digital Image Based TexGen models

The TexGen tool is used again. All the data collected in the previous section will be used to produce new models of geometry, from the simplest but already more representative than the first "naive" CAD model produced, to the most realistic. The idea is to better represent first the yarn path and then the evolution of the sections.

4.1.3.3 Yarn path

In TexGen, the wire path can be defined in the form of a smooth curve. The idea here is to find a simple curve which passes as close as possible to the centers of sections identified at the levels of the crossings (called "master nodes"). Said curve must also be periodic.

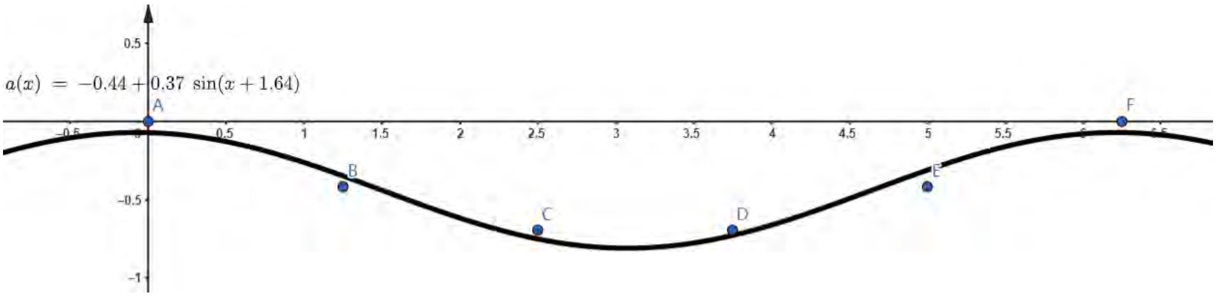

Figure 4.12: The sinusoidal function used here in TexGen to interpolate the yarn path. The blue points correspond to the "master nodes" whose position is estimated from the segmented tomographies.

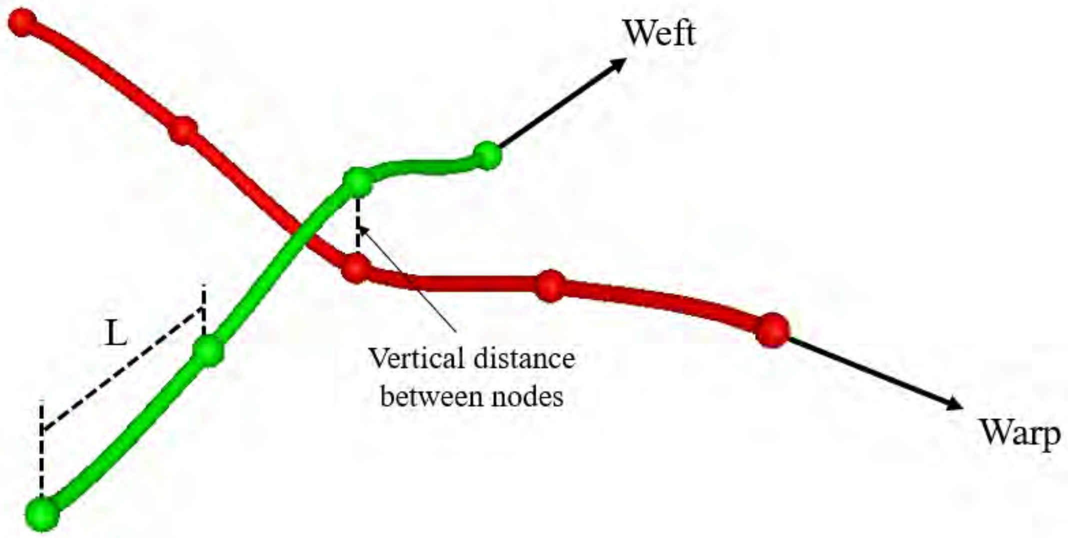

Figure 4.13: Schematic diagram showing the sine paths of two intersecting yarns and the nodes used in TexGen.

The first master node, centre of the warp yarn section at position n_1 shown in Fig.4.9 (b) is assumed to be the coordinate origin. As stated earlier, the horizontal distance L between two consecutive nodes is set at 1.25 mm. The "out of plane" position of the other "master nodes" on the warp yarn are derived from the measurements made in DragonFly in the previous section. For the sake of simplicity, we have chosen to represent the yarn path using a simple sine $Asin(ax + b) + c$. The optimal path is presented in Fig.4.12. It appears that other functions (polynomials, splines, etc.) would probably make it possible to fit the data better. However, keep in mind that the measurements are the result of a series of manual operations.

The vertical distance between two master nodes at crossings is not really constant. This is due to the different forces on the yarn at each position. The average thickness of the yarn was previously estimated: $h = s \approx 0.51$ mm. If we assume that the thickness of the wire is uniform, the master nodes at a crossing are therefore 0.51 mm apart, as shown in Fig.4.13. It is thus possible to position all the paths in relation to each other as shown on Fig.4.14 (a).

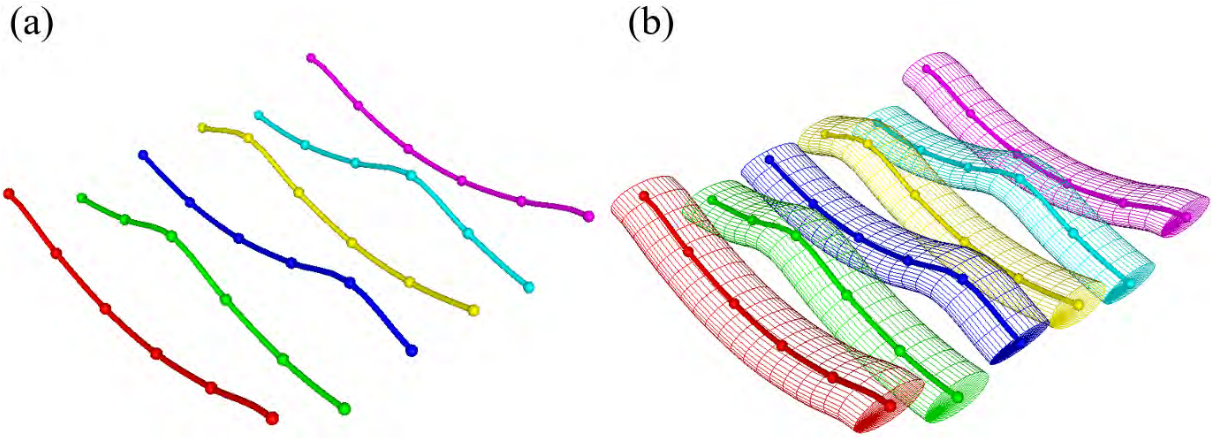

Figure 4.14: (a) Warp yarn paths in the unit cell; (b) CAD model of the warp yarns obtained by sweeping an elliptical section along the paths.

As mentioned earlier, the cross section of all yarns is assumed to be elliptical and homogeneous. No rotation of the cross section is introduced at first. The yarns then basically result from a sweep of the elliptical section along the paths. could be constructed as shown in Fig.4.14 (b). A typical result for warp strands is shown in Fig. 4.16 (a). Compared to the actual fabric, the shape of the model is clearly too uniform to reflect the deformation of the warp and weft yarns due to their interactions.

4.1.3.4 Optimization of the cross section definition

We now take into account the orientation of the sections measured in Fig.4.10 in order, precisely to better account for the interactions between the warp and weft yarns. The change can be visualized in Fig.4.15. A comparison of the unit cell CAD models before and after section optimisation is shown in Fig.4.16. It can be seen that the interpenetrations between the modelled yarns are large when rotation is not taken into account (a) and are greatly reduced by this simple trick (b).

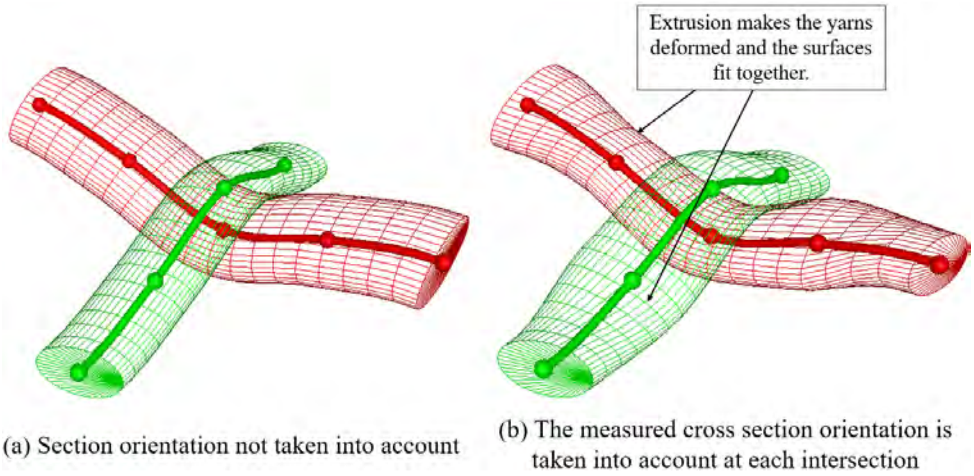

Figure 4.15: Taking into account the orientation of the section (resulting from the measurements on the segmented tomographic sections) makes it possible to partially restore the effects of the interaction between the warp and weft yarns.

This latest model, although it probably still has a lot of room for improvement, reproduces the real geometry of the fabric much better. The difference with the first 'naive' CAD model (Fig. 4.7) is striking. The Fig.4.17 shows the fabric unit cell model after the optimization and Fig.4.17 (b) shows the corresponding unit cell once meshed in Abaqus.

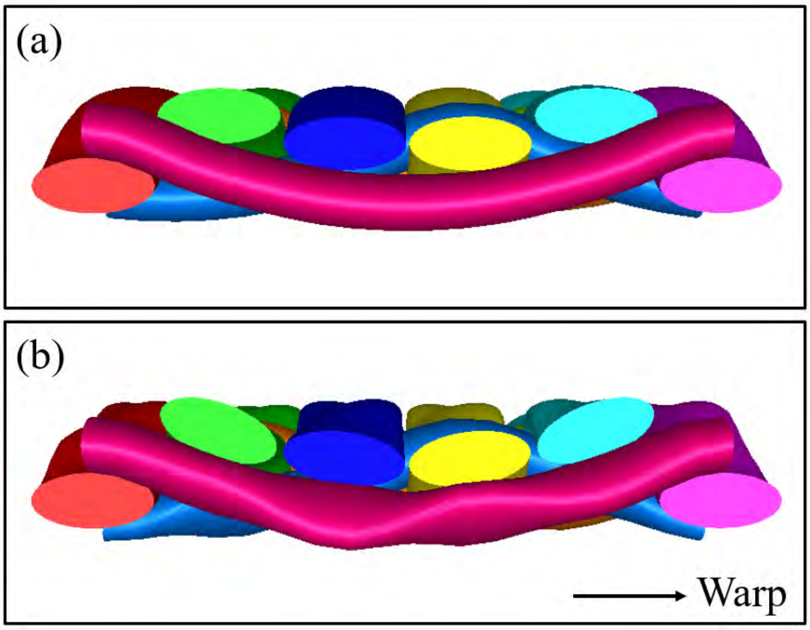

Figure 4.16: Comparison of TexGen CAD models before and after "optimisation" of yarn sections of yarn sections (taking into account cross section rotation)

4.1.4 FE model of a mini bias extension test

The previous CAD modelling of the mesh obtained via Texgen (Fig.4.18 (a)) is now used to generate a first FE model of a (mini) bias extension test. The way the mesh is

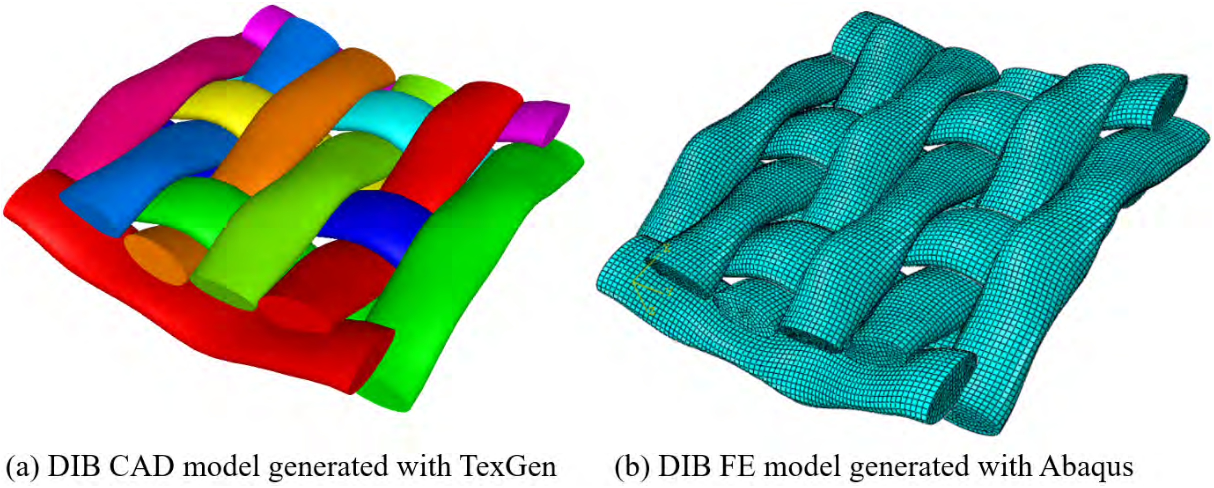

(a) DIB CAD model generated with TexGen (b) DIB FE model generated with Abaqus

Figure 4.17: Final unit cell DIB model obtained by integrating the yarn path, a typical "mean" yarn cross-section and its orientation at crossings: (a) Texgen CAD; and (b) Abaqus FE mesh.

generated, the constituent parameters and the boundary conditions are presented below.

4.1.4.1 Mesh design

A STEP file generated by TexGen is imported into Abaqus. The Abaqus mesh generator is then used to generate the volume mesh shown in Fig.4.17 (b) or Fig.4.18 (b). This type of 3D mesh could be used partially or completely for the generation of a mesh for FE-DIC measurements at this scale.

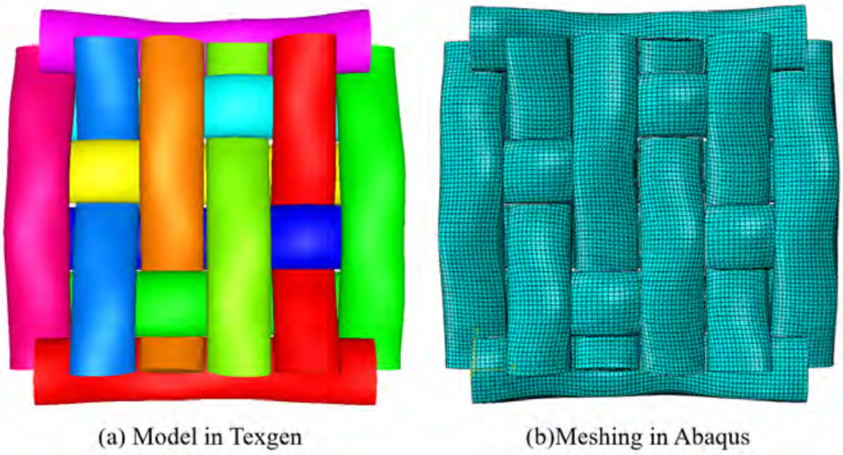

(a) Model in Texgen (b)Meshing in Abaqus

Figure 4.18: (a) Model in Texgen; (b) meshing of textile cell.

Simulating a bias test involves solving a very expensive non-linear problem. Therefore, simplification of the model and mesh is necessary to reduce the computing time without, however, compromising too much on the quality of the geometric model. During this process, we need to pay particular attention to the following:

1. We must avoid inappropriate meshes. As shown in Fig.4.19, the highlighted elements are of poor quality (highly distorted) and the geometry of the mesh regions is too

complex for sweep meshing. The reason for this phenomenon is that the surface of the fabric is too curved. This curvature causes the sides of the wire to be too finely meshed, as shown in Fig.4.19. This phenomenon is already present in Abaqus when the model file is imported and could not be optimised by changing the mesh type.

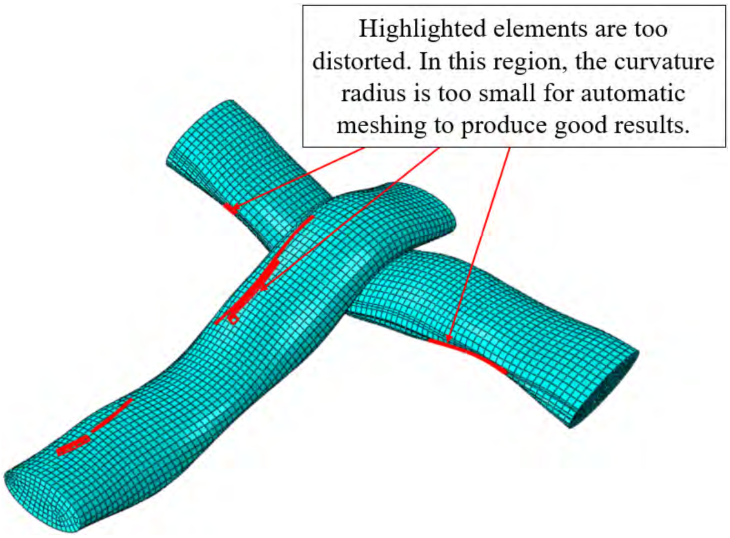

Highlighted elements are too distorted. In this region, the curvature radius is too small for automatic meshing to produce good results.

Figure 4.19: A small local curvature radius can locally lead to an unreasonable discretisation of the section edge in Texgen. Once imported into Abaqus, this discretisation can lead to highly distorted elements.

2. The mesh size should not be too fine. The main reason for long run times is the complexity of the model (contact, friction, etc.), but also the level of mesh refinement (or mesh size). The smaller the mesh size, the longer the run time. As shown in Fig.4.20(a), when the "Approximate Global Size" of the mesh is small (here 0.2), the surface of the model is accurately captured, but the computation time becomes prohibitive.

3. Mesh coarsening should preserve geometry. As shown in Fig.4.20(b), increasing the mesh size (here only to 0.3) directly in Abaqus can greatly alter the description of the local geometry, especially in the area of higher curvature. Such an imperfection would affect the results of subsequent calculations.

The remedy here, rather than trying to remesh in Abaqus, is to simplify the model in Texgen as shown in Fig.4.21. The simplification involves smoothing the model surface. This results in some interpenetrations between yarns (white dotted lines in Fig.4.21 (a)). These cause the simulation to fail. The practical solution to eliminate them here was to slightly reduce the yarn width (1.14 mm to 1.1 mm) and increase the distance between the top and bottom knots (0.51 mm to 0.55 mm). As shown in figure 4.21 (b), the interference is completely eliminated.

Fig.4.22 shows the model of our miniature specimen obtained with the parameters given above. Its size is approximately 15.9 mm × 10.6 mm. It is possible to verify the representativeness of such a model for the expressed need (*i.e.* to test the FE-DIC) by superimposing this simplified mesh and the tomography.

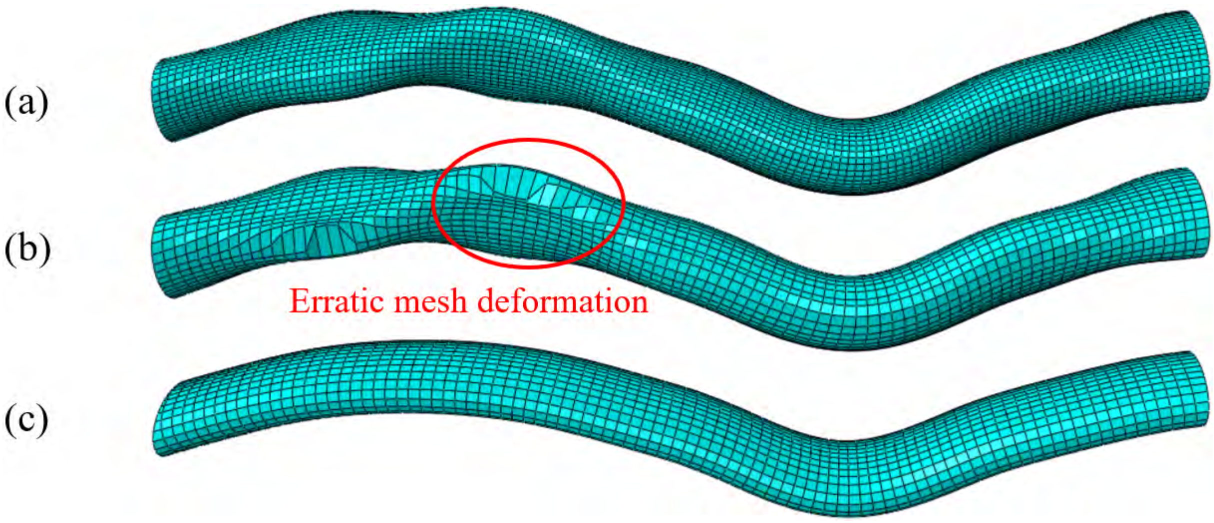

Figure 4.20: Comparison of yarns before and after simplifying : (a) mesh overly granular (mesh size is 0.2) ; (b) mesh deformation (mesh size is 0.3); (c) simplified model.

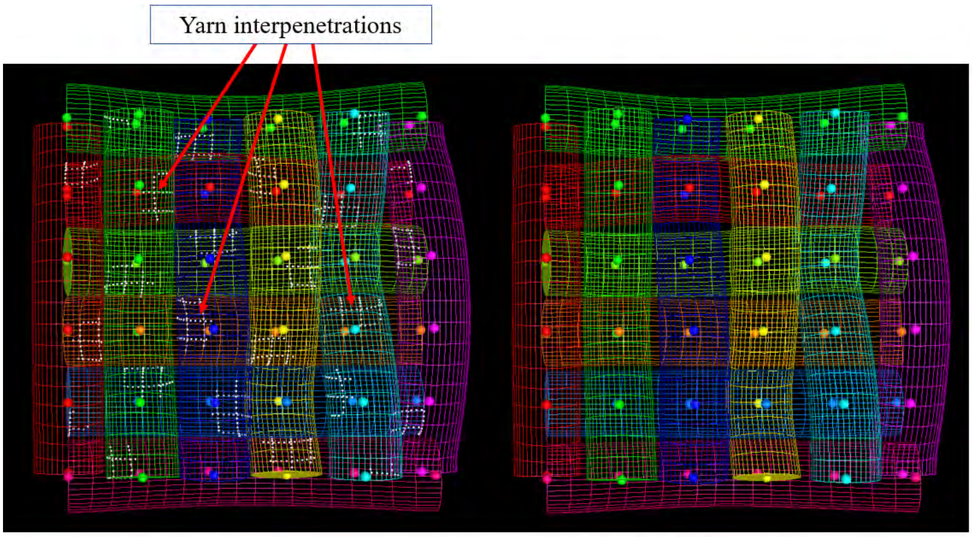

(a) Model after the smoothing process

(b) Model after updating some geometric parameters

Figure 4.21: Model simplification procedure in Texgen (a) the CAD model is simplified by a smoothing operation; it follows interpenetrations of yarns, here highlighted by the white dotted lines (b) The yarn size and the distance between the yarns at the crossings are slightly modified in order to obtain a suitable model for the FE analysis.

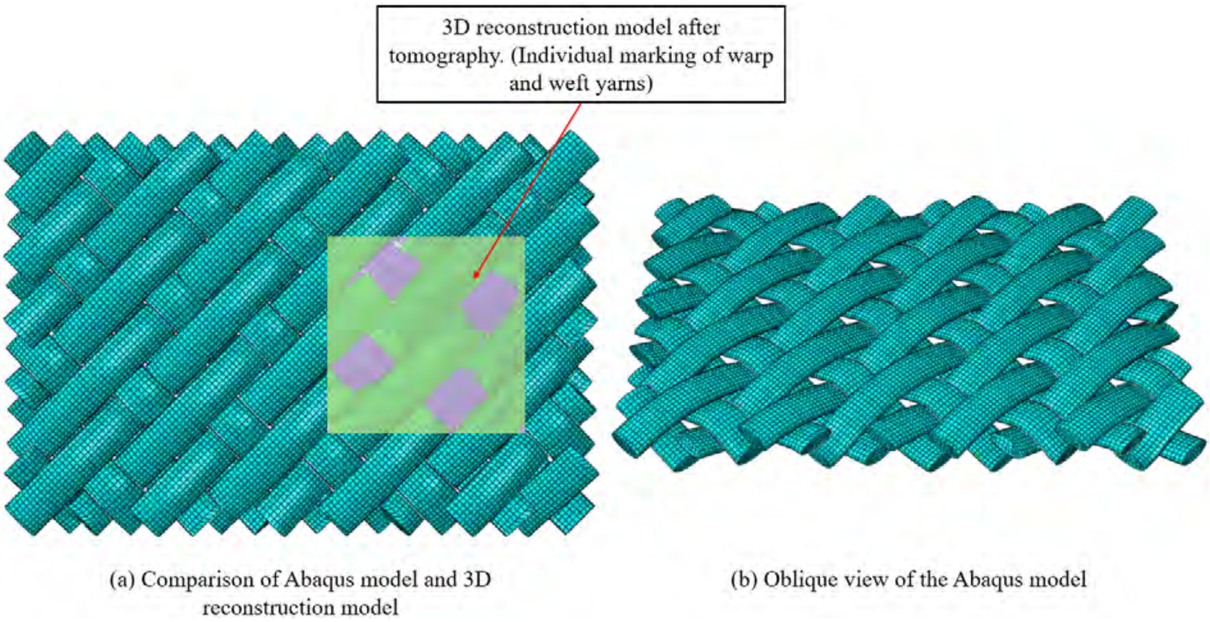

(a) Comparison of Abaqus model and 3D reconstruction model

(b) Oblique view of the Abaqus model

Figure 4.22: Simplified model compare with the 3D reconstructed model obtained from tomography.

4.1.4.2 Yarn mechanical properties

A simple linear isotropic behaviour is considered for the yarns. The properties of the glass fibres used in the fabric are given in Table 4.2 (see section 1.1.1.1). We use these values directly for the yarn. We are fully aware that this modelling is crude for such a fibrous medium. More advanced models could of course be chosen, such as those used, for instance, in (Badel et al., 2007; Hamila and Boisse, 2007; Lomov et al., 2007; Durville, 2010; Naouar et al., 2015). Again, we are not trying to model the behaviour exactly. We simply want to validate the DIB approach and simulate a more realistic kinematics first (to challenge the FE-DIC).

No.	Item	Value	Unit
1.	Mass Density	2.58	g/cm^3
2.	Young's Modulus	72.3	GPa
3.	Poisson's Ratio	0.2	
4.	Tensile strength	3.445	GPa
5.	Plastic Strain	0	

Table 4.2: Glass fibers properties

4.1.4.3 Contact between yarns

Frictional contact between the strands is assumed. (Montero et al., 2017) studied the evolution of the friction between the yarns as a function of their relative orientation

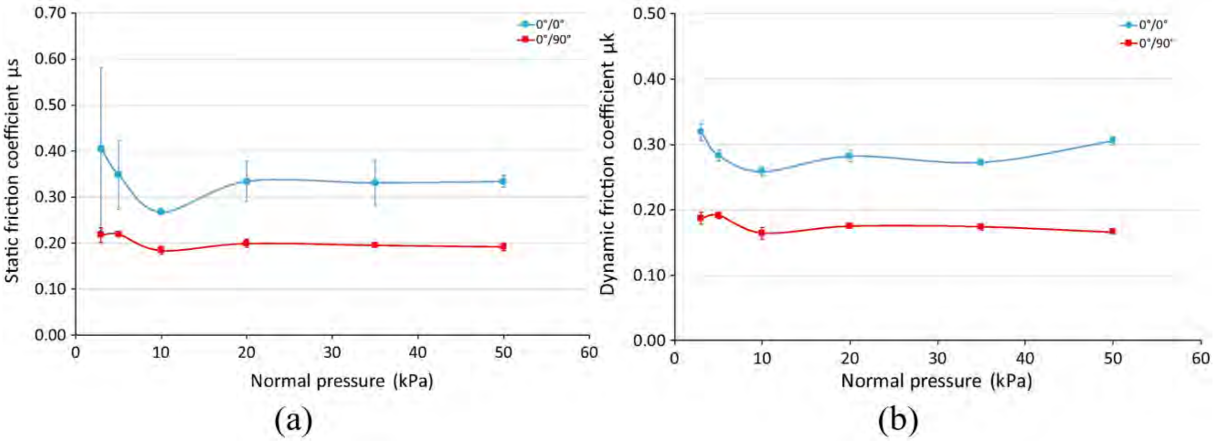

Figure 4.23: Evolution of (a) the static friction coefficient µs, and (b) the dynamic friction coefficient µk between yarns versus normal pressure at a speed of 1 mm/sec. Error bars represent standard deviations. These curves are taken from the work of (Montero et al., 2017)

and of the normal pressure. The main results are summarised in Fig.4.23: it shows the evolution of the glass fabric/fabric (a) static coefficient of friction µs and (b) dynamic coefficient of friction µk as a function of the normal pressure at a speed of 1 mm/s. In the following, the static friction is set to 0.2 and the dynamic friction to 0.17.

There are two approaches to defining the interaction between yarns: (1) create a 'surface' for each yarn and then define the interaction for adjacent yarns one at a time. This method defines the interactions very accurately, but is cumbersome. (2) The "Find Contact Pairs" function is used to automatically find possible interactions. The advantage is that the operation is relatively simple, but the calculation time increases. The first method is used in this section.

4.1.4.4 Loading and boundary conditions

With regard to the boundary conditions, their purpose is to represent a kind of mini-bias extension test, but they have been chosen to stabilise the calculation. It should be remembered that the aim here is to generate a realistic displacement field to test the FE-DIC and not, at least at this stage, to predict the behaviour of the fabric. The boundary conditions adopted for the simulations presented below can be broken down as follows:

1. The nodes on the right edge are assumed to be clamped to represent gripping.

2. A uniform displacement is applied to the left edge to simulate the displacement of the other grips. The motion speed is fixed at 2 mm/s.

3. To stabilise the calculation, the other two edges (upper and lower) are not left completely free. Only movements in the X and Y planes and rotation around the Z axis are allowed.

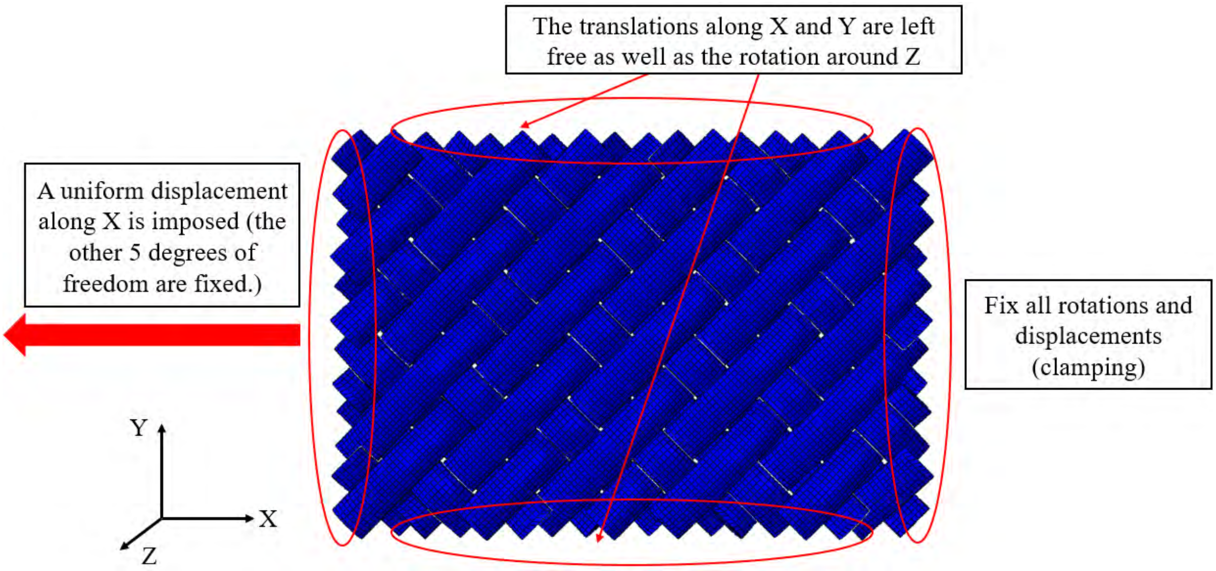

Figure 4.24: Initial mesh and associated boundary conditions (clamped on the right, displacement imposed on the left and out-of-plane displacements restricted on the top and bottom 'free' edges)

4.1.5 Simulation results for a mini bias extension test

Once all the constitutive parameters and boundary conditions have been integrated, the calculation is started in Abaqus. Such a calculation, with all the simplifying assumptions, takes more than 11 hours to run on a standard laptop PC (LAPTOP-6266RGEL; Intel(R) Core(TM) i7-9750h CPU @ 2.60GHz 2.59GHz; Installed RAM 8.00GB; System type: 64-bit Operating System, x64 Processor).

The displacement field shown in Fig.4.25 corresponds to a displacement of the left edge of 2 mm (t = 1 s). The simulation does not recover the pure shear zone, as the aspect ratio of the model is only about 1.5 (a factor of 2 is usually required for a bias extension test). However, the non-shear zone is clearly distinguishable and the semi-shear zone can be inferred.

The magnitude of the displacement field is shown in Fig.4.25(a). The areas of maximum displacement (2.8mm) are indicated by the red circles. We observe that the maximum displacements occur in two places: (1) a very free yarn at top and bottom. (2) on the yarn which is located at the boundary of the division of the zones. This phenomenon is also observed in the tomograms obtained during the in situ test (Fig. 4.40). Figures (b) and (c) show the displacement fields in the horizontal and vertical directions respectively (X and Y axes). The distribution of non-shear and semi-shear zones is more clearly seen in these maps. These results were considered sufficiently convincing for the generation of realistic synthetic images (see section 2.3).

4.1.6 Intermediate summary for the DIB models part

An initial sample preparation procedure inspired by the previous chapters proved satisfactory. The PMMA tube used as a support for the sample during the scan fulfilled its role perfectly. X ray Tomographies carried out under highly representative data acquisition

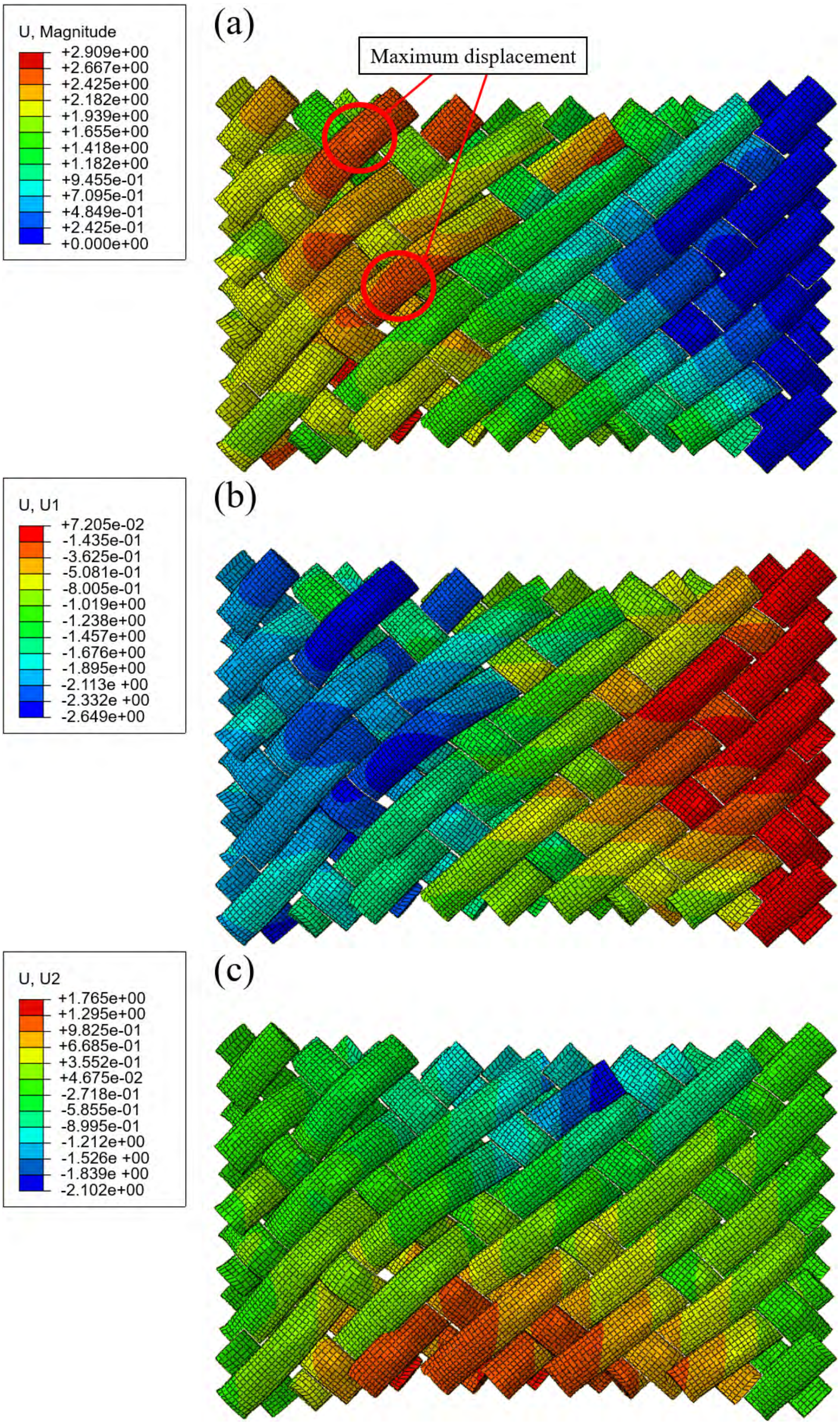

Figure 4.25: Displacement field resulting from the simulation of a "mini" bias test in Abaqus: (a) displacement magnitude; (b) and (c) are respectively the components of the displacement field in the horizontal and vertical axes (along X and Y, respectively).

conditions provided nice and informative volumic images. The results obtained, however, suggest favoring in the following a partial scan of the sample rather than trying to scan the whole of it. A manual segmentation process helps to identify the sections of the strands, to follow their position and to estimate their dimensions as well as their orientation. A Digital Image Based CAD model was derived from the latter using TexGen. Automation of the segmentation process, or even of the mesh, would obviously be desirable. One idea could be to rely on the knowledge of CAD *a priori*. An ANR project (ANR AVATAR) on this subject is underway at the Clément Ader Institute (Dorian Bichet's PhD thesis, in progress).

Secondly, we have shown how it is possible to generate FE simulations in Abaqus from CAD DIB models previously created in TexGen. After slightly simplifying the geometry, a first FE model of a mini-bias test was proposed. If the modelling of the strands is kept simple, the model integrates the friction between the strands and a relatively representative set of boundary conditions. This model was not intended to be perfect. It was only used to generate realistic displacement fields and corresponding synthetic images to test a DIC procedure (see section 2.3). Nevertheless, such a model could be perfectly used to regularise a measurement, as suggested in (Rouwane et al., 2023b). To make these simulations more predictive, it would be necessary to improve the DIB model, to refine the description of the behaviour of the yarns, and to simulate "larger" pieces of fabric. It is at this point that we could then consider the possibility of establishing a dialogue with the measurements in order to identify some of its constitutive parameters.

4.2 Toward multi instrumented *in situ* bias extension tests

We now aim at performing a first bias extension test inside the μCT. In the previous section we saw that adding a frame to the fabric greatly simplifies handling. We have taken up the same idea here. A special *in situ* tensile machine has been designed to accommodate the large displacements expected. A very similar PMMA tube to that used to support the specimens in the previous section is used here to transfer the loads. This means that the scans can be taken in similar conditions to those used previously. We therefore know that the images obtained can be used to produce DIB models. The machine's operation is first tested *ex situ*, and images are taken through the tube using a telecentric lens. The idea is then to test the possibility of supplementing X-ray monitoring with surface field measurements by means of stereo FE-DIC in the future.

This section begins with an explanation of the preparation of the samples, followed by a description of the in-house designed machine, then a presentation of the *ex situ* tests, and finally the first results of an *in situ* test performed on your X-ray tomography system.

4.2.1 Preparation of samples for mini bias extention tests

The specimens used for the *in situ* tests in the μCT are similar in all respects to those used in section 2, except that they are smaller and must not interfere with the tomography. Since this solution was satisfactory in the previous part, we will again use 0.71 mm thick cardboard to make the frame of the specimen. However, two methods have been tested: the frame is assembled from different pre-cut pieces and the frame is obtained by a series of cutting operations.

4.2.1.1 Frame made by gluing together multiple pre-cut pieces of cardboard

This first method is similar to the one used in the 4.1.1 section. The parts needed to make the pattern (the heels and the uprights of the frame) are pre-cut, assembled and then glued to the fabric to act as a frame. Figure 4.26 illustrates the various elements used:

1. The glass fabric carefully pre-cut to size 90mm × 20mm
2. 4 tabs. These are glued to the ends as shown.
3. 2 strips to act as side posts for the frame. These are glued to the heels.
4. 2 Protective caps are placed around the frame to protect it before the experiment begins (they will of course be removed before the jaws are gripped).

This protocol is feasible, but the method has not proved sufficiently robust. In fact, it sometimes took several attempts to obtain samples that met the specifications (condition of the fabric, position in the frame, etc.). The main reason for this is that there are too many components and the preparation process, including cutting, is purely manual.

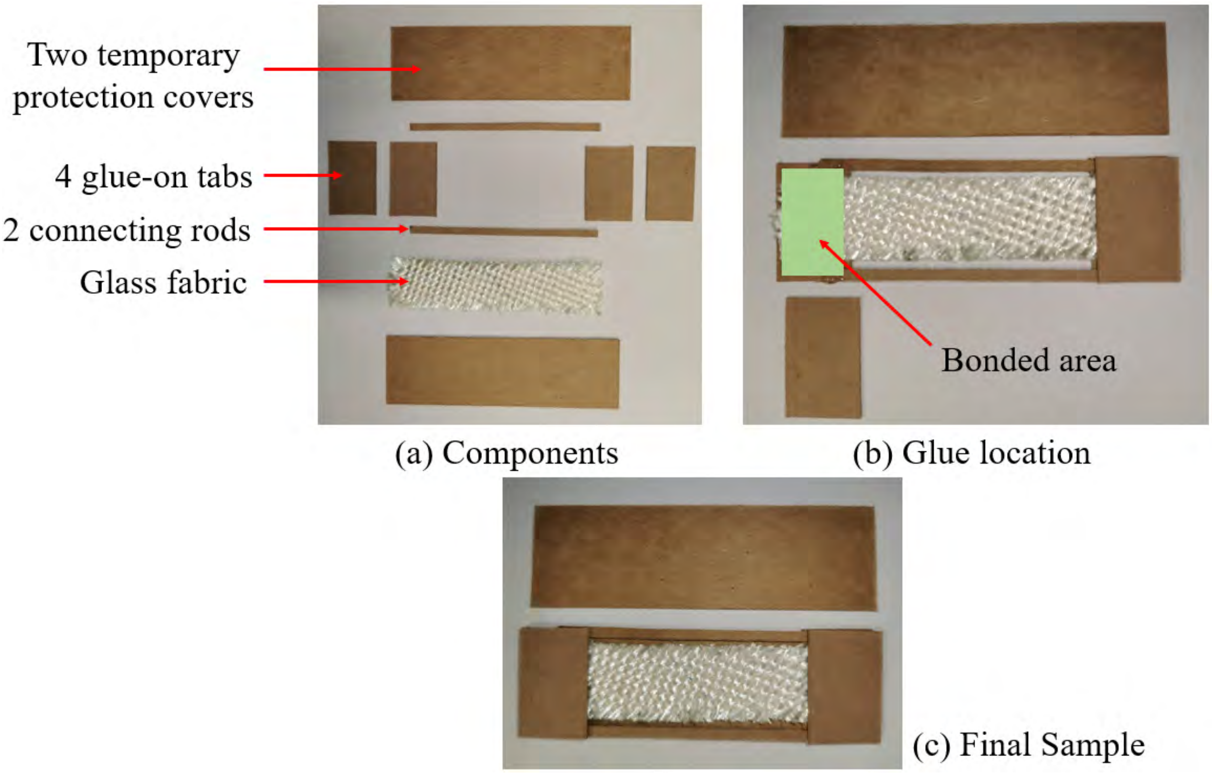

(a) Components (b) Glue location

(c) Final Sample

Figure 4.26: Principle of the solution by assembling and gluing pre-cut pieces

4.2.1.2 Use of pre-cut frame

This new method has been proposed to eliminate the dispersion observed with the previous technique. The idea is to pre-cut the frame. Two approaches were studied. In both cases, only a rectangular piece of fabric and two rectangular pieces of cardboard are used, the external dimensions of the latter being 100 mm × 30 mm (future frame).

For the first option, a 60 mm × 20 mm rectangle is precisely cut out of the centre of the cardboard pieces to form the frame before gluing, as shown in Fig. 4.27. A scalpel is used for this. The 90 mm × 20 mm piece of fibreglass is cut with a pair of scissors. Fraying is observed. The fabric is then adjusted and glued to the frames as best as possible. The green rectangles shown in Fig.4.27 (a) indicate the glued areas. Adjusting the position of the fabric and cardboard pieces to ensure the relative orientation of the yarns and the orientation of the fabric in relation to the edge of the sample is therefore easy, provided the fabric piece has been cut correctly.

A variant of this technique has subsequently been developed. It largely follows the proposal made in section 2.1.2, except that the main tool used is the scalpel. The key points of the procedure are detailed in Fig.4.28. Here a 90 mm × 30 mm glass fabric is used. As in section 2.1.2, two slits (dashed yellow lines indicated in 4.28) are cut into the cardboard pieces near their ends to define the future limits of the tabs (60 mm from each other) and to limit the support of the glued area. These pre-cut 100mm × 30mm cardboard plates are then glued to the fabric in the tab area (the glued areas are indicated by the green rectangles in fig.4.28 (a)). The final step in the process is to cut the entire sandwich lengthwise to delimit the fabric gauge area and remove the useless cardboard rectangle in this area. This last step proved to be particularly tricky due to the thickness

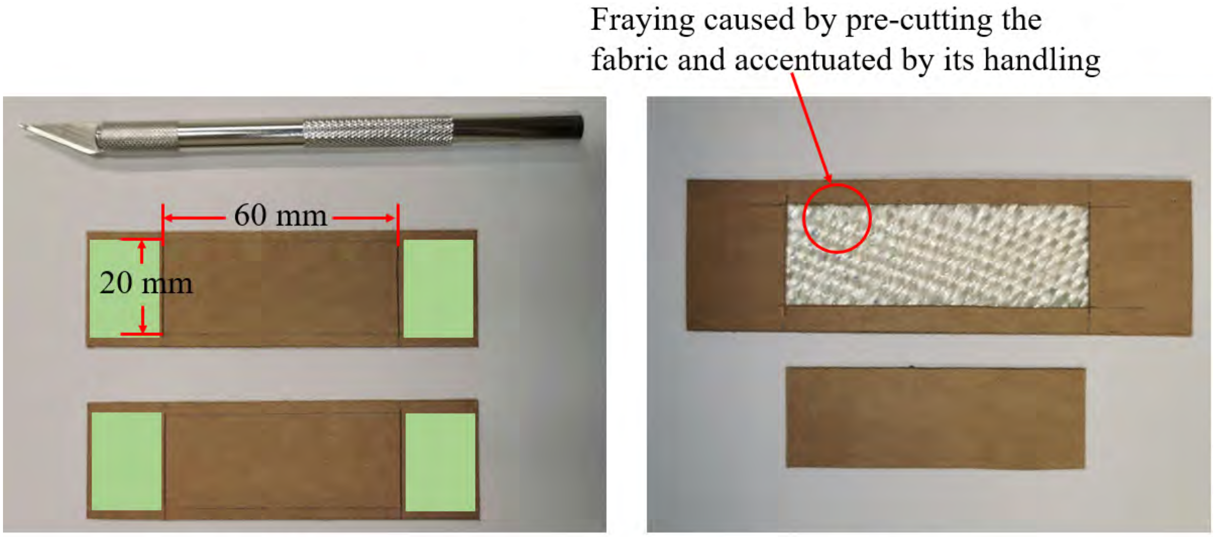

(a) Future frame with outline of the future cut and scalpel used

(b) Final Sample

Figure 4.27: Use of a prefabricated cardboard frame. First option: (a) Use a scalpel to remove the 60 mm × 20 mm rectangle pieces in the centre of the two 100 mm × 30 mm cardboard base pieces; Glue is deposited in the areas shown in green; (b) The pre-cut 90 mm × 20 mm piece of fabric is carefully fitted and glued to the two pre-made frames. The removed covers can be used to protect the specimen during manipulation.

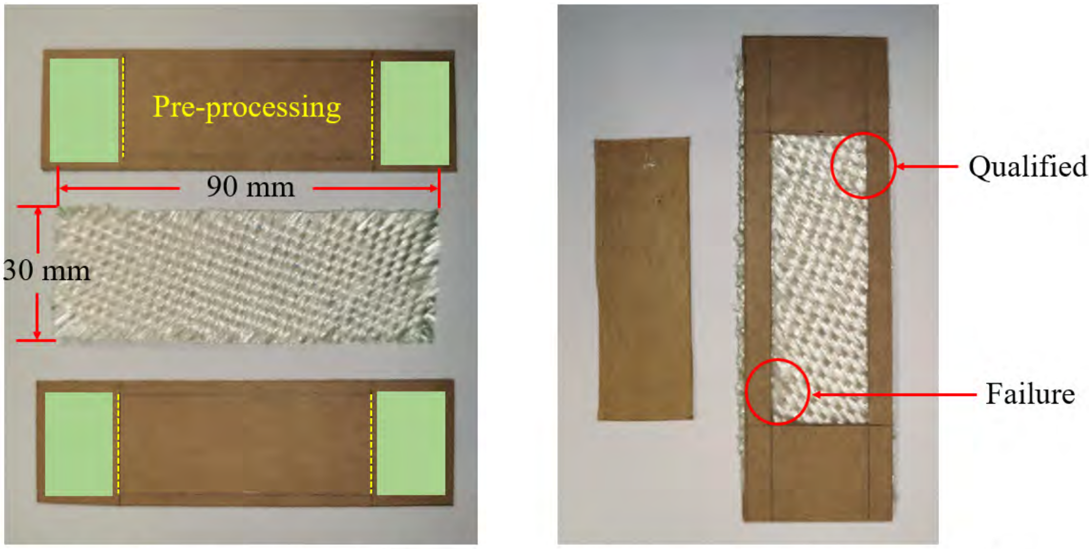

(a) Future frame: dotted yellow lines indicate the unique cut made at this stage

(b) The entire sample is cut lengthwise to obtain the final sample

Figure 4.28: Use of a prefabricated cardboard frame. Second option: (a) The two pieces of cardboard that will act as the frame are cut only along the yellow dotted lines. The green areas are pre-glued. The fabric is carefully positioned and then sandwiched between these two pre-cut pieces. (b) The assembly is cut lengthwise to define the future useful area of the specimen and the central part is removed (to be used for protection until the test).

of the sandwich. It led to some inconveniences as shown in figure 4.28. Despite the significant pressure exerted on the ruler to hold the parts together by adhesion and the sharp scalpel used, fraying is again sometimes observed. The frame was sometimes even damaged. Finally, even if the scalpel is held as vertically as possible, the trajectory of the scalpel on the underside is not controlled. Several attempts were necessary before achieving good results. We didn't have time to try, but a laser cut could have been attempted.

Both options which consists in using a pre-cut frame give better results in terms of orientation control than the previous proposal. The second option gives better results in the end. But the first, which corresponds to the best simplicity/result compromise, was finally retained.

4.2.2 In-house developed *in situ* tensile machine

A specific machine was developed in-house for this study's needs. It allows for the testing of small specimens and is suitable for the large displacements expected when performing bias extension tests.

4.2.2.1 *in-situ* tensile machine design

The proposed design is relatively conventional. The loads are transferred from the part connected to the actuator to the fixed part via a PMMA tube, in view of the extremely low loads to be expected. The idea is to avoid columns that would interfere with the reconstruction of the tomographic image. Furthermore, to minimise the vibrations of the machine (due to its high slenderness ratio), particular care was taken to make it as "axisymmetric" as possible to prevent imbalance.

The following points made it possible to specify the specifications of the machine

1. The inner diameter of the tube must be greater than 30 mm, since the size of the sample is 60 mm × 20 mm and that of the sample with its frame is about 30 mm. In order to obtain interesting resolutions (in terms of fibre size), the outer diameter should be as small as possible.

2. If the width of the fabric is 20mm, the maximum expected tensile force should not exceed 100N (based on the results obtained with 50mm samples, using a simple rule of three). We know that breakage will occur much earlier on such samples (2 elementary cells only in the width).

3. For a fabric of 60 mm × 20 mm, the maximum elongation expected should not exceed 25 mm. However, the machine and/or the specimens could be modified to test larger and therefore longer specimens.

The main machine components retained in the proposed design are presented in. Fig. 4.29. Their main characteristics in this work are specified below:

1. **Electromechanical actuator**. We have chosen a captive linear actuator developed by Nanotec. It is equipped with a NEMA17 (42mm) stepper motor. Its stroke is approximately 63.5 mm and the maximum peak force it can be subjected to is approximately 46 daN. The motor is fitted with an encoder which allows us to know its exact rotation and therefore the position of the cylinder rod.

2. **PMMA tube**. The radial dimensions of this cylinder is 38 mm × 32 mm × 3 mm, that is to say identical to those adopted in section 4.1.1. Its length has adjusted to accommodate the present samples.

3. **Load cell**. An in-line strain gauge based sensor has been chosen to measure the longitudinal load applied to the specimen. The maximum capacity of the miniature threaded load cell selected in this work is 50 N.

4. **Grips**. Two stainless steel mini mechanical vice grips were purchased commercially. They can transmit up to 500N and fit inside the tube.

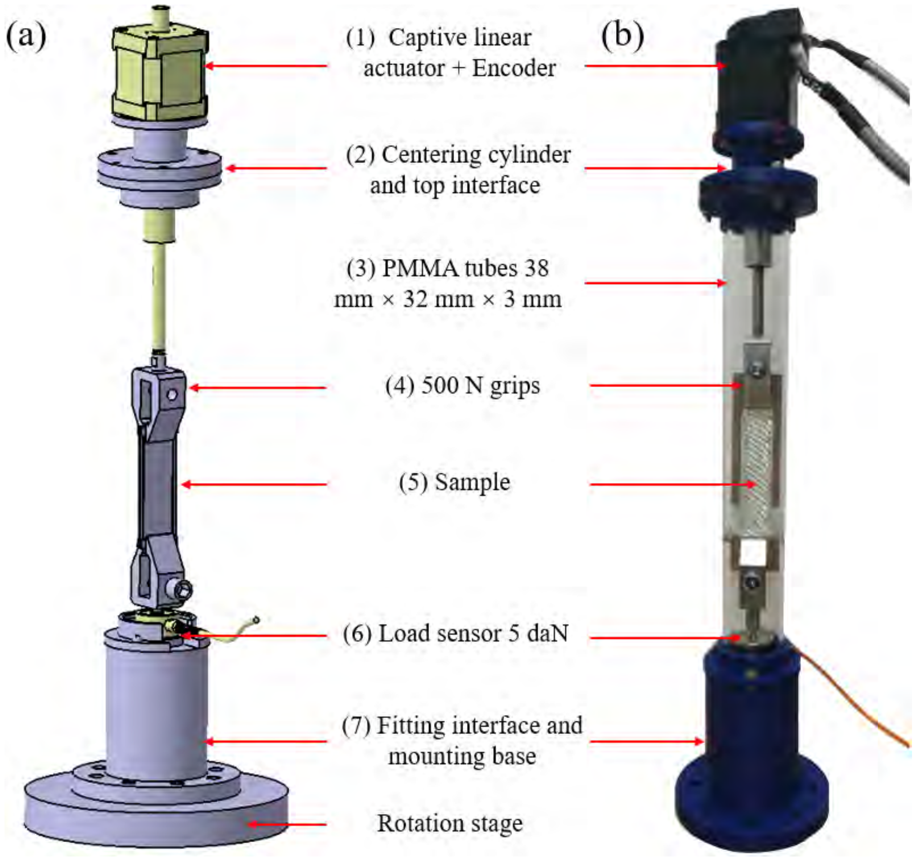

Figure 4.29: *in-situ* tensile machine designed in-house for the purposes of this study: (a) CAD of the machine without the tube and (b) first manufactured version. The main interfaces connecting the commercial parts were obtained by 3D printing.

The machine was then designed around these "commercial" parts. The work therefore consisted mainly in developing interfaces. A CAD view of the machine (without the PMMA tube) and the first manufactured machine used during this thesis are shown in Fig. 4.29. For this first achievement, all the main interfaces were made using plastic additive manufacturing (ABS 3D printing) and the tube was bonded to the interface parts (with Araldite 2011).

4.2.2.2 Machine control and displacement force data acquisition

We chose a commercial solution to control the machine and collect data during the tests. A USB card is used to control the actuator via a microstep driver and to record its position and the force applied to the specimen. The software (Depex) supplied with the machine has a graphical interface that simplifies operations both during test preparation and later when exporting data. A schematic of the whole system is shown in Fig. 4.30 It should be noted that the system is robust in the sense that the cables of the machine can be disconnected during manipulations.

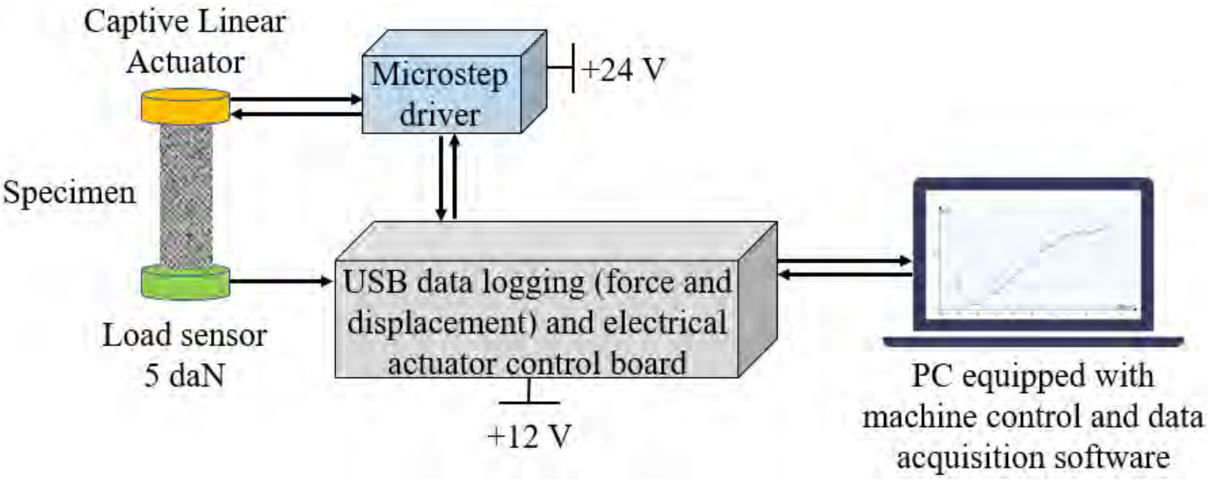

Figure 4.30: Schematic diagram of the system chosen for the control of the machine and the acquisition of data.

4.2.3 *ex-situ* bias extension tests

In this section, we present the first tests carried out *ex-situ* with the machine developed. There are several objectives:

1. It was important to prepare for the tests in the tomograph. Among other things, the assembly of the specimens is a delicate phase. The first step is to align the jaws. In practice, a rotation around the machine axis can be released between actuator and base. The idea is then, as with conventional machines, to grip a martyr test piece (much stiffer than our sample) once the machine is assembled, in order to force the jaws to align. Rotation is then prohibited. The sample can then be mounted with a minimum of twisting.

2. An important objective is to test the operation of the machine under less restrictive conditions in preparation for the *in-situ* test. For example, we want to record the effort/displacement curve on several such small samples in order to anticipate the load levels at which we will stop the machine to perform the scans (the scans are performed here, classically, with the movement stopped and the effort stabilised).

3. We wish to verify that field measurements by stereo DIC could be made through the tube. Eventually, we plan to add a camera in the tomograph and capture images

of the sample in the visible during its rotation (Fouque et al., 2022). We imagine using a telecentric lens (although we are fully aware that this will not eliminate the distortions induced by the PMMA tube, it could simplify the optical modeling)

4. Finally, in connection with the previous point, we want to take advantage of this campaign to estimate the effect of the speckle deposited by the procedure proposed in the section 2.1.1 on the behaviour of such small samples.

4.2.3.1 Mini bias extension tests on speckled specimens

EXPERIMENTAL SETUP

Several specimens are prepared according to the procedure described in section 4.2.1.2. Four specimens are speckled according to the procedure introduced in section 2.1.1. They are tested *ex-situ* using the mini-machine placed on a fixed support (see figure 4.31 (b)). After releasing the specimen by cutting the frame posts (in this version, two rectangular slots, visible in Fig. 4.31 (b), are made on both sides of the PMMA tube - another configuration has been adopted for tomography), the specimens are subjected to a monotonic tensile load until the specimen separates. The Depex software makes it easy to program the test (direction of applied displacement, displacement speed, automatic stop after a drop in force, definition of end-of-test conditions, etc.). The travel speed is set at 6 mm/minute.

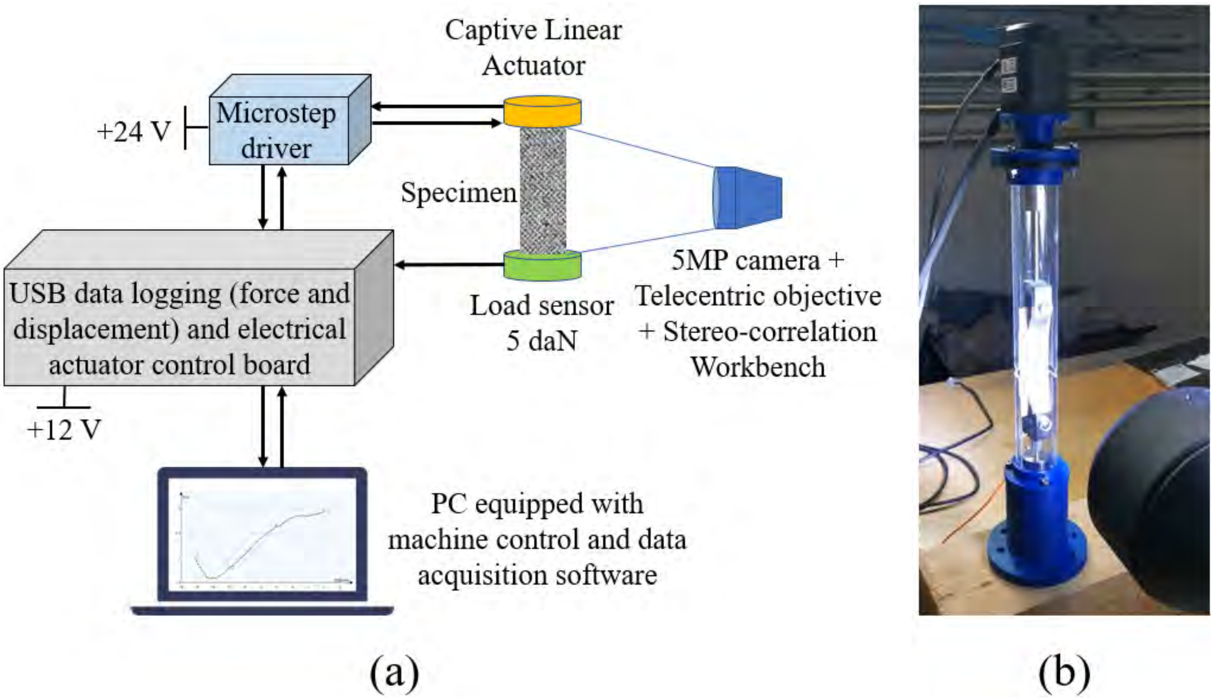

Figure 4.31: Bias extension tests carried out *ex situ* with the miniature tensile machine: (a) experimental setup: the stereo bench, which did not yield convincing results, is not represented; (b) photo of the machine fixed on a table: the side slits made in the PMMA tube allow the fabric to be released (by cutting the side posts of the frame) before the test

Optical instrumentation similar to that described in Chap. 2 is setup. It includes a 5Mp stereo correlation bench, a 5Mp camera equipped with a telecentric lens (Opto

Engineering TCZR lens visible in Fig.4.31 (b)). Special care has been taken to position the camera + telecentric assembly so that the optical axis is perpendicular to the surface of the sample. The frame rate is set to 1 fps.

FORCE VS DISPLACEMENT RESULTS

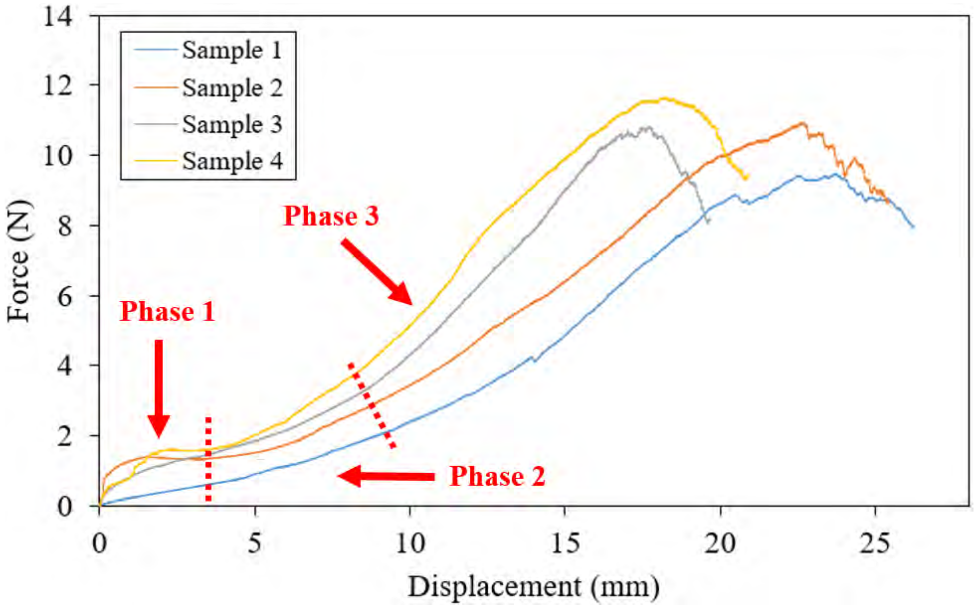

Figure 4.32: Force (N)/Displacement (mm) curves for the tension-extension test performed on speckled glass fabric samples using a miniature tensile machine.

All of the Force (N)/Displacement (mm) curves obtained are shown in Fig.4.32. A quick comparison with Fig.2.5 obtained for reference samples of 150mm×50 mm reveals notable differences in terms of appearance and values. In particular, we observe a huge difference in maximum load flow in the width of the specimen (12N/20mm against a little more than 300N/50mm for the macro reference) and in the relative elongation (25/60 in the present case against just over 40/150 for the macro reference). Given the few cells included in the width, the shearing and frictional forces between the threads when the fabric is stretched are greatly reduced. These tests carried out with the micro-machine could however still be divided into three phases indicarted in Fig. 4.32:

1. The yarns spin at the crossing between warp and weft with a relatively small force. The short duration of this phase is due to the small dimensions of the sample and the rapid change in shear angle, which allows adjacent wires in the same direction to approach each other more quickly.

2. The second phase is the shear locking phenomenon. Adjacent threads in the same direction touch each other and produce lateral compression. However, for the small specimens studied in this section, the observed wire movement is significantly different from the usual shear blocking phenomenon. This leads to two observations: (i) in terms of load, as shown in Fig.4.32, the experiment begins to show a significant increase in tensile force as it enters the second stage. However, the associated slope is very small (ii) the inter-wire kinematics, as shown in Fig.4.33(b), the shear angle

could be measured to vary from about 3° to 11° in the second stage of the experiment. However, no significant sliding phenomenon is observed. The main reason for this discrepancy is the size of the sample. The number of yarns perpendicular to the direction of traction is about 11 to 12 (2 patterns), a much smaller number than the 28 to 29 (5 patterns) in the sample in chapter 2. So the friction between warp and weft yarns is too small (compared to the friction in the sample in chapter 2). This is the main reason for the overall small traction force. Noteworthy is the short duration of this phenomenon, which will quickly enter to the third phase.

3. The tensile force gradually increases with shear angle in phase 3. The main reason for this is attributed to the evolution of the interactions between the yarns due to the stretching and rotation of the yarns. In particular, the evolution of the friction as the shear increases. In other words, as the shear angle increases, the compressive force between the strands becomes progressively greater, resulting in progressively greater friction. In addition, according to the study by L. Montero (Montero et al., 2017), the adherence and dynamic friction coefficients increase significantly when the angle between the glass strands decreases from 90° to 0°. In their case, they go from 0.20 to 0.33 and from 0.17 to 0.28 respectively (for a given pressure between the strands). Some slippage between the warp and weft yarns could be observed as shown in Fig.4.33(c). When the shear angle reaches a critical value (for a 60 mm **x** 20 mm speckled glass fabric, this shear angle is estimated to be 11°), a significant slipping phenomenon between the yarns is observed.

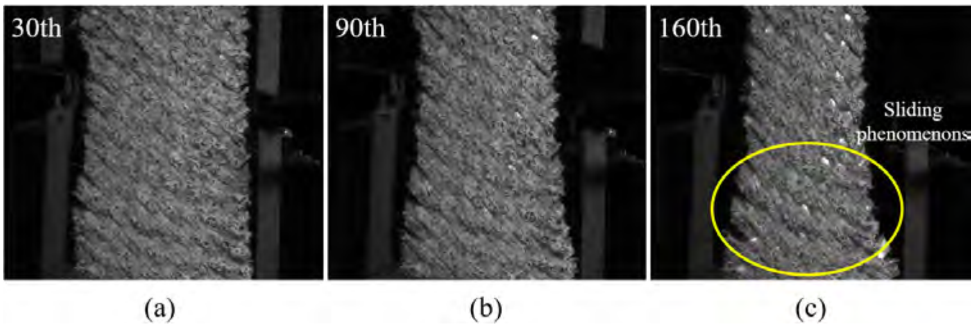

Figure 4.33: Images of the deformed specimen taken by the 5Mp+ telecentric camera system for extensions of 3mm (30th), 9mm (90th) and 16mm (160th).

These results made it possible to get to grips with the miniature traction machine. The latter fully satisfies the experimental requirements. The stepper motor provides smooth operation, and the displacement resolution is more than sufficient for this type of testing. The 50 N force sensor is widely and its resolution is considered excellent.

FE-DIC MEASUREMENTS

The images taken by the previously calibrated DIC stereo bench confirmed our fears. We were unable to make a shape measurement. We attribute this to light reflections from the surface of the tube and, to a lesser extent, to the fact that the tube was not included in the calibration process. Only the images taken by the telecentric were used afterwards.

A 2D measurement is then attempted using FE-DIC. A uniformly structured square mesh based on QUADTREE elements is again retained. It is rotated by 45° with respect to the tensile direction, as suggested in the chapter 2. The mesh (i.e. ROI) is adjusted so that it touches the lower tabs and the edges of the specimen. The different mesh sizes tested are given in Table 4.2.3.1. This table also gives the approximate number of pixels used by each element. The optical resolution in this case is about 2.86×10^{-2} mm/px.

Table 4.3: Mesh size in mm and approximate number of pixels used by an element.

Number of elements	22	15	11	8	6
Mesh size [mm]	0.943	1.371	1.857	2.571	3.429
Approximate number of pixels used by an element	33×33	48×48	65×65	90×90	120×120

Before we start our measurements, we want to estimate the final measurement resolution that can be expected with these settings. The classical approach described in Chapter 2 is used again (sub pixel artificial translations of the reference image).

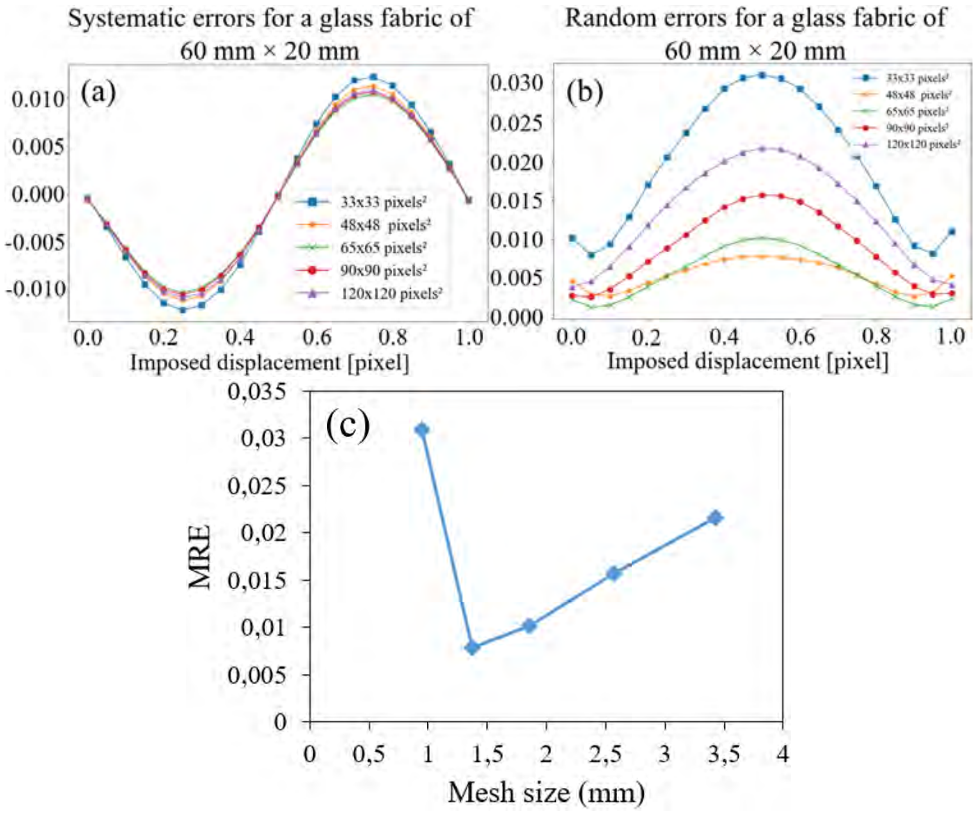

Figure 4.34: Evolution of the ultimate error as a function of mesh size for a 60 mm × 20 mm specimen of speckled glass fabric: evolution of the systematic error (a), the random error σ_e (b) and the median value of the random error, denoted MRE (c).

Fig.4.34 shows the evolution of the systematic error (a) and the random error (b) as a function of the element size considered. It can be seen that the systematic error is less affected by the variation of the element size. Moreover, its level remains low compared to that reached by the random error for a displacement of 0.5 pixels. Therefore, as in chapter 2, we now focus on the evolution of the median value of the random error (MRE), shown in Fig.4.34 (c).The minimum value of the MRE is reached when 15 elements are used in the width of the mesh, i.e. an element size close to 1.371 mm.

FE-DIC between reference and current image

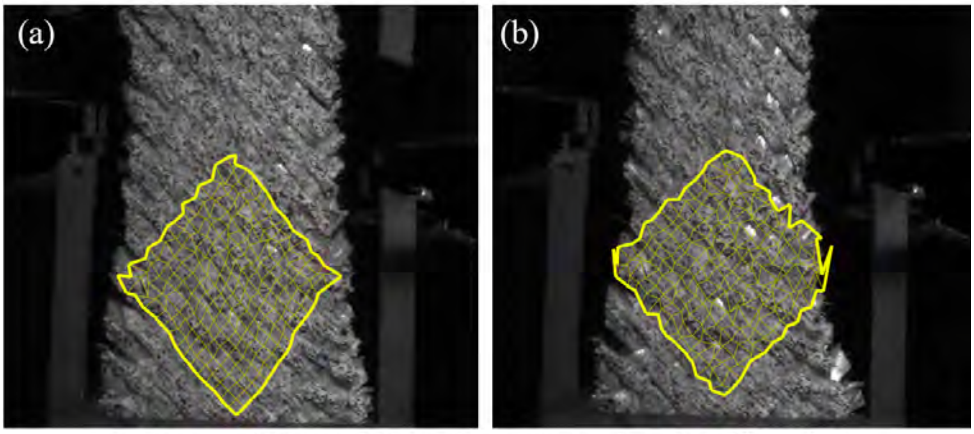

Incremental FE-DIC the reference image is updated based on the correlation residual.

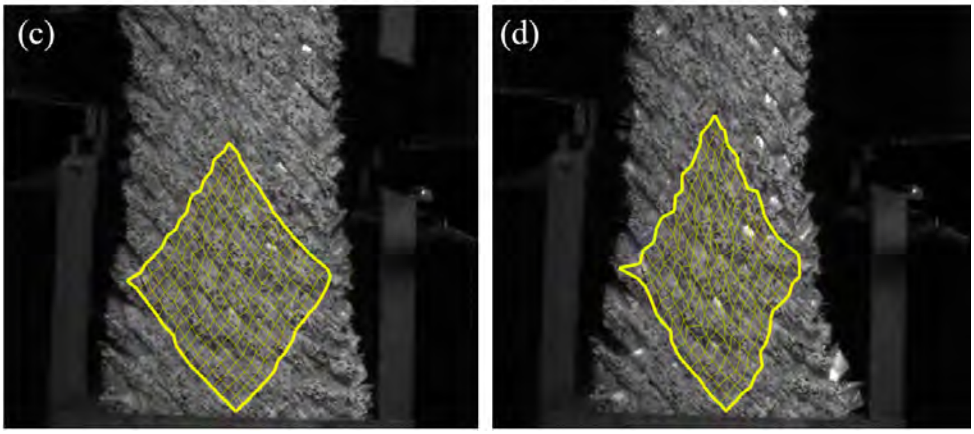

Figure 4.35: Displacement fields measured by FE-DIC (with Pyxel) when the displacement reaches 9 mm (left - 90th image) then 16 mm (right - 160th image): the deformed mesh is superimposed on the image. (a), (b) present the result obtained when the FE-DIC is carried out between the reference image and the considered image while (c), (d) present the result delivered by an incremental approach (in this case, updating the reference image when the correlation residual reaches 6%).

Fig. 4.35 shows the results of the FE-DIC measurements with the same mesh (15 elements wide), but either in the "classical" or in the "incremental" way (see chapter 3). Figs. 4.35 (a) and (b) show displacement fields measured "classically", i.e. without updating the reference image. The proposed images correspond respectively to displacements of 9 mm and 16 mm (corresponding to the 90th and 160th images, respectively). We observe that this method "unhooks" significantly (b), and this well before 16 mm of displacement is reached. Figs.4.35 (c) and (d) show the displacement field measured by regularly updating the reference image once the residual R residual reaches 6 %. Again, the incremental version of FE-DIC gives a much more satisfactory result for large transformations.

This section has demonstrated that a 2D FE-DIC measurement through the PMMA tube is possible. However, as mentioned earlier, we are fully aware that the results obtained, even with a telecentric system, should be questioned. In fact, the system should be calibrated to account for the presence of the PMMA tube in the optical path. If such a calibration is carried out, and taking advantage of the rotation of the machine during the RX scan, it should be possible to make stereo measurements on the surface of the samples during future in-situ tests (Pierré et al., 2017; Fouque et al., 2022).

4.2.3.2 Mini bias extension tests on speckle free specimens

The idea here is to assess the effect of speckle on the mechanical behaviour of such specimens. The small sample size makes this question all the more crucial. We therefore decided to perform bias tests on four untreated samples to make a comparison. The control parameters and the acquisition parameters are not changed: The image capture rate is set to 1 frame/sec and the motion speed is again set to 6 mm/minute.

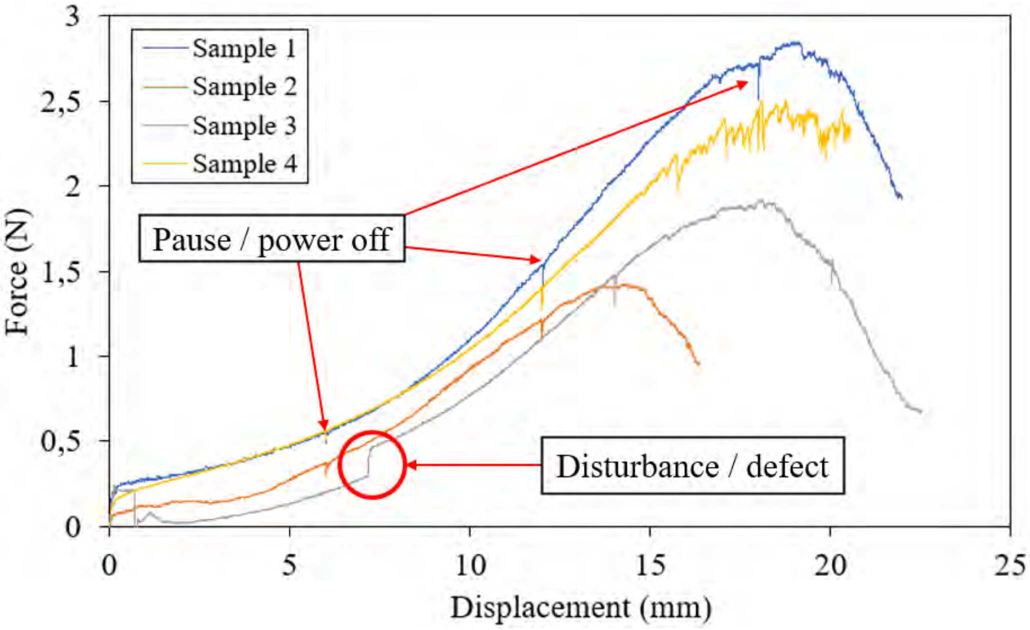

Figure 4.36: Force (N)/Displacement (mm) curves for the tension-extension test performed on unspeckled glass fabric samples using a miniature tensile machine.

Fig.4.36 unifies all the force-displacement curves obtained for the 4 unspeckled samples. There are significant differences with the previous results:

1. The first difference, which is obvious, is the huge difference in the maximum load supported by the specimens (minimum over 9N for speckled specimens, maximum under 2.8N for unspeckled specimens). The deposition of speckles must have several effects that can explain this observation: it can cause local sticking and/or increase the adhesion of the strands and fibres of the yarns to each other, thus increasing the rigidity of the glass fabric and the friction between the yarns. If the levels are different, the curve still retains the same appearance.
2. Overall, the maximum displacement seems slightly less important without speckle. Again, speckle seems to delay sample separation. However, this effect remains less pronounced than the previous one.

3. The results obtained for the non-speckled samples appear to be much more dispersed. Despite all the care taken in preparing the samples and setting them up, it seems that some of the observed dispersions come from these phases. Sample 2, for example, behaves very differently from the others (see Fig. 4.36). On closer inspection, the sample was not perfectly perpendicular to the horizontal plane (about 2.5° inclined) when it was mounted. The very low force values measured also give rise to measurement 'noise' and the effect of external disturbances due to the lower load, as shown by the area circled in red in the 4.36.

4.2.3.3 Intermediate summary for the *ex situ* testing part

In this part, we have implemented a miniature tensile testing machine that was developed on the occasion of this thesis. The machine was at this stage tested *ex situ* and several samples of speckled and unspeckled glass fabrics were tested. The machine worked perfectly and the results obtained demonstrate

- the efficiency of the sample preparation method.
- the considerable influence of the speckling on such small samples. This observation will lead us to reconsider our speckling technique to make the DIC measurement much less intrusive in the future. In addition, the results obtained on the unspeckled fabric encourage us to consider future studies on slightly larger fabrics with potentially smaller patterns.
- that it would be possible to perform stereo DIC on the surface of the specimen in the tomograph during the test in situ. However, a calibration phase linked to the presence of the PMMA tube between the objective and the tissue must be considered.

It was also checked that the electronics could be connected and disconnected without any adverse effect on the test and the measurements taken. This will make our task much simpler (no cables that could wind up in a dangerous and erratic way).

Finally, on the basis of this work, we can now define in advance a sequence of stages during the loading of the specimen *in situ* during which the specimen is scanned.

4.3 *In situ* bias extension tests

4.3.1 Experimental setup and operation

We are now carrying out the first in situ bias extension tests with our machine in our μCT. Figure 4.37 shows a schematic diagram of the complete installation and a photo of the experimental setup in the X-ray protection cabin.

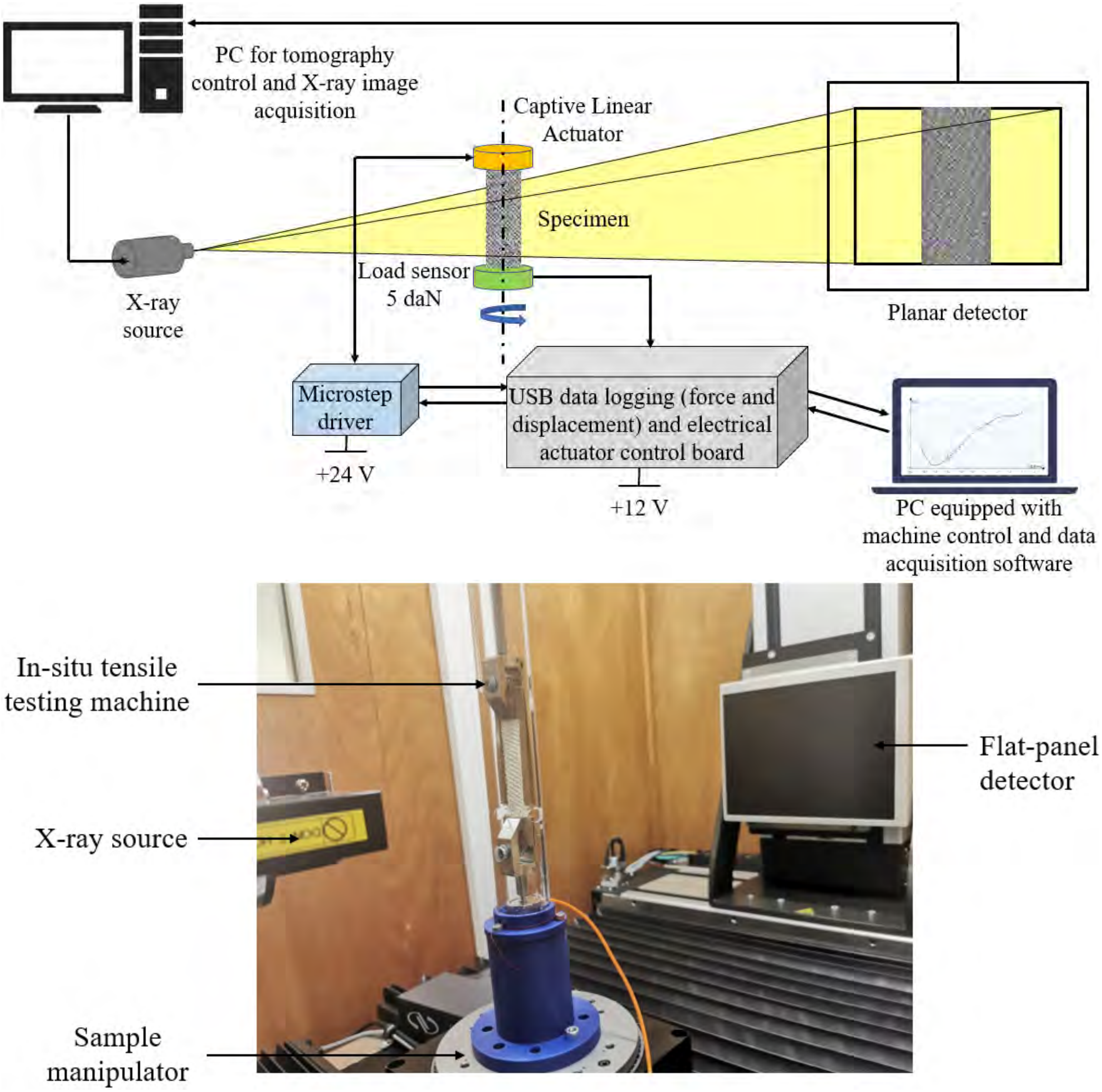

Figure 4.37: Photo showing the *in-situ* traction machine mounted in the ICA tomograph (bottom). A diagram shows the entire system implemented during these tests (top)

The main phases of the installation are described below. The sample is first mounted inside the mini machine and the entire process is initialised outside the tomograph (start-up, acquisition and control parameter settings, displacement/load zeroing, etc.). The travel speed is set at 6 mm/minute. The *in situ* machine is disconnected, then mounted in the CT scanner as shown in Fig. 4.37. Its mounting base is screwed onto the rotation plate. The side posts of the frame are finally cut to release the tissue (the necessary holes have been moved so that they do not appear in the tomographic image).

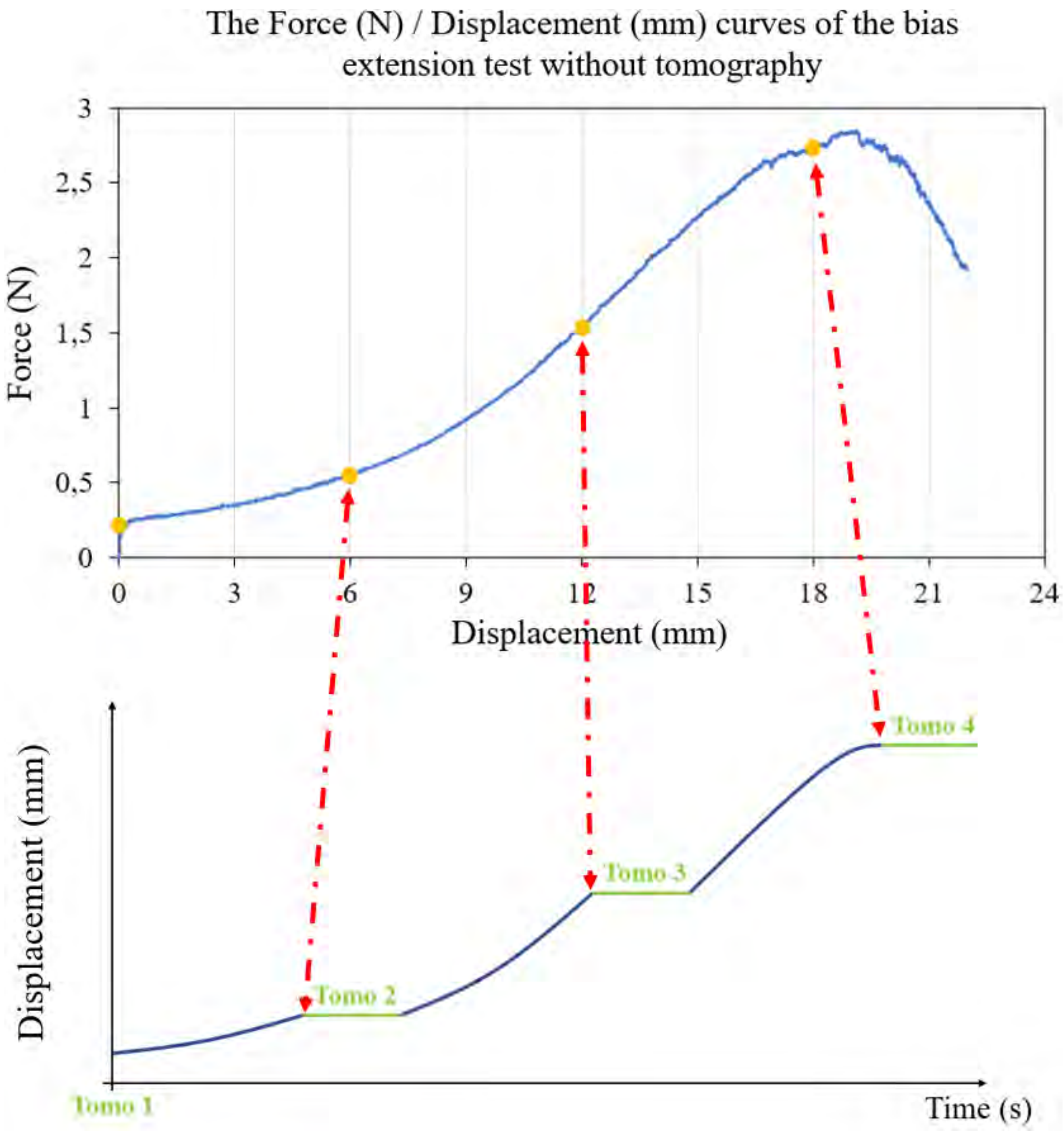

Figure 4.38: Typical load/displacement curve obtained for a glass fiber specimen. The yellow dots indicate the levels at which the scans were planned. In practice, each scan requires an interruption of the displacement. The plateaus required are symbolized in the displacement/time figure presented above and last approximately 48 minutes here.

We had planned to do about 4 CT scans. In addition to the reference image, we wanted to take at least 3 'deformed' images. One of these should be close to the peak load. The typical elongation of an unspeckled fibreglass sample close to the separation is around 18 mm (see Fig. 4.38). Figure 4.38 illustrates the sequence of these scans.

After the first tomography, the electrical cables were reconnected to the machine, a displacement of 6 mm was requested on the mobile grips and the load and displacement acquisition started again. Once the displacement and effort have stabilised, the cables are disconnected and a new scan is performed. The operation is repeated until the peak is reached.

The CT acquisition parameters are given in the table 4.4. The resolution of the image obtained here is of the order of 26 μm/vx. Each plateau here lasts about 48 minutes. The imaged region does not cover the entire height of the tissue sample, but more than half of it. It focuses on the lower part of the sample, starting to the right of the lower heels. In this way, the area of interest remains within the imaged region. In fact, we want to follow the deformation of the transition zones for as long as possible, without sacrificing too much resolution (to give us every chance of still being able to guess the orientation of the fibres and reconstruct DIB models in good conditions).

	Parameters	**Value**	**Unit**
X-ray focal spot size	Tube power	21	W
	Tube voltage	70	kV
	Tube intensity	300	μA
Imager	Mode	1×1 0.5pF VG1	
	Frames per second	4	
	Calibration	128	
	Digital gain	1	
	Rotate/mirror	Normal	
	Average	8	
Control	Generator H	206.2585	mm
	Generator V	0.0000	mm
	Imager H	203.8464	mm
	Imager V	-234.5667	mm
	Imager Zoom	-1.1082	mm
	Rotation	180.4425	°
	Zoom	0.0000	mm
Acquisition	Total number of images	1440	
	Geometrical Zoom	4.85	
	Optical Zoom	1.00	
	Voxelsize	26.21	μm
	Volume height	35.1	mm
	Volume diameter	47.6	mm
	Slices	1339	
	Estimated time	0:48	hh : mm

Table 4.4: Filters and settings of the parameters during the tomography experiment.

4.3.2 Results

Fig.4.39 shows the force (N)/displacement (mm) curve recorded during the *in situ* test. This curve is similar to that obtained in the previous section, with a maximum force estimated at 1.914 N and a maximum strain of approximately 16.345 mm. Minor, almost imperceptible disturbances of the measurements (especially of the load) result from the various connection and disconnection operations.

In terms of tomography, 4 scans were actually performed. The displacement levels at which the scans were performed are reported in Fig. 4.39. The corresponding recon-

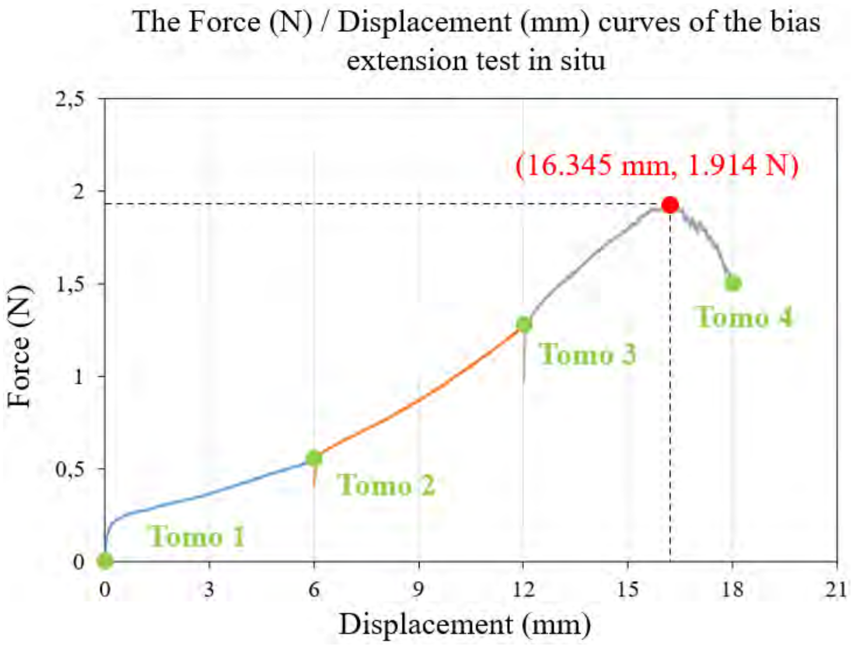

Figure 4.39: Load (N)/displacement (mm) curve recorded during the bias extension test performed in the ICA tomograph. Completed scans are reported (displacement = 0, 6, 12 and 18 mm).

structed images are shown in Fig. 4.40. Compared to the high resolution images obtained in section 4.1.2, a decrease in resolution and sharpness can be observed. We no longer distinguish individual fibres, but the architecture of the fabric is perfectly defined at the yarn level.

The manipulation went perfectly, and this first *in situ* bias extension test is a success. The manipulation went perfectly and this first in situ bias extension test is a success. Nevertheless, it would be desirable to simplify the operations, in particular by limiting the number of connections and disconnections. An evolution of the machine and/or the wiring is planned. Finally, the whole system would benefit from better integration.

4.3.2.1 The evolution of yarns during the bias extension test (preliminary observations)

The movements and cross sectional changes of the warp and weft yarns during the experiment could be observed from the reconstructed images (Fig. 4.40). On the macroscopic scale, the scans corresponding to the 12 mm and 18 mm displacements are particularly revealing. At a stretch length of 12 mm, the shear angle between the warp and weft yarns has not yet reached its maximum value. When the stretch length is 18 mm, we have passed the peak and the shear angle has already reached its maximum value. The slippage and separation between the warp and weft yarns develops in the green zone. It is clear that the warp and weft yarns where separation occurs are at the boundary of three zones (shear-free zone, semi-shear zone and pure shear zone). This phenomenon is related to the complexity of the shear forces at the boundaries. This phenomenon is also due to the small width of the sample and wrinkles are observed when the sample size is large enough.

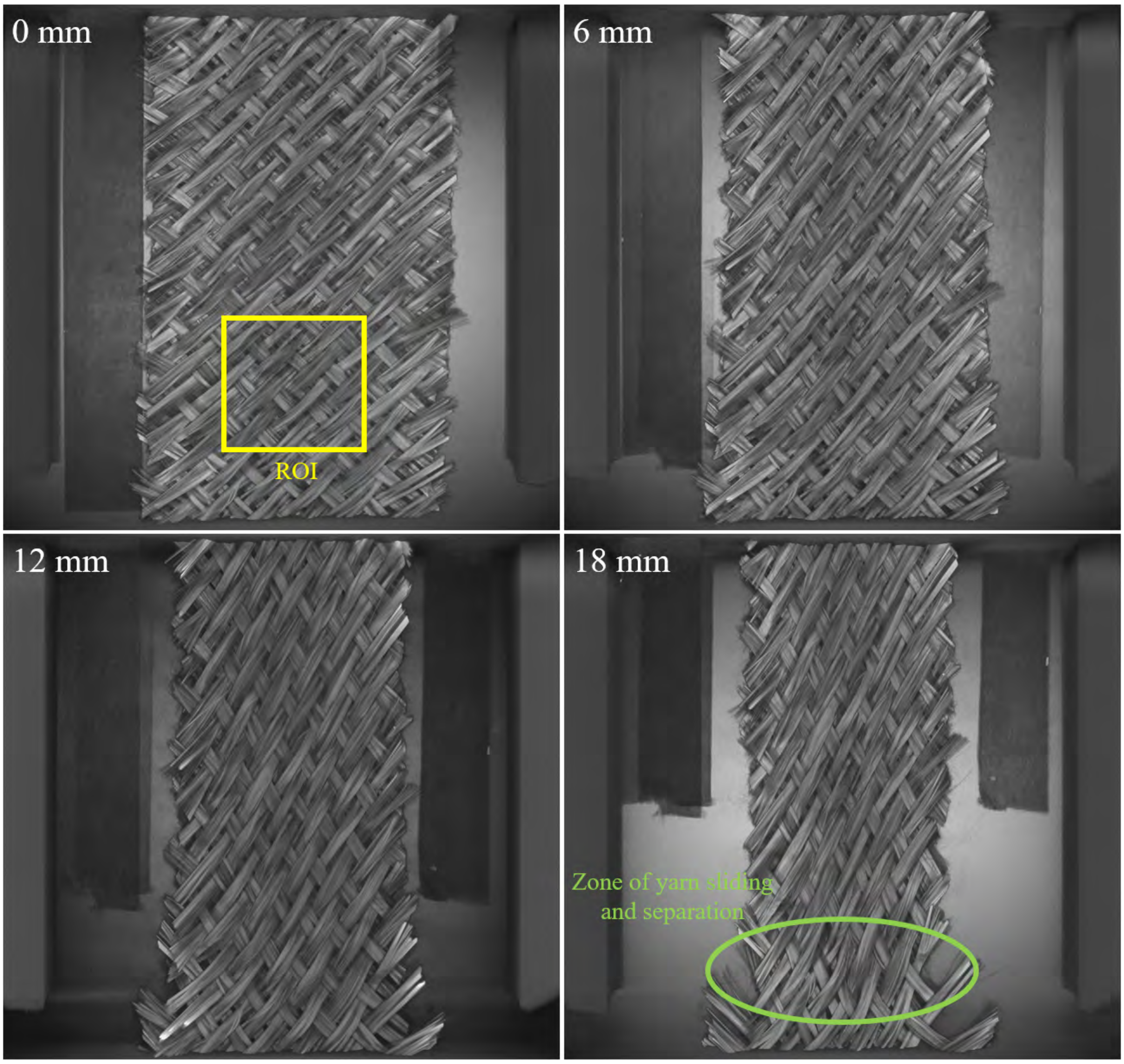

Figure 4.40: 3D reconstructed images from scans taken at the four different stages of the bias-extension test. The yellow area is the ROI and the green area is the zone where warp and weft yarn slippage and separation were observed.

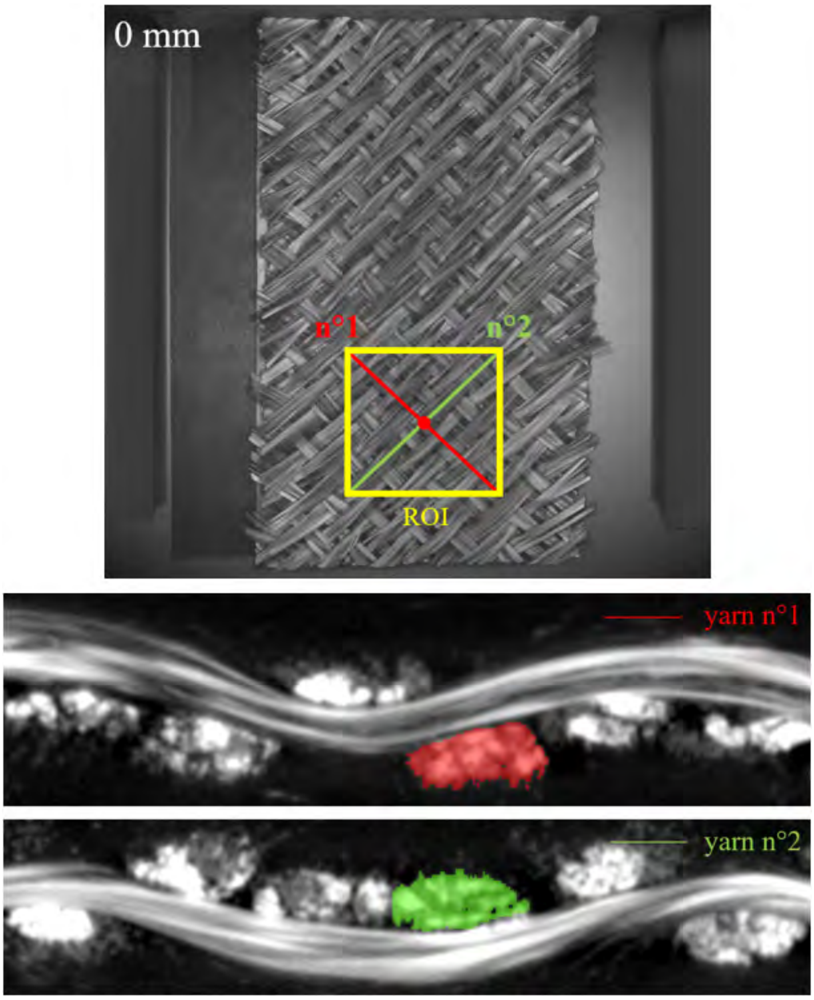

Figure 4.41: The position of the selected cross sections.

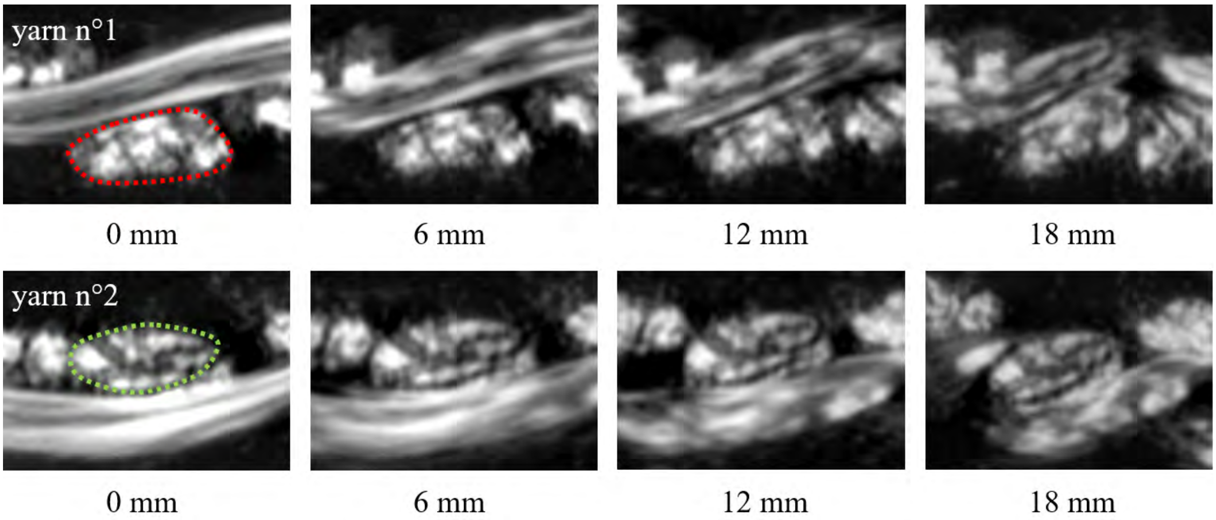

0 mm 6 mm 12 mm 18 mm

0 mm 6 mm 12 mm 18 mm

Figure 4.42: The evolution of yarns' sections during the bias extension test.

On the mesoscopic scale (yarn scale), more complex kinematics between the yarns are observed. Here, as shown in Fig. 4.41, we focus on the warp and weft threads located at the intersection of the three regions are selected (yarns n°1 and n°2). The shape of these threads changes as the stretch length increases. Let's consider yarn no.1. We can see that:

1. Its cross-section at 6 mm extension shows no significant change from the initial state. All that can be observed is that the distribution of pores in the cross-section of the yarn crossing it has changed. This means that the angle between the warp and weft wires changes and the interaction force is weaker. The shear force applied is counteracted by the reduced distance between the threads. And there are always gaps between adjacent threads.

2. When the imposed displacement reaches 12 mm, the first thing observed is the aggregation of adjacent parallel yarns. It is obvious that the gap between the threads disappears. This is due to the reduction in the angle between the warp and weft threads caused by the shearing force. It can also be seen that the pores within yarn n1 are reduced and the cross-sectional shape is slightly altered due to the interaction with adjacent yarns. The cross-section of n1 is rotated relative to the initial state due to the compressive force of the adjacent wires. The interaction forces between the wires become greater in this state and the change accelerates.

3. When the stretching length is 18 mm, the wires are closer together than before. And because of the interaction between wires, it is possible to observe a large change in the shape and position of adjacent wires. The cross-section of the wire is reduced once again.

4.3.2.2 FE-DIC from radiographs?

We did not to try a DVC Bay et al. (1999); Roux et al. (2008) measurement on the reconstructed tomographic images at this stage. On the other hand, we tested a 2D FE-DIC based directly on the x-rays projections, just out of curiosity (Russell and Sutton, 1989). The Pyxel library is again used to perform FE-DIC.

Four "orthogonal" projections (sample parallel to the detector) are extracted from the four scans performed (see Fig. 4.43). The dimensions of the obtained grayscale images are 1289 × 974 pixels². The ROI is restricted to the lower part of the specimen as depicted on Fig 4.43. The measurement FE mesh is square, structured, uniform and is based on Q4 linear elements. It is generated with Gmsh software. The size of the elements is obtained by fixing the number of elements to the width of the ROI, as shown in Table.4.3.2.2 :

Table 4.5: Element size in mm and approximate number of pixels used by an element.

Number of elements	13	9	7	5	4
Element size [mm]	1.362	2	2.553	3.617	4.511
The approximate number of pixels used by an element	32×32	47×47	60×60	85×85	106×106

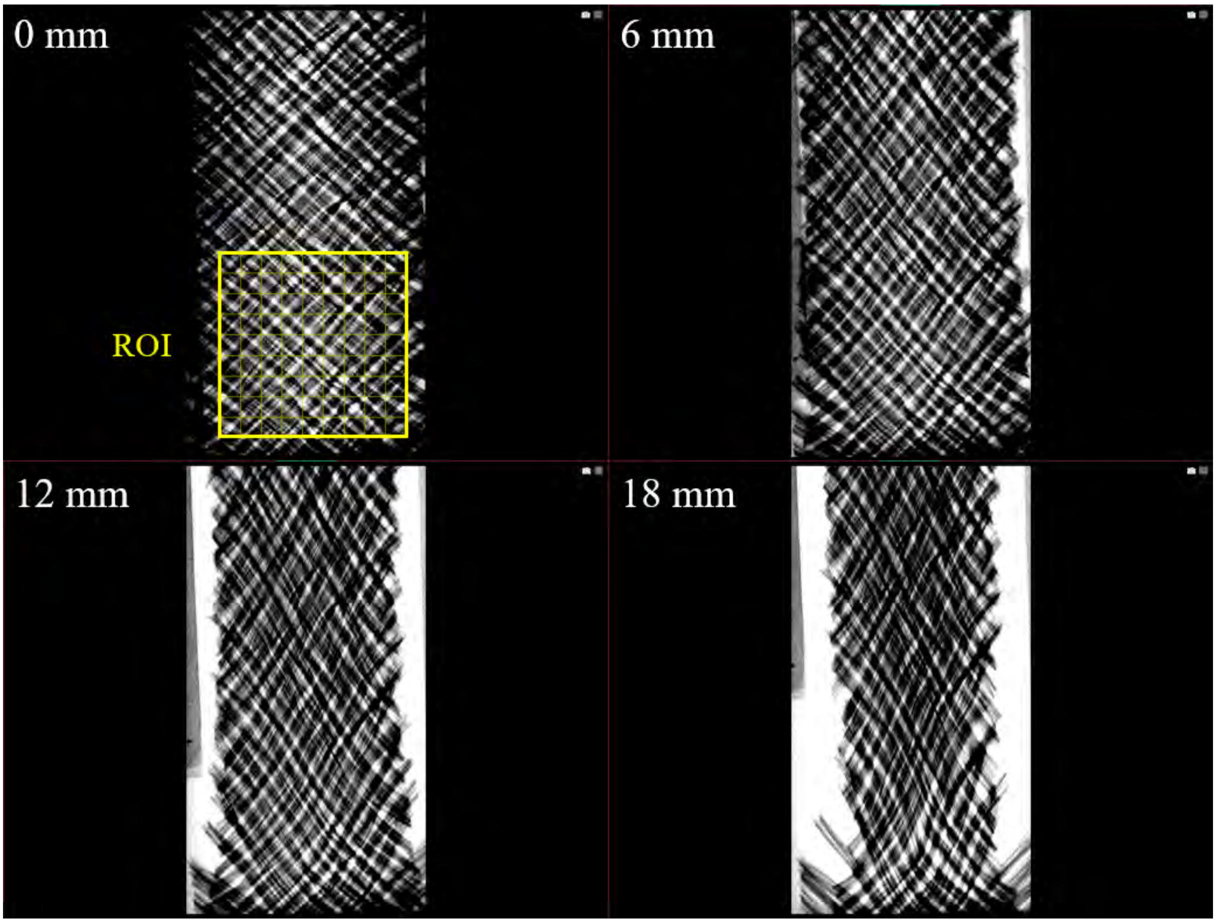

Figure 4.43: Orthogonal projections are extracted from the scans for the four steps of the bias test to test a radiograph-based 2D FE-DIC. The yellow square indicates the ROI.

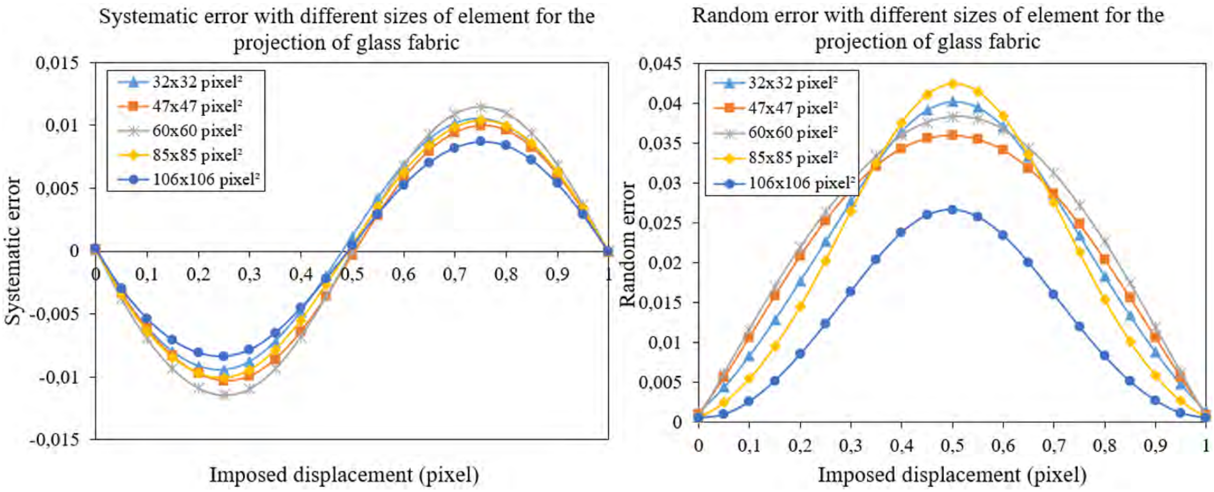

Figure 4.44: Evolution of the systematic error and the random error as a function of the size of the elements in the case of a 2D FE-DIC analysis based on simple radiographic projections.

The usable texture here is simply consecutive to attenuation gradients. Once again, an *a priori* study based on "artificial subpixel translations" is considered. Fig. 4.44 shows the evolution of systematic and random errors as a function of the element size. The median random error (MRE) reaches a minimum value when the mesh size is around 4.5 mm. However, such a coarse mesh will not allow to properly capture the kinematics. In what follows, an element size of 2 mm will rather be adopted.

(a) The displacement field calculated by the DIC-FE method with the mesh size of 2 mm.

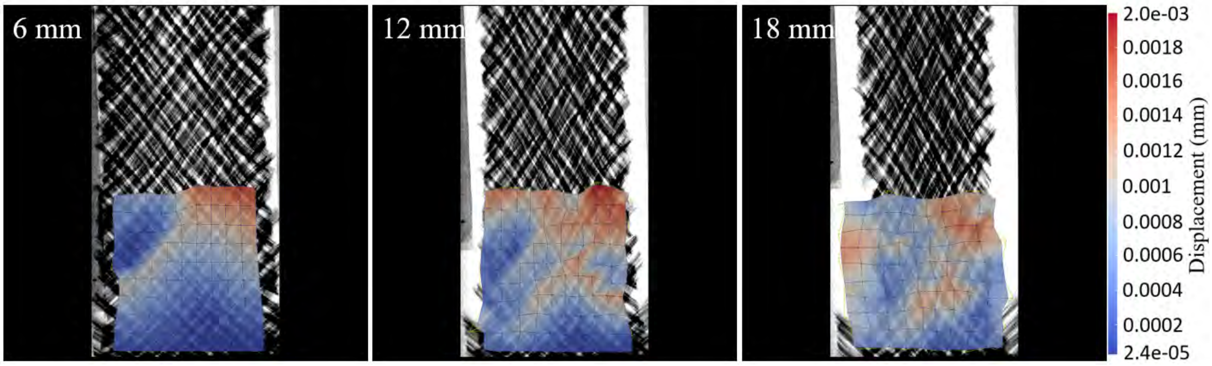

(b) Correlation residual map calculated for the projection of glass fabric

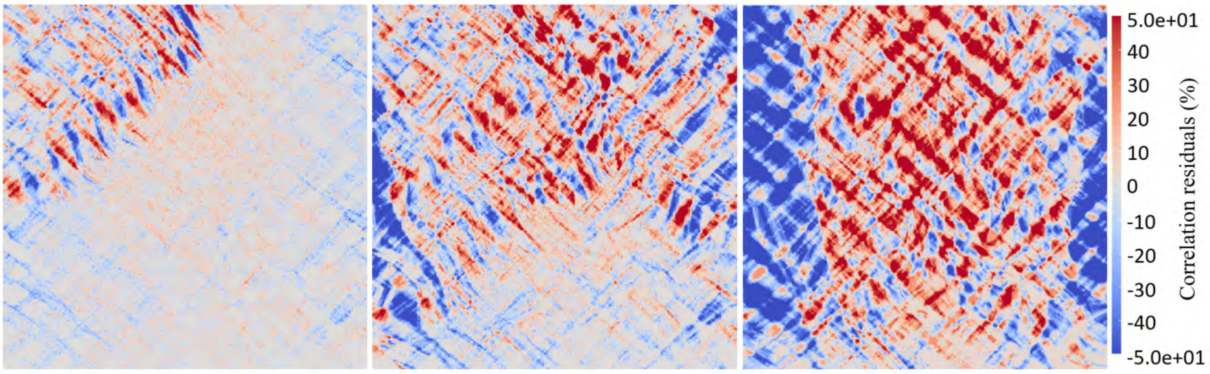

Figure 4.45: FE-DIC measurements based on radiographs with the mesh size of 2 mm (displayed with ParaView). (a) Displacement field along the loading direction, in mm (b) Correlation residual map (in %).

The 2D FE-DIC results obtained using Pyxel are shown in Fig.4.45. Fig.4.45 (a) shows the displacement field measured using an incremental approach (such as the first one introduced in Section 3.2.1). The reference image is here updated at new level. For the first displacement level studied, the method manages to provide results consistent with our expectations in a good part of the ROI, as evidenced by the low correlation residuals (cf. Fig.4.45 (b)). However, a non-negligible part of the ROI (top left of the ROI) gives aberrant results. This is probably due to the initialization of the DIC, which is difficult to achieve given the level of deformation. It is in this part of the specimen that displacements are most significant. The size of this region increases as displacement increases, and the mesh gets increasingly " unstuck ". In the second stage, for a displacement of 12 mm, only the "unsheared" part still gives realistic results. At the last stage, the algorithm is totally lost.

In addition to the significant impact of the relative displacement between two images (6mm/60mm), which is probably the main cause of our concerns, the architecture of the material is also evolving and may not help to correlate images.

4.3.2.3 Attempt to automatically generate DIB models from manually segmented images

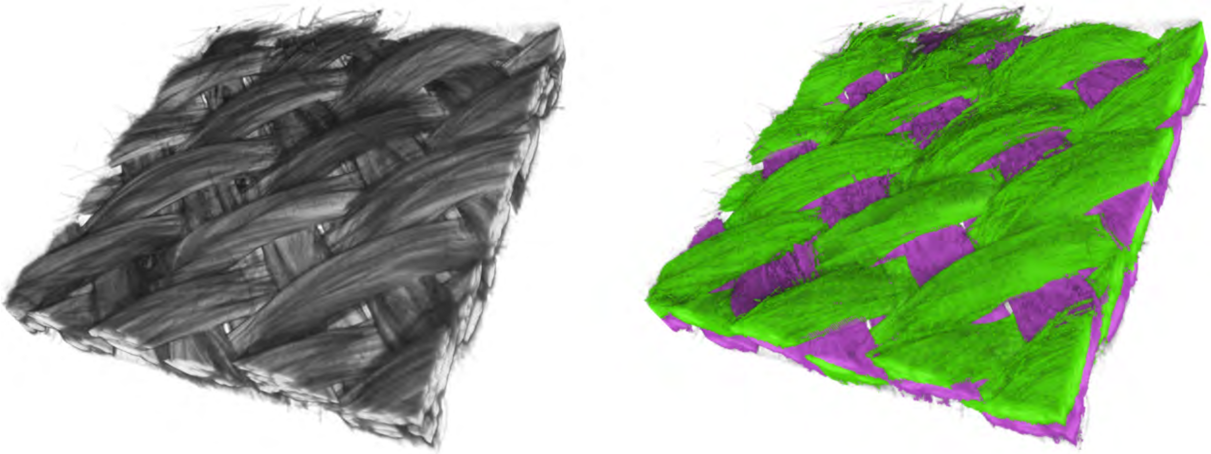

(a) 3D reconstruction model

(b) Individual marking of warp and weft yarns

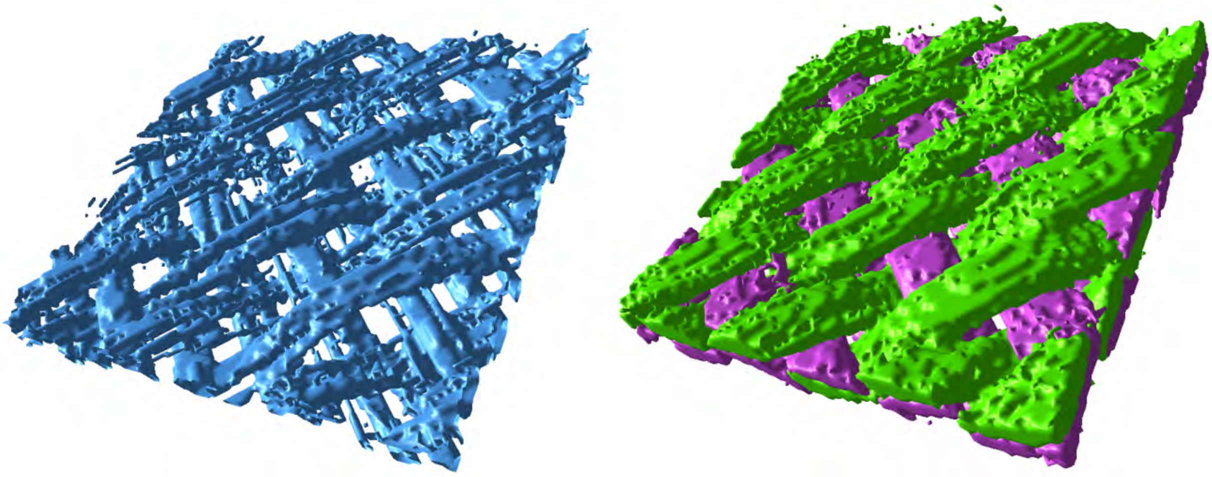

(c) Contour mesh of 3D reconstruction model

(d) Contour mesh of the model after marking

Figure 4.46: Contour surface meshes (STL) obtained from the reference volume image : (a) raw reconstructed tomographic image cropped in the ROI; (b) segmented image produced by manual individual marking of warp and weft yarns; (c) contour surface mesh directly generated from the reference reconstructed image; (d) Contour surface meshes automatically generated and based on the segmented images

In this part, we want to evaluate the potential of reconstructed tomographic images for the generation of DIB models. As we no longer had time to repeat the approach proposed at the beginning of this chapter (by updating a TexGen model), we just attempted a manual 3D segmentation and meshing of the yellow area of the ROI in Fig.4.40. The reconstructed image cropped in the ROI is shown in Fig. 4.46 (a). Fig. 4.46. The warp and weft strands are marked separately on each tomographic image, in order to separate the strands. Fig. 4.46 (b) illustrates the result of a segmentation. The warp and weft threads are well separated. Fig. 4.46 (c) shows a contour surface mesh (STL) based directly on the reconstructed image. If the warp and weft strands are recognizable, their shape and the contacts between them are not well represented. Fig. 4.46 (d) presents the contour mesh of the model produced this time after segmentation. This contour mesh seems more representative than the previous one.

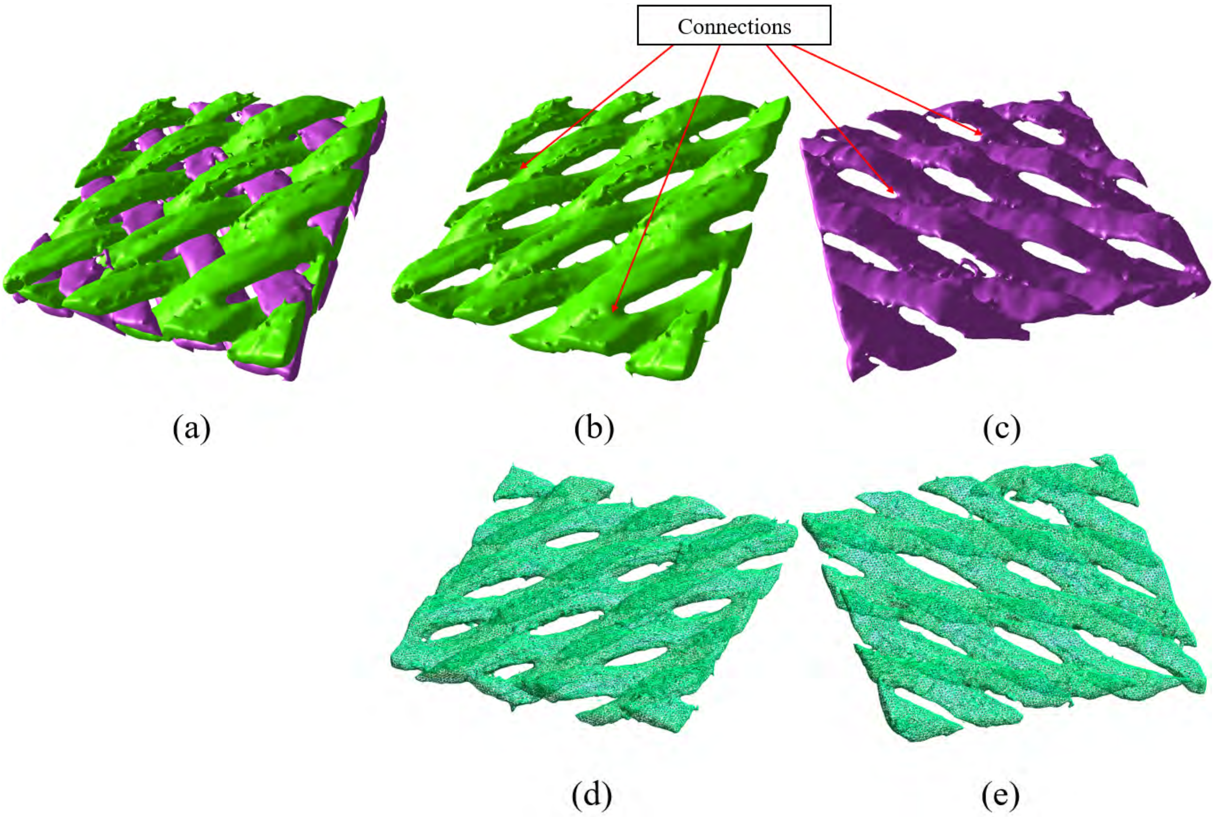

Figure 4.47: (a) Contour surface mesh after smoothing; (b) warp yarns; (c) weft yarns; (d) warp yarns surface mesh imported by Gmsh; (e) weft yarns imported by Gmsh.

However, on closer inspection, the contour meshes obtained from the segmented image have a major flaw. Figs.4.47 (b) and (c) indeed show that there are still "menisci" between the wires in the same direction. This is caused by errors when marking the wires and when generating the contour mesh using the Dragonfly software. Contour mesh files can be opened and edited in Gmsh software. Figures (d) and (e) correspond to two meshes thus treated. This processing can be tedious and becomes eminently manual.

This experiment shows that the mesh of the images captured during the in situ test must be able to be used to generate DIB moodels. It also reinforces our desire to move towards a segmentation based on a geometric a priori (use of a CAD model).

4.3.3 Intermediate summary for the *in situ* tensile test

This section completed the *in situ* bias test with x-ray tomography. And three orientations were proposed based on the experimentally obtained 3D reconstruction models and projections: (1) The most intuitive one is the study of yarn scale observation through 3D reconstruction models. The main target is the study of the structure between yarns and the kinematics of the yarns during the bias test. A simple modeling of the textile unit cell was carried out by Texgen software. Also, it was observed the change of shapes and rotations of yarns at the yarn scale through 3D reconstruction models at different stages of the experiments. Due to the small size of the sample, relative sliding between yarns was observed in the second half of the experiment. This conclusion cannot be generalized to large size fabric samples for the time being. (2) The connection between the bias test and X-ray tomography was found by tracking the displacement field with the grayscale images of the projections. And the feasibility of tracking the displacement field of samples by grayscale images of projections was verified. However, due to the time limitation of the experiment, the bias test was not divided into sufficient number of stages. This resulted in excessive errors in the calculated displacement field. The solution is to increase the number of tomography in order to obtain more projections. (3) An attempt was made to directly export a model from the 3D reconstruction model that could be used for numerical simulations. However, the results were not satisfactory. The reason is that the ROI region in the tomography is too large and the resolution is too low. It is possible to try to reduce the ROI region of the tomography.

In addition, a lot of work needs to be done on the wiring to make the machine easier to use. Finally, in order not to compromise the project, a large proportion of the machine's parts were produced using polymer additive manufacturing. For the tests envisaged in this thesis (very low loads), this type of solution was viable. However, the machine is intended to be used for other applications. Since the trials, a version more in line with the initial design (machined aluminum alloy parts) has been assembled and tested.

Automation of segmentation and labeling tasks would make sense in the future if the work were to be repeated.

Finally, a bias-extension test, unpublished to our knowledge, was carried out. During the test, four intermediate resolution scans (between that obtained by zooming to maximum and that which would allow the entire specimen to be followed from the beginning to the end of the test) are recorded. They make it possible to perfectly follow the deformation of the reinforcement in the transition zones. Two rapid attempts to exploit these images have been proposed. The first concerns the measurement of displacement which relies directly on radiographs. The results simply reinforces the idea that the measurement of displacement by volume correlation from such tomographic images in such a context is a real challenge (e.g., large displacement, texture/microstructure link, complex kinematics). The idea of assisting the measurement by relying on a DIB model seems particularly attractive Rouwane et al. (2023b). The second attempt concerns the "fast" generation of a DIB model which would dispense with the CAD modeling step (eg carried out with TexGen). The results then highlight the challenge represented by the segmentation and meshing of such microstructures. These observations confirm that the idea of adjusting a CAD model from the images is probably a way to be preferred.

4.4 Chapter summary

Our aim was to set up the necessary ingredients for a meaningful test-computation dialogue at the mesoscopic scale on the basis of a bias extension test carried out in a lab μCT. An image-based model generation approach is proposed and a specific mini-machine is built and operated. In this chapter, we have succeeded in removing several obstacles that we will have to face in order to achieve such a goal:

- **Preparation of small samples**. Glass fibre satin samples have been manufactured. Their dimensions are chosen with the aim of obtaining favourable tomographic images while maintaining 2 unit cells in width. A procedure inspired by that used in previous chapters has enabled us to produce test specimens. The addition of a cardboard frame is suggested. This arrangement has greatly simplified handling, for example during the first tomography tests carried out under representative conditions, and above all the mounting of the specimens during the *in situ* test. The first reconstructed tomographic images produced are sufficiently well resolved to allow perfect identification of the yarns and even their structure.

- **Image analysis**. The tomographic images reconstructed under *in situ* test conditions thus provides a wealth of information on the material's architecture. When we zoom to the maximum (max resolution), voxel size is close to the glass fiber diameter. The high-resolution images produced even make it possible to highlight each individual glass fibre and facilitate the manual image segmentation. It should also help defining the local orientation of the fibers within the yarn. During the *in situ* test, slightly more than the bottom half is scanned. Even if we move away from the ultimate resolution, this choice makes it possible to reduce the scanning time while following the displacement of the transition regions until the separation of the sample. Those images enables us to trace certain key dimensional and structural parameters of the glass fabric during the experiment.

- **DIB model**. Textile unit cell modelling was carried out using the reconstructed HR images with Texgen software. The images obtained beforehand allow a segmentation of the image which helps to extract some key parameters of description of the architecture. The TexGen were subsequently updated and more realistic CAD models are produced. First EF simulations of a "micro" bias extension test based on a simplified (but realistic) microstructure CAD model are performed in Abaqus. The results obtained have been used to generate the synthetic images used in section 2.3.

- ***in situ* tensile machine**. A miniature tensile machine adapted to bias testing on small samples was designed and assembled during this thesis. It enables samples to be subjected to high levels of deformation while simultaneously observing the material's internal architecture and visualizing its surface. It was first tested *ex situ* by testing several speckled or unspeckled glass fabric specimens. These experiments allowed us to familiarize ourselves with the machine and to check its operation. We were also able to verify that the machine will make it possible to obtain usable images of the surface of the sample.

- **2D FE-DIC during an *ex situ* test performed with the mini tensile machine**. A speckle pattern was deposited on some samples, and tests monitored by a camera equipped with a telecentric lens were carried out using the miniature machine *ex situ*. 2D FE-DIC measurements were successfully carried out on the surface of the fabric through the PMMA tube.

- ***in situ* bias extension test**. An experiment was finally successfully carried out in an X-ray microtomograph. Four scans were taken at different stages of loading. The evolution of the material's architecture is clearly visible. The limitations of conventional approaches that could be carried out with these scans are then illustrated: first, a 2D FE-DIC method based on radiography is tested, as well as automated mesh generation.

The first ambition for the future is to use the X-ray CT to automatically build a digital image-based (DIB) model of the unit cell and track its deformation during a test performed *in situ*. In particular, we plan to measure kinematics by combining regularised volume correlation (Rouwane et al., 2023b) and surface measurements using stereo DIC (Fouque et al., 2022). Secondly, in a longer perspective, we aim to identify some constitutive parameters introduced in the (meso) model. We have clearly identified limits with this respect.

- For example, the question of the impact of speckle on the behavior of fabrics in this type of situation cannot be eluded. We have to develop speckling techniques that limit its effect.

- Another hard point concerns the construction of DIB model. For the time being, a large number of manual operations are necessary and the model results from several operations (segmentation, measurements, generation of meshes, etc.). The ANR AVATAR project should contribute to finding a way to use an *a priori* on the geometry (in the form of the CAD model) to automate the generation of such models.

- Our initial simulations also highlight the challenge posed by the simulation part of a test. Even though the models used are small and only incorporate part of the non-linearities (only friction between the strands is taken into account), the calculation times observed are deemed prohibitive in relation to the objectives (e.g. for identifying the constituent parameters).

- Even in its latest version, which incorporates all the major aluminium alloy interface parts, the in-house developed machine still has some limitations. In its current state, it can only handle certain types of samples. It is planned to purchase other actuators and develop other equipment to extend the range of applications.

Conclusion and outlook

The initial aim of the thesis was to evaluate FE-DIC in the context of fabric characterisation and forming experiments. This technique, which has not yet been used in this context, would greatly simplify the dialogue between the tests and the simulation. In this work, we have focused on the bias extension test. 3 types of fabrics were tested: glass, carbon and C/PPS (commingled) fabric.

Chapter 2 discusses the evaluation of 2D FE-DIC measurements in such a context. The experiments are imaged using a telecentric lens which targets a restricted ROI of the sample on the side of the fixed grip (including the 'rich' transition regions between the 3 typical zones encountered in these tests). The level of deformation remains moderate. A simple uniformly structured mesh based on Q4 linear elements is used. A speckle development work was carried out for each of the fabrics. An original procedure for specimen preparation, based on the addition of a temporary frame, was also proposed. It allows good control of the test and greatly simplifies the handling prior to the test. Two elements are taken into account to select the appropriate measurement mesh size and orientation: the final error of the FE-DIC estimated from the reference images of the speckled specimens, and the correlation residual (indication of the quality of the registration performed). These studies show that the mesh size must be carefully adjusted. Initially, the reduction in the ultimate error encourages the use of rather large elements, but then the natural texture of the fabric makes correlation difficult. In a rather unconventional way, this study leads to an ideal element size which seems to be close to the width of the yarns. The correlation residuals, on the other hand, show that it is essential to use small elements to represent the complex underlying kinematics. The residuals also highlight all the places where a continuous description of the displacement field is inappropriate. A linear interpolation in a large element (with respect to the yarn width) can in no way represent the true underlying kinematics, particularly at the level of a crossing between yarns. Finally, for some fabrics, the orientation of the mesh seems to have a clear impact on the overall level of the correlation residuals. It appears that, at least when the size of the element is greater than the width of the yarns, the mesh is more likely to be oriented when the direction of the yarns is indicated. However, some experimental results were not consistent with this conclusion. The factors influencing this phenomenon could be further investigated by repeating the experiment and using synthetic data. A first step towards the synthesis of representative test images to challenge FE-DIC is then presented. An image-based 3D model is built (see chapter 4) and then manually coloured. A non-linear calculation in Abaqus is then used to generate images of plausible situations. For now, the "synthetic" speckle and its generation are perfectible. Finally, in spite of the care taken to produce the "real" speckle, it has shown its limitations (flaking, reflections, etc.).

Chapter 3 is concerned with the delicate issue of the measurement of large deformations of the fabric in the presence of large deformations. Indeed, in this case the kinematics become increasingly difficult to describe and it is less and less possible to say that the texture is passively advected. In this work, the initial reference nodes were followed visually to have a point of comparison. We first show that the measurement error with a "classical" FE-DIC (without updating the reference image) leads to both large measurement errors and large correlation residuals. A first incremental method is then proposed. The idea is to update the reference image and the mesh every time a new image is acquired. The gain is obvious, but the measurement errors remain significant. These errors result from the accumulation of the measurement uncertainties associated with the very large number of incremental measurements (uncertainty in the displacement obtained and incorrect positioning of the deformed mesh for the future measurement). An incremental method constrained by the level of the correlation residual is therefore proposed. Its contribution is illustrated on the basis of tests carried out on glass fabrics. The results obtained for different residual levels are compared. An "optimal" threshold is then identified. This type of incremental approach has also shown interest for other fabrics. However, the error generated by the complex kinematics between the yarns is enormous for carbon fabrics, especially in the transition zones.

If we were to continue to use a telecentric lens to carry out 2D FE-DIC, it seems to us that an attractive way would be to use a conformal mesh, which would be built from the knowledge of weaving, in order to follow each yarn independently. Each yarn would then be meshed independently. In particular, the knowledge of the weave would be used to deal with visibility problems. On the other hand, with similar image definitions and speckles as those encountered in the tests presented, it is inconceivable to hope to make measurements with proper resolution (even with a single element in the width of the yarn). We are therefore considering the use of regularisation techniques. In particular, we plan to test the technique proposed by (Chapelier et al., 2021). Another possibility under consideration would be to take advantage of a beam-type kinematics (Hild et al., 2009).

The fourth chapter sets up elementary building blocks to establish a 3D test/simulation dialogue at yarn scale using data acquired during a mini-bias extension test performed *in situ* in a X-Ray μCT. The idea is to take advantage of X-ray scans to build a Digital Image Based (DIB) model of the fabric and to better estimate its deformation by FE-DIC (conformal mesh inherited from the model) and/or Digital Volume Correlation (DVC). Miniature specimens attached to a temporary frame are designed and scanned. The reconstructed volumetric images are manually segmented in order to adjust the dimensions and orientations of the sections of the yarns defined in the CAD model prepared in TexGen. A simulation of a micro-test mimicking a bias extension test was carried out in Abaqus.The latter were used to generate the synthetic images presented in Chapter 2. The difficulties associated with several steps requiring human intervention (segmentation, CAD registration, meshing) are highlighted. A mini tensile machine designed to perform *in situ* tests is then used to perform bias extension tests on specimens (comparable to the previous ones). The operation of the machine is validated *ex situ*. The feasibility of 2D FE-DIC measurements is demonstrated. On the other hand, the tests carried out on speckled and unspeckled specimens show an important influence of the speckling. Finally, an *in situ* test is performed. CT scans performed on an intermediate resolution ROI allow to follow the region where the transition zones are located until the end of the test, while providing informative images for the construction of DIB models. The scans performed at different stages of the experiment provide valuable information on the architecture of the fabric.

We believe that an image data assimilation approach based on an *in-situ* experiments performed in X-ray CT is of primary interest to the fabric mechanics community. Our initial results with a simple bias extension test support the feasibility of such an approach. The most attractive route for us now is thus to carry out new multi-instrumented in-situ bias extension tests (coupling X-Ray with surface information). We would remain "zoomed in" on the same region (transition zones and strong relative sliding between the yarns). The work revealed several areas for improvement:

- Specimen preparation, especially for tomography, can probably be improved and even automated. We would like to limit the fraying to the edges. For example, we would like to try laser cutting.
- The speckle pattern has many limitations. As it stands, the speckles deposited are too coarse to be able to go down to the scale of the yarn. It tends to flake off during deformation (more so on some fabrics). The deposition method is also very manual and difficult to reproduce. In addition, there is evidence that it has a strong influence on the behaviour of the fabric. It is therefore planned to rework this point and, at the same time, to work on the lighting and/or the filters to limit the effects of reflections.
- The creation phase of a DIB model is too user dependent. It needs to be automated. The use of Virtual Image Correlation to automatically re-adjust the CAD geometry on the tomography (Semin et al., 2011; Passieux et al., 2023) is being considered. This work is in progress in the framework of the ANR AVATAR (PhD thesis of Dorian Bichet).
- The scan time is currently approximately 45 minutes. Therefore, in order to reduce the time and cost of a test, only four stress levels were performed in this thesis. This results in a large difference in the state of the samples between two scans. An alternative would be to scan 'correctly' only in the first step and be satisfied with a faster acquisition in the following steps. It will also be necessary to finalise the design of the wiring of the machine so that it is no longer necessary to connect and disconnect the electrical cables at each new step.
- It is planned to place a camera in the μCT. The rotation of the sample during the CT scan could then be used to measure the surface deformations on either side, by 2D or by stereo FE-DIC (Pierré et al., 2017), or even to perform a scan of the surface in order to move towards photogrammetric FE-DIC (Fouque et al., 2022). The FE-DIC measurement through the tube requires however taking into account the distortions it induces. In addition, the issue of lighting will have to be addressed. Finally, the camera must be shielded.

Bibliography

F. Ackermann. Digital image correlation: performance and potential application in photogrammetry. *The Photogrammetric Record*, 11(64):429–439, 1984. *citations pages 1*

J. Ahrens, B. Geveci, and C. Law. ParaView: An end-user tool for large data visualization. In *Visualization Handbook*. Elesvier, 2005. ISBN 978-0123875822. *2 citations pages xv and 61*

S. Ai, W. Song, and Y. Chen. Stress field and damage evolution in c/sic woven composites: Image-based finite element analysis and in situ x-ray computed tomography tests. *Journal of the European Ceramic Society*, 41(4):2323–2334, 2021. *citations pages 111*

Y. Aimène, E. Vidal-Sallé, B. Hagège, F. Sidoroff, and P. Boisse. A hyperelastic approach for composite reinforcement large deformation analysis. *Journal of Composite materials*, 44(1):5–26, 2010. *citations pages 2*

M. A. Ali, Q. Guan, R. Umer, W. J. Cantwell, and T. Zhang. Efficient processing of μct images using deep learning tools for generating digital material twins of woven fabrics. *Composites Science and Technology*, 217:109091, 2022. *citations pages 111*

H. Altenbach, J. Altenbach, W. Kissing, and H. Altenbach. *Mechanics of composite structural elements*. Springer, 2004. *2 citations pages xiii and 7*

M. Anwander, B. G. Zagar, B. Weiss, and H. Weiss. Noncontacting strain measurements at high temperatures by the digital laser speckle technique. *Experimental mechanics*, 40:98–105, 2000. *citations pages 83*

M. A. Asghar, A. Imad, Y. Nawab, M. Hussain, and A. Saouab. Effect of yarn singeing and commingling on the mechanical properties of jute/polypropylene composites. *Polymer Composites*, 42(2):828–841, 2021. *4 citations pages xiii, 12, 13, and 50*

M. F. Ashby and Y. J. Bréchet. Designing hybrid materials. *Acta materialia*, 51(19): 5801–5821, 2003. *citations pages 6*

P. Badel, E. Vidal-Sallé, and P. Boisse. Computational determination of in-plane shear mechanical behaviour of textile composite reinforcements. *Computational materials science*, 40(4):439–448, 2007. *3 citations pages 1, 83, and 131*

P. Badel, E. Vidal-Sallé, and P. Boisse. Large deformation analysis of fibrous materials using rate constitutive equations. *Computers & Structures*, 86(11-12):1164–1175, 2008a. *2 citations pages 1 and 83*

P. Badel, E. Vidal-Sallé, E. Maire, and P. Boisse. Simulation and tomography analysis of textile composite reinforcement deformation at the mesoscopic scale. *Composites Science and Technology*, 68(12):2433–2440, 2008b. *citations pages 2*

R. Bai, Y. Ma, Z. Lei, Y. Feng, J. Zou, and D. Liu. Shear deformation and energy absorption analysis of flexible fabric in yarn pullout test. *Composites Part A: Applied Science and Manufacturing*, 128:105678, 2020. *citations pages 36*

R. Bai, B. Chen, J. Colmars, and P. Boisse. Physics-based evaluation of the drapability of textile composite reinforcements. *Composites Part B: Engineering*, 242:110089, 2022. *2 citations pages xiv and 31*

R. Balcaen, L. Wittevrongel, P. Reu, P. Lava, and D. Debruyne. Stereo-dic calibration and speckle image generator based on fe formulations. *Experimental Mechanics*, 57: 703–718, 2017. *citations pages 68*

M. Barburski, I. Straumit, X. Zhang, M. Wevers, and S. V. Lomov. Micro-ct analysis of internal structure of sheared textile composite reinforcement. *Composites Part A: Applied Science and Manufacturing*, 73:45–54, 2015. *2 citations pages 2 and 111*

M. Barile, L. Lecce, M. Iannone, S. Pappadà, and P. Roberti. Thermoplastic composites for aerospace applications. *Revolutionizing aircraft materials and processes*, pages 87–114, 2020. *citations pages 6*

Y. Barranger, P. Doumalin, J.-C. Dupré, and A. Germaneau. Strain measurement by digital image correlation: influence of two types of speckle patterns made from rigid or deformable marks. *Strain*, 48(5):357–365, 2012. *citations pages 51*

B. K. Bay. Texture correlation: a method for the measurement of detailed strain distributions within trabecular bone. *Journal of Orthopaedic Research*, 13(2):258–267, 1995. *citations pages 36*

B. K. Bay, T. S. Smith, D. P. Fyhrie, and M. Saad. Digital volume correlation: three-dimensional strain mapping using x-ray tomography. *Experimental mechanics*, 39(3): 217–226, 1999. *4 citations pages 33, 45, 111, and 155*

S. Bel, P. Boisse, and F. Dumont. Analyses of the deformation mechanisms of non-crimp fabric composite reinforcements during preforming. *Applied Composite Materials*, 19: 513–528, 2012. *3 citations pages 1, 25, and 83*

R. B. Berke and J. Lambros. Ultraviolet digital image correlation (uv-dic) for high temperature applications. *Review of Scientific Instruments*, 85(4):045121, 2014. *citations pages 51*

R. Bernatas, S. Dagréou, A. Despax-Ferreres, and A. Barasinski. Recycling of fiber reinforced composites with a focus on thermoplastic composites. *Cleaner Engineering and Technology*, 5:100272, 2021. *citations pages 6*

G. Besnard, F. Hild, and S. Roux. "finite-element" displacement fields analysis from digital images: application to portevin–le châtelier bands. *Experimental mechanics*, 46 (6):789–803, 2006. *4 citations pages xiv, 2, 35, and 36*

P. Bhat, J. Merotte, P. Simacek, and S. G. Advani. Process analysis of compression resin transfer molding. *Composites Part A: Applied Science and Manufacturing*, 40(4): 431–441, 2009. *citations pages 1*

P. Bhatt and A. Goe. Carbon fibres: production, properties and potential use. *Material Science Research India*, 14(1):52–57, 2017. *citations pages 10*

S. Bickerton, H. C. Stadtfeld, K. V. Steiner, and S. G. Advani. Design and application of actively controlled injection schemes for resin-transfer molding. *Composites Science and Technology*, 61(11):1625–1637, 2001. *citations pages 16*

L. D. Bloom. *On the relationship between layup time, material properties and mould geometry in the manufacture of composite components*. PhD thesis, University of Bristol, 2015. *2 citations pages xiii and 14*

S. Blusseau, Y. Wielhorski, Z. Haddad, and S. Velasco-Forero. Instance segmentation of 3d woven fabric from tomography images by deep learning and morphological pseudo-labeling. *Composites Part B: Engineering*, 247:110333, 2022. *citations pages 111*

F. Boey and S. Lye. Effects of vacuum and pressure in an autoclave curing process for a thermosetting fibre-reinforced composite. *Journal of materials processing technology*, 23(2):121–131, 1990. *citations pages 18*

P. Boisse. *Mise en forme des renforts fibreux de composites*. Ed. Techniques Ingénieur, 2004. *4 citations pages xiii, 22, 25, and 83*

P. Boisse, N. Hamila, E. Vidal-Sallé, and F. Dumont. Simulation of wrinkling during textile composite reinforcement forming. influence of tensile, in-plane shear and bending stiffnesses. *Composites Science and Technology*, 71(5):683–692, 2011. *3 citations pages 1, 25, and 83*

P. Boisse, N. Hamila, and A. Madeo. Modelling the development of defects during composite reinforcements and prepreg forming. *Philosophical Transactions of the Royal Society A: Mathematical, Physical and Engineering Sciences*, 374(2071):20150269, 2016. *2 citations pages 1 and 29*

P. Boisse, N. Hamila, E. Guzman-Maldonado, A. Madeo, G. Hivet, et al. The bias-extension test for the analysis of in-plane shear properties of textile composite reinforcements and prepregs: a review. *International Journal of Material Forming*, 10(4): 473–492, 2017. *5 citations pages 1, 2, 25, 36, and 52*

P. Boisse, J. Colmars, N. Hamila, N. Naouar, and Q. Steer. Bending and wrinkling of composite fiber preforms and prepregs. a review and new developments in the draping simulations. *Composites Part B: Engineering*, 141:234–249, 2018a. *citations pages 29*

P. Boisse, N. Hamila, and A. Madeo. The difficulties in modeling the mechanical behavior of textile composite reinforcements with standard continuum mechanics of cauchy. some possible remedies. *International Journal of Solids and Structures*, 154:55–65, 2018b. *2 citations pages 1 and 83*

R. Bonnaire, J. Patou, E. de Luycker, T. Cutard, and G. Bernhart. Using x-ray tomography to evaluate porosities in composite parts. In *24e Congrès Français de Mécanique (CFM 2019)*, 2019. *citations pages 45*

M. Bornert, F. Brémand, P. Doumalin, J.-C. Dupré, M. Fazzini, M. Grédiac, F. Hild, S. Mistou, J. Molimard, J.-J. Orteu, et al. Assessment of digital image correlation measurement errors: methodology and results. *Experimental mechanics*, 49:353–370, 2009. *4 citations pages xv, 55, 59, and 60*

M. Bornert, P. Doumalin, J.-C. Dupré, C. Poilâne, L. Robert, E. Toussaint, and B. Wattrisse. Assessment of digital image correlation measurement accuracy in the ultimate error regime: improved models of systematic and random errors. *Experimental Mechanics*, 58(1):33–48, 2018. *citations pages 55*

P.-E. Bourban. *Matériaux composites à matrice organique: constituants, procédés, propriétés*, volume 15. PPUR presses polytechniques, 2004. *citations pages 9*

R. Brault, A. Germaneau, J.-C. Dupré, P. Doumalin, S. Mistou, and M. Fazzini. In-situ analysis of laminated composite materials by x-ray micro-computed tomography and digital volume correlation. *Experimental Mechanics*, 53(7):1143–1151, 2013. *citations pages 111*

D. E. Breen, D. H. House, and M. J. Wozny. A particle-based model for simulating the draping behavior of woven cloth. *Textile Research Journal*, 64(11):663–685, 1994a. *citations pages 30*

D. E. Breen, D. H. House, and M. J. Wozny. Predicting the drape of woven cloth using interacting particles. In *Proceedings of the 21st annual conference on Computer graphics and interactive techniques*, pages 365–372, 1994b. *citations pages 30*

L. Brown and A. Long. Modeling the geometry of textile reinforcements for composites: Texgen. In *Composite reinforcements for optimum performance*, pages 237–265. Elsevier, 2021. *citations pages 119*

A. Brunon, K. Bruyere-Garnier, and M. Coret. Mechanical characterization of liver capsule through uniaxial quasi-static tensile tests until failure. *Journal of biomechanics*, 43(11):2221–2227, 2010. *citations pages 36*

P. Buckenham. Bias-extension measurements on woven fabrics. *Journal of the Textile Institute*, 88(1):33–40, 1997. *2 citations pages 1 and 25*

K. Buet-Gautier and P. Boisse. Experimental analysis and modeling of biaxial mechanical behavior of woven composite reinforcements. *Experimental mechanics*, 41(3):260–269, 2001. *citations pages 1*

J.-Y. Buffiere, E. Maire, J. Adrien, J.-P. Masse, and E. Boller. In situ experiments with x ray tomography: an attractive tool for experimental mechanics. *Experimental mechanics*, 50(3):289–305, 2010. *2 citations pages 45 and 111*

S. Caba and M. Koch. Analysis of the resin transfer molding (rtm) process for frp and its process simulation fundamentals. In *AIP Conference Proceedings*, volume 1664, page 060010. AIP Publishing LLC, 2015. *citations pages 17*

Z. Cai. Simplified mold filling simulation in resin transfer molding. *Journal of Composite Materials*, 26(17):2606–2630, 1992. *citations pages 17*

J. Cao, R. Akkerman, P. Boisse, J. Chen, H. Cheng, E. De Graaf, J. Gorczyca, P. Harrison, G. Hivet, J. Launay, et al. Characterization of mechanical behavior of woven fabrics: experimental methods and benchmark results. *Composites Part A: Applied Science and Manufacturing*, 39(6):1037–1053, 2008. *4 citations pages xiii, 1, 25, and 26*

Y. Chai, Y. Wang, Z. Yousaf, N. T. Vo, T. Lowe, P. Potluri, and P. J. Withers. Damage evolution in braided composite tubes under torsion studied by in-situ x-ray computed tomography. *Composites Science and Technology*, 188:107976, 2020. *citations pages 111*

M. Chapelier, R. Bouclier, and J.-C. Passieux. Free-form deformation digital image correlation (ffd-dic): a non-invasive spline regularization for arbitrary finite element measurements. *Computer Methods in Applied Mechanics and Engineering*, 384:113992, 2021. *2 citations pages 78 and 164*

B. Chatterjee and S. Bhowmik. Evolution of material selection in commercial aviation industry—a review. *Sustainable engineering products and manufacturing technologies*, pages 199–219, 2019. *citations pages 6*

B. Choi, O. Diestel, and P. Offermann. Commingled cf/peek hybrid yarns for use in textile reinforced high performance rotors. In *12th Int. Conf. Compos. Mater.(ICCM), Paris*, pages 796–806, 1999. *2 citations pages xiii and 13*

T. Chu, W. Ranson, and M. A. Sutton. Applications of digital-image-correlation techniques to experimental mechanics. *Experimental mechanics*, 25(3):232–244, 1985. *citations pages 33*

D. Colin, S. Bel, T. Hans, M. Hartmann, and K. Drechsler. Virtual description of non-crimp fabrics at the scale of filaments including orientation variability in the fibrous layers. *Applied Composite Materials*, 27(4):337–355, 2020. *3 citations pages xiv, 31, and 32*

J. R. Correia. Pultrusion of advanced composites. In *Advanced Fiber-Reinforced Polymer (FRP) Composites for Structural Applications*, pages 137–177. Elsevier, 2023. *2 citations pages xiii and 9*

G. Crammond, S. Boyd, and J. Dulieu-Barton. Speckle pattern quality assessment for digital image correlation. *Optics and Lasers in Engineering*, 51(12):1368–1378, 2013. *2 citations pages xiv and 42*

G. Creech and A. K. Pickett. Meso-modelling of non-crimp fabric composites for coupled drape and failure analysis. *Journal of materials science*, 41(20):6725–6736, 2006. *citations pages 31*

H. Çuvalci, K. Erbay, and H. İpek. Investigation of the effect of glass fiber content on the mechanical properties of cast polyamide. *Arabian Journal for Science and Engineering*, 39(12):9049–9056, 2014. *citations pages 8*

M. W. Czabaj, M. L. Riccio, and W. W. Whitacre. Numerical reconstruction of graphite/epoxy composite microstructure based on sub-micron resolution x-ray computed tomography. *Composites Science and Technology*, 105:174–182, 2014. *citations pages 111*

L. Daelemans, J. Faes, S. Allaoui, G. Hivet, M. Dierick, L. Van Hoorebeke, and W. Van Paepegem. Finite element simulation of the woven geometry and mechanical behaviour of a 3d woven dry fabric under tensile and shear loading using the digital element method. *Composites Science and Technology*, 137:177–187, 2016. *citations pages 1*

M. Danisman, G. Tuncol, A. Kaynar, and E. M. Sozer. Monitoring of resin flow in the resin transfer molding (rtm) process using point-voltage sensors. *Composites Science and Technology*, 67(3-4):367–379, 2007. *citations pages 16*

E. De Luycker. *Simulation et expérimentation en mise en forme de renforts composites 3D interlocks.* PhD thesis, Lyon INSA, 2009. *3 citations pages xiv, 42, and 43*

E. De Luycker and N. Hamila. Modeling of hyperelastic bending of fibrous media using second-gradient isogeometric analysis: Weaving and braiding applications. *Composites Part A: Applied Science and Manufacturing*, 167:107415, 2023. *citations pages 1*

R. De Oliveira, S. Lavanchy, R. Chatton, D. Costantini, V. Michaud, R. Salathé, and J.-A. Månson. Experimental investigation of the effect of the mould thermal expansion on the development of internal stresses during carbon fibre composite processing. *Composites Part A: Applied Science and Manufacturing*, 39(7):1083–1090, 2008. *2 citations pages 18 and 20*

J.-F. Delerue, S. V. Lomov, R. Parnas, I. Verpoest, and M. Wevers. Pore network modeling of permeability for textile reinforcements. *Polymer composites*, 24(3):344–357, 2003. *citations pages 111*

D. E. Depuydt, J. Soete, Y. D. Asfaw, M. Wevers, J. Ivens, and A. W. Van Vuure. Sorption behaviour of bamboo fibre reinforced composites, why do they retain their properties? *Composites Part A: Applied Science and Manufacturing*, 119:48–60, 2019. *citations pages 2*

M. Derradji, J. Wang, and W. Liu. 5 - fiber-reinforced phthalonitrile composites. In M. Derradji, J. Wang, and W. Liu, editors, *Phthalonitrile Resins and Composites*, Plastics Design Library, pages 241–294. William Andrew Publishing, 2018. ISBN 978-0-12-812966-1. doi: https://doi.org/10.1016/B978-0-12-812966-1.00005-6. URL `https://www.sciencedirect.com/science/article/pii/B9780128129661000056`. *citations pages 8*

F. Desplentere, S. V. Lomov, D. Woerdeman, I. Verpoest, M. Wevers, and A. Bogdanovich. Micro-ct characterization of variability in 3d textile architecture. *Composites Science and Technology*, 65(13):1920–1930, 2005. *2 citations pages 2 and 111*

D. Di Lecce, V. Marangon, W. Du, D. J. Brett, P. R. Shearing, and J. Hassoun. The role of synthesis pathway on the microstructural characteristics of sulfur-carbon composites: X-ray imaging and electrochemistry in lithium battery. *Journal of Power Sources*, 472:228424, 2020. *citations pages 2*

Y. Dong and B. Pan. A review of speckle pattern fabrication and assessment for digital image correlation. *Experimental Mechanics*, 57(8):1161–1181, 2017. *2 citations pages 41 and 43*

J.-B. Donnet and R. C. Bansal. *Carbon fibers*. Crc Press, 1998. *citations pages 10*

C. Dufour, P. Wang, F. Boussu, and D. Soulat. Experimental investigation about stamping behaviour of 3d warp interlock composite preforms. *Applied Composite Materials*, 21 (5):725–738, 2014. *citations pages 1*

C. Dufour, F. Boussu, P. Wang, and D. Soulat. Local strain measurements of yarns inside of 3d warp interlock fabric during forming process. *International Journal of Material Forming*, 11:775–788, 2018. *citations pages 33*

D. Durville. Simulation of the mechanical behaviour of woven fabrics at the scale of fibers. *International journal of material forming*, 3(2):1241–1251, 2010. *3 citations pages 1, 125, and 131*

P. Egan, M. P. Whelan, F. Lakestani, and M. J. Connelly. Small punch test: An approach to solve the inverse problem by deformation shape and finite element optimization. *Computational materials science*, 40(1):33–39, 2007. *2 citations pages 1 and 25*

M. J. Emerson, K. M. Jespersen, A. B. Dahl, K. Conradsen, and L. P. Mikkelsen. Individual fibre segmentation from 3d x-ray computed tomography for characterising the fibre orientation in unidirectional composite materials. *Composites Part A: Applied Science and Manufacturing*, 97:83–92, 2017. *citations pages 2*

M. Engelfried, J. Fial, M. Tartler, P. Böhler, D. Hägele, and P. Middendorf. A mesoscopic approach for draping simulation of preforms manufactured by direct fibre placement. In *AIP conference proceedings*, volume 1896, page 030016. AIP Publishing LLC, 2017. *citations pages 30*

J. Engqvist, M. Wallin, M. Ristinmaa, and S. A. Hall. Modelling and experiments of glassy polymers using biaxial loading and digital image correlation. *International Journal of Solids and Structures*, 102:100–111, 2016. *citations pages 36*

R. Fouque, R. Bouclier, J.-C. Passieux, and J.-N. Périé. Fractal pattern for multiscale digital image correlation. *Experimental Mechanics*, 61(3):483–497, 2021. *2 citations pages 43 and 55*

R. Fouque, R. Bouclier, J.-C. Passieux, and J.-N. Périé. Photometric dic: a unified framework for global stereo digital image correlation based on the construction of textured digital twins. *Journal of Theoretical, Computational and Applied Mechanics*, 2022. *5 citations pages 111, 142, 147, 162, and 165*

S. Garcea, Y. Wang, and P. Withers. X-ray computed tomography of polymer composites. *Composites Science and Technology*, 156:305–319, 2018. *citations pages 2*

A. Gasser, P. Boisse, and S. Hanklar. Mechanical behaviour of dry fabric reinforcements. 3d simulations versus biaxial tests. *Computational materials science*, 17(1):7–20, 2000. *citations pages 1*

R. Gauvin and M. Chibani. The modelling of mold filling in resin transfer molding. *International Polymer Processing*, 1(1):42–46, 2022. *citations pages 17*

K. Genovese, L. Casaletto, J. Rayas, V. Flores, and A. Martinez. Stereo-digital image correlation (dic) measurements with a single camera using a biprism. *Optics and Lasers in Engineering*, 51(3):278–285, 2013. *citations pages 40*

T. Gereke, O. Döbrich, M. Hübner, and C. Cherif. Experimental and computational composite textile reinforcement forming: A review. *Composites Part A: Applied Science and Manufacturing*, 46:1–10, 2013. *citations pages 25*

C. Geuzaine and J.-F. Remacle. Gmsh: A 3-d finite element mesh generator with built-in pre-and post-processing facilities. *International journal for numerical methods in engineering*, 79(11):1309–1331, 2009. *citations pages 55*

C. Goidescu, H. Welemane, C. Garnier, M. Fazzini, R. Brault, E. Péronnet, and S. Mistou. Damage investigation in cfrp composites using full-field measurement techniques: Combination of digital image stereo-correlation, infrared thermography and x-ray tomography. *Composites Part B: Engineering*, 48:95–105, 2013. *citations pages 40*

L. Gomes Perini. *La PGD au service de la corrélation volumique pour l'analyse du comportement des composites à l'échelle micro.* PhD thesis, Université de Toulouse, Université Toulouse III-Paul Sabatier, 2014. *citations pages 111*

J. L. Gorczyca-Cole, J. A. Sherwood, and J. Chen. A friction model for thermostamping commingled glass–polypropylene woven fabrics. *Composites Part A: Applied Science and Manufacturing*, 38(2):393–406, 2007. *citations pages 1*

P. Grant. Spray forming. *Progress in Materials science*, 39(4-5):497–545, 1995. *citations pages 21*

P. Grant. Solidification in spray forming. *Metallurgical and Materials Transactions A*, 38 (7):1520–1529, 2007. *2 citations pages xiii and 21*

S. Green, A. Long, B. El Said, and S. Hallett. Numerical modelling of 3d woven preform deformations. *Composite Structures*, 108:747–756, 2014. *citations pages 111*

P. Groche and G. v. Breitenbach. Roll forming strategies for welded tubes. *steel research international*, 79(1):40–46, 2008. *2 citations pages xiii and 18*

L. Grunenfelder, A. Dills, T. Centea, and S. Nutt. Effect of prepreg format on defect control in out-of-autoclave processing. *Composites Part A: Applied Science and Manufacturing*, 93:88–99, 2017. *citations pages 18*

R. Guduru, R. Scattergood, C. Koch, K. Murty, and A. Nagasekhar. Finite element analysis of a shear punch test. *Metallurgical and Materials Transactions A*, 37(5): 1477–1483, 2006. *2 citations pages 1 and 25*

R. Guldberg, S. Hollister, and G. Charras. The accuracy of digital image-based finite element models. *Journal of Biomechanical Engineering*, 120(2):289–295, 1998. *citations pages 45*

A. Gusev, M. Heggli, H. R. Lusti, and P. J. Hine. Orientation averaging for stiffness and thermal expansion of short fiber composites. *Advanced Engineering Materials*, 4(12): 931–933, 2002. *2 citations pages 18 and 20*

E. Guzman-Maldonado, P. Wang, N. Hamila, and P. Boisse. Experimental and numerical analysis of wrinkling during forming of multi-layered textile composites. *Composite Structures*, 208:213–223, 2019. *citations pages 29*

N. Hamila and P. Boisse. A meso–macro three node finite element for draping of textile composite preforms. *Applied composite materials*, 14:235–250, 2007. *citations pages 131*

K. Han, S. Jiang, C. Zhang, and B. Wang. Flow modeling and simulation of scrimp for composites manufacturing. *Composites Part A: Applied Science and Manufacturing*, 31 (1):79–86, 2000. *citations pages 18*

M.-G. Han and S.-H. Chang. Draping simulation of carbon/epoxy plain weave fabrics with non-orthogonal constitutive model and material behavior analysis of the cured structure. *Composites Part A: Applied Science and Manufacturing*, 110:172–182, 2018. *citations pages 30*

P. Harrison, M. J. Clifford, and A. Long. Shear characterisation of viscous woven textile composites: a comparison between picture frame and bias extension experiments. *Composites science and technology*, 64(10-11):1453–1465, 2004. *4 citations pages 1, 25, 26, and 27*

I. Harry, B. Saha, and I. Cumming. Surface properties of electrochemically oxidised viscose rayon based carbon fibres. *Carbon*, 45(4):766–774, 2007. *citations pages 10*

M. Hassan, A. Othman, and S. Kamaruddin. A review on the manufacturing defects of complex-shaped laminate in aircraft composite structures. *The International Journal of Advanced Manufacturing Technology*, 91:4081–4094, 2017. *citations pages 6*

J. D. Helm. Digital image correlation for specimens with multiple growing cracks. *Experimental mechanics*, 48:753–762, 2008. *citations pages 51*

J. D. Helm, S. R. McNeill, and M. A. Sutton. Improved three-dimensional image correlation for surface displacement measurement. *Optical Engineering*, 35(7):1911–1920, 1996. *citations pages 33*

S. Hesseler, S. E. Stapleton, L. Appel, S. Schöfer, and B. Manin. Modeling of reinforcement fibers and textiles. In *Advances in Modeling and Simulation in Textile Engineering*, pages 267–299. Elsevier, 2021. *2 citations pages xiii and 6*

F. Hild, S. Roux, R. Gras, N. Guerrero, M. E. Marante, and J. Flórez-López. Displacement measurement technique for beam kinematics. *Optics and Lasers in Engineering*, 47(3-4):495–503, 2009. *citations pages 164*

T. Himmer, T. Nakagawa, and M. Anzai. Lamination of metal sheets. *Computers in Industry*, 39(1):27–33, 1999. *citations pages 17*

G. Hivet and P. Boisse. Consistent mesoscopic mechanical behaviour model for woven composite reinforcements in biaxial tension. *Composites Part B: Engineering*, 39(2): 345–361, 2008. *citations pages 1*

G. Hivet, S. Allaoui, B. T. Cam, P. Ouagne, and D. Soulat. Design and potentiality of an apparatus for measuring yarn/yarn and fabric/fabric friction. *Experimental mechanics*, 52:1123–1136, 2012. *citations pages 1*

A. Hosseini, M. H. Kashani, F. Sassani, A. Milani, and F. Ko. Identifying the distinct shear wrinkling behavior of woven composite preforms under bias extension and picture frame tests. *Composite Structures*, 185:764–773, 2018. *2 citations pages 26 and 27*

J. Hu, S.-F. Chen, and J. Teng. Numerical drape behavior of circular fabric sheets over circular pedestals. *Textile Research Journal*, 70(7):593–603, 2000. *citations pages 30*

Y. Hu, Z. Liang, S. Feng, W. Yin, J. Qian, Q. Chen, and C. Zuo. Calibration and rectification of bi-telecentric lenses in scheimpflug condition. *Optics and Lasers in Engineering*, 149:106793, 2022. *3 citations pages xiv, 39, and 40*

T. Hua, H. Xie, S. Wang, Z. Hu, P. Chen, and Q. Zhang. Evaluation of the quality of a speckle pattern in the digital image correlation method by mean subset fluctuation. *Optics & Laser Technology*, 43(1):9–13, 2011. *2 citations pages xiv and 43*

J. Huang, L. Qin, X. Peng, T. Zhu, C. Xiong, Y. Zhang, and J. Fang. Cellular traction force recovery: An optimal filtering approach in two-dimensional fourier space. *Journal of Theoretical Biology*, 259(4):811–819, 2009. *citations pages 36*

J. Huang, L. Wang, C. Xiong, and F. Yuan. Elastic hydrogel as a sensor for detection of mechanical stress generated by single cells grown in three-dimensional environment. *Biomaterials*, 98:103–112, 2016. *citations pages 36*

W. Huang, P. Causse, V. Brailovski, H. Hu, and F. Trochu. Reconstruction of mesostructural material twin models of engineering textiles based on micro-ct aided geometric modeling. *Composites Part A: Applied Science and Manufacturing*, 124:105481, 2019. *citations pages 2*

X. Huang. Fabrication and properties of carbon fibers. *Materials*, 2(4):2369–2403, 2009. *citations pages 9*

P. Hubert, G. Fernlund, and A. Poursartip. Autoclave processing for composites. In *Manufacturing techniques for polymer matrix composites (PMCs)*, pages 414–434. Elsevier, 2012. *citations pages 20*

M. Inagaki. Chapter 2.1 - advanced carbon materials. In S. Somiya, editor, *Handbook of Advanced Ceramics (Second Edition)*, pages 25–60. Academic Press, Oxford, second edition edition, 2013. ISBN 978-0-12-385469-8. doi: https://doi.org/10.1016/B978-0-12-385469-8.00002-2. URL `https://www.sciencedirect.com/science/article/pii/B9780123854698000022`. *citations pages 11*

A. Iwata, T. Inoue, N. Naouar, P. Boisse, and S. V. Lomov. Coupled meso-macro simulation of woven fabric local deformation during draping. *Composites Part A: Applied Science and Manufacturing*, 118:267–280, 2019. *2 citations pages xiv and 30*

D. Jauffrès, J. A. Sherwood, C. D. Morris, and J. Chen. Discrete mesoscopic modeling for the simulation of woven-fabric reinforcement forming. *International Journal of Material Forming*, 3:1205–1216, 2010. *citations pages 2*

A. A. Johnston. *An integrated model of the development of process-induced deformation in autoclave processing of composite structures.* PhD thesis, University of British Columbia, 1997. *citations pages 20*

E. Jones and M. Iadicola. International digital image correlation society, a good practices guide for digital image correlation 2018. *URL: http://doi. org/10.32720/idics/gpg. ed1*, 2018. *citations pages 51*

E. M. Jones, M. A. Iadicola, et al. A good practices guide for digital image correlation. *International Digital Image Correlation Society*, 10:1–110, 2018. *2 citations pages 41 and 42*

J. P. Jose and K. Joseph. Advances in polymer composites: macro-and microcomposites–state of the art, new challenges, and opportunities. *Polymer composites*, pages 1–16, 2012. *citations pages 18*

S. V. Joshi, L. Drzal, A. Mohanty, and S. Arora. Are natural fiber composites environmentally superior to glass fiber reinforced composites? *Composites Part A: Applied science and manufacturing*, 35(3):371–376, 2004. *citations pages 7*

M. H. Kashani, A. Hosseini, F. Sassani, F. Ko, and A. Milani. Understanding different types of coupling in mechanical behavior of woven fabric reinforcements: A critical review and analysis. *Composite Structures*, 179:558–567, 2017. *citations pages 1*

K. B. Katnam, L. Da Silva, and T. Young. Bonded repair of composite aircraft structures: A review of scientific challenges and opportunities. *Progress in Aerospace Sciences*, 61: 26–42, 2013. *citations pages 6*

M. A. Khan, T. Mabrouki, E. Vidal-Sallé, and P. Boisse. Numerical and experimental analyses of woven composite reinforcement forming using a hypoelastic behaviour. application to the double dome benchmark. *Journal of materials processing technology*, 210(2):378–388, 2010. *citations pages 31*

D. S. Kim and C. W. Macosko. Reaction injection molding process of glass fiber reinforced polyurethane composites. *Polymer Engineering & Science*, 40(10):2205–2216, 2000. *citations pages 22*

H. Krieger, T. Gries, and S. E. Stapleton. Shear and drape behavior of non-crimp fabrics based on stitching geometry. *International Journal of Material Forming*, 11(5):593–605, 2018. *citations pages 31*

T. Kruckenberg and R. Paton. *Resin transfer moulding for aerospace structures*. Springer Science & Business Media, 2012. *citations pages 16*

E. Kunze, B. Schwarz, T. Weber, M. Müller, R. Böhm, and M. Gude. Forming analysis of internal plies of multi-layer unidirectional textile preforms using projectional radiography. *Procedia Manufacturing*, 47:17–23, 2020. *citations pages 33*

N. M. Larson and F. W. Zok. Insights from in-situ x-ray computed tomography during axial impregnation of unidirectional fiber beds. *Composites Part A: Applied Science and Manufacturing*, 107:124–134, 2018. *citations pages 111*

J. Launay, F. Lahmar, P. Boisse, and P. Vacher. Strain measurement in tests on fibre fabric by image correlation method. *Advanced composites letters*, 11(1):096369350201100102, 2002. *citations pages 33*

J. Launay, G. Hivet, A. V. Duong, and P. Boisse. Experimental analysis of the influence of tensions on in plane shear behaviour of woven composite reinforcements. *Composites science and technology*, 68(2):506–515, 2008. *6 citations pages xiv, 1, 25, 26, 27, and 28*

S. Laurenzi and M. Marchetti. Advanced composite materials by resin transfer molding for aerospace applications. *Composites and their properties*, pages 197–226, 2012. *citations pages 16*

A. Lawley and D. Apelian. Spray forming of metal matrix composites. *Powder metallurgy*, 37(2):123–128, 1994. *citations pages 21*

J. M. Lawrence, K.-T. Hsiao, R. C. Don, P. Simacek, G. Estrada, E. M. Sozer, H. C. Stadtfeld, and S. G. Advani. An approach to couple mold design and on-line control to manufacture complex composite parts by resin transfer molding. *Composites Part A: Applied Science and Manufacturing*, 33(7):981–990, 2002. *citations pages 16*

G. Lebrun, M. N. Bureau, and J. Denault. Evaluation of bias-extension and picture-frame test methods for the measurement of intraply shear properties of pp/glass commingled fabrics. *Composite structures*, 61(4):341–352, 2003. *4 citations pages 1, 25, 26, and 28*

D. Lecompte, A. Smits, S. Bossuyt, H. Sol, J. Vantomme, D. Van Hemelrijck, and A. Habraken. Quality assessment of speckle patterns for digital image correlation. *Optics and lasers in Engineering*, 44(11):1132–1145, 2006. *citations pages 51*

D. Lecompte, S. Bossuyt, S. Cooreman, H. Sol, and J. Vantomme. Study and generation of optimal speckle patterns for dic. In *Proceedings of the annual conference and exposition on experimental and applied mechanics*, volume 3, pages 1643–1649, 2007. *2 citations pages 41 and 43*

G.-W. Lee, N.-J. Lee, J. Jang, K.-J. Lee, and J.-D. Nam. Effects of surface modification on the resin-transfer moulding (rtm) of glass-fibre/unsaturated-polyester composites. *Composites Science and Technology*, 62(1):9–16, 2002. *citations pages 17*

J. M. Lee, G. Y. Noh, B. G. Kim, Y. Yoo, W. J. Choi, D.-G. Kim, H. G. Yoon, and Y. S. Kim. Synthesis of poly (phenylene polysulfide) networks from elemental sulfur and p-diiodobenzene for stretchable, healable, and reprocessable infrared optical applications. *ACS Macro Letters*, 8(8):912–916, 2019. *citations pages 12*

J. Li, N. Hamila, G. L'Hostis, and P. Wang. Shear deformation characteristics under tensile stress during forming of tubular braided fabrics. *Composites Part A: Applied Science and Manufacturing*, 167:107458, 2023. *citations pages 1*

M. Li, H.-y. Sun, X.-l. Liu, H.-y. Xu, Y. Ren, D.-l. Cui, and X. Tao. Preparation of porous boehmite nanosolid and its composite fluorescent materials by a novel hydrothermal hot-press method. *Materials Letters*, 60(21-22):2738–2742, 2006. *citations pages 20*

Z. Li, X. Qian, Y. Xiang, L. Zeng, Z. Zhuang, and J. Tan. Profile change law of clad rebars and the formation mechanism of composite interfaces during hot rolling. *Materials*, 15 (21):7735, 2022. *citations pages 18*

B. Liang and P. Boisse. A review of numerical analyses and experimental characterization methods for forming of textile reinforcements. *Chinese Journal of Aeronautics*, 34(8): 143–163, 2021. *citations pages 83*

S. T. Lim and W. I. Lee. An analysis of the three-dimensional resin-transfer mold filling process. *Composites Science and Technology*, 60(7):961–975, 2000. *citations pages 17*

G. Lionello, C. Sirieix, and M. Baleani. An effective procedure to create a speckle pattern on biological soft tissue for digital image correlation measurements. *Journal of the mechanical behavior of biomedical materials*, 39:1–8, 2014. *citations pages 51*

B. Liu, S. Bickerton, and S. G. Advani. Modelling and simulation of resin transfer moulding (rtm)—gate control, venting and dry spot prediction. *Composites Part A: applied science and manufacturing*, 27(2):135–141, 1996. *citations pages 16*

X.-Y. Liu, R.-L. Li, H.-W. Zhao, T.-H. Cheng, G.-J. Cui, Q.-C. Tan, and G.-W. Meng. Quality assessment of speckle patterns for digital image correlation by shannon entropy. *Optik*, 126(23):4206–4211, 2015. *2 citations pages 42 and 43*

S. V. Lomov, D. S. Ivanov, I. Verpoest, M. Zako, T. Kurashiki, H. Nakai, and S. Hirosawa. Meso-fe modelling of textile composites: Road map, data flow and algorithms. *Composites science and technology*, 67(9):1870–1891, 2007. *citations pages 131*

S. V. Lomov, P. Boisse, E. Deluycker, F. Morestin, K. Vanclooster, D. Vandepitte, I. Verpoest, and A. Willems. Full-field strain measurements in textile deformability studies. *Composites Part A: Applied Science and Manufacturing*, 39(8):1232–1244, 2008. *5 citations pages 1, 33, 49, 83, and 111*

B. London, R. N. Yancey, and J. Smith. High-resolution x-ray computed tomography of composite materials. *Materials Evaluation*, 48:604–608, 1990. *citations pages 2*

A. Long and M. Clifford. Composite forming mechanisms and materials characterisation. *Composites forming technologies*, pages 1–21, 2007. *3 citations pages xiii, 22, and 23*

A. C. Long. *Design and manufacture of textile composites.* Elsevier, 2005. *3 citations pages xiii, 15, and 16*

P. R. Lord. *Weaving: Conversion of yarn to fabric*, volume 12. Woodhead Publishing, 1982. *citations pages 14*

J. Lyons, J. Liu, and M. Sutton. High-temperature deformation measurements using digital-image correlation. *Experimental mechanics*, 36(1):64–70, 1996. *citations pages 33*

A. Maazouz, J. Dupuy, and G. Seytre. Polyurethane and unsaturated polyester hybrid networks: chemorheological and dielectric study for the resin transfer molding process (rtm). *Polymer Engineering & Science*, 40(3):690–701, 2000. *citations pages 17*

A. Mallach, F. Härtel, F. Heieck, J.-P. Fuhr, P. Middendorf, and M. Gude. Experimental comparison of a macroscopic draping simulation for dry non-crimp fabric preforming on a complex geometry by means of optical measurement. *Journal of Composite Materials*, 51(16):2363–2375, 2017. *citations pages 33*

V. Mazars, O. Caty, G. Couégnat, A. Bouterf, S. Roux, S. Denneulin, J. Pailhès, and G. L. Vignoles. Damage investigation and modeling of 3d woven ceramic matrix composites from x-ray tomography in-situ tensile tests. *Acta Materialia*, 140:130–139, 2017. *citations pages 111*

G. McGuinness and C. ÓBrádaigh. Characterisation of thermoplastic composite melts in rhombus-shear: the picture-frame experiment. *Composites Part A: Applied Science and Manufacturing*, 29(1-2):115–132, 1998. *citations pages 27*

S. McNeill, W. Peters, and M. Sutton. Estimation of stress intensity factor by digital image correlation. *Engineering fracture mechanics*, 28(1):101–112, 1987. *citations pages 33*

M. Mehdikhani, C. Breite, Y. Swolfs, J. Soete, M. Wevers, S. V. Lomov, and L. Gorbatikh. Digital volume correlation for meso/micro in-situ damage analysis in carbon fiber reinforced composites. *Composites Science and Technology*, 213:108944, 2021. *citations pages 111*

H. Mei, Z. Ali, Y. Yan, I. Ali, and L. Cheng. Influence of mixed isotropic fiber angles and hot press on the mechanical properties of 3d printed composites. *Additive Manufacturing*, 27:150–158, 2019. *citations pages 20*

Q. Mei, J. Gao, H. Lin, Y. Chen, H. Yunbo, W. Wang, G. Zhang, and X. Chen. Structure light telecentric stereoscopic vision 3d measurement system based on scheimpflug condition. *Optics and Lasers in Engineering*, 86:83–91, 2016. *citations pages 39*

A. Mendoza, J. Schneider, E. Parra, and S. Roux. The correlation framework: Bridging the gap between modeling and analysis for 3d woven composites. *Composite Structures*, 229:111468, 2019. *citations pages 111*

B. Middleton. 3 - composites: Manufacture and application. In V. Goodship, B. Middleton, and R. Cherrington, editors, *Design and Manufacture of Plastic Components for Multifunctionality*, pages 53–101. William Andrew Publishing, Oxford, 2016. ISBN 978-0-323-34061-8. doi: https://doi.org/10.1016/B978-0-323-34061-8.00003-X. URL `https://www.sciencedirect.com/science/article/pii/B978032334061800003X`. *citations pages 8*

D. Mikhaluk, T. Truong, A. Borovkov, S. V. Lomov, and I. Verpoest. Experimental observations and finite element modelling of damage initiation and evolution in carbon/epoxy non-crimp fabric composites. *Engineering Fracture Mechanics*, 75(9):2751–2766, 2008. *citations pages 29*

A. Moffat, P. Wright, J.-Y. Buffière, I. Sinclair, and S. M. Spearing. Micromechanisms of damage in 0 splits in a [90/0] s composite material using synchrotron radiation computed tomography. *Scripta Materialia*, 59(10):1043–1046, 2008. *citations pages 111*

U. Mohammed, C. Lekakou, and M. Bader. Experimental studies and analysis of the draping of woven fabrics. *Composites Part A: Applied science and manufacturing*, 31 (12):1409–1420, 2000a. *citations pages 29*

U. Mohammed, C. Lekakou, L. Dong, and M. Bader. Shear deformation and micromechanics of woven fabrics. *Composites Part A: Applied Science and Manufacturing*, 31 (4):299–308, 2000b. *3 citations pages 1, 25, and 27*

L. Montero, S. Allaoui, and G. Hivet. Characterisation of the mesoscopic and macroscopic friction behaviours of glass plain weave reinforcement. *Composites Part A: Applied Science and Manufacturing*, 95:257–266, 2017. *4 citations pages xx, 131, 132, and 144*

M. Moore and R. Bland. Rtm equipment and process automation. *SAMPE Journal(USA)*, 35(2):39–46, 1999. *citations pages 17*

A. Morales-Rodriguez, P. Reynaud, G. Fantozzi, J. Adrien, and E. Maire. Porosity analysis of long-fiber-reinforced ceramic matrix composites using x-ray tomography. *Scripta Materialia*, 60(6):388–390, 2009. *citations pages 45*

N. Naouar, E. Vidal-Sallé, J. Schneider, E. Maire, and P. Boisse. Meso-scale fe analyses of textile composite reinforcement deformation based on x-ray computed tomography. *Composite Structures*, 116:165–176, 2014. *4 citations pages xiv, 44, 45, and 83*

N. Naouar, E. Vidal-Salle, J. Schneider, E. Maire, and P. Boisse. 3d composite reinforcement meso fe analyses based on x-ray computed tomography. *Composite Structures*, 132:1094–1104, 2015. *3 citations pages 83, 111, and 131*

N. Naouar, D. Vasiukov, C. Park, S. Lomov, and P. Boisse. Meso-fe modelling of textile composites and x-ray tomography. *Journal of Materials Science*, 55:16969–16989, 2020. *citations pages 83*

J. Neggers, B. Blaysat, J. P. Hoefnagels, and M. G. Geers. On image gradients in digital image correlation. *International Journal for Numerical Methods in Engineering*, 105 (4):243–260, 2016. *citations pages 36*

N. Nguyen, A. Hao, J. G. Park, and R. Liang. In situ curing and out-of-autoclave of interply carbon fiber/carbon nanotube buckypaper hybrid composites using electrical current. *Advanced engineering materials*, 18(11):1906–1912, 2016. *citations pages 18*

M. Nishi, T. Hirashima, and T. Kurashiki. Textile composite reinforcement forming analysis considering out-of-plane bending stiffness and tension dependent in-plane shear behavior. In *Proceedings of the 16th European Conference On Composite Materials, Seville, Spain*, 2014. *citations pages 83*

F. Nosrat-Nezami, T. Gereke, C. Eberdt, and C. Cherif. Characterisation of the shear–tension coupling of carbon-fibre fabric under controlled membrane tensions for precise simulative predictions of industrial preforming processes. *Composites Part A: Applied Science and Manufacturing*, 67:131–139, 2014. *citations pages 83*

A. R. Offringa. Thermoplastic composites—rapid processing applications. *Composites Part A: Applied Science and Manufacturing*, 27(4):329–336, 1996. *citations pages 6*

J.-J. Orteu. 3-d computer vision in experimental mechanics. *Optics and lasers in engineering*, 47(3-4):282–291, 2009. *citations pages 35*

J.-J. Orteu, D. Garcia, L. Robert, and F. Bugarin. A speckle texture image generator. In *Speckle06: speckles, from grains to flowers*, volume 6341, pages 104–109. SPIE, 2006. *citations pages 43*

J. D. O'Sullivan, J. Behnsen, T. Starborg, A. S. MacDonald, A. T. Phythian-Adams, K. J. Else, S. M. Cruickshank, and P. J. Withers. X-ray micro-computed tomography (μct): an emerging opportunity in parasite imaging. *Parasitology*, 145(7):848–854, 2018. *3 citations pages xiv, 44, and 45*

M. Owen, V. Middleton, and C. Rudd. Fibre reinforcement for high volume resin transfer moulding (rtm). *Composites Manufacturing*, 1(2):74–78, 1990. *citations pages 17*

T. Palin-Luc, E. Sellier, F. d'Errico, and M. Vanhaeren. Elastomer and resin replicas for sem observation of metallic materials. *Experimental techniques*, 26(3):33–37, 2002. *citations pages 22*

B. Pan. Recent progress in digital image correlation. *Experimental mechanics*, 51(7): 1223–1235, 2011. *2 citations pages xiv and 35*

B. Pan. Digital image correlation for surface deformation measurement: historical developments, recent advances and future goals. *Measurement Science and Technology*, 29 (8):082001, 2018. *6 citations pages xiv, 33, 34, 40, 41, and 77*

B. Pan, Z. Lu, and H. Xie. Mean intensity gradient: an effective global parameter for quality assessment of the speckle patterns used in digital image correlation. *Optics and Lasers in Engineering*, 48(4):469–477, 2010. *2 citations pages 41 and 43*

B. Pan, W. Dafang, and X. Yong. Incremental calculation for large deformation measurement using reliability-guided digital image correlation. *Optics and Lasers in Engineering*, 50(4):586–592, 2012. *3 citations pages 83, 90, and 107*

B. Pan, L. Yu, and D. Wu. High-accuracy 2d digital image correlation measurements with bilateral telecentric lenses: error analysis and experimental verification. *Experimental Mechanics*, 53(9):1719–1733, 2013. *citations pages 35*

B. Pan, L. Yu, and Q. Zhang. Review of single-camera stereo-digital image correlation techniques for full-field 3d shape and deformation measurement. *Science China Technological Sciences*, 61(1):2–20, 2018. *citations pages 40*

R. Parai and S. Bandyopadhyay-Ghosh. Engineered bio-nanocomposite magnesium scaffold for bone tissue regeneration. *Journal of the mechanical behavior of biomedical materials*, 96:45–52, 2019. *citations pages 2*

J.-C. Passieux. jcpassieux/pyxel: pyxel v1.0, Mar. 2021. URL `https://doi.org/10.5281/zenodo.4654018`. *6 citations pages xiv, xv, 36, 38, 55, and 61*

J.-C. Passieux and R. Bouclier. Classic and inverse compositional gauss-newton in global dic. *International Journal for Numerical Methods in Engineering*, 119(6):453–468, 2019. *citations pages 36*

J.-C. Passieux, F. Bugarin, C. David, J.-N. Périé, and L. Robert. Multiscale displacement field measurement using digital image correlation: Application to the identification of elastic properties. *Experimental Mechanics*, 55:121–137, 2015. *2 citations pages 2 and 78*

J.-c. Passieux, R. Bouclier, and O. Weeger. Image-based isogeometric twins of lattices with virtual image correlation for varying cross-section beams. *International Journal for Numerical Methods in Engineering*, 124(10):2237–2260, 2023. *citations pages 165*

J. Patou. *Élaboration de pièces composites complexes par consolidation autoclave à partir de préformes textiles thermoplastiques renforcées fibres de carbone.* PhD thesis, Ecole des Mines d'Albi-Carmaux, 2018. *3 citations pages xiii, 20, and 40*

J. Patou, R. Bonnaire, E. De Luycker, and G. Bernhart. Influence of consolidation process on voids and mechanical properties of powdered and commingled carbon/pps laminates. *Composites Part A: Applied Science and Manufacturing*, 117:260–275, 2019. *7 citations pages xiii, 1, 12, 14, 50, 52, and 83*

X. Peng, J. Cao, J. Chen, P. Xue, D. Lussier, and L. Liu. Experimental and numerical analysis on normalization of picture frame tests for composite materials. *Composites Science and Technology*, 64(1):11–21, 2004. *3 citations pages 1, 25, and 27*

J.-N. Périé, S. Calloch, C. Cluzel, and F. Hild. Analysis of a multiaxial test on a c/c composite by using digital image correlation and a damage model. *Experimental Mechanics*, 42(3):318–328, 2002. *citations pages 36*

W. Peters and W. Ranson. Digital imaging techniques in experimental stress analysis. *Optical engineering*, 21(3):427–431, 1982. *citations pages 33*

J.-E. Pierré, J.-C. Passieux, J.-N. Périé, F. Bugarin, and L. Robert. Unstructured finite element-based digital image correlation with enhanced management of quadrature and lens distortions. *Optics and Lasers in Engineering*, 77:44–53, 2016. *4 citations pages xiv, 33, 36, and 38*

J.-E. Pierré, J.-C. Passieux, and J.-N. Périé. Finite element stereo digital image correlation: framework and mechanical regularization. *Experimental Mechanics*, 57(3): 443–456, 2017. *8 citations pages 25, 35, 36, 39, 40, 42, 147, and 165*

S. Pillay, U. K. Vaidya, and G. M. Janowski. Liquid molding of carbon fabric-reinforced nylon matrix composite laminates. *Journal of Thermoplastic Composite Materials*, 18 (6):509–527, 2005. *citations pages 17*

K. D. Potter. The early history of the resin transfer moulding process for aerospace applications. *Composites Part A: applied science and manufacturing*, 30(5):619–621, 1999. *citations pages 16*

D. K. Rajak, D. D. Pagar, P. L. Menezes, and E. Linul. Fiber-reinforced polymer composites: Manufacturing, properties, and applications. *Polymers*, 11(10):1667, 2019. *2 citations pages xiii and 19*

K. Raju, S. Ojha, and A. Harsha. Spray forming of aluminum alloys and its composites: an overview. *Journal of materials science*, 43(8):2509–2521, 2008. *citations pages 21*

M. Ramezankhani, B. Crawford, H. Khayyam, M. Naebe, R. Seethaler, and A. S. Milani. A multi-objective gaussian process approach for optimization and prediction of carbonization process in carbon fiber production under uncertainty. *Advanced Composites and Hybrid Materials*, 2(3):444–455, 2019. *2 citations pages 10 and 11*

D. Reagan, A. Sabato, and C. Niezrecki. Feasibility of using digital image correlation for unmanned aerial vehicle structural health monitoring of bridges. *Structural Health Monitoring*, 17(5):1056–1072, 2018. *citations pages 36*

G. Requena, G. Fiedler, B. Seiser, P. Degischer, M. Di Michiel, and T. Buslaps. 3d-quantification of the distribution of continuous fibres in unidirectionally reinforced composites. *Composites Part A: Applied Science and Manufacturing*, 40(2):152–163, 2009. *citations pages 111*

P. L. Reu, B. Blaysat, E. Andò, K. Bhattacharya, C. Couture, V. Couty, D. Deb, S. S. Fayad, M. A. Iadicola, S. Jaminion, et al. Dic challenge 2.0: Developing images and guidelines for evaluating accuracy and resolution of 2d analyses: Focus on the metrological efficiency indicator. *Experimental Mechanics*, 62(4):639–654, 2022. *citations pages 68*

C. R. Rios-Soberanis, R. H. Cruz-Estrada, J. Rodriguez-Laviada, and E. Perez-Pacheco. Study of mechanical behavior of textile reinforced composite materials. *Dyna*, 79(176): 115–123, 2012. *citations pages 83*

D. Rohe and E. Jones. Generation of synthetic digital image correlation images using the open-source blender software. *Experimental Techniques*, 46(4):615–631, 2022. *citations pages 68*

D. Rouison, M. Sain, and M. Couturier. Resin transfer molding of natural fiber reinforced composites: cure simulation. *Composites science and technology*, 64(5):629–644, 2004. *2 citations pages 15 and 17*

A. Rouwane, R. Bouclier, J.-C. Passieux, and J.-N. Périé. Architecture-driven digital image correlation technique (addict) for the measurement of sub-cellular kinematic fields in speckle-free cellular materials. *International Journal of Solids and Structures*, 234:111223, 2022. *2 citations pages 78 and 111*

A. Rouwane, P. Doumalin, R. Bouclier, J.-C. Passieux, and J.-N. Périé. Architecture-driven digital volume correlation: application to the analysis of in-situ crushing of a polyurethane foam. *Experimental Mechanics*, pages 1–17, 2023a. *2 citations pages 78 and 80*

A. Rouwane, P. Doumalin, R. Bouclier, J.-C. Passieux, and J.-N. Périé. Architecture-driven digital volume correlation: application to the analysis of in-situ crushing of a polyurethane foam. *Experimental Mechanics*, 2023b. *6 citations pages 108, 111, 112, 135, 160, and 162*

S. Roux, F. Hild, P. Viot, and D. Bernard. Three-dimensional image correlation from x-ray computed tomography of solid foam. *Composites Part A: Applied science and manufacturing*, 39(8):1253–1265, 2008. *citations pages 155*

O. Rozant, P.-E. Bourban, and J.-A. Månson. Drapability of dry textile fabrics for stampable thermoplastic preforms. *Composites Part A: Applied Science and Manufacturing*, 31(11):1167–1177, 2000. ISSN 1359-835X. doi: https://doi.org/10.1016/S1359-835X(00)00100-7. URL `https://www.sciencedirect.com/science/article/pii/S1359835X00001007`. *citations pages 22*

C. D. Rudd, A. C. Long, K. Kendall, and C. Mangin. *Liquid moulding technologies: Resin transfer moulding, structural reaction injection moulding and related processing techniques*. Elsevier, 1997. *2 citations pages 15 and 22*

S. Russell and M. Sutton. Strain-field analysis acquired through correlation of x-ray radiographs of a fiber-reinforced composite laminate. *Experimental Mechanics*, 29:237–240, 1989. *citations pages 155*

L. Salvo, P. Cloetens, E. Maire, S. Zabler, J. J. Blandin, J.-Y. Buffiere, W. Ludwig, E. Boller, D. Bellet, and C. Josserond. X-ray micro-tomography an attractive characterisation technique in materials science. *Nuclear instruments and methods in physics research section B: Beam interactions with materials and atoms*, 200:273–286, 2003. *citations pages 2*

T. Sathishkumar, S. Satheeshkumar, and J. Naveen. Glass fiber-reinforced polymer composites–a review. *Journal of reinforced plastics and composites*, 33(13):1258–1275, 2014. *citations pages 9*

C. Sawaryn, S. Kreiling, R. Schönfeld, K. Landfester, and A. Taden. Benzoxazines for industrial applications comparison with other resins, formulation and toughening know-how, and water-based dispersion technology. In *Handbook of Benzoxazine Resins*, pages 605–620. Elsevier, 2011. *2 citations pages xiii and 10*

C. Scarponi, C. Pizzinelli, S. Sánchez-Sáez, and E. Barbero. Impact load behaviour of resin transfer moulding (rtm) hemp fibre composite laminates. *Journal of Biobased Materials and Bioenergy*, 3(3):298–310, 2009. *citations pages 15*

P. J. Schilling, B. R. Karedla, A. K. Tatiparthi, M. A. Verges, and P. D. Herrington. X-ray computed microtomography of internal damage in fiber reinforced polymer matrix composites. *Composites science and technology*, 65(14):2071–2078, 2005. *citations pages 111*

E. Schmachtenberg, J. S. Zur Heide, and J. Töpker. Application of ultrasonics for the process control of resin transfer moulding (rtm). *Polymer testing*, 24(3):330–338, 2005. *2 citations pages 16 and 17*

E. Schöberl, C. Breite, A. Melnikov, Y. Swolfs, M. N. Mavrogordato, I. Sinclair, and S. M. Spearing. Fibre-direction strain measurement in a composite ply under quasi-static tensile loading using digital volume correlation and in situ synchrotron radiation computed tomography. *Composites Part A: Applied Science and Manufacturing*, 137: 105935, 2020. *citations pages 111*

A. Schulz, V. Uhlenwinkel, C. Escher, R. Kohlmann, A. Kulmburg, M. C. Montero, R. Rabitsch, W. Schützenhöfer, D. Stocchi, and D. Viale. Opportunities and challenges of spray forming high-alloyed steels. *Materials Science and Engineering: A*, 477(1-2): 69–79, 2008. *citations pages 21*

A. Scott, M. Mavrogordato, P. Wright, I. Sinclair, and S. Spearing. In situ fibre fracture measurement in carbon–epoxy laminates using high resolution computed tomography. *Composites Science and Technology*, 71(12):1471–1477, 2011. *citations pages 111*

J. A. Seibert. Iterative reconstruction: how it works, how to apply it. *Pediatric radiology*, 44(3):431–439, 2014. *citations pages 44*

B. Semin, H. Auradou, and M. L. M. François. Accurate measurement of curvilinear shapes by virtual image correlation. *The European Physical Journal-Applied Physics*, 56(1):10701, 2011. *citations pages 165*

R. Sencu, Z. Yang, Y. Wang, P. Withers, C. Rau, A. Parson, and C. Soutis. Generation of micro-scale finite element models from synchrotron x-ray ct images for multidirectional carbon fibre reinforced composites. *Composites Part A: Applied Science and Manufacturing*, 91:85–95, 2016. *citations pages 111*

X. Shao, X. Dai, Z. Chen, Y. Dai, S. Dong, and X. He. Calibration of stereo-digital image correlation for deformation measurement of large engineering components. *Measurement Science and Technology*, 27(12):125010, 2016. *citations pages 40*

Y. Shi, B. Blaysat, H. Chanal, and M. Grédiac. Designing patterns for dic with poisson image editing. *Experimental Mechanics*, 62(7):1093–1117, 2022. *citations pages 79*

A. Sibellas, J. Adrien, D. Durville, and E. Maire. Experimental study of the fiber orientations in single and multi-ply continuous filament yarns. *The Journal of The Textile Institute*, 111(5):646–659, 2020. *citations pages 125*

Y. Sinchuk, Y. Pannier, R. Antoranz-Gonzalez, and M. Gigliotti. Analysis of moisture diffusion induced stress in carbon/epoxy 3d textile composite materials with voids by μ-ct based finite element models. *Composite Structures*, 212:561–570, 2019. *citations pages 111*

A. Singer. Metal matrix composites made by spray forming. *Materials Science and Engineering: A*, 135:13–17, 1991. *citations pages 21*

L. S. Singer. Carbon fibres from mesophase pitch. *Fuel*, 60(9):839–847, 1981. *citations pages 10*

J. Sirtautas, A. Pickett, and P. Lépicier. A mesoscopic model for coupled drape-infusion simulation of biaxial non-crimp fabric. *Composites Part B: Engineering*, 47:48–57, 2013. *citations pages 31*

S. Soukane and F. Trochu. Application of the level set method to the simulation of resin transfer molding. *Composites Science and Technology*, 66(7-8):1067–1080, 2006. *citations pages 1*

C. Soutis. Fibre reinforced composites in aircraft construction. *Progress in aerospace sciences*, 41(2):143–151, 2005a. *citations pages 6*

C. Soutis. Fibre reinforced composites in aircraft construction. *Progress in aerospace sciences*, 41(2):143–151, 2005b. *citations pages 20*

E. Sozer, P. Simacek, and S. Advani. Resin transfer molding (rtm) in polymer matrix composites. In *Manufacturing techniques for polymer matrix composites (PMCs)*, pages 245–309. Elsevier, 2012. *citations pages 15*

P. Sreekumar, J. M. Saiter, K. Joseph, G. Unnikrishnan, and S. Thomas. Electrical properties of short sisal fiber reinforced polyester composites fabricated by resin transfer molding. *Composites Part A: Applied Science and Manufacturing*, 43(3):507–511, 2012. *citations pages 17*

T. S. Srivatsan and E. Lavernia. Use of spray techniques to synthesize particulate-reinforced metal-matrix composites. *Journal of materials science*, 27:5965–5981, 1992. *citations pages 21*

W. Stark, J. Doring, V. Bovtun, and C. Kurten. Monitoring of curing reaction of poly-condensating thermosets at press and injection moulding. *Journal of Nondestructive Testing & Ultrasonics(Germany)*, 3(11):141, 1998. *citations pages 16*

J. M. Stickel and M. Nagarajan. Glass fiber-reinforced composites: From formulation to application. *International Journal of Applied Glass Science*, 3(2):122–136, 2012. *2 citations pages xiii and 8*

J. Stinville, M. Echlin, D. Texier, F. Bridier, P. Bocher, and T. Pollock. Sub-grain scale digital image correlation by electron microscopy for polycrystalline materials during elastic and plastic deformation. *Experimental mechanics*, 56:197–216, 2016. *citations pages 51*

Y. Su and Q. Zhang. Glare: A free and open-source software for generation and assessment of digital speckle pattern. *Optics and Lasers in Engineering*, 148:106766, 2022. *citations pages 43*

Y. Su, Q. Zhang, X. Xu, and Z. Gao. Quality assessment of speckle patterns for dic by consideration of both systematic errors and random errors. *Optics and Lasers in Engineering*, 86:132–142, 2016. *citations pages 41*

J. Summerscales and T. Searle. Low-pressure (vacuum infusion) techniques for moulding large composite structures. *Proceedings of the institution of mechanical engineers, Part L: Journal of materials: design and applications*, 219(1):45–58, 2005. *2 citations pages 18 and 19*

Y. Sun, J. H. Pang, C. K. Wong, and F. Su. Finite element formulation for a digital image correlation method. *Applied optics*, 44(34):7357–7363, 2005. *4 citations pages xiv, 2, 35, and 36*

F. Sur, B. Blaysat, and M. Grédiac. Rendering deformed speckle images with a boolean model. *Journal of Mathematical Imaging and Vision*, 60:634–650, 2018. *citations pages 43*

M. A. Sutton, W. Wolters, W. Peters, W. Ranson, and S. McNeill. Determination of displacements using an improved digital correlation method. *Image and vision computing*, 1(3):133–139, 1983. *2 citations pages 33 and 35*

M. A. Sutton, J. Yan, V. Tiwari, H. Schreier, and J.-J. Orteu. The effect of out-of-plane motion on 2d and 3d digital image correlation measurements. *Optics and Lasers in Engineering*, 46(10):746–757, 2008. *2 citations pages 34 and 40*

M. A. Sutton, J. J. Orteu, and H. Schreier. *Image correlation for shape, motion and deformation measurements: basic concepts, theory and applications*. Springer Science & Business Media, 2009. *4 citations pages 33, 40, 51, and 59*

N. Svensson, R. Shishoo, and M. Gilchrist. Manufacturing of thermoplastic composites from commingled yarns-a review. *Journal of Thermoplastic Composite Materials*, 11 (1):22–56, 1998. *citations pages 1*

E. Syerko, S. Comas-Cardona, and C. Binetruy. Models for shear properties/behavior of dry fibrous materials at various scales: a review. *International Journal of Material Forming*, 8(1):1–23, 2015. *citations pages 22*

I. Taha, Y. Abdin, and S. Ebeid. Comparison of picture frame and bias-extension tests for the characterization of shear behaviour in natural fibre woven fabrics. *Fibers and Polymers*, 14:338–344, 2013. *3 citations pages 1, 25, and 26*

K. Takenaka and M. Ichigo. Thermal expansion adjustable polymer matrix composites with giant negative thermal expansion filler. *Composites science and technology*, 104: 47–51, 2014. *2 citations pages 18 and 20*

Z. Tang, J. Liang, Z. Xiao, and C. Guo. Large deformation measurement scheme for 3d digital image correlation method. *Optics and lasers in engineering*, 50(2):122–130, 2012. *citations pages 90*

E. T. Thostenson, Z. Ren, and T.-W. Chou. Advances in the science and technology of carbon nanotubes and their composites: a review. *Composites science and technology*, 61(13):1899–1912, 2001. *citations pages 18*

H. Toda, I. Sinclair, J.-Y. Buffière, E. Maire, T. Connolley, M. Joyce, K. Khor, and P. Gregson. Assessment of the fatigue crack closure phenomenon in damage-tolerant aluminium alloy by in-situ high-resolution synchrotron x-ray microtomography. *Philosophical Magazine*, 83(21):2429–2448, 2003. *citations pages 45*

R. D. Toledo Filho, F. de Andrade Silva, E. Fairbairn, and J. de Almeida Melo Filho. Durability of compression molded sisal fiber reinforced mortar laminates. *Construction and building materials*, 23(6):2409–2420, 2009. *citations pages 17*

M. Toloczko, M. Hamilton, and G. Lucas. Ductility correlations between shear punch and uniaxial tensile test data. *Journal of nuclear materials*, 283:987–991, 2000. *2 citations pages 1 and 25*

Toray. Category carbon fiber. https://www.toraycma.com/products/carbon-fiber/#pattern6_1, 2022. *citations pages 11*

H. Towsyfyan, A. Biguri, R. Boardman, and T. Blumensath. Successes and challenges in non-destructive testing of aircraft composite structures. *Chinese Journal of Aeronautics*, 33(3):771–791, 2020. *citations pages 6*

I. Tretiak and R. A. Smith. A parametric study of segmentation thresholds for x-ray ct porosity characterisation in composite materials. *Composites Part A: Applied Science and Manufacturing*, 123:10–24, 2019. *2 citations pages 2 and 45*

T. C. Truong, M. Vettori, S. Lomov, and I. Verpoest. Carbon composites based on multi-axial multi-ply stitched preforms. part 4. mechanical properties of composites and damage observation. *Composites Part A: applied science and manufacturing*, 36 (9):1207–1221, 2005. *citations pages 29*

G. Tuncol, M. Danisman, A. Kaynar, and E. M. Sozer. Constraints on monitoring resin flow in the resin transfer molding (rtm) process by using thermocouple sensors. *Composites Part A: Applied Science and Manufacturing*, 38(5):1363–1386, 2007. *2 citations pages 16 and 17*

M.-K. Um and W. I. Lee. A study on the mold filling process in resin transfer molding. *Polymer Engineering & Science*, 31(11):765–771, 1991. *citations pages 17*

K. Vanclooster, S. V. Lomov, and I. Verpoest. Experimental validation of forming simulations of fabric reinforced polymers using an unsymmetrical mould configuration. *Composites Part A: Applied Science and Manufacturing*, 40(4):530–539, 2009. *citations pages 33*

B. Vieille, V. M. Casado, and C. Bouvet. About the impact behavior of woven-ply carbon fiber-reinforced thermoplastic-and thermosetting-composites: a comparative study. *Composite structures*, 101:9–21, 2013. *citations pages 6*

T. Vijayaram, S. Sulaiman, A. Hamouda, and M. Ahmad. Fabrication of fiber reinforced metal matrix composites by squeeze casting technology. *Journal of Materials Processing Technology*, 178(1-3):34–38, 2006. *citations pages 22*

J. Vilà, F. Sket, F. Wilde, G. Requena, C. González, and J. LLorca. An in situ investigation of microscopic infusion and void transport during vacuum-assisted infiltration by means of x-ray computed tomography. *Composites science and technology*, 119:12–19, 2015. *citations pages 111*

I. C. Visconti and A. Langella. Analytical modelling of pressure bag technology. *Composites Manufacturing*, 3(1):3–6, 1992. *citations pages 19*

J. R. Wagner. 10 - blown film, cast film, and lamination processes. In J. R. Wagner, editor, *Multilayer Flexible Packaging (Second Edition)*, Plastics Design Library, pages 137–145. William Andrew Publishing, second edition edition, 2016. ISBN 978-0-323-37100-1. doi: https://doi.org/10.1016/B978-0-323-37100-1.00010-7. URL https://www.sciencedirect.com/science/article/pii/B9780323371001000107. *2 citations pages xiii and 18*

M. Wakeman, L. Zingraff, P.-E. Bourban, J.-A. Månson, and P. Blanchard. Stamp forming of carbon fibre/pa12 composites–a comparison of a reactive impregnation process and a commingled yarn system. *Composites Science and Technology*, 66(1):19–35, 2006. *2 citations pages 1 and 25*

H. Wang, H. Xie, Y. Li, and J. Zhu. Fabrication of micro-scale speckle pattern and its applications for deformation measurement. *Measurement Science and Technology*, 23 (3):035402, 2012. *citations pages 43*

J. Wang, P. Wang, N. Hamila, and P. Boisse. Mesoscopic analyses of the draping of 3d woven composite reinforcements based on macroscopic simulations. *Composite Structures*, 250:112602, 2020. *citations pages 2*

P. Wang, N. Hamila, P. Pineau, and P. Boisse. Thermomechanical analysis of thermoplastic composite prepregs using bias-extension test. *Journal of Thermoplastic Composite Materials*, 27(5):679–698, 2014. *2 citations pages 1 and 25*

P. Wang, N. Hamila, P. Boisse, P. Chaudet, and D. Lesueur. Thermo-mechanical behavior of stretch-broken carbon fiber and thermoplastic resin composites during manufacturing. *Polymer Composites*, 36(4):694–703, 2015. *citations pages 13*

P. Wang, H. Lei, X. Zhu, H. Chen, C. Wang, and D. Fang. Effect of manufacturing defect on mechanical performance of plain weave carbon/epoxy composite based on 3d geometrical reconstruction. *Composite Structures*, 199:38–52, 2018a. *citations pages 111*

Y. Wang, L. P. Mikkelsen, G. Pyka, and P. J. Withers. Time-lapse helical x-ray computed tomography (ct) study of tensile fatigue damage formation in composites for wind turbine blades. *Materials*, 11(11):2340, 2018b. *citations pages 2*

Z. Wang, M. Bobbert, C. Dammann, C. Zinn, C. Lauter, R. Mahnken, G. Meschut, M. Schaper, and T. Troester. Influences of interface and surface pretreatment on the mechanical properties of metal-cfrp hybrid structures manufactured by resin transfer moulding. *International Journal of Automotive Composites*, 2(3-4):272–298, 2016. *citations pages 17*

J. Wannasin and M. Flemings. Fabrication of metal matrix composites by a high-pressure centrifugal infiltration process. *Journal of Materials Processing Technology*, 169(2): 143–149, 2005. *citations pages 22*

A. Willems, S. V. Lomov, I. Verpoest, and D. Vandepitte. Optical strain fields in shear and tensile testing of textile reinforcements. *Composites Science and Technology*, 68 (3-4):807–819, 2008. *3 citations pages 1, 33, and 83*

A. Willems, S. V. Lomov, I. Verpoest, and D. Vandepitte. Drape-ability characterization of textile composite reinforcements using digital image correlation. *Optics and Lasers in Engineering*, 47(3-4):343–351, 2009. *citations pages 83*

C. Williams, J. Summerscales, and S. Grove. Resin infusion under flexible tooling (rift): a review. *Composites Part A: Applied Science and Manufacturing*, 27(7):517–524, 1996. *citations pages 19*

P. Xue, J. Cao, and J. Chen. Integrated micro/macro-mechanical model of woven fabric composites under large deformation. *Composite structures*, 70(1):69–80, 2005. *citations pages 1*

S.-Q. Yang, P.-F. Yin, Y.-H. Huang, and J.-L. Cheng. Strength, deformability and x-ray micro-ct observations of transversely isotropic composite rock under different confining pressures. *Engineering Fracture Mechanics*, 214:1–20, 2019. *citations pages 2*

J. Ye, S. André, and L. Farge. Kinematic study of necking in a semi-crystalline polymer through 3d digital image correlation. *International Journal of Solids and Structures*, 59:58–72, 2015. *citations pages 36*

L. Ye, Y. Lu, Z. Su, and G. Meng. Functionalized composite structures for new generation airframes: a review. *Composites science and technology*, 65(9):1436–1446, 2005. *citations pages 6*

B. Yenilmez and E. M. Sozer. A grid of dielectric sensors to monitor mold filling and resin cure in resin transfer molding. *Composites part a: applied science and manufacturing*, 40(4):476–489, 2009. *citations pages 17*

H. Yin, X. Peng, T. Du, and Z. Guo. Draping of plain woven carbon fabrics over a double-curvature mold. *Composites Science and Technology*, 92:64–69, 2014. *citations pages 30*

W.-B. Young. Three-dimensional nonisothermal mold filling simulations in resin transfer molding. *Polymer composites*, 15(2):118–127, 1994. *citations pages 17*

Z. Yousaf, P. Withers, and P. Potluri. Compaction, nesting and image based permeability analysis of multi-layer dry preforms by computed tomography (ct). *Composite Structures*, 263:113676, 2021. *citations pages 111*

J. Zhang, V. S. Chevali, H. Wang, and C.-H. Wang. Current status of carbon fibre and carbon fibre composites recycling. *Composites Part B: Engineering*, 193:108053, 2020. *citations pages 6*

B. Zhu, T. Yu, and X. Tao. An experimental study of in-plane large shear deformation of woven fabric composite. *Composites science and technology*, 67(2):252–261, 2007a. *2 citations pages xiv and 27*

B. Zhu, T. Yu, and X. Tao. Large deformation and slippage mechanism of plain woven composite in bias extension. *Composites Part A: Applied Science and Manufacturing*, 38(8):1821–1828, 2007b. *3 citations pages 1, 2, and 83*

B. Zhu, T. Yu, H. Zhang, and X. Tao. Experimental investigation of formability of commingled woven composite preform in stamping operation. *Composites Part B: Engineering*, 42(2):289–295, 2011. *citations pages 2*